Pathology & Oncology Research

Pathology & Oncology Research–Editors' Picks from 2021

Issue Editors

József Tímár
Semmelweis University, Hungary

László Kopper
Semmelweis University, Hungary

Andrea Ladányi
National Institute of Oncology (NIO), Hungary

Anna Sebestyén
Semmelweis University, Hungary

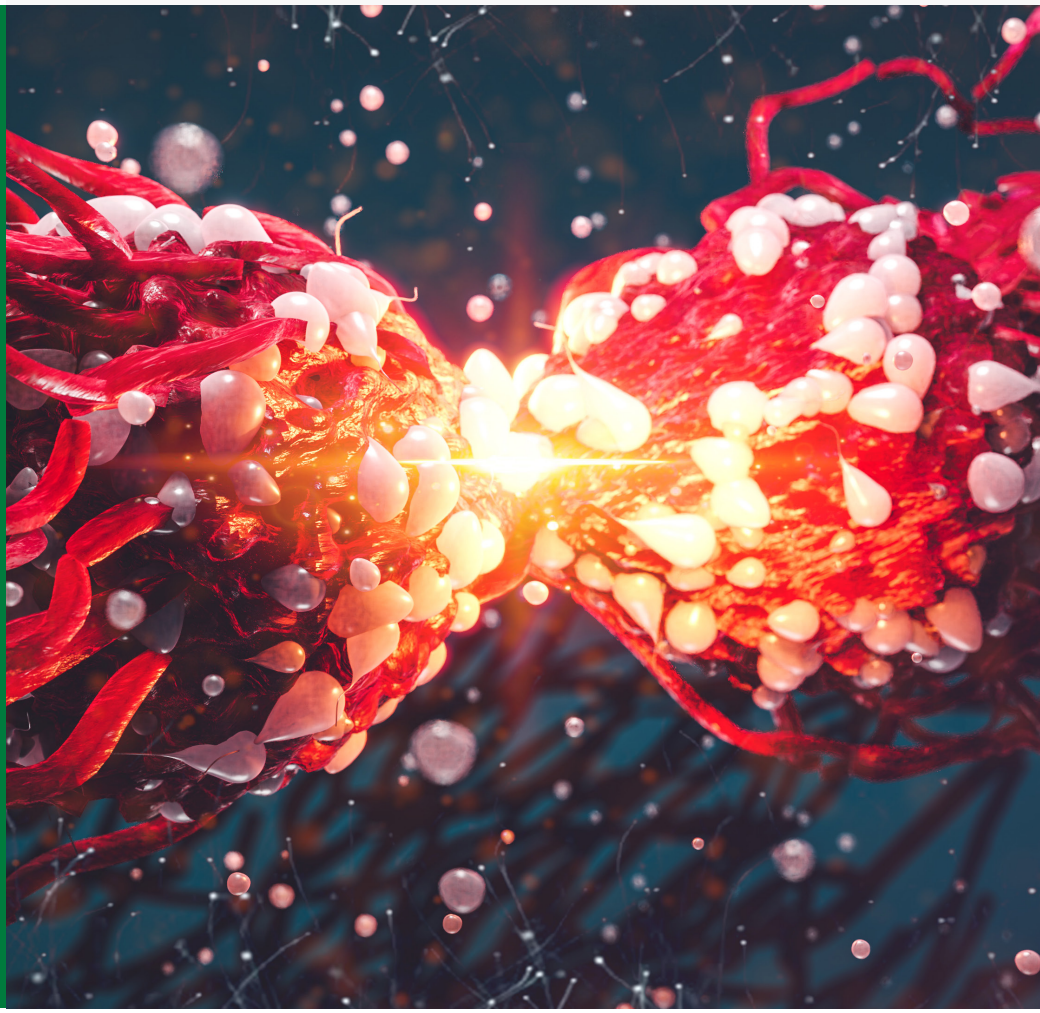

frontiers | Publishing Partnerships

Pathology & Oncology Research

Pathology & Oncology Research–Editors' Picks from 2021

ISSN 2813-7108
ISBN 978-2-88974-770-2
DOI 10.3389/978-2-88974-770-2

We are pleased to introduce the collection Pathology & Oncology Research–Editors' Picks from 2021. This collection showcases the most well-received stand-alone articles published in 2021, selected with care by our Editors-in-Chief and Associate Editors.

The work presented here highlights the broad diversity of research published across the journal and aims to spotlight themes of topical interest. All research presented here displays compelling advancement of the fields of pathology and oncology, as well as work bridging the gap between basic research and clinical medicine. The selected articles cover four main categories: preclinical research, clinical research, oncology, and non-oncology. This collection aims to further support the journal's strong community of scholars by recognizing highly deserving authors, as well as contributing editors and reviewers.

Pathology & Oncology Research

Table of contents

Pathology & Oncology Research

frontiers

ORIGINAL RESEARCH
published: 26 March 2021
doi: 10.3389/pore.2021.636088

HDAC Inhibition Induces Cell Cycle Arrest and Mesenchymal-Epithelial Transition in a Novel Pleural-Effusion Derived Uterine Carcinosarcoma Cell Line

***Paul Stockhammer*[1,2†], *Özlem Okumus*[1], *Luca Hegedus*[1], *Dominika Rittler*[3], *Till Ploenes*[1], *Thomas Herold*[4], *Stavros Kalbourtzis*[4], *Agnes Bankfalvi*[4], *Antje Sucker*[5], *Rainer Kimmig*[6], *Clemens Aigner*[1†] *and Balazs Hegedus*[1*†]**

[1]*Department of Thoracic Surgery, Ruhrlandklinik, West German Cancer Center, University Hospital Essen, University Duisburg-Essen, Essen, Germany,* [2]*Division of Thoracic Surgery, Medical University of Vienna, Vienna, Austria,* [3]*2nd Institute of Pathology, Semmelweis University, Budapest, Hungary,* [4]*Institute of Pathology, University Hospital Essen, University Duisburg-Essen, Essen, Germany,* [5]*Department of Dermatology, University Hospital Essen, University Duisburg-Essen, Essen, Germany,* [6]*Department of Gynecology and Obstetrics, University Hospital Essen, University Duisburg-Essen, Essen, Germany*

Objective: Uterine carcinosarcoma (UCS) is a rare but highly aggressive malignancy with biphasic growth pattern. This morphology can be attributed to epithelial-mesenchymal transition (EMT) that often associates with tumor invasion and metastasis. Accordingly, we analyzed a novel patient-derived preclinical model to explore whether EMT is a potential target in UCS.

Methods: A novel UCS cell line (PF338) was established from the malignant pleural effusion of a 59-year-old patient at time of disease progression. Immunohistochemistry was performed in primary and metastatic tumor lesions. Oncogenic mutations were identified by next-generation sequencing. Viability assays and cell cycle analyses were used to test *in vitro* sensitivity to different standard and novel treatments. E-cadherin, β-catenin and pSMAD2 expressions were measured by immunoblot.

Results: Whereas immunohistochemistry of the metastatic tumor showed a predominantly sarcomatous vimentin positive tumor that has lost E-cadherin expression, PF338 cells demonstrated biphasic growth and carried mutations in *KRAS*, *PIK3CA*, *PTEN* and *ARID1A*. PF338 tumor cells were resistant to MEK- and TGF-β signaling-inhibition but sensitive to PIK3CA- and PARP-inhibition and first-line chemotherapeutics. Strikingly, histone deacetylase (HDAC) inhibition markedly reduced cell viability by inducing a dose-dependent G0/1 arrest and led to mesenchymal-epithelial transition as evidenced by morphological change and increased E-cadherin and β-catenin expression.

Conclusions: Our data suggest that HDAC inhibition is effective in a novel UCS cell line by interfering with both viability and differentiation. These findings emphasize the dynamic manner of EMT/MET and epigenetics and the importance of molecular profiling to pave the way for novel therapies in UCS.

OPEN ACCESS

Edited by:
Andrea Ladányi,
National Institute of Oncology (NIO), Hungary

***Correspondence:**
Balazs Hegedus
balazs.hegedues@rlk.uk-essen.de

†ORCID:
Paul Stockhammer
orcid.org/0000-0002-3321-0421
Clemens Aigner
orcid.org/0000-0002-7787-991X
Balazs Hegedus
orcid.org/0000-0002-4341-4153

Received: *30 November 2020*
Accepted: *01 March 2021*
Published: *26 March 2021*

Citation:
Stockhammer P, Okumus Ö, Hegedus L, Rittler D, Ploenes T, Herold T, Kalbourtzis S, Bankfalvi A, Sucker A, Kimmig R, Aigner C and Hegedus B (2021) HDAC Inhibition Induces Cell Cycle Arrest and Mesenchymal-Epithelial Transition in a Novel Pleural-Effusion Derived Uterine Carcinosarcoma Cell Line. Pathol. Oncol. Res. 27:636088. doi: 10.3389/pore.2021.636088

Keywords: uterine carcinosarcoma, targeted therapy, HDAC inhibition, epithelial-mesenchymal transition, mesenchymal-epithelial transition, ARID1A

INTRODUCTION

Uterine carcinosarcoma (UCS) is a highly aggressive tumor that accounts for less than 5% of uterine malignancies [1, 2]. As a type of malignant mixed Müllerian tumors and related to poorly differentiated endometrial carcinomas, UCS is characterized by biphasic morphology with carcinomatous and sarcomatous differentiation [3, 4]. Compared to endometrial carcinoma, UCS has a worse prognosis with a high postoperative recurrence rate and a 5-year survival rate below 40% [5, 6]. In UCS, *TP53* has been identified as the most frequently mutated gene, followed by mutations in the PI3K pathway, *KRAS*, cell cycle regulators including *FBXW7* and chromatin remodeling and histone genes including *ARID1A* [7–9]. Importantly, UCS is the prototype tumor for epithelial-mesenchymal transition (EMT), a reversible biological process that associates with tumor progression and metastasis and in which epithelial cells transform into more invasive mesenchymal cells by losing their epithelial properties [10–12]. In UCS, several studies identified characteristic EMT-related expression signatures including active TGF-β signaling in tissue and cell lines [7, 11, 13, 14]. Interestingly, expression patterns of EMT-related markers including E-cadherin and ZEB1 were shown to differ between UCS carcinomatous and sarcomatous tumor areas [14]. The difference in E-cadherin expression is suggested to contribute to the biphasic growth pattern in UCS [15].

Recently, a transcriptome sequencing study in UCS demonstrated a strong correlation between EMT scores and epigenetic alterations [7]. In this regard, *ARID1A*, a commonly mutated chromatin remodeling gene in UCS, as well as the tumor suppressor *FBXW7* have been associated with EMT [16, 17]. Furthermore, mutations in either of them conferred sensitivity to histone deacetylase inhibition (HDACi) [18, 19]. In fact, histone modification by histone deacetylases is a major contributor to epigenetic changes in tumor cells and evidence suggests a functional role of HDAC inhibitors in EMT and phenotypic transformation of cancer cells [12, 20].

Suberoylanilide hydroxamic acid (SAHA), a pan-HDACi, and valproate are currently evaluated in various malignancies [20]. Although a significant portion of UCS harbor mutations in epigenetic regulators, evidence about HDACi in this entity is scarce. Previous studies found increased HDAC2 expression in endometrial stromal sarcomas and SAHA treatment in a uterine sarcoma cell line effectively suppressed growth [21, 22]. Accordingly, a recent study testing SAHA in UCS (NCT03509207) was initiated but soon after terminated due to issues in patient recruitment and access to medication. The potential of molecularly tailored therapies in UCS still needs to be further evaluated and novel UCS patient-derived cell lines are urgently needed as they are ideal models to study novel approaches. So far, there are just few reports of the successful establishment of UCS cell lines [23]. Accordingly, we aimed to investigate HDACi among other novel tailored approaches in a newly established UCS cell line. In this regard, we identified HDACi as a promising and reasonable approach targeting both epigenetics and EMT in UCS.

MATERIAL AND METHODS

Cell Culture and Reagents

The PF338 line was established from malignant pleural effusion. 5ml of effusion were centrifuged at 1,200 × *g* at room temperature for 10 min. The pellet was resuspended in RPMI1640 fortified by 10% FBS and 1% penicillin/streptomycin and seeded in a culture flask. More than 15 passages of the adherent cells with a minimum of three freezing-thawing cycles were done before experiments were initiated in order to use a tumor cell culture without non-tumorous cells. The A375 melanoma cell line was purchased from the ATCC and cultured in DMEM supplemented with 10% fetal bovine serum and 1% penicillin/streptomycin in culture flasks. Single Nucleotide Polymorphism (SNP) profiling was performed for PF338 and A375 tumor cell lines by Multiplex Cell Line Authentication (Multiplexion, Heidelberg, Germany) to confirm A375 cell line identity and PF338 unique cell line identity. Selumetinib, galunisertib, olaparib and BEZ235 were purchased from Selleck Chemicals (Houston, TX, United States) and dissolved in DMSO. SAHA and valproate were purchased from Sigma-Aldrich (St. Luis, MO, United States) and dissolved in DMSO and water, respectively. Paclitaxel (Kabi Fresenius, IL, United States) and cisplatin (Accord, Munich, Germany) were dissolved in 0.7% NaCl.

Immunohistochemistry

Immunohistochemistry was performed using the Ventana BenchMark Ultra system (Roche Tissue Diagnostics, Grenzach-Vyhlen, Germany). 3 µm sections were prepared from formalin-fixed and paraffin embedded (FFPE) tumors and PF338 cellblock. The following primary antibodies were used: CD10 (Clone 56C6, 1:50, Leica Biosystems, Nussloch Germany), E-cadherin (Clone: NCH-38, Dako-Agilent, Waldbronn, Germany), vimentin (Clone: V9, Dako-Agilent, Waldbronn, Germany), progesterone receptor (Clone: 1E2; RTU, Roche Tissue Diagnostics) and estrogen receptor (Clone SP1, RTU, Roche Tissue Diagnostics). Color development was performed by the OptiView staining kit (Roche Tissue Diagnostics) followed by hematoxylin counterstaining. All stainings were evaluated by a senior pathologist (AB) and representative images were taken.

Chemosensitivity Assays

Total protein amount-based Sulforhodamine B (SRB) assays were performed as follows. 5×10^3 (PF338) or 2×10^3 (A375) tumor cells /well were plated on the inner 60 wells of a 96-well plate and first incubated for 48 h. After 72 h of treatment with drugs, 10% TCA was used for fixation, followed by SRB dye (Sigma-Aldrich,

St. Louis, MO, United States), and wash out with 1% acetic acid. 10mM Tris puffer dissolved the protein-bound dye and optical density (OD) was read at 570 nm by using a microplate reader (EL800, bioTec Instruments, Winooski, VT, United States). IC_{50} were calculated by using the CompuSyn software (ComboSyn, Inc., Paramus, NJ). Viability results are illustrated as ratio to control viability. For colony-formation assays, 1,000 tumor cells /well were plated on 6-well plates, incubated for 48 h and subsequently treated every 3–4 days with increasing drug concentrations for 10 days. 10% TCA was used for fixation, followed by SRB dye and wash out with 1% acetic acid. Colonies were counted manually. Experiments were repeated thrice.

Cell Viability and Cell Cycle Analysis

In order to test the viability of cells after freezing and thawing at various passages the cell viability was measured on the NucleoCounter NC-3000TM system (Chemometec, Allerod, Denmark) using the cell viability reagents and protocol right after thawing and after 72 h in culture.

For cell cycle analysis, PF338 tumor cells were seeded on 6-well plates in 2×10^5 cells/well concentration and incubated for 48 h, followed by 72 h of treatment. Cells were trypsinized and incubated with lysis buffer containing DAPI for 5 min at 37°C. Stabilization buffer was added, and cellular fluorescence was measured by the NucleoCounter NC-3000TM system (Chemometec, Allerod, Denmark). Cell cycle phases were identified based on the DNA content of the cells.

Immunoblot

PF338 tumor cells were seeded into 6-well plates. After a recovery period of 24 h, cells were treated for 72 h with either HDACi (SAHA, valproate), galunisertib or solvent and precipitated with 6% TCA for 1 h, 4°C followed by centrifugation for 10 min at 9000 rpm. The total cellular protein pellets were resuspended in electrophoresis sample buffer (62.5 mM Tris–HCl, pH 6.8, 2% SDS, 10% glycerol, 5 mM EDTA, 125 mg/ml urea, 100 mM dithiothreitol) to be later loaded on 10% acrylamide gels in equal protein amounts. For immunostaining rabbit anti-E-cadherin (Cell Signaling, 24E10, 1:1,000), anti-beta-catenin (Santa Cruz, Sc-7199, 1:500), anti-pSMAD2 (Cell Signaling, 138D4, 1:1,000) and polyclonal anti-beta-tubulin (Abcam, ab6046, 1:1,000) were used. As secondary antibody HRP-conjugated anti-rabbit antibody (Jackson ImmunoResearch, 1: 10.000) was used. For development ECL Western Blotting Substrate (Thermo Scientific, Waltham, MS, United States) was applied followed by luminography. Three independent experiments were performed.

Next-Generation Sequencing (NGS)

DNA from PF338 cells was isolated according to the manual's instructions by using DNeasy Blood and Tissue Kit (Qiagen, MD, United States). FFPE tissue DNA was isolated according to the manual's instructions by using QIAamp DNA FFPE Tissue Kit (Qiagen, MD, United States). DNA concentrations were determined by Qubit® 2.0 Fluorometer dsDNA HS assay kit (LifeTechnologies, CA, United States).

A total amount of 45 ng DNA was used for multiplex-PCR. Multiplex PCR and purification were performed with the GeneRead DNAseq Custom Panel and PCR Kit V2 (Qiagen, MD, United States) and Agencourt® AMPure® XP Beads (Beckman, CA, United States). The library preparation was performed with NEBNext Ultra DNA Library Prep Set for Illumina (New England Biolabs, MA, United States), according to the manufacturer's recommendations by using 24 different indices per run. The pooled library was sequenced on MiSeq (Illumina; 2 × 150 bases paired-end run) and analyzed by Biomedical Genomics Workbench (CLC Bio, Qiagen, MD, United States). For targeted sequencing a customized comprehensive cancer-panel was designed containing regions of interest.

Time-Lapse Video Microscopy

Video microscopy was performed as previously [24] and now described in Supplementary materials.

Statistics

Two-way ANOVA with Bonferroni posttest was applied to describe significant differences between cell lines and treatment lines. One-way ANOVA with Dunn´s multiple comparison test was applied to identify significant differences between treatment lines. $^{*}p < 0.05$; $^{**}p < 0.01$; $^{***}p < 0.001$, and $^{****}p < 0.0001$ represented significant differences. All calculations were done in GraphPad Prism 8 (GraphPad Software Inc., San Diego, CA).

RESULTS

Clinical History

A 59-year-old female patient was diagnosed with UCS and underwent radical resection yielding a pT3aN0M0 FIGO IIIA tumor containing both a dominant stromal sarcomatous and a focal endometroid carcinomatous component (**Figure 1**). No adjuvant treatment was applied, however, 2.5 months later the patient developed retroperitoneal recurrence, for which chemotherapy consisting of three cycles paclitaxel/carboplatin was started. Re-staging indicated a tumor response and thus three additional cycles of chemotherapy were applied, followed by resection of the metastatic lesion. Histological analyses at that time revealed positive tumor margins, justifying adjuvant iliac radiation therapy. Due to rapid locoregional spread infiltrating diaphragm, chest wall and pleura accompanied by accumulating pleural effusions, the patient underwent partial resections including laparotomy and video-assisted thoracoscopy. Finally, treatment was switched to supportive chemotherapy, however, the patient continued to deteriorate and succumbed to the disease 12.5 months after initial diagnosis.

Histological Tumor Characterization

To compare the primary tumor lesion at diagnosis with the metastatic tumor we performed immunohistochemical analyses (**Figure 2A**). At diagnosis, the tumor contained a dominant sarcomatous component positive for vimentin and a focal

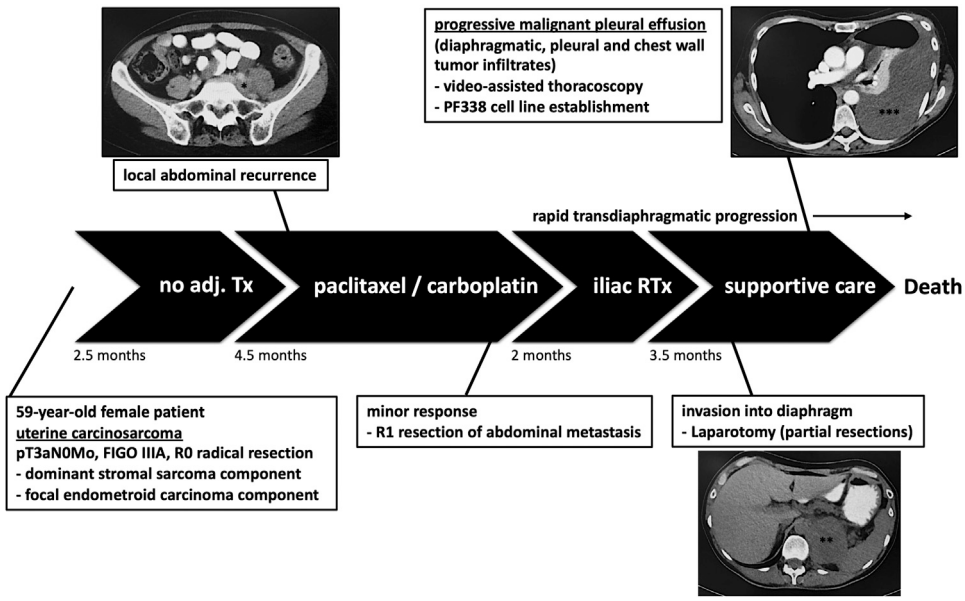

FIGURE 1 | Patient's history. The patient underwent resection without adjuvant treatment (Tx). Due to retroperitoneal recurrence, chemotherapy was initiated followed by surgery and adjuvant radiation therapy (RTx). However, the tumor progressed leading to pleural effusion justifying laparotomy and video-assisted thoracoscopy. At that time we established the pleural-effusion derived tumor cell line PF338. *retroperitoneal recurrence; **tumor infiltrate; ***transdiaphragmatic spread and pleural effusion.

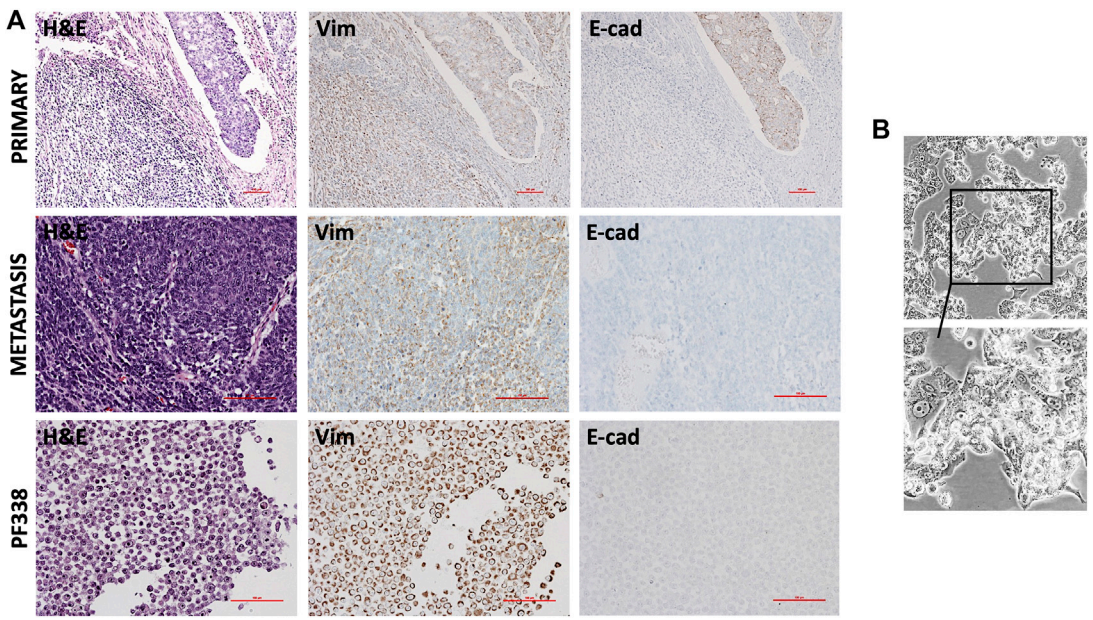

FIGURE 2 | Histopathological and *in vitro* characterization **(A)** Hematoxylin and eosin (H & E) and immunohistochemical stainings of the primary tumor, the recurrent tumor and of PF338 tumor cells. Whereas the primary tumor expressed both E-cadherin and vimentin, E-cadherin expression was lost in both the metastatic lesion and the cell line **(B)** PF338 tumor cell growth *in vitro*.

carcinomatous component positive for E-cadherin. At recurrence, hematoxylin and eosin (H&E) staining revealed mainly spindle-shaped tumor cells diffusely positive for vimentin but negative for E-cadherin. To confirm the origin of the metastatic tumor, we demonstrated that tumor cells were, although only in foci, positive for CD10, a marker for Müllerian system-derived neoplastic mesenchymal cells [25] (**Supplementary Figure S1A**). In addition, a proliferation rate

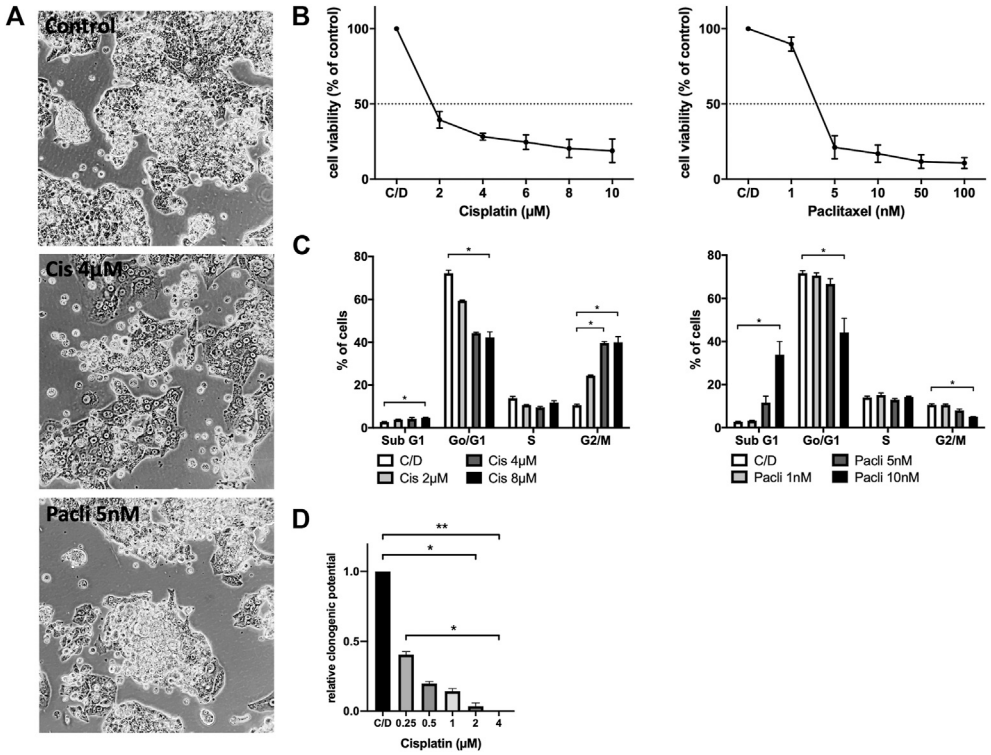

FIGURE 3 | PF338 tumor cells are sensitive to both cisplatin and paclitaxel **(A)** Cisplatin reduced the mesenchymal-like cell fraction of PF338 cells **(B)** Cells were sensitive to cisplatin (IC_{50}: 0.96 μM) and paclitaxel (IC_{50}: 3.81 nM) **(C)** Cisplatin induced G2/M arrest and paclitaxel apoptosis **(D)** Tumor cells could still form colonies when treated with IC_{50} concentrations of cisplatin. Error bars = means ± SE from three repeats. C/D, control, $*p < 0.05$, $**p < 0.01$.

of up to 60% was detected in hotspot areas by Ki67 staining (**Supplementary Figure S1A**). Stainings for estrogen- and progesterone-receptor (ER, PR) indicated only heterogeneous nuclear expression patterns (**Supplementary Figure S1A**).

Taken together, the metastatic resected specimen was highly proliferative, had lost the carcinomatous histological component and was heterogeneously positive for CD10, ER and PR.

PF338 Cell Line Establishment and Mutational Characterization

At time of progression, we obtained pleural effusion and could successfully establish the PF338 UCS cell line. Congruent to the metastatic tissue, immunohistochemical stainings of the cell block indicated focal positivity for CD10, strong positivity for vimentin and negative staining for E-cadherin (**Figure 2A**; **Supplementary Figure S1B**). *In vitro*, PF338 tumor cells demonstrated a biphasic growth pattern consisting of an epithelial-like component growing in a monolayer and a mesenchymal-like component growing in multiple layers (**Figure 2B**; **Supplementary Video S1**). In order to study the effect of multiple freezing cycles on tumor cell viability, we compared viability of PF338 cell passage 16 vs. passage 26 and found no differences (viability right after thawing 81.6 vs. 84.2%, viability after 72 h in culture 98.6% vs. 97.2%).

To illuminate the mutational background of the tumor cell line and the primary/metastatic tumor tissues we performed NGS for a predefined mutational panel that included the most commonly mutated genes in UCS (**Supplementary Table S1**). We identified a G13C mutation in *KRAS*, a R130Q mutation in *PTEN* and a mutation in *ARID1A*. Interestingly, an R93Q mutation in *PIK3CA* was only detected in the metastatic tumor and the cell line but not in the primary tumor.

PF338 Tumor Cells Are Sensitive to Cisplatin and Paclitaxel *in vitro*

In order to test whether PF338 cells are sensitive to standard-of-care UCS treatment paclitaxel plus platinum-based chemotherapy we performed *in vitro* sensitivity testing for both drugs. Accordingly, PF338 cells were sensitive to cisplatin and paclitaxel, with IC_{50} values of 0.96 μM and 3.81 nM, respectively (**Figures 3A,B**). Interestingly, whereas cisplatin induced morphology changes to a more uniform, flat phenotype, paclitaxel treatment did not interfere with morphology (**Figure 3A**). Cell cycle analyses for cisplatin revealed a dose-dependent G2/M arrest, whereas paclitaxel induced apoptosis in a dose-dependent manner (**Figure 3C**). Despite being sensitive to cisplatin, a significant fraction of cells (15%) remained viable when treated with cisplatin at IC_{50} concentrations for 10 days (**Figure 3D**; **Supplementary Figure S2**).

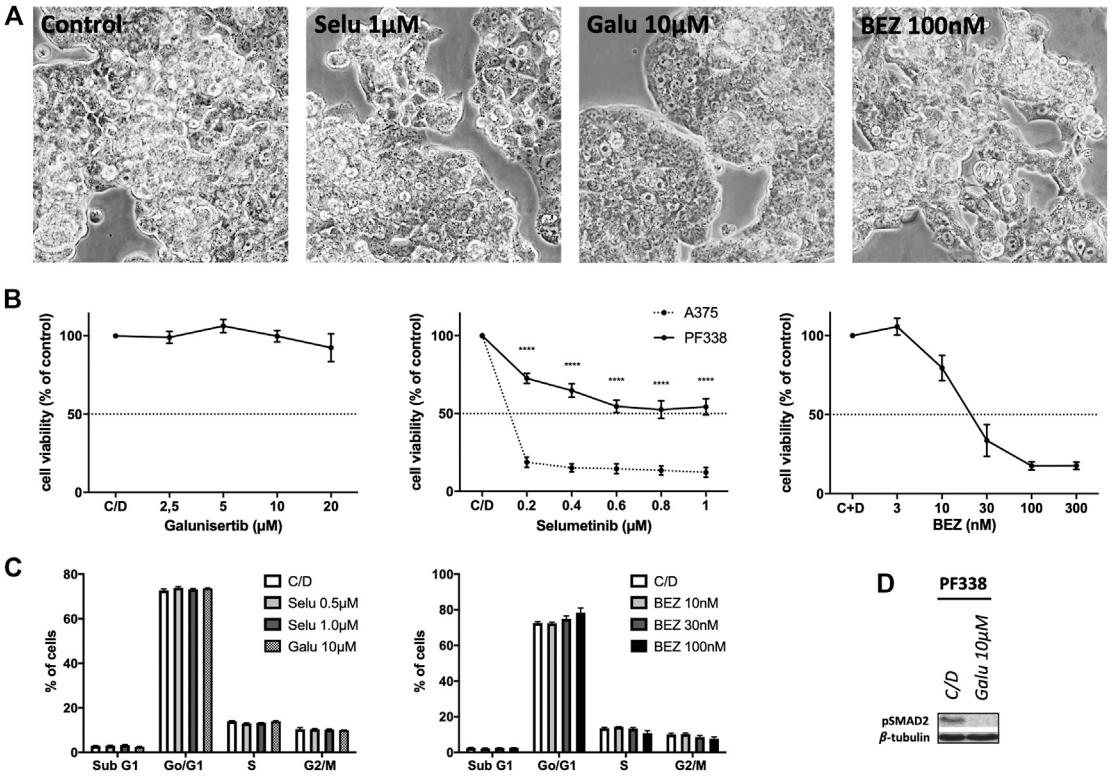

FIGURE 4 | PF338 tumor cells are resistant to MEK and TGF-βRI-kinase inhibition but sensitive to PI3K inhibition **(A)** selumetinib (Selu), galunisertib (Galu) and BEZ235 (BEZ) did not affect PF338 cell morphology **(B)** PF338 cells were resistant to selumetinib (A375 cells were used as control) and galunisertib, but sensitive to BEZ235 (IC_{50}: 63.42 nM) **(C)** BEZ235 induced a modest G0/G1 arrest **(D)** Galunisertib reduced pSMAD2 expression. Error bars = means ± SE from three repeats. C/D, control, $^{****}p < 0.0001$.

Targeted Therapy With Kinase Inhibitors in PF338 Tumor Cells

In order to test whether *KRAS*-mutant PF338 cells are sensitive to MAPK pathway inhibition, we used selumetinib, a MEK inhibitor that has been tested in *KRAS*-mutant tumors [26]. As sensitive control we used the *BRAFV600E* mutant A375 melanoma line [27]. We also tested the dual PI3K/mTOR inhibitor BEZ235 due to the mutations in the PI3K pathway and also treated the cells with galunisertib, a TGF-βRI-kinase inhibitor. PF338 cells were resistant to both selumetinib and galunisertib but strongly sensitive to PI3K/mTOR inhibition (IC_{50}: 63.42 nM) (**Figures 4A,B**). Cell cycle analyses revealed no changes upon selumetinib or galunisertib treatment and only a modest dose-dependent G0/G1 arrest upon BEZ235 treatment (**Figure 4C**). However, despite the resistance to galunisertib, pSMAD2 expression was abrogated by the treatment (**Figure 4D**).

PF338 Tumor Cells Are Highly Sensitive to HDAC and PARP Inhibition

Recent work in ovarian cancer demonstrated that mutations in *ARID1A* confer sensitivity to HDACi [18]. Furthermore, UCS frequently harbor alterations in cell cycle regulators and thus may show susceptibility to certain targeted therapies including PARP inhibitors [7]. Strikingly, PF338 cells were sensitive to both HDACi SAHA and PARP inhibitor olaparib with IC_{50} of 0.38 and 4.60 µM, respectively (**Figures 5A,B**). SAHA treatment induced two distinct cell cycle patterns: a dose dependent G0/1 arrest at low drug concentrations and both a G2/M arrest and induction of apoptosis at high concentrations. In contrary, olaparib-treated cells went into G2/M arrest in a dose-dependent manner (**Figure 5C**). Importantly, PF338 tumor cells changed morphology from the initial biphasic to an epithelial phenotype upon SAHA treatment (**Figure 5A**; **Supplementary Video S2**). These phenotypic changes were accompanied by a dose-dependent upregulation of epithelial markers E-cadherin and—to a lesser extent—β-catenin (**Figure 5D**). Importantly, phenotypic and expression changes were also observed upon treatment with high-dose SAHA (4 µM) or valproate (**Supplementary Figures S3A–D**).

DISCUSSION

The highly invasive and aggressive growth pattern of UCS in combination with a still poorly understood tumorigenic molecular background contribute to dismal patient prognosis [28]. Due to the low incidence and a very limited number of clinical trials, multicenter studies investigating novel agents and

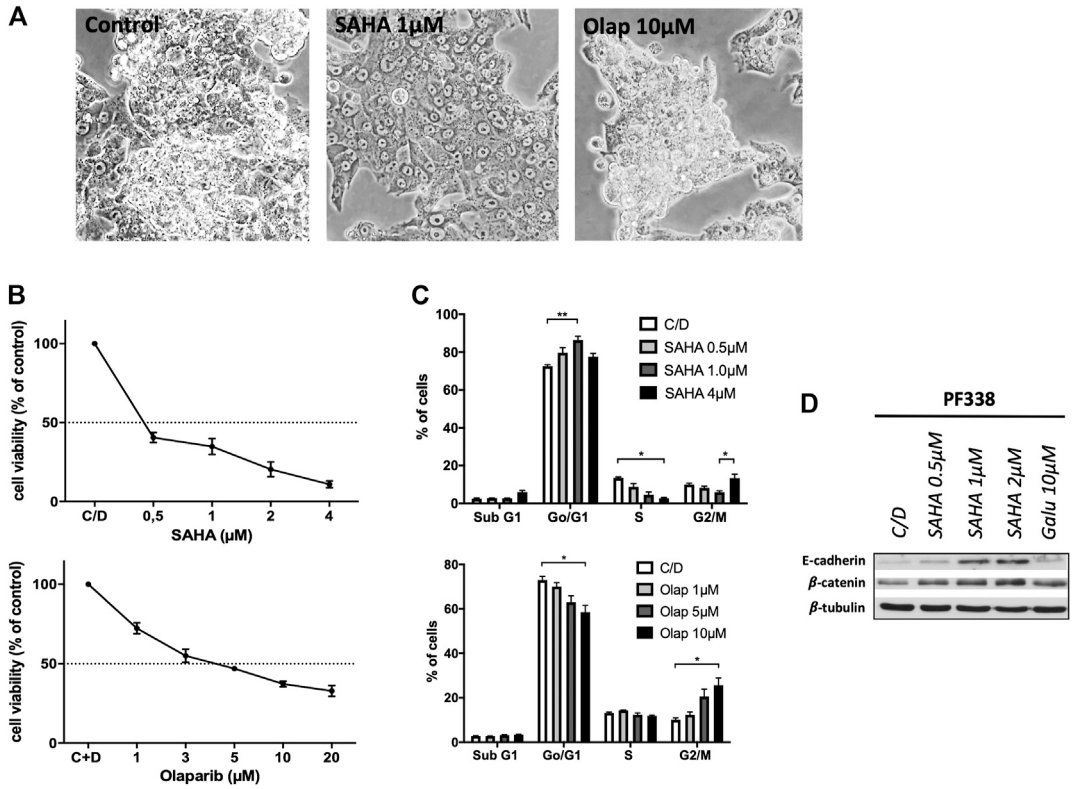

FIGURE 5 | PF338 tumor cells are highly sensitive to HDAC inhibition and change differentiation **(A)** SAHA treatment changed morphology from biphasic to epithelial **(B)** Cells were sensitive to SAHA (IC_{50}: 0.38 μM) and olaparib (IC_{50}: 4.60 μM) **(C)** SAHA induced a G0/1 arrest and with higher concentrations both a G2M arrest and apoptosis; olaparib induced G2/M arrest **(D)** SAHA dose-dependently upregulated the expression of E-cadherin and β-catenin. Error bars = means ± SE from three repeats. C/D, control, $^{*}p < 0.05$, $^{**}p < 0.01$.

combinations are of utmost importance to offer evidence-based therapies. Accordingly, patient-derived tumor cell lines are crucial to identify novel therapeutics. Our study describes a newly established UCS cell line and to our best knowledge is the first report of *in vitro* HDAC inhibition in UCS.

Our patient underwent multiple surgeries followed by chemo- and radiotherapy; however, despite initial treatment response she rapidly relapsed and succumbed to the disease. There is still no consensus regarding the optimal therapeutic management for UCS patients and as in our case, UCS tumors tend to relapse within two years after diagnosis despite initial systemic treatment response [29]. Although certain multimodal approaches were shown to be potentially effective in UCS patients, prospective validation studies and novel approaches are urgently needed [30].

In our case, the resected metastatic lesion showed mainly sarcomatous differentiated tumor cells without E-cadherin expression. In contrast, a dominant sarcomatous and a focal carcinomatous E-cadherin positive histological component were present at initial diagnosis. This histological change together with rapid progression is in line with a recent study identifying sarcomatous component on recurrence to be significantly associated with poor disease-free interval [31]. Metastatic UCS lesions were described as predominantly carcinomatous or biphasic tumors but no pure sarcomas in a large retrospective cohort [1]. To study the dynamic process of differentiation changes in UCS, a biphasic cell model representing both morphologies *in vitro* is an invaluable asset. However, there are just a few patient-derived UCS cell lines, and the majority of those are of sarcomatous differentiation [23]. Importantly, our novel UCS cell line demonstrated biphasic differentiation as illustrated by *in vitro* morphology and growth. Of note, a similar biphasic phenotype *in vitro* was described for UCS cell lines SNU-685 and EMTOKA [32, 33].

For the majority of previously established UCS lines analyses of driver mutations were not performed. PF338 cells harbor the G13C mutation in *KRAS* but are resistant against MEK-inhibition. According to the fourth dataset of the AACR GENIE project, the majority of $KRAS^{G13C}$ mutant tumors are non-small cell lung cancers and colorectal carcinomas. However, four of the $KRAS^{G13C}$ mutant tumors were uterine cancers [34]. To the best of our best knowledge, there is no data available regarding RAS/MAPK pathway inhibition in $KRAS^{G13C}$ cells and according to the ATCC there are only two lung adenocarcinoma lines with this mutation. The other *KRAS* mutant UCS line TU-ECS-1has the more common G12D mutation in addition to several *TP53* mutations [35].

PF338 tumor cells harbored mutations in *PIK3CA* and *PTEN* and were sensitive to dual PI3K/mTOR inhibition. Importantly,

alterations in the PI3K pathway have been described for the majority of UCS and about one quarter of UCS demonstrate simultaneous mutations in *PTEN* and *PIK3CA* [7–9]. Several clinical trials are investigating PI3K pathway inhibition in endometrial carcinoma but data for UCS are missing [7]. Interestingly, in our case, the *PIK3CA* mutation was only present at the time of metastasis and not at diagnosis. Similar findings were reported in a melanoma study in which one of eight tested cases had a *PIK3CA* mutation only present in the metastatic lesion [36]. However, in UCS, McConechy et al. found that *PIK3CA* mutations were uniformly present in both the diagnostic and metastatic lesions and hence they hypothesized that such mutations may occur early during tumorigenesis [9].

As in our case, in patients with recurrent UCS, chemotherapy consisting of different combinations of carboplatin/cisplatin, paclitaxel and ifosfamide are treatment of choice [4–6]. Our patient initially responded to chemotherapy and in line with that, PF338 cells were sensitive to both cisplatin and paclitaxel *in vitro*. These findings are similar to the data from the TU-ESC-1 cell line which was shown to be sensitive to both drugs as well [35]. However, our long-term treatment showed that a fraction of PF338 cells remained viable when treated with high cisplatin concentrations. This could explain why UCS patients tend to respond to chemotherapy at first but ultimately relapse within two years [29].

Due to emerging evidence suggesting a functional role of EMT in UCS tumorigenesis and its biphasic growth by definition, UCS is the prototype tumor to study EMT [4, 11]. Importantly, EMT has been linked to the transition from endometrial carcinoma to carcinosarcoma and to the metastatic process during disease progression [37]. In two sarcomatoid UCS lines certain TGF-β family members were found to be expressed and inhibition with galunisertib could partially abrogate TGF-β mediated effects on proliferation, migration and EMT. Importantly, galunisertib alone did reduce pSMAD2 expression but did not affect cell viability [13]. This is in line with our data of no change in cell viability, cell cycle distribution and cell morphology but a downregulation of pSMAD2 expression following galunisertib treatment. Putting this into context, blocking TGF-β signaling in UCS might not be effective as single agent but rather in combinatory approaches. Accordingly, Dwivedi et al. could recently demonstrate promising results by combining galunisertib with standard chemotherapy *in vivo* by treating xenografts established from a UCS cell line with high relative TGF-β and TGF-βRI expression [38]. A phase IB trial investigating galunisertib with chemotherapy in UCS is currently recruiting patients (NCT03206177). Given that our PF338 tumor cells did not change viability or morphology to TGF-β signaling inhibition despite reduced pSMAD2 expression upon galunisertib treatment, we concluded that TGF-β signaling may not be the major driver for EMT and cell proliferation in our model. Additional investigations will be necessary to better describe the role of TGF-β blockade in UCS.

The PARP inhibitor olaparib affected viability by inducing a G2/M arrest in PF338 cells. Alterations in cell cycle regulators, which are frequently detected in UCS, potentially induce susceptibility to PARP inhibition [7]. Furthermore, a large study investigating PARP1 expression in various tumors found that the majority of UCS markedly overexpressed PARP1 [39]. However, data with regard to FDA-approved PARP inhibitors in UCS are missing and our data is the first to suggest PARP inhibition as effective in UCS.

We detected an *ARID1A* mutation in our case. Importantly, 10–30% of UCS harbor mutations in *ARID1A*, representing the most frequently altered chromatin remodeling gene in UCS [7–9]. Recent evidence demonstrated a link between EMT and epigenetic alterations in UCS [7]. One study reported that loss of *ARID1A* leads to the expression of EMT genes and epithelial transdifferentiation in the endometrium [16]. Furthermore, ARID1A normally suppresses certain HDACs and tumor cells with *ARID1A* mutations lose this feedback, become HDAC dependent and hence highly sensitive to HDACi [18, 40]. Our findings that SAHA and valproate interfered with cell viability, cell cycle distribution and cell differentiation in ARID1A mutant PF338 tumor cells strongly support this hypothesis. Upon SAHA treatment, tumor cells dose-dependently underwent reverse EMT, a process also called mesenchymal-epithelial transition (MET), characterized by increased E-cadherin and β-catenin expression and morphological re-differentiation into an epithelial phenotype. To the best of our knowledge, the current study provides the first evidence showing HDACi to be effective in UCS *in vitro* by interfering with EMT/MET. In fact, re-expression of E-cadherin is considered a major marker of MET in tumor cells [41]. Our findings of HDACi interfering with EMT/MET are in line with a number of studies in different malignancies [12]. Downregulation of E-cadherin by epigenetic changes in cancer has been extensively described and linked to tumor invasiveness, dissemination and progression [42]. In contrast, MET, the reverse process, has been linked to tumor cell re-differentiation [43]. Considering the fact that the majority of UCS tumors relapse after radical surgery, targeting histone modification and differentiation by HDACi might be an effective novel approach to prevent UCS tumor cells from metastasizing. Although a recent clinical trial (NCT03509207) already aimed to investigate SAHA in UCS, molecular explanations justifying its rational and clinical implementation were scarce and limited to a study in a uterine sarcoma cell line [21, 22]. HDAC inhibition is a rapidly growing field in cancer therapy throughout various malignancies. Based on our findings, targeting epigenetics and consequently EMT by using HDACi in UCS might be a promising novel approach and should be further explored in future clinical trials. Furthermore, identifying the mutational background of UCS at time of tumor progression is of utmost importance to better predict sensitivity to targeted therapies including PI3K pathway, PARP and HDAC inhibition.

DATA AVAILABILITY STATEMENT

The original contributions presented in the study are included in the article/**Supplementary Material**, further inquiries can be directed to the corresponding author.

ETHICS STATEMENT

The studies involving human participants were reviewed and approved by the Ethics Committee at the University of Duisburg-Essen (18–8208-BO). The patients/participants provided their written informed consent to participate in this study.

AUTHOR CONTRIBUTIONS

PS: Conceptualization, Methodology, Formal Analysis, Validation, Visualization, Investigation, Writing—Original Draft; ÖO, TH, AS, DR and SK: Investigation, Methodology, Validation, Writing—Review and Editing; LH: Conceptualization, Resources, Methodology, Validation, Writing—Review and Editing; AB: Conceptualization, Resources, Writing—Review and Editing, Project Administration; RK and TP: Conceptualization, Writing—Review and Editing; Project Administration; CA: Conceptualization, Validation, Resources, Writing—Review and Editing, Supervision, Project Administration; BH: Conceptualization, Investigation, Methodology, Writing—Review and Editing, Supervision, Project Administration

CONFLICT OF INTEREST

The authors declare that the research was conducted in the absence of any commercial or financial relationships that could be construed as a potential conflict of interest.

ACKNOWLEDGMENTS

We thank Eva Gottstein for her dedicated contribution regarding PF338 primary cell culture. The PF338 cell line was established in collaboration with the West German Biobank Essen (WBE).

SUPPLEMENTARY MATERIAL

The Supplementary Material for this article can be found online at: https://www.por-journal.com/articles/10.3389/pore.2021.636088/full#supplementary-material.

REFERENCES

1. Silverberg SG, Major FJ, Blessing JA, Fetter B, Askin FB, Liao S-Y, et al. Carcinosarcoma (malignant mixed mesodermal tumor) of the uterus. *Int J Gynecol Pathol* (1990). 9(1):1–19. doi:10.1097/00004347-199001000-00001
2. Kernochan LE, Garcia RL. Carcinosarcomas (malignant mixed müllerian tumor) of the uterus: advances in elucidation of biologic and clinical characteristics. *J Natl Compr Canc Netw* (2009). 7(5):550–7. doi:10.6004/jnccn.2009.0037
3. Murali R, Davidson B, Fadare O, Carlson JA, Crum CP, Gilks CB, et al. High-grade endometrial carcinomas. *Int J Gynecol Pathol* (2019). 38(Suppl. 1): S40–S63. doi:10.1097/pgp.0000000000000491
4. Pang A, Carbini M, Moreira AL, Maki RG. Carcinosarcomas and related cancers: tumors caught in the act of epithelial-mesenchymal transition. *Jco* (2018). 36(2):210–6. doi:10.1200/jco.2017.74.9523
5. Callister M, Ramondetta LM, Jhingran A, Burke TW, Eifel PJ. Malignant mixed müllerian tumors of the uterus: analysis of patterns of failure, prognostic factors, and treatment outcome. *Int J Radiat Oncology*Biology*Physics* (2004). 58(3): 786–96. doi:10.1016/s0360-3016(03)01561-x
6. Zhu J, Wen H, Bi R, Wu X. Clinicopathological characteristics, treatment and outcomes in uterine carcinosarcoma and grade 3 endometrial cancer patients: a comparative study. *J Gynecol Oncol* (2016). 27(2):e18. doi:10.3802/jgo.2016.27.e18
7. Cherniack AD, Shen H, Walter V, Stewart C, Murray BA, Bowlby R, et al. Integrated molecular characterization of uterine carcinosarcoma. *Cancer Cell* (2017). 31(3):411–23. doi:10.1016/j.ccell.2017.02.010
8. Jones S, Stransky N, McCord CL, Cerami E, Lagowski J, Kelly D, et al. Genomic analyses of gynaecologic carcinosarcomas reveal frequent mutations in chromatin remodelling genes. *Nat Commun* (2014). 5:5006. doi:10.1038/ncomms6006
9. McConechy MK, Hoang LN, Chui MH, Senz J, Yang W, Rozenberg N, et al. In-depth molecular profiling of the biphasic components of uterine carcinosarcomas. *J Path: Clin Res* (2015). 1(3):173–85. doi:10.1002/cjp2.18
10. Xu J, Lamouille S, Derynck R. TGF-β-induced epithelial to mesenchymal transition. *Cell Res* (2009). 19(2):156–72. doi:10.1038/cr.2009.5
11. Chiyoda T, Tsuda H, Tanaka H, Kataoka F, Nomura H, Nishimura S, et al. Expression profiles of carcinosarcoma of the uterine corpus-are these similar to carcinoma or sarcoma?. *Genes Chromosom Cancer* (2012). 51(3):229–39. doi:10.1002/gcc.20947
12. Wawruszak A, Kalafut J, Okon E, Czapinski J, Halasa M, Przybyszewska A, et al. Histone deacetylase inhibitors and phenotypical transformation of cancer cells. *Cancers (Basel)* (2019). 11(2). doi:10.3390/cancers11020148
13. Dwivedi SK, McMeekin SD, Slaughter K, Bhattacharya R. Role of TGF-β signaling in uterine carcinosarcoma. *Oncotarget* (2015). 6(16):14646–55. doi:10.18632/oncotarget.3711
14. Osakabe M, Fukagawa D, Sato C, Sugimoto R, Uesugi N, Ishida K, et al. Immunohistochemical analysis of the epithelial to mesenchymal transition in uterine carcinosarcoma. *Int J Gynecol Cancer* (2019). 29(2):277–281. doi:10.1136/ijgc-2018-000038
15. Nishimura I, Ohishi Y, Oda Y, Kishimoto J, Yasunaga M, Okuma E, et al. Expression and localization of E-cadherin and β-catenin in uterine carcinosarcoma. *Virchows Arch* (2011). 458(1):85–94. doi:10.1007/s00428-010-1002-9
16. Wilson MR, Reske JJ, Holladay J, Wilber GE, Rhodes M, Koeman J, et al. ARID1A and PI3-kinase pathway mutations in the endometrium drive epithelial transdifferentiation and collective invasion. *Nat Commun* (2019). 10(1):3554. doi:10.1038/s41467-019-11403-6
17. Cuevas IC, Sahoo SS, Kumar A, Zhang H, Westcott J, Aguilar M, et al. Fbxw7 is a driver of uterine carcinosarcoma by promoting epithelial-mesenchymal transition. *Proc Natl Acad Sci USA* (2019). 116(51):25880–90. doi:10.1073/pnas.1911310116
18. Fukumoto T, Park PH, Wu S, Fatkhutdinov N, Karakashev S, Nacarelli T, et al. Repurposing pan-HDAC inhibitors for arid1a-mutated ovarian cancer. *Cell Rep* (2018). 22(13):3393–400. doi:10.1016/j.celrep.2018.03.019
19. Garnett MJ, Edelman EJ, Heidorn SJ, Greenman CD, Dastur A, Lau KW, et al. Systematic identification of genomic markers of drug sensitivity in cancer cells. *Nature* (2012). 483(7391):570–5. doi:10.1038/nature11005
20. Li Y, Seto E. HDACs and HDAC inhibitors in cancer development and therapy. *Cold Spring Harb Perspect Med* (2016). 6(10):a026831. doi:10.1101/cshperspect.a026831
21. Hrzenjak A, Moinfar F, Kremser M-L, Strohmeier B, Staber PB, Zatloukal K, et al. Valproate inhibition of histone deacetylase 2 affects differentiation and decreases proliferation of endometrial stromal sarcoma cells. *Mol Cancer Ther* (2006). 5(9):2203–10. doi:10.1158/1535-7163.mct-05-0480

22. Hrzenjak A, Moinfar F, Kremser M-L, Strohmeier B, Petru E, Zatloukal K, et al. Histone deacetylase inhibitor vorinostat suppresses the growth of uterine sarcomas *in vitro* and *in vivo*. *Mol Cancer* (2010). 9:49. doi:10.1186/1476-4598-9-49
23. Schulten H-J, Wolf-Salgó J, Gründker C, Gunawan B, Füzesi L. Characterization of a newly established uterine carcinosarcoma cell line featuring the sarcomatous phenotype of the tumor *in vitro*. *Int J Gynecol Cancer* (2008). 18(2):339–44. doi:10.1111/j.1525-1438.2007.01004.x
24. Laszlo V, Hoda MA, Garay T, Pirker C, Ghanim B, Klikovits T, et al. Epigenetic down-regulation of integrin α7 increases migratory potential and confers poor prognosis in malignant pleural mesothelioma. *J Pathol* (2015). 237(2):203–14. doi:10.1002/path.4567
25. Mikami Y, Hata S, Kiyokawa T, Manabe T. Expression of CD10 in malignant müllerian mixed tumors and adenosarcomas: an immunohistochemical study. *Mod Pathol* (2002). 15(9):923–30. doi:10.1097/01.mp.0000026058.33869.db
26. Bernabé R, Patrao A, Carter L, Blackhall F, Dean E. Selumetinib in the treatment of non-small-cell lung cancer. *Future Oncol* (2016). 12(22): 2545–60. doi:10.2217/fon-2016-0132
27. Hanson K, Robinson SD, Al-Yousuf K, Hendry AE, Sexton DW, Sherwood V, et al. The anti-rheumatic drug, leflunomide, synergizes with MEK inhibition to suppress melanoma growth. *Oncotarget* (2018). 9(3):3815–29. doi:10.18632/oncotarget.23378
28. Yamada SD, Burger RA, Brewster WR, Anton D, Kohler MF, Monk BJ. Pathologic variables and adjuvant therapy as predictors of recurrence and survival for patients with surgically evaluated carcinosarcoma of the uterus. *Cancer* (2000). 88(12):2782–6. doi:10.1002/1097-0142(20000615)88:12<2782:aid-cncr17>3.0.co;2-k
29. Wolfson A, Brady M, Rocereto T, Mannel R, Lee Y, Futoran R, et al. A gynecologic oncology group randomized phase III trial of whole abdominal irradiation (WAI) vs. cisplatin-ifosfamide and mesna (CIM) as post-surgical therapy in stage I-IV carcinosarcoma (CS) of the uterus. *Gynecol Oncol* (2007). 107(2):177–85. doi:10.1016/j.ygyno.2007.07.070
30. Pectasides D, Pectasides E, Papaxoinis G, Xiros N, Sykiotis C, Papachristodoulou A, et al. Combination chemotherapy with carboplatin, paclitaxel and pegylated liposomal doxorubicin for advanced or recurrent carcinosarcoma of the uterus: clinical experience of a single institution. *Gynecol Oncol* (2008). 110(3):299–303. doi:10.1016/j.ygyno.2008.05.017
31. Abdulfatah E, Lordello L, Khurram M, Van de Vijver K, Alosh B, Bandyopadhyay S, et al. Predictive histologic factors in carcinosarcomas of the uterus. *Int J Gynecol Pathol* (2019). 38(3):205–15. doi:10.1097/pgp.0000000000000497
32. Yuan Y, Kim W-H, Han HS, Lee J-H, Park H-S, Chung J-K, et al. Establishment and characterization of cell lines derived from uterine malignant mixed müllerian tumor. *Gynecol Oncol* (1997). 66(3):464–74. doi:10.1006/gyno.1997.4802
33. Gorai I, Doi C, Minaguchi H. Establishment and characterization of carcinosarcoma cell line of the human uterus. *Cancer* (1993). 71(3):775–86. doi:10.1002/1097-0142(19930201)71:3<775:aid-cncr2820710321>3.0.co;2-c
34. Consortium APG. AACR project GENIE: powering precision medicine through an international consortium. *Cancer Discov* (2017). 7(8):818–31. doi:10.1158/2159-8290.CD-17-0151
35. Chiba Y, Sato S, Itamochi H, Suga Y, Fukagawa T, Oumi N, et al. Establishment and characterization of a novel uterine carcinosarcoma cell line, TU-ECS-1, with mutations of TP53 and KRAS. *Hum Cell* (2017). 30(2):140–8. doi:10.1007/s13577-016-0154-6
36. Miraflor AP, de Abreu FB, Peterson JD, Turner SA, Amos CI, Tsongalis GJ, et al. Somatic mutation analysis in melanoma using targeted next generation sequencing. *Exp Mol Pathol* (2017). 103(2):172–7. doi:10.1016/j.yexmp.2017.08.006
37. Somarelli JA, Boss MK, Epstein JI, Armstrong AJ, Garcia-Blanco MA. Carcinosarcomas: tumors in transition?. *Histol Histopathol* (2015). 30(6): 673–87. doi:10.14670/HH-30.673
38. Dwivedi SKD, Rao G, Dey A, Buechel M, Zhang Y, Zhang M, et al. Targeting the TGFβ pathway in uterine carcinosarcoma. *Cell Stress* (2020). 4(11):252–60. doi:10.15698/cst2020.11.234
39. Ossovskaya V, Koo IC, Kaldjian EP, Alvares C, Sherman BM. Upregulation of poly (ADP-Ribose) polymerase-1 (PARP1) in triple-negative breast cancer and other primary human tumor types. *Genes Cancer* (2010). 1(8):812–21. doi:10.1177/1947601910383418
40. Bitler BG, Wu S, Park PH, Hai Y, Aird KM, Wang Y, et al. ARID1A-mutated ovarian cancers depend on HDAC6 activity. *Nat Cell Biol* (2017). 19(8): 962–73. doi:10.1038/ncb3582
41. Wells A, Yates C, Shepard CR. E-cadherin as an indicator of mesenchymal to epithelial reverting transitions during the metastatic seeding of disseminated carcinomas. *Clin Exp Metastasis* (2008). 25(6):621–8. doi:10.1007/s10585-008-9167-1
42. Yao D, Dai C, Peng S. Mechanism of the mesenchymal-epithelial transition and its relationship with metastatic tumor formation. *Mol Cancer Res* (2011). 9(12):1608–20. doi:10.1158/1541-7786.mcr-10-0568
43. Hernández-Vargas H, Palacios J, Moreno-Bueno G. Telling cells how to die: docetaxel therapy in cancer cell lines. *Cell Cycle* (2007). 6(7):780–3. doi:10.4161/cc.6.7.4050

Pathology & Oncology Research

frontiers

ORIGINAL RESEARCH
published: 31 March 2021
doi: 10.3389/pore.2021.605017

Heterogeneous Expression of Proangiogenic and Coagulation Proteins in Gliomas of Different Histopathological Grade

Marek Z. Wojtukiewicz[1,2], Marta Mysliwiec[1], Elwira Matuszewska[2], Stanislaw Sulkowski[3], Lech Zimnoch[3], Barbara Polityńska[4,5], Anna M. Wojtukiewicz[4], Stephanie C. Tucker[6,7] and Kenneth V. Honn[8]*

[1]Department of Oncology, Medical University of Bialystok, Bialystok, Poland, [2]Department of Clinical Oncology, Comprehensive Cancer Center of Bialystok, Bialystok, Poland, [3]Department of General Pathomorphology, Medical University of Bialystok, Bialystok, Poland, [4]Department of Philosophy and Human Psychology, Medical University of Bialystok, Bialystok, Poland, [5]Robinson College, University of Cambridge, Cambridge, United Kingdom, [6]Department of Pathology-School of Medicine, Bioactive Lipids Research Program, Wayne State University, Detroit, MI, United States, [7]Karmanos Cancer Institute, Detroit, MI, United States, [8]Department of Chemistry, Wayne State University, Detroit, MI, United States

Brain gliomas are characterized by remarkably intense invasive growth and the ability to create new blood vessels. Angiogenesis is a key process in the progression of these tumors. Coagulation and fibrinolysis factors play a role in promoting angiogenesis. The aim of the study was to evaluate the expression of proangiogenic proteins (VEGF and bFGF) and hemostatic proteins (TF, fibrinogen, fibrin, D-dimers) associated with neoplastic cells and vascular endothelial cells in brain gliomas of various degrees of malignancy. Immunohistochemical tests were performed using the ABC method with the use of mono- and polyclonal antibodies. The obtained results indicated that both neoplastic cells and vascular endothelial cells in gliomas of various degrees of malignancy are characterized by heterogeneous expression of proteins of the hemostatic system and angiogenesis markers. The strongest expression of proangiogenic factors and procoagulant factors was demonstrated in gliomas of higher-grade malignancy.

Keywords: angiogenesis, VEGF, bFGF, D-dimers, blood coagulation, fibrin, tissue factor, glial tumors 3

OPEN ACCESS

Edited by:
József Tímár,
Semmelweis University, Hungary

****Correspondence:***
Marek Z. Wojtukiewicz
mzwojtukiewicz@gmail.com

Received: *11 September 2020*
Accepted: *09 February 2021*
Published: *31 March 2021*

Citation:
Wojtukiewicz MZ, Mysliwiec M, Matuszewska E, Sulkowski S, Zimnoch L, Polityńska B, Wojtukiewicz AM, Tucker SC and Honn KV (2021) Heterogeneous Expression of Proangiogenic and Coagulation Proteins in Gliomas of Different Histopathological Grade. Pathol. Oncol. Res. 27:605017. doi: 10.3389/pore.2021.605017

INTRODUCTION

In view of the fact that the hemostatic system is anatomically and functionally related to vascularization, its influence on the process of angiogenesis in neoplastic tumors would appear interesting. Since 1971, when J. Folkman promulgated the hypothesis that the growth of solid tumors depends on angiogenesis, and that therapeutic measures aimed at inhibiting this process may be an effective element of anticancer therapy [1, 2], the era of intensive research into anti-angiogenic treatment was initiated. From the outset, this therapy is considered appropriate for glial tumors. Among them, greatest interest has been paid to immature polymorphic glioblastomas (*glioblastoma multiforme*), which constitute more than half of all gliomas, show the highest degree of malignancy and have exceptionally poor prognosis.

Glial tumors are characterized by remarkably intense invasive growth and the ability to create new blood vessels. In glioblastoma multiforme, vascular density is decidedly higher than in tumors with lower histological malignancy [3]. Studies on astrocytomas have described an inverse correlation

between vessel density and overall survival time and indicate that the number of vessels in the tumor biopsy may be an important prognostic factor [4, 5]. Angiogenesis is a key process in the progression of malignant neoplasms, namely an essential stage for tumor growth above 2–3 mm^3 and the development of metastases [6]. Activation of this process may result not only from an increase in the activity of factors stimulating angiogenesis, but also from a decrease in the activity of inhibitors of this process [7].

Among the proangiogenic factors, the main contributing mediators in vascularization of the neoplastic tumor are the growth factors: vascular endothelial growth factor (VEGF) and basic fibroblast growth factor (bFGF). Studies on glioblastoma multiforme have demonstrated that VEGF production is particularly induced in tumor cells close to the foci of necrosis. The coexistence of glomerular proliferation with areas of extensive necrosis indicates that the angiogenic response is a secondary effect of increased VEGF production by hypoxic tumor tissue [8]. It is known that hypoxia plays an important role in the expression of the VEGF gene, inducing its activity at the level of transcription with the participation of HIF-1 (hypoxia inducible factor-1) [9]. VEGF increases the permeability of blood vessels (it is approx.50,000 times more potent as a factor affecting small blood vessel permeability than histamine) [10].

An increase in VEGF expression under the influence of bFGF has been demonstrated, as well as a synergistic effect of both factors in the angiogenesis process [11]. Despite the fact that bFGF also stimulates the proliferation of cells other than endothelial cells, it meets the basic criteria characterizing the proangiogenic factor: it stimulates the proliferation of endothelial cells *in vitro*, induces angiogenesis *in vivo*, and is often present in areas of vascular growth [8, 12]. bFGF is implicated in brain tumor progression and localizes in the microvasculature as well as in the tumor cells in human gliomas [8]. FGF receptor (FGFR) plays an important role in the survival and angiogenesis of glioblastoma cells through phosphatidylinositol 3-kinase (PI3K)/protein kinase B or AKT/mammalian target of the rapamycin (mTOR) molecular signaling pathway [13, 14].

Tissue Factor (TF) expression has been demonstrated on the surface of many normal cells as well as neoplastic cells [15]. The process of developing malignant brain tumors damages normal brain tissue and the structure of its blood vessels. Therefore, a growing tumor may lead to an increase in TF expression [16]. The protumorigenic function of TF is to activate cell signaling through the interaction of its cytoplasmic domain with protease-activated receptors (PARs). Antibodies blocking the cytoplasmatic signaling domain of TF have been shown to result in reduced tumor growth, but had no effect on the ability of TF to initiate coagulation [17]. Tissue factor is assigned a special role in the angiogenesis process. It has been shown to participate in the processes of adhesion and migration of neoplastic cells through a mechanism independent of clotting activation [18]. At the same time, it has been demonstrated that over-expression of the gene encoding TF leads to increased transcription of the gene encoding the VEGF factor, as well as to the reduction of the gene responsible for the synthesis of the angiogenesis inhibitor—thrombospondin-1 [15].

The procoagulant activity of thrombin leads to the conversion of fibrinogen into fibrin. Increased fibrinogen turnover and shortened plasma half-life are often found in cancer patients [19]. The presence of fibrin in the extravascular space, confirming that the activation of blood coagulation has taken place there, has been documented in a number of malignant neoplasms [20–24]. Fibrin and fibrinogen induce the expression of TF, which consequently leads to overproduction of fibrin. The resulting fibrin network provides "scaffolding" that promotes the growth of new blood vessels. Additionally, fibrin and fibrinogen facilitate the activation and stability of bFGF and other proangiogenic factors.

The aim of the study was to evaluate the expression of proangiogenic proteins (VEGF and bFGF) and coagulation/fibrinolysis proteins (TF, fibrinogen, fibrin, D-dimers) associated with neoplastic cells and vascular endothelial cells in brain gliomas of various degrees of malignancy.

MATERIALS AND METHODS

Glioma tissues and tissues from the margin of these tumors were obtained at surgical resection of 40 cancer patients. The material consisted of 13 lower-grade and 27 higher-grade malignant tumors.

Immunohistochemical (IHC) studies were performed on G2-grade gliomas (8 astrocytomas, 5 oligodendrogliomas) and high-grade gliomas (G3–12 anaplastic astrocytomas, 4 anaplastic oligodendrogliomas; G4–11 glioblastomas multiforme), as well as control fragments of respective normal tissues, which were derived from the neoplasm-free surgical margins.

The study protocol was approved by the local Ethics Committee of the Medical University in Bialystok, Poland (approval number R-I-002/256/2003). Informed consent was obtained from the patients.

Antigens were detected with avidin-biotin complex technique (ABC) using reagents (Vectastain Kits, Vector Laboratories, Burlingame, CA, United States) which have been described previously [25].

The following mouse monoclonal antibodies were used:

- 1-8C6 antibody to fibrinogen and fibrin-I, which requires intact 14Arg-15Gly binding on the Bβ chain of fibrinogen and therefore does not react with fibrin II (lacking fibrinopeptide B, FPB).
- T2G1 antibody to fibrin-II, which reacts with the amino-terminal part of the Bβ chain of fibrinogen only after cleavage by thrombin of fibrinopeptide B (FPB, Bβ 1–14) and therefore does not react with fibrinogen and fibrin I.
- GC4 antibody to D-dimers
- Antibody to human recombinant TF – kindly provided by Dr. Walter Kisiel, University of New Mexico, Dept. of Pathology, School of Medicine, Albuquerque, United States. The antibody was employed in our earlier studies [26].

TABLE 1 | Number of tumors exhibiting distinct intensity of IHC reactions toward proteins of hemostatic system and angiogenesis markers in gliomas of different malignancy.

Proangiogenic factors	Localization	Low-grade gliomas (n = 13) IHC score		High-grade gliomas (n = 27) IHC score		*p* value
		<200	≥200	<200	≥200	
VEGF	Cancer cells	9 (69, 2%)	4 (30, 8%)	2 (7, 4%)	25 (92, 6%)	*p* <0,001
	Endothelial cells	2 (15, 4%)	11 (84, 6%)	1 (3, 7%)	26 (96, 3%)	NS
	Neuropil	13 (100%)	0	1 (3, 7%)	26 (96, 3%)	*p* <0,001
bFGF	Cancer cells	2 (15, 4%)	11 (84, 6%)	24 (88, 9%)	3 (11, 1%)	*p* <0,001
	Endothelial cells	1 (7, 7%)	12 (92, 3%)	25 (92, 6%)	2 (7, 4%)	*p* <0,001
	Neuropil	13 (100%)	0	27 (100%)	0	NS
TF	Cancer cells	8 (61, 5%)	5 (38, 5%)	3 (11, 1%)	24 (88, 9%)	*p* = 0,03
	Endothelial cells	13 (100%)	0	5 (18, 5%)	22 (81, 5%)	*p* <0,001
	Neuropil	2 (15, 4%)	11 (84, 6%)	4 (14, 8%)	23 (85, 2%)	NS
Fibrinogen	Cancer cells	12 (92, 3%)	1 (7, 7%)	22 (81, 5%)	5 (18, 5%)	NS
	Tumor stroma in the vicinity of blood vessels	10 (76, 9%)	3 (23, 1%)	23 (85, 2%)	4 (14, 8%)	NS
Fibrin	Cancer cells	11 (84, 6%)	2 (15, 4%)	24 (88, 9%)	3 (11, 1%)	NS
	Tumor stroma in the vicinity of blood vessels	4 (30, 8%)	9 (69, 2%)	6 (22, 2%)	21 (77, 8%)	NS
D-dimers	Cancer cells	3 (23, 1%)	10 (76, 9%)	2 (7, 4%)	25 (92, 6%)	NS
	Tumor stroma in the vicinity of blood vessels	5 (38, 5%)	8 (61, 5%)	3 (11, 1%)	24 (88, 9%)	NS

Antibodies (1-8C6, T2G1, GC4) were kindly provided by Dr. Bohdan Kudryk, Lindsley F. Kimball Research, Blood Center, NY, United States and used in our earlier studies [22].

The following polyclonal antibodies were used:

- Goat antibody to human recombinant VEGF 121 and VEGF 165–R&D Systems, United States
- Goat antibody to human recombinant bFGF-R&D Systems, United States

The results of staining of the glioma tissues were compared with matched normal tissues, which were processed simultaneously. Antigens of the proteins tested were detected as the brown reaction product of the avidin-biotin complex with the substrate. Visual assessment of protein expression was performed in 10 random high-power fields by two independent observers.

Intensity of IHC reactions was evaluated acc. to Hirsch et al [27] in modification by Pirker et al [28]. A score for each tissue core was generated using a semi-quantitative approach according to the following algorithm: the percentage of positive tumor cells per slide (0–100%) was multiplied by the dominant intensity pattern of staining (0–negative for trace; 1-weak; 2–moderate; 3 intense). Hence the range for the overall score was 0–300. Specimens with a score of 0–199 were classified as being negative, while those with a score between 200–300 as positive. The IHC score was calculated based on the following formula: 1x (percentage of cells staining weakly [1+]) +2 x (percentage of cells staining moderately [2+] + 3 x (percentage of cells staining strongly [3+]) [28].

$\chi 2$ test was employed for statistical analysis. p value of <0.05 was considered statistically significant.

RESULTS

The strongest expression of the VEGF antigen was obtained in glioblastoma multiforme cells and the endothelium of their blood vessels, with weaker but distinct expression in G3 tumors (anaplastic gliomas) and the weakest in endothelial cells and a few G2 glioma neoplastic cells (**Table 1**).

Clear and consistent expression of bFGF was found in tumor cells and in lower-grade malignant glioma vascular endothelial cells, while in gliomas of higher-grade, bFGF expression was less pronounced (**Table 1**).

A positive color reaction to the presence of TF antigen was demonstrated in neoplastic cells and vascular endothelial cells in high-grade glioma tissues (**Figures 1A,B**; **Table 1**) and a non-uniform, diffuse positive reaction in neuropil and in the necrotic areas of these high-grade gliomas.

A clear, positive reaction to fibrinogen antigens was above all demonstrated in the lumen of the blood vessels of all the examined tumors (**Table 1**), as well as in areas of vascular effusions. The presence of fibrinogen in the extravascular space was confirmed in the form of a weak positive reaction in the vicinity of small blood vessels and in the neuropil of anaplastic gliomas. There was no correlation between the presence of fibrinogen antigens and the intensity of the color reaction in relation to the degree of malignancy of the gliomas.

Fibrin antigens were located in the neuropil around small blood vessels, in necrotic foci and in individual tumor cells (**Table 1**). No systematic relationship was observed with regard to the degree of malignancy of the gliomas, either in the distribution of the antigens or in the degree of intensity of the color reaction.

The strongest expression of D-dimer antigens was found in higher-grade gliomas (**Table 1**).

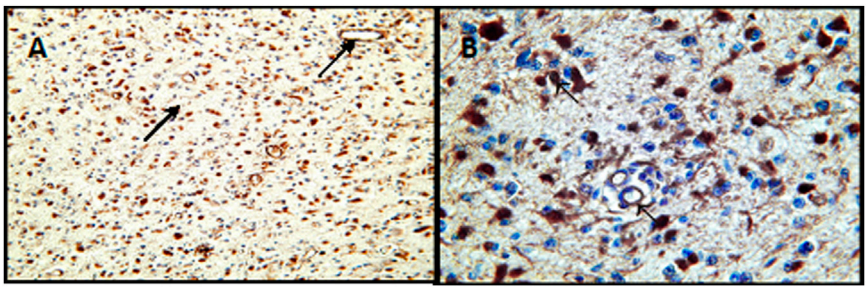

FIGURE 1 | Expression of tissue factor in G3 astrocytomas. **(A)** Positive immunohistochemical reaction for the presence of TF in neoplastic cells and vasuclar endothelial cells-arrows at lower magnification (×100). **(B)** Positive innunohistochemical staining for the presence of TF at higher magnification (×400). Arrows show staining of staining of tumor cells and vascular endothelial cells.

DISCUSSION

The importance of angiogenesis as an independent prognostic factor in brain gliomas has long been recognized. An inverse correlation has been found between the intensity of angiogenesis and the survival time of patients with gliomas [8]. Different factors involved in the hemostatic system, as well as the impact of individual elements of this system on cancer cells and the vascular endothelium are extremely important in the process of angiogenesis. The contribution of these factors and their reaction products in relation to tumor growth, metastasis and new vessel formation in tumor tissue has been documented [8, 19, 29, 30]. These angiogenic factors are upregulated by a variety of mechanisms like oncogene activation, loss of tumor suppressor gene function, and/or a hypoxic microenvironment [31]. It has been shown that the expression of growth factors in glioblastoma tissues increases with the growth of their malignancy, and the expression of some hemostatic system factors correlates with the expression of growth factors [8].

On the basis of our own research and data from the literature [32, 33], it has been confirmed that VEGF expression in glioma cells correlates with the degree of tumor malignancy. The strongest expression of VEGF was observed in the cells of glioblastoma multiforme and the endothelial cells of their blood vessels, with weaker but distinct expression in anaplastic gliomas and the weakest in a few neoplastic cells and vascular endothelial cells of lower-grade malignant gliomas. Similar results have been reported by Carrol et al. [34]. Studies conducted on various glioblastoma cell lines and in human glioblastoma tissues revealed the interaction of VEGF with angiopoietins: Ang-1 and Ang-2 and their Tie-2 receptor, with the consequent effect of aiding the maturation and stabilization of blood vessels [35]. Ang-2 is an antagonist of the Tie-2 receptor. As the tumor grows, the amount of synthesized Ang-2 increases, which leads to destabilization of the capillary wall. As a result of this process, in the absence of VEGF, the blood vessels regress and form necrotic foci in the center of the tumor. However, in the presence of VEGF, which is expressed later than Ang-2, an increase in Ang-2 secretion leads to increased angiogenesis, especially at the periphery of the tumor [35, 36]. Increased VEGF expression has been associated with aggressiveness of the tumor and poorer prognosis in patients with uterine cancer, ovarian cancer [37], breast cancer [37–39], gastric cancer [40], melanoma [41], head and neck cancer [37], and non-small cell lung cancer [38]. In addition, a high level of VEGF coexists with shortened survival time and an increased likelihood of recurrence of malignant tumors of the colon, rectum and kidney [37], and may also contribute to the initiation of the metastatic process [42].

One of the most exciting developments is the discovery, that autocrine and paracrine VEGF signaling contributes to vital aspects of tumorigenesis, namely cancer stem cells (CSCs) function, independently of angiogenesis. An alternative form of blood supply is vasculogenic mimicry, a process resembling embryonic vascular network, which is carried out by CSCs [43]. The cells are capable to transdifferentiate and form vascular-tube structures in the absence of endothelial cells [43]. It is of interest, that glioblastoma stem cells (GSCs) are also endowed with an ability to differentiate into endothelial cells and thus promote angiogenesis [43].

The neuropilins (NRPs), in addition to VEGF receptor tyrosine kinases, are fundamental for mediating the effects of VEGF on CSCs, due to their ability to affect the function of growth factor receptors and integrins [45]. VEGF signaling mediated by the NRPs impacts tumor cells, independently of its function in angiogenesis and vascular permeability. It is noteworthy that VEGF–NRP2 signaling in tumor cells is associated with poor prognosis and therapy resistance. In such case, targeting VEGF may turn out ineffective [46].

The expression of bFGF in the conducted studies was demonstrated in glioma cells of various degrees of malignancy, as well as in vascular endothelial cells. There was no correlation between bFGF and VEGF expression in glioma tissues. Other authors have also failed to demonstrate a correlation between bFGF expression and the intensity of angiogenesis in gliomas [47]. Additionally, similar results have been obtained for rectal cancer [48] and gastric cancer [49]. In turn, Ahir et al. [8] have shown in their studies that the combination of VEGF with bFGF with/or without platelet-derived growth factor demonstrated a synergistic effect in inducing neovascularization *in vivo*. The expression of these growth factors correlates with tumor progression in high-grade tumors expressing higher levels of growth factors when compared to low-grade tumors. Yet other

studies have revealed that bFGF is implicated in brain tumor progression and is localized in the microvasculature as well as in tumor cells in human gliomas [50–52]. bFGF levels correlate with the degree of glioma malignancy and vascularity as determined by immunohistochemical analysis [51]. It has previously been demonstrated that antibodies for bFGF inhibit glioma growth *in vivo* model and lead to reduced blood vessel densities in glioma tumors of treated animals [53].

In our own studies, the presence of TF antigens was demonstrated in neoplastic cells and vascular endothelial cells of all higher-grade malignant gliomas, but only in a few lower-grade malignant glioma neoplastic cells. TF antigens were also demonstrated in neuropil, and the intensity of the color reaction was directly correlated with the tumor grade, which is consistent with studies by Hamada et al. 1996 [54]. Similar results were obtained by other researchers who demonstrated strong or moderate TF expression in 91% of G4 gliomas, 46% of G3 gliomas, and only 16% of G1 and G2 gliomas [55]. Studies have shown that brain gliomas are a rich source of TF [54, 56] and the level of TF is directly correlated with the grade of their histological malignancy [56, 57].

In our own research, we have also demonstrated a correlation between the expression of TF and VEGF antigens, which is indicative of a relationship between TF and the intensity of angiogenesis in gliomas. The results obtained by other researchers have also confirmed this relationship [57, 58]. In a group of 23 glioblastoma multiforme tumors, the vascular density of tumors with strong TF-expression in endothelial cells was significantly higher than in those whose endothelial cells did not express TF [57]. The same study confirmed the correlation between the presence of TF and VEGF in glioblastoma extracts, which indicates the likely cooperation of both factors in the angiogenesis process in brain gliomas.

TF is believed to indirectly influence tumor angiogenesis through its procoagulant activity leading to thrombin generation and the formation of proangiogenic fibrin [59–61]. The results of the current study confirm the presence of fibrin and fibrinogen antigens in the extravascular space of the examined glioma tissues. However, no correlation was found between the intensity of expression of these antigens and the degree of malignancy of the gliomas. Other researchers have demonstrated the presence of stabilized fibrin deposits in glioblastoma multiforme between the tumor foci as well as on the periphery of the tumors [62]. In the same study, however, there was a different distribution of fibrin in brain metastatic tumors whose primary site was the lung. Fibrin deposits were only observed around the periphery of these tumors. Fibrin deposits around the tumor and in the tumor stroma provide double protection for the tumor against the host's immune system, namely they create a barrier against cells of the immune system and mask tumor antigens, and support angiogenesis [19, 63].

Thrombin generation, formation of a fibrin network and secondary fibrinolysis are evidenced by the presence of fibrin breakdown products found around small blood vessels and in association with glioblastoma cancer cells. Expression of D-dimers was clearly stronger in higher-grade gliomas. Compared to lower-grade malignant gliomas, anaplastic and multiforme gliomas are characterized by a stronger expression of proangiogenic factors and procoagulant factors involved in the processes of tumor growth and progression. When analyzing the expression of D-dimers and fibrin in the tissues, an inverse correlation was observed between these antigens: low fibrin expression was accompanied by high D-dimer expression, while strong fibrin expression was accompanied by low D-dimer expression.

The above results indicate that neoplastic cells and vascular endothelial cells in gliomas of various degrees of malignancy are characterized by heterogeneous expression of proteins of the hemostatic system and angiogenesis markers. Compared to lower-grade gliomas, higher-grade gliomas express more proangiogenic factors and procoagulant factors involved in tumor angiogenesis and progression. In anaplastic oligodendrogliomas, the expression and distribution of the tested antigens is similar to that in low-grade gliomas.

There are multiple links between coagulation activation and angiogenesis in cancer. Coagulation activation with subsequent fibrin formation takes place in the extravascular compartment of glial tumors. This solid phase coagulopathy may, at least in part, account for more pronounced angiogenesis observed in higher-grade gliomas, and thus contribute to more malignant course of the tumors.

DATA AVAILABILITY STATEMENT

The original contributions presented in the study are included in the article/Supplementary Material, further inquiries can be directed to the corresponding author.

ETHICS STATEMENT

The study protocol was approved by the local Ethics Committee of the Medical University in Bialystok, Poland (approval number R-I-002/256/2003) Informed consent was obtained from the patients.

AUTHOR CONTRIBUTIONS

MW–concept of the study, supervision, interpreting results, writing draft of the manuscript, approval of the final manuscript. EM-collecting material, interpreting the results, performing experiments, approval of the manuscript. MM–writing the manuscript, literature searching, approval of the final manuscript. LZ–collecting material, pathomorphological examination. BP-writing of the final version of the manuscript, approval of the final manuscript. AW-writing of the final version of the manuscript, approval of the final manuscript. ST–writing of the final version of the manuscript, approval of the final manuscript. KH–writing final version of the manuscript, approval of the final manuscript. SS–pathomorphological examination, statistical analysis

FUNDING

This work was supported by research grant 6P05A 096 21 from Polish Committee for Scientific Research to MW.

CONFLICT OF INTEREST

The authors declare that the research was conducted in the absence of any commercial or financial relationships that could be construed as a potential conflict of interest.

REFERENCES

1. Folkman J. Tumor angiogenesis: therapeutic implications. *N Engl J Med* (1971). 285:1182–6. doi:10.1056/nejm197108122850711
2. Folkman J. What is the evidence that tumors are angiogenesis dependent? *J Nat Cancer Inst* (1990). 82:4–7. doi:10.1093/jnci/82.1.4
3. Wesseling P, van der Laak JAWM, Link M, Teepen HLJM, Ruiter DJ. Quantitative analysis of microvascular changes in diffuse astrocytic neoplasms with increasing grade of malignancy. *Hum Pathol* (1998). 29: 352–8. doi:10.1016/s0046-8177(98)90115-0
4. Leon SP, Folkerth RD, Black PM. Microvessel density is a prognostic indicator for patients with astroglial brain tumors. *Cancer* (1996). 77:362–72. doi:10.1002/(sici)1097-0142(19960115)77:2<362::aid-cncr20>3.0.co;2-z
5. Li VW, Yu Ab C, Folkman J, Scott RM, McL Black P, Folkerth R, et al. Microvessel count and cerebrospinal fluid basic fibroblast growth factor in children with brain tumours. *The Lancet* (1994). 344:82–6. doi:10.1016/s0140-6736(94)91280-7
6. Jain RK, di Tomaso E, Duda DG, Loeffler JS, Sorensen AG, Batchelor TT. Angiogenesis in brain tumours. *Nat Rev Neurosci* (2007). 8:610–22. doi:10.1038/nrn2175
7. Rak J, Mitsuhashi Y, Bayko L, Filmus J, Shirasawa S, Sasazuki T, et al. Mutant ras oncogenes upregulate VEGF/VPF expression: implications for induction and inhibition of tumor angiogenesis. *Cancer Res* (1995). 55:4575–80.
8. Ahir BK, Engelhard HH, Lakka SS. Tumor development and angiogenesis in adult brain tumor: glioblastoma. *Mol Neurobiol* (2020). 57:2461–78. doi:10.1007/s12035-020-01892-8
9. Johnson LD. Hypoxia: a key regulator of angiogenesis in cancer. *Cancer Metast Rev* (2007). 26:281–90. doi:10.1007/s10555-007-9066-y
10. Dvorak HF. Angiogenesis: update 2005. *J Thromb Haemost* (2005). 3:1835–42. doi:10.1111/j.1538-7836.2005.01361.x
11. Seghezzi G, Patel S, Ren CJ, Gualandris A, Pintucci G, Robbins ES, et al. Fibroblast growth factor-2 (FGF-2) induces vascular endothelial growth factor (VEGF) expression in the endothelial cells of forming capillaries: an autocrine mechanism contributing to angiogenesis. *J Cel Biol* (1998). 141:1659–73. doi:10.1083/jcb.141.7.1659
12. Murakami M, Simons M. Fibroblast growth factor regulation of neovascularization. *Curr Opin Hematol* (2008). 15:215–20. doi:10.1097/moh.0b013e3282f97d98
13. Batchelor TT, Reardon DA, de Groot JF, Wick W, Weller M. Antiangiogenic therapy for glioblastoma: current status and future prospects. *Clin Cancer Res* (2014). 20:5612–9. doi:10.1158/1078-0432.ccr-14-0834
14. McCubrey JA, Steelman LS, Chappell WH, Abrams SL, Franklin RA, Montalto G, et al. Ras/Raf/MEK/ERK and PI3K/PTEN/Akt/mTOR cascade inhibitors: how mutations can result in therapy resistance and how to overcome resistance. *Oncotarget* (2012). 3:1068–111. doi:10.18632/oncotarget.659
15. Grover SP, Mackman N. Tissue FactorAn essential mediator of hemostasis and trigger of thrombosis. *Arterioscler Thromb Vasc Biol* (2018). 38:709–25. doi:10.1161/atvbaha.117.309846
16. Ornstein DL, Meehan KR, Zacharski LR. The coagulation system as a target for the treatment of human gliomas. *Semin Thromb Hemost* (2002). 28:21–7. doi:10.1055/s-2002-20561
17. Versteeg HH, Schaffner F, Kerver M, Petersen HH, Ahamed J, Felding-Habermann B, et al. Inhibition of tissue factor signaling suppresses tumor growth. *Blood* (2008). 111:190–9. doi:10.1182/blood-2007-07-101048
18. Rao LVM. Tissue Factor as a tumor procoagulant. *Cancer Metastasis Rev* (1992). 11:249–266. doi:10.1007/bf01307181
19. Wojtukiewicz MZ, Sierko E, Rak J. Contribution of the hemostatic system to angiogenesis in cancer. *Semin Thromb Hemost* (2004). 30:5–20. doi:10.1055/s-2004-822967
20. Wojtukiewicz MZ, Zacharski LR, Memoli VA, Kisiel W, Kudryk BJ, Rousseau SM, et al. Abnormal regulation of coagulation/fibrinolysis in small cell carcinoma of the lung. *Cancer* (1990). 65:481–5. doi:10.1002/1097-0142(19900201)65:3<481::aid-cncr2820650318>3.0.co;2-u
21. Wojtukiewicz MZ, Zacharski LR, Memoli VA, Kisiel W, Kudryk BJ, Rousseau SM, et al. Fibrinogen-fibrin transformation *in situ* in renal cell carcinoma. *Anticancer Res* (1990). 10:579–82.
22. Wojtukiewicz MZ, Zacharski LR, Memoli VA, Kisiel W, Kudryk BJ, Rousseau SM, et al. Malignant melanoma: interaction with coagulation and fibrinolysis pathways *in situ*. *Am J Clin Pathol* (1990). 93:516–21. doi:10.1093/ajcp/93.4.516
23. Wojtukiewicz MZ, Sierko E, Zacharski LR, Zimnoch L, Kudryk B, Kisiel W. Tissue factor-dependent coagulation activation and impaired fibrinolysis *in situ* in gastric cancer. *Semin Thromb Hemost* (2003). 29:291–300. doi:10.1055/s-2003-40967
24. Wojtukiewicz MZ, Rucinska M, Zimnoch L, Jaromin J, Piotrowski Z, Rózanska-Kudelska M, et al. Expression of prothrombin fragment 1+2 in cancer tissue as an indicator of local activation of blood coagulation. *Thromb Res* (2000). 97:335–42. doi:10.1016/s0049-3848(99)00169-3
25. Hsu SM, Raine L, Fanger H. Use of avidin-biotin-peroxidase complex (ABC) in immunoperoxidase techniques: a comparison between ABC and unlabeled antibody (PAP) procedures. *J Histochem Cytochem* (1981). 29:577–80. doi:10.1177/29.4.6166661
26. Wojtukiewicz MZ, Zacharski LR, Rucińska M, Zimnoch L, Jaromin J, Rózańska-Kudelska M, et al. Expression of tissue factor and tissue factor pathway inhibitor *in situ* in laryngeal carcinoma. *Thromb Haemost* (1999). 82: 1659–62.
27. Hirsch FR, Varella-Garcia M, Bunn PA, Jr, Di Maria MV, Veve R, Bremnes RM, et al. Epidermal growth factor receptor in non-small-cell lung carcinomas: correlation between gene copy number and protein expression and impact on prognosis. *Jco* (2003). 21:3798–807. doi:10.1200/jco.2003.11.069
28. Pirker R, Pereira JR, von Pawel J, Krzakowski M, Ramlau R, Park K, et al. EGFR expression as a predictor of survival for first-line chemotherapy plus cetuximab in patients with advanced non-small-cell lung cancer: analysis of data from the phase 3 FLEX study. *Lancet Oncol* (2012). 13:33–42. doi:10.1016/s1470-2045(11)70318-7
29. Constantini V, Zacharski LR. The role of fibrin in tumor metastasis. *Cancer Metast Rev* (1992). 11:283–90. doi:10.1007/BF01307183
30. Devy L, Blacher S, Grignet-Debrus C, Bajou K, Masson V, Gerard RD, et al. The pro- or antiangiogenic effect of plasminogen activator inhibitor 1 is dose dependent. *FASEB j.* (2002). 16:147–54. doi:10.1096/fj.01-0552com
31. Siemann DW, Chaplin DJ, Horsman MR. Realizing the potential of vascular targeted therapy: the rationale for combining vascular disrupting agents and anti-angiogenic agents to treat cancer. *Cancer Invest* (2017). 35:519–34. doi:10.1080/07357907.2017.1364745
32. Och W, Mariak Z, Smółka M, Badowski J, Koziorowski M. [Vascular endothelial growth factor expression in cerebral neoplasms]. *Neurol Neurochir Pol* (2001). 35:1071–9.
33. Plate KH, Breier G, Weich HA, Mennel HD, Risau W. Vascular endothelial growth factor and glioma angiogenesis: coordinate induction of VEGF receptors, distribution of VEGF protein and possibleIn vivo regulatory mechanisms. *Int J Cancer* (1994). 59:520–9. doi:10.1002/ijc.2910590415
34. Carrol RS, Zhang J, Melnick MB, Maruyama T, McL-Black P. KDR activation in astrocytic neoplasm. *Cancer* (1999). 86:1335–41. doi:10.1002/(sici)1097-0142(19991001)86:7<1335::aid-cncr32>3.0.co;2-z
35. Holash J, Maisonpierre PC, Comton D, Boland P, Alexander CR, Zagzag D, et al. Vessel cooption, regression, and growth in tumors mediated by angiopoietins and VEGF. *Science* (1999). 284:1994–8. doi:10.1126/science.284.5422.1994
36. Poech M, Farion R, Hiou A, Le Bas JF, Pasquier B, Remy C. Immunohistochemical study of VEGF, angiopoietin 2 and their receptors

in the neovascularization following microinjection of C6 glioma cells into rat brain. *Anticancer Res* (2002). 22(4):2147-51.
37. Jubb AM, Pham TQ, Hanby AM, Frantz GD, Peale FV, Wu TD, et al. Expression of vascular endothelial growth factor, hypoxia inducible factor 1 , and carbonic anhydrase IX in human tumours. *J Clin Pathol* (2004). 57: 504–12. doi:10.1136/jcp.2003.012963
38. Turner HE, Harris AL, Melmed S, Wass JAH. Angiogenesis in endocrine tumors. *Endocr Rev* (2003). 24:600–32. doi:10.1210/er.2002-0008
39. Dabrosin C. Variability of vascular endothelial growth factor in normal human breast tissue *in vivo* during the menstrual cycle. *J Clin Endocrinol Metab* (2003). 88:2695–8. doi:10.1210/jc.2002-021584
40. Maeda K, Chung Y-s., Ogawa Y, Kang S-M, Ogawa M, Sawada T, et al. Prognostic value of vascular endothelial growth factor expression in gastric carcinoma. *Cancer* (1996). 77:858–63. doi:10.1002/(sici)1097-0142(19960301) 77:5<858::aid-cncr8>3.0.co;2-a
41. Salven P, Heikkilä P, Joensuu H. Enhanced expression of vascular endothelial growth factor in metastatic melanoma. *Br J Cancer* (1997). 76:930–4. doi:10. 1038/bjc.1997.486
42. Weidner N, Semple JP, Welch WR, Folkman J. Tumor angiogenesis and metastasis - correlation in invasive breast carcinoma. *N Engl J Med* (1991). 324: 1–8. doi:10.1056/nejm199101033240101
43. Lizárraga-Verdugo E, Avendaño-Félix M, Bermúdez M, Ramos-Payán R, Pérez-Plasencia C, Aguilar-Medina M. Cancer stem cells and its role in angiogenesis and vasculogenic mimicry in gastrointestinal cancers. *Front Oncol* (2020). 10:413. doi:10.3389/fonc.2020.00413
44. Xin M, Yin-Sheng C, Fu-Rong C, Shao-Yan X, Zhong-Ping C. Glioblastomas stem cell differentiation into endothelial cells evidenced through live-cell imaging. *Neuro-Oncology* (2017). 19(8):1109–18. doi:10.1093/neuonc/nox016
45. Mercurio A. VEGF/Neuropilin signaling in cancer stem cells. *Ijms* (2019). 20: 490. doi:10.3390/ijms20030490
46. Elaimy AL, Amante JJ, Zhu LJ, Wang M, Walmsley CS, FitzGerald TJ, et al. The VEGF receptor neuropilin 2 promotes homologous recombination by stimulating YAP/TAZ mediated Rad51 expression. *Proc Natl Acad Sci U S A* (2019). 9(116):14174–80. doi:10.1073/pnas.1821194116
47. Ke LD, Shi YX, Im SA, Chen X, Yung WK. The relevance of cell proliferation, vascular endothelial growth factor, and basic fibroblast growth factor production to angiogenesis and tumorigenicity in human glioma cell lines. *Clin Cancer Res* (2000). 6:2562–72.
48. Landriscina M, Cassano A, Ratto C, Longo R, Ippoliti M, Palazzotti B, et al. Quantitative analysis of basic fibroblast growth factor and vascular endothelial growth factor in human colorectal cancer. *Br J Cancer* (1998). 78:765–70. doi:10.1038/bjc.1998.575
49. Takahashi Y, Ellis LM, Ohta T, Mai M. Angiogenesis in poorly differentiated medullary carcinoma of the stomach. *Surg Today* (1998). 28:367–72. doi:10. 1007/s005950050143
50. Brem S, Tsanaclis AMC, Gately S, Gross JL, Herblin WF. Immunolocalization of basic fibroblast growth factor to the micro vasculature of human brain tumors. *Cancer* (1992). 70:2673–80. doi:10.1002/1097-0142(19921201)70: 11<2673::aid-cncr2820701118>3.0.co;2-f
51. Takahashi JA, Fukumoto M, Igarashi K, Oda Y, Kikuchi H, Hatanaka M. Correlation of basic fibroblast growth factor expression levels with the degree of malignancy and vascularity in human gliomas. *J Neurosurg* (1992). 76: 792–8. doi:10.3171/jns.1992.76.5.0792
52. Zagzag D, Miller DC, Sato Y, Rifkin DB, Burstein DE. Immunohistochemical localization of basic fibroblast growth factor in astrocytomas. *Cancer Res* (1990). 50:7393–8.
53. Stan AC, Nemati MN, Pietsch T, Walter GF, Dietz H. *In vivo* inhibition of angiogenesis and growth of the human U-87 malignant glial tumor by treatment with an antibody against basic fibroblast growth factor. *J Neurosurg* (1995). 82:1044–52. doi:10.3171/jns.1995.82.6.1044
54. Hamada K, Kuratsu J, Saitoh Y, Takeshima H, Nishi T, Ushio Y. Expression of tissue factor correlates with grade of malignancy in human glioma. *Cancer* (1996). 77:1877–83. doi:10.1002/(SICI)1097-0142(19960501)77:9<1877::AID-CNCR18>3.0.CO;2-X
55. Takano S, Tsuboi K, Tomono Y, Mitsui Y, Nose T. Tissue factor, osteopontin, alphavbeta3 integrin expression in microvasculature of gliomas associated with vascular endothelial growth factor expression. *Br J Cancer* (2000). 82:1967–73. doi:10.1054/bjoc.2000.1150
56. Hamada K, Kuratsu J-i., Saitoh Y, Takeshima H, Nishi T, Ushio Y. Expression of tissue factor correlates with grade of malignancy in human glioma. *Cancer* (1996). 77:1877–83. doi:10.1002/(sici)1097-0142(19960501)77:9<1877::aid-cncr18>3.0.co;2-x
57. Morrissey JH, Neuenschwander PF, Huang Q, McCallum CD, Su B, Johnson AE. Factor VIIa-tissue factor: functional importance of protein-membrane interactions. *Thromb Haemost* (1997). 78:112–6.
58. Guan M, Jin J, Su B, Liu WW, Lu Y. Tissue factor expression and angiogenesis in human glioma. *Clin Biochem* (2002). 35:321–5. doi:10.1016/s0009-9120(02) 00312-0
59. Abe K, Shoji M, Chen J, Bierhaus A, Danave I, Micko C, et al. Regulation of vascular endothelial growth factor production and angiogenesis by the cytoplasmic tail of tissue factor. *Proc Natl Acad Sci* (1999). 96:8663–8. doi:10.1073/pnas.96.15.8663
60. Folkman J. Angiogenesis in cancer, vascular, rheumatoid and other disease. *Nat Med* (1995). 1:27–30. doi:10.1038/nm0195-27
61. Zhang Y, Deng Y, Luther T, Müller M, Ziegler R, Waldherr R, et al. Tissue factor controls the balance of angiogenic and antiangiogenic properties of tumor cells in mice. *J Clin Invest* (1994). 94:1320–7. doi:10.1172/ jci117451
62. Bárdos H, Molnár P, Csécsei G, Adány R. Fibrin deposition in primary and metastatic human brain tumours. *Blood Coagul Fibrinolysis* (1996). 7:536–48.
63. Wojtukiewicz MZ, Sierko E, Klementt P, Rak J. The hemostatic system and angiogenesis in malignancy. *Neoplasia* (2001). 3:371–84. doi:10.1038/sj.neo. 7900184

Pathology & Oncology Research

frontiers

ORIGINAL RESEARCH
published: 20 April 2021
doi: 10.3389/pore.2021.613099

Napsin A Expression in Human Tumors and Normal Tissues

*Sören Weidemann[1], Jan Lukas Böhle[1], Hendrina Contreras[1], Andreas M. Luebke[1], Martina Kluth[1], Franziska Büscheck[1], Claudia Hube-Magg[1], Doris Höflmayer[1], Katharina Möller[1], Christoph Fraune[1], Christian Bernreuther[1], Michael Rink[2], Ronald Simon[1], Anne Menz[1], Andrea Hinsch[1], Patrick Lebok[1], Till Clauditz[1], Guido Sauter[1], Ria Uhlig[1], Waldemar Wilczak[1], Stefan Steurer[1], Eike Burandt[1], Rainer Krech[3], David Dum[1], Till Krech[1,3], Andreas Marx[1,4] and Sarah Minner[1]**

[1]*Institute of Pathology, University Medical Center Hamburg-Eppendorf, Hamburg, Germany,* [2]*Department of Urology, University Medical Center Hamburg-Eppendorf, Hamburg, Germany,* [3]*Institute of Pathology, Clinical Center Osnabrueck, Osnabrueck, Germany,* [4]*Department of Pathology, Academic Hospital Fuerth, Fuerth, Germany*

Background: Novel aspartic proteinase of the pepsin family A (Napsin A, TAO1/TAO2) is a functional aspartic proteinase which is involved in the maturation of prosurfactant protein B in type II pneumocytes and the lysosomal protein catabolism in renal cells. Napsin A is highly expressed in adenocarcinomas of the lung and is thus commonly used to affirm this diagnosis. However, studies have shown that other tumors can also express Napsin A.

Methods: To comprehensively determine Napsin A expression in normal and tumor tissue, 11,957 samples from 115 different tumor types and subtypes as well as 500 samples of 76 different normal tissue types were evaluable by immunohistochemistry on tissue microarrays.

Results: Napsin A expression was present in 16 different tumor types. Adenocarcinoma of the lung (85.6%), clear cell adenocarcinoma of the ovary (71.7%), clear cell adenocarcinoma of the endometrium (42.8%), papillary renal cell carcinoma (40.2%), clear cell (tubulo) papillary renal cell carcinoma (16.7%), endometrial serous carcinoma (9.3%), papillary thyroid carcinoma (9.3%) and clear cell renal cell carcinoma (8.2%) were among the tumors with the highest prevalence of Napsin A positivity. In papillary and clear cell renal cell carcinoma, reduced Napsin A expression was linked to adverse clinic-pathological features ($p \leq 0.03$).

Conclusion: This methodical approach enabled us to identify a ranking order of tumors according to their relative prevalence of Napsin A expression. The data also show that loss of Napsin A is linked to tumor dedifferentiation in renal cell carcinomas.

Keywords: napsin A, immunohistochemistry, tissue micro array, diagnostic, human cancer types

Abbreviations: CSS, cancer specific survival; EMT, epithelial-mesenchymal transition; IHC, Immunohistochemistry; ISUP, International Society of Uropathology; Napsin A, Novel aspartic proteinase of the pepsin family A; RFS, recurrence free survival; TMA, tissue microarray; TTF1, thyroid transcription factor 1; UICC, Union internationale contre le cancer.

OPEN ACCESS

Edited by:
Andrea Ladányi,
National Institute of Oncology (NIO), Hungary

****Correspondence:***
Sarah Minner
s.minner@uke.de

Received: *01 October 2020*
Accepted: *26 February 2021*
Published: *20 April 2021*

Citation:
Weidemann S, Böhle JL, Contreras H, Luebke AM, Kluth M, Büscheck F, Hube-Magg C, Höflmayer D, Möller K, Fraune C, Bernreuther C, Rink M, Simon R, Menz A, Hinsch A, Lebok P, Clauditz T, Sauter G, Uhlig R, Wilczak W, Steurer S, Burandt E, Krech R, Dum D, Krech T, Marx A and Minner S (2021) Napsin A Expression in Human Tumors and Normal Tissues. Pathol. Oncol. Res. 27:613099. doi: 10.3389/pore.2021.613099

INTRODUCTION

Novel aspartic proteinase of the pepsin family A (Napsin A, TAO1/TAO2) belongs to the peptidase A1 family, such as Cathepsin E, renin, and pepsin and is encoded by the *NAPSA* gene located at chromosome 19q13.3 [1–3]. Napsin A is a functional aspartic proteinase, harboring two aspartic acids inside the catalytical center that cleaves proteins and peptides to produce mature or active forms of these molecules [2, 3]. Napsin A is mainly expressed in the cytoplasm of type II pneumocytes, intra-alveolar macrophages, proximal and convoluted renal tubules, and pancreatic acini and ducts [4, 5] as well as adenocarcinomas of the lung, papillary renal cell carcinomas, and ovarian clear cell carcinomas [1, 6, 7]. Physiologically, Napsin A is involved in the maturation of prosurfactant protein B in type II pneumocytes [8], potentially in phagocytosis by macrophages [3] and the lysosomal protein catabolism in renal cells [9]. In addition, it was demonstrated that Napsin A is regulated by thyroid transcription factor 1 (TTF1), a diagnostic marker in lung cancer [3]. A recent study has shown that downregulation of Napsin A promotes TGF-ß induced cell proliferation in lung adenocarcinoma cells [10].

In diagnostic pathology, Napsin A immunohistochemistry (IHC) is primarily utilized for typing of non-small cell carcinoma, since Napsin A is expressed in a high percentage of adenocarcinomas of the lung (>80%) but only rarely in squamous carcinomas of the lung [3]. When Napsin A was first described around 25 years ago, it was thought to be a lung-specific marker [1], but soon after it was shown that Napsin A is also expressed in kidney tumors [6], compatible with its physiologic expression in proximal renal tubules. Since then, several studies have shown that Napsin A can also be expressed in other tumor types [7, 11, 12]. For example, immunohistochemical Napsin A positivity was found in 0%–52% of clear cell renal cell carcinomas [6, 13–22], 72%–97% of papillary renal cell carcinomas [6, 13, 14, 16–18, 20–22], 0%–48% of thyroid tumors [10, 11, 16, 18, 19, 23, 24], 69%–100% of clear cell carcinomas of the ovary [7, 19, 25–32] and 0%–9% of cholangiocarcinomas [12, 19, 33, 34]. Partially conflicting results with respect to positivity rates between these studies may be due to the use of different antibodies, the use of different immunostaining protocols as well as different criteria to determine positivity in these studies. For many other tumor types, Napsin A expression has never been analyzed.

Since the lung is a frequent site for metastasis of various tumors it is of utmost importance to understand the relative frequency of Napsin A expression in other tumor types and normal tissues. We therefore analyzed Napsin A expression by immunohistochemistry in a tissue microarray format of which 11,957 tumor tissue samples from 115 different tumor types and subtypes as well as 76 non-neoplastic tissue types were evaluable.

MATERIALS AND METHODS

Tissue Microarrays (TMAs)

In order to study Napsin A expression in normal and neoplastic human tissues, preexisting TMAs containing 14,692 primary tumors from 115 tumor types and subtypes were used. Only one core (0.6 mm in diameter) was taken from each tumor. This approach is supported by a large number of TMA studies [35]. The normal tissue microarray contains eight samples respectively from 76 different normal tissues, resulting in a total of 608 spots. All samples were derived from the archives of the Institute of Pathology, University Hospital of Hamburg, Germany, the Institute of Pathology, Clinical Center Osnabrueck, Germany, and the Department of Pathology, Academic Hospital Fuerth, Germany. Tissues were fixed in 4% buffered formalin and then embedded in paraffin. TMA tissue spot diameter is 0.6 mm.

The use of archived remnants of diagnostic tissues for manufacturing of TMAs and their analysis for research purposes as well as patient data analysis has been approved by local laws (HmbKHG, §12) and by the local ethics committee (Ethics commission Hamburg, WF-049/09). All work has been carried out in compliance with the Helsinki Declaration.

Immunohistochemistry

Freshly cut TMA sections were immunostained on one day and in one experiment. Slides were deparaffinized with xylol, rehydrated through a graded alcohol series and exposed to heat-induced antigen retrieval for 5 min in an autoclave at 121°C in pH nine DakoTarget Retrieval Solution™ (Agilent, CA, United States; #S2367). Endogenous peroxidase activity was blocked with Dako peroxidase Blocking Solution™ (Agilent, CA, United States; #52023) for 10 min. Primary antibody specific against Napsin A protein (mouse monoclonal, MS Validated Antibodies, MSVA-112; Hamburg, Germany) was applied at 37°C for 60 min at a dilution of 1:400. Bound antibody was then visualized using the EnVision Kit™ (Agilent, CA, United States; #K5007) according to the manufacturer's directions. The sections were counterstained with Hemalaun. This specific antibody was selected because of a favorable signal to noise ratio and its staining pattern in normal tissues coincided with data described in "The Protein Atlas".

For tumor tissues, the percentage of positive neoplastic cells was estimated, and the staining intensity was semiquantitatively recorded (0, 1+, 2+, 3+). For statistical analyses, the staining results were categorized into four groups. Tumors without any staining were considered as negative. Tumors with 1 + staining intensity in ≤70% of cells and 2 + intensity in ≤30% of cells were considered weakly positive. Tumors with 1 + staining intensity in >70% of cells, 2 + intensity in 31–70%, or 3 + intensity in ≤30% were considered moderately positive. Tumors with 2 + intensity in >70% or 3 + intensity in >30% of cells were considered strongly positive. The analysis was performed by one pathologist (SM).

Prognostic Evaluation of Napsin A in a Subset of Renal Cell Carcinomas

The tissue specimens were available from patients with renal cell tumors, undergoing surgery between 1994 and 2015 at the Department of Urology, University Medical Center Hamburg-Eppendorf. Detailed histopathological data on ISUP, Fuhrman, and Thoenes grade, UICC, tumor stage (pT), and lymph node metastasis (pN) were available from 575 clear cell and 152

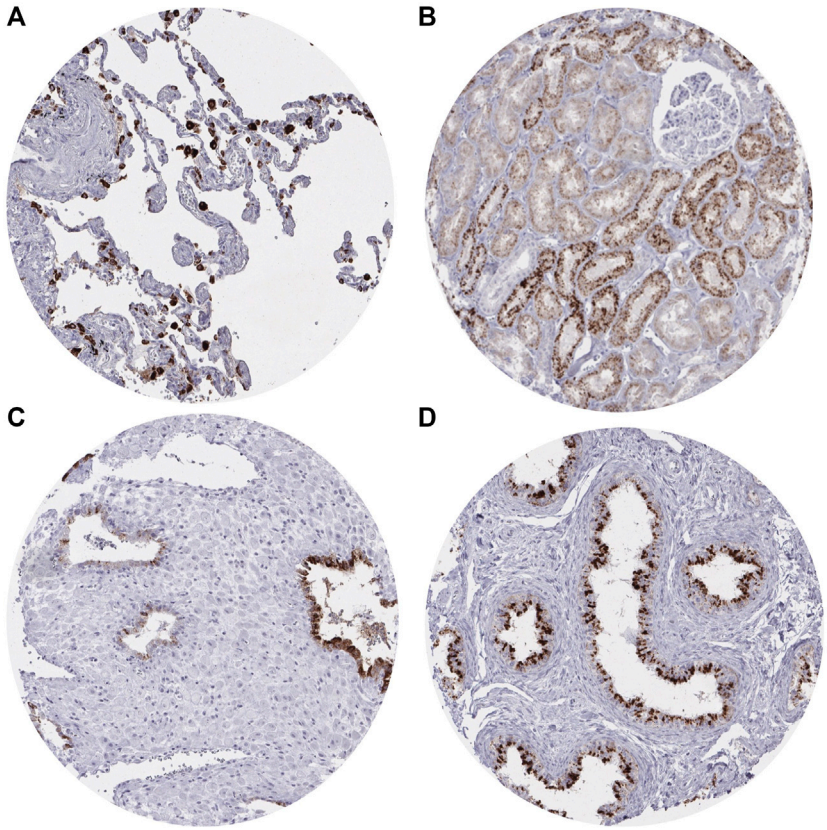

FIGURE 1 | Representative images of Napsin A immunostaining in non-neoplastic tissue.**(A)** Positive staining in pneumocytes in the lung. **(B)** Positive staining in the renal cortex of the kidney (proximal tubules > distal tubules). **(C)** Positive staining in endometrial glands in decidualized stroma. **(D)** Positive staining in the tubules of the epididymis.

papillary renal cell carcinomas. Clinical follow up data were available from 531 clear cell and 136 papillary renal cell carcinomas with a median follow-up of 40/40months (range 1–250/2–247 months). To thoroughly analyze the potential prognostic value of Napsin A, the subset was separately analyzed at two different antibody dilutions (1:400 and 1:135). This subset of renal cell carcinomas with clinicopathological information has been used in several previously published studies (for example [36–42]).

Statistics

Statistical calculations were performed with JMP 14 software (SAS Institute Inc., NC, United States). Contingency tables and the chi^2-test were performed to search for associations between Napsin A and tumor phenotype. Survival curves were calculated according to Kaplan-Meier. Log-Rank test and univariable cox proportional hazard regression was applied to detect significant differences between different Napsin A immunostaining groups. Multivariable cox proportional hazard analysis was performed to test the statistical independence and significance between clinico-patholigcal variables and Napsin A immunostaining in relation to recurrence free survival and cancer specific survival.

RESULTS

Technical Issues

A total of 11,957 (81.4%) of 14,692 tumor samples and 500 (82.2%) of 608 normal samples were interpretable for Napsin A immunostaining in our TMA analysis. Non-interpretable samples (2,843; 18.6%) either lacked unequivocal tumor cells or were lost from the TMA during the technical procedures.

Napsin A in Normal Tissue

A moderate to strong (2+/3+) cytoplasmic Napsin A staining was found in pneumocytes and alveolar macrophages of the lung (**Figure 1A**), and the renal medulla and cortex of the kidney (proximal > distal) (**Figure 1B**). In addition, strong cytoplasmic Napsin A staining was found occasionally in endometrial glands in decidualized stroma (**Figure 1C**), and weak to moderate (1+/2+) staining was found in the tubules of the epididymis (**Figure 1D**). In contrast to previous studies [5] we did not find any Napsin A staining in seven evaluable spots with normal pancreatic tissue. Napsin A immunostaining was also absent in endothelium and media of the aorta, the heart, striated muscle, tongue muscle, myometrium of the uterus, muscular wall of the appendix,

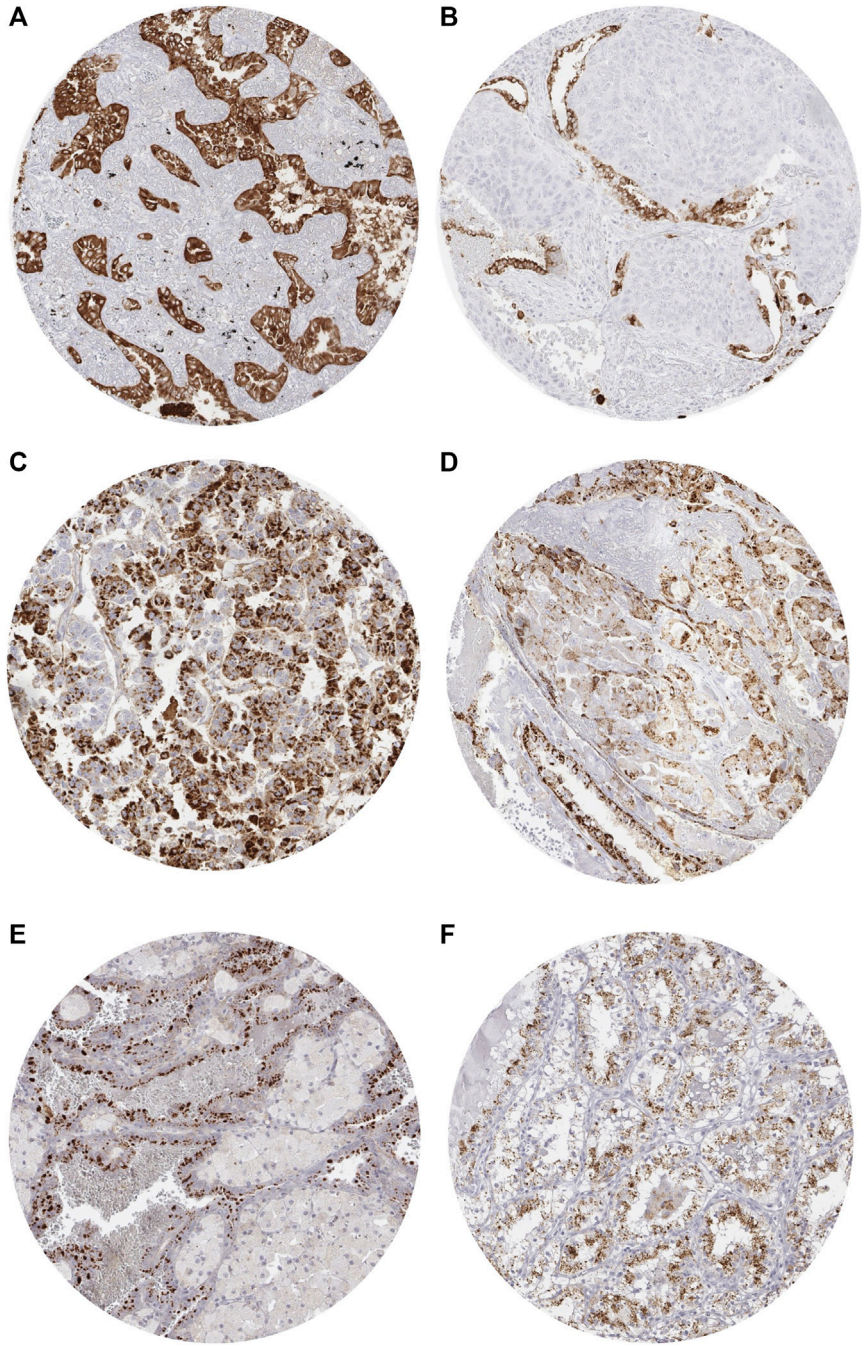

FIGURE 2 | Representative images of Napsin A immunostaining in tumors. **(A)** Positive staining in adenocarcinoma of the lung. **(B)** Absent staining in a squamous carcinoma of the lung with scattered positive pneumocytes. **(C)** Positive staining in clear cell carcinoma of the ovary. **(D)** Positive staining in endometrial clear cell carcinoma. **(E)** Positive staining in papillary renal cell carcinoma. **(F)** Positive staining in clear cell (tubulo) papillary renal cell carcinoma.

esophagus, stomach, ileum, colon descendens, kidney pelvis, and urinary bladder, corpus spongiosum of the penis, corpus luteum, and follicular cyst of the ovary, ovarian stroma, fallopian tube, fat, skin (including hair follicles and sebaceous glands), oral mucosa of the lip, oral cavity, surface epithelium of the tonsil, transitional mucosa and skin of the anal canal, ectocervix, squamous epithelium of the esophagus, urothelium of the kidney pelvis and urinary bladder, amnion and chorion of the mature placenta, lymph nodes, spleen, thymus, tonsil, mucosa of the stomach (antrum and corpus), duodenum, ileum, appendix, colon descendens, rectum, and gall bladder, liver, parotid, submandibular, and

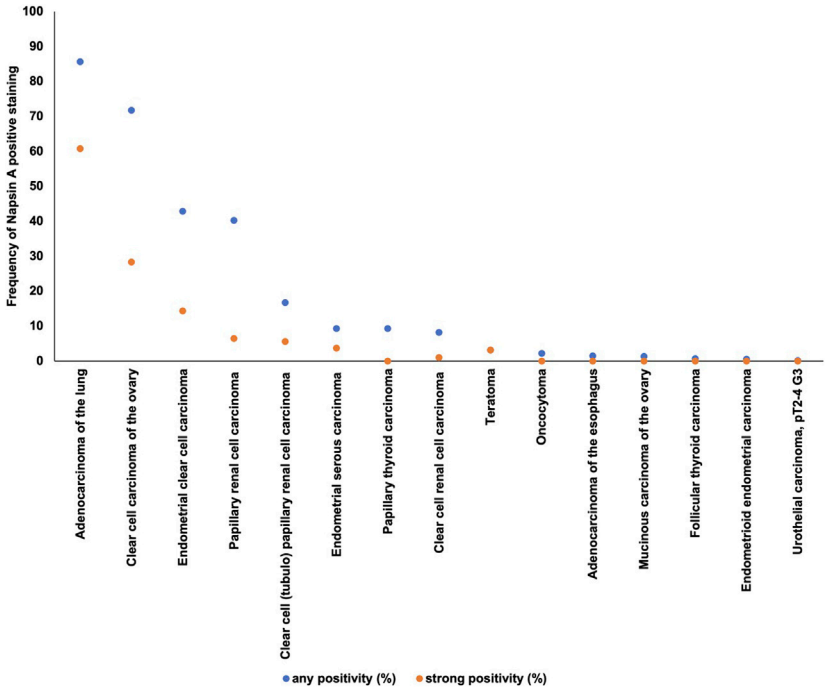

FIGURE 3 | Ranking order of Napsin A immunostaining in human tumors. Both the frequency of positive cases (blue dots) and the frequency of strongly positive cases (orange dots). 98 additional tumor entities without any Napsin A positive cases are not shown due to space restrictions.

sublingual gland, bone marrow, Brunner gland of the duodenum, prostate, seminal vesicle, testis, mucosa and glands of the bronchus, sinus paranasales, breast, endocervix, proliferative and secreting endometrium, adrenal gland, parathyroid, thyroid gland, stratum moleculare and neuronorum of the cerebellum, white and gray cerebrum, and posterior and anterior lobe of the pituitary.

Napsin A in Tumor Cells

Positive Napsin A immunostaining was detectable in 396 (3.3%) of the 11,957 analyzable tumors, including 156 (1.3%) with weak, 82 (0.7%) with moderate, and 158 (1.3%) with strong immunostaining. Representative images of Napsin A positive tumors are shown in **Figure 2** and **Supplementary Figure S1**. Overall, 16 (13.9%) of 115 tumor categories showed a detectable Napsin A expression with 8 (7.0%) tumor categories showing at least in a small proportion of cases strong positivity (**Supplementary Table S1**). The highest rate of positive staining was found in adenocarcinoma of the lung (85.6%, **Figure 2A**), clear cell carcinoma of the ovary (71.7%, **Figure 2C**), endometrial clear cell carcinoma (42.8%, **Figure 2D**), and papillary renal cell carcinoma (40.2%, **Figure 2E**). Important tumor types with low or absent Napsin A immunostaining included various squamous cell carcinomas (e.g. lung, larynx, esophagus), different subtypes of breast carcinomas, adenocarcinomas of the prostate, non-invasive papillary urothelial carcinomas, various soft tissue tumors, and bone tumors. A graphical representation of a ranking order of Napsin A positive and strongly positive cancers is given in **Figure 3**.

Prognostic Value of Napsin A in Renal Cell Carcinomas

Clear cell and papillary renal cell carcinoma were analyzed at different antibody dilutions. As expected at an antibody dilution of 1:135 the number of positive tumors was higher than at 1:400. In the subgroup of clear cell carcinomas there were 8.4% cases at a dilution of 1:400 compared to 44.0% at a dilution of 1:135. Correspondingly, there were 37.3% positive papillary renal cell carcinomas at a dilution of 1:400 compared to 80.9% at a dilution of 1:135. Representative images of Napsin A staining at different dilutions are given in **Supplementary Figure S2**. There was no correlation with any clinicopathological features such as tumor stage, tumor grade, lymph node status or with survival or recurrence at a dilution of 1:400, but at a dilution of 1:135 there was a positive correlation with low tumor grade (p = 0.0055) and late recurrence (p = 0.0063) in the subgroup of clear cell carcinomas and a correlation with low tumor stage (p = 0.027), late recurrence (p = 0.001) and long tumor-specific survival (p = 0.011) in the subgroup of papillary renal cell carcinomas (**Table 1**; **Figure 4**). Multivariable analyses showed no independent prognostic relevance from the established clinico-pathological parameters in relation to recurrence free survival and cancer specific survival (**Table 2**).

DISCUSSION

Our extensive analysis of 11,957 evaluable tumors from 115 different tumor entities identified 16 tumor types with at least

TABLE 1 | Napsin A immunostaining (dilution 1:135) and tumor phenotype of clear cell and papillary renal cell carcinoma.

	Napsin a immunostaining in clear cell renal cell carcinomas						Napsin a immunostaining in papillary renal cell carcinomas					
	n	Negative	Weak	Moderate	Strong	*p* value	n	Negative	Weak	Moderate	Strong	*p* value
All cancers	575	56.0	27.5	8.2	8.3		152	19.1	14.5	12.5	53.9	
ISUP												
1	192	51.0	29.2	9.4	10.4	0.0134	32	15.6	15.6	12.5	56.3	0.5198
2	178	55.1	29.2	6.7	9.0		70	14.3	14.3	12.9	58.6	
3	163	55.8	28.2	9.8	6.1		48	29.2	12.5	10.4	47.9	
4	34	85.3	8.8	0.0	5.9		1	0.0	100.0	0.0	0.0	
Fuhrmann												
1	27	40.7	33.3	14.8	11.1	0.0241	1	0.0	0.0	0.0	100.0	0.2896
2	339	54.0	28.6	8.0	9.4		102	14.7	14.7	12.8	57.8	
3	167	56.3	27.5	9.6	6.6		45	26.7	13.3	11.1	48.9	
4	41	80.5	14.6	0.0	4.9		3	66.7	33.3	0.0	0.0	
Thoenes												
1	205	51.2	28.8	8.3	11.7	0.0055	40	12.5	12.5	15.0	60.0	0.7994
2	316	55.1	28.8	9.2	7.0		102	20.6	15.7	10.8	52.9	
3	53	79.2	15.1	1.9	3.8		9	33.3	11.1	11.1	44.4	
UICC												
1	251	57.0	27.5	7.6	8.0	0.8788	85	14.1	15.3	11.8	58.8	0.0540
2	30	50.0	30.0	6.7	13.3		9	33.3	0.0	22.2	44.4	
3	76	64.5	23.7	6.6	5.3		3	0.0	66.7	0.0	33.3	
4	62	64.5	21.0	8.1	6.5		11	45.5	9.1	0.0	45.5	
Tumor stage (pT)												
1	332	55.1	28.0	7.5	9.3	0.8502	109	12.8	15.6	12.8	58.7	0.0270
2	59	55.9	27.1	6.8	10.2		27	22.2	7.4	18.5	51.9	
3–4	180	57.8	26.7	9.4	6.1		11	54.6	18.2	0.0	27.3	
Lymphnode metastasis (pN)[a]												
0	103	57.3	29.1	4.9	8.7	0.2725	16	25.0	25.0	6.3	43.8	0.2322
≥1	13	61.5	23.1	15.4	0.0		7	42.9	0.0	0.0	57.1	

[a]*Numbers do not always add up to the total number in the different categories because of cases with missing data.*

minimal Napsin A expression in at least one case. Tumor entities with highest rates of Napsin A positivity included adenocarcinoma of the lung (85.6%), papillary renal cell carcinoma (40.2%), clear cell adenocarcinoma of the endometrium (42.8%) and the ovary (71.7%) and clear cell (tubulo) papillary renal cell carcinoma (16.7%). Tumor entities found to be potentially Napsin A positive also included three types of neoplasia for which Napsin A expression has not yet been reported, such as follicular thyroid carcinoma (n = 2; 0.7%), urothelial carcinoma of the bladder (n = 2; 0.1%) and teratoma (n = 1; 3.1%).

More than 70 studies have previously analyzed Napsin A expression in tumors by IHC. The studies showed a wide range of Napsin A positivity for each tumor entity, for example, published Napsin A positivity rates ranged from 0% to 100% in adenocarcinoma of the lung [11, 13, 16, 18, 20, 22, 24, 43–66], 0%–48% in papillary thyroid carcinoma [11, 16, 18, 19, 24], 0%–52% in clear cell renal cell carcinoma [6, 13, 15–19, 22, 24], 0%–17% in small cell carcinoma of the lung [13, 22, 50, 61, 63], 0–10% in squamous cell carcinoma of the lung [16, 18, 22, 24, 46–48, 50, 52, 57–59, 61–65, 67–69], 69–100% in clear cell adenocarcinoma of the ovary [7, 19, 25, 27–32, 34], 72%–97% in papillary renal cell carcinoma [6, 16–18, 20–22] and 67%–89% in clear cell adenocarcinoma of the endometrium [7, 30, 70, 71]. The analysis of a large number of different tumor entities under highly standardized conditions enabled us to clarify the relative importance of Napsin A expression across tumor entities and to generate a ranking list according to the expected rate of Napsin A positivity. In **Figure 5**, the data of previous studies are summarized and compared with data from our study.

In tumor pathology, Napsin A IHC is mainly used for subtyping of lung tumors and for differentiating ovarian high grade carcinomas. Major therapeutic advances have been made in recent years in the lung cancer field with different therapeutic strategies for different tumor types, making it inevitable for the pathologist to make an exact diagnosis on a small biopsy. A strong role of Napsin A in the difficult distinction of adenocarcinoma and squamous cell carcinoma in the lung is strongly supported by our Napsin positivity of 85.6% in 198 adenocarcinomas, while none of our 79 squamous cell carcinomas were found positive. That none of 296 analyzed squamous cell carcinomas from other organs of origin were Napsin A positive further emphasizes that this protein is virtually absent in cells with squamous differentiation. It is of note that other investigators have reported Napsin A positivity in 0–10% of pulmonary squamous cell carcinomas in studies analyzing 14–569 tumors [16, 18, 22, 24, 46–48, 50, 52, 57–59, 61–65, 67–69]. One possible reason for a perceived Napsin A positivity in squamous cell carcinomas that we and others encountered is entrapped normal lung tissue with Napsin A positive hyperplastic pneumocytes or Napsin A positive intra-alveolar macrophages

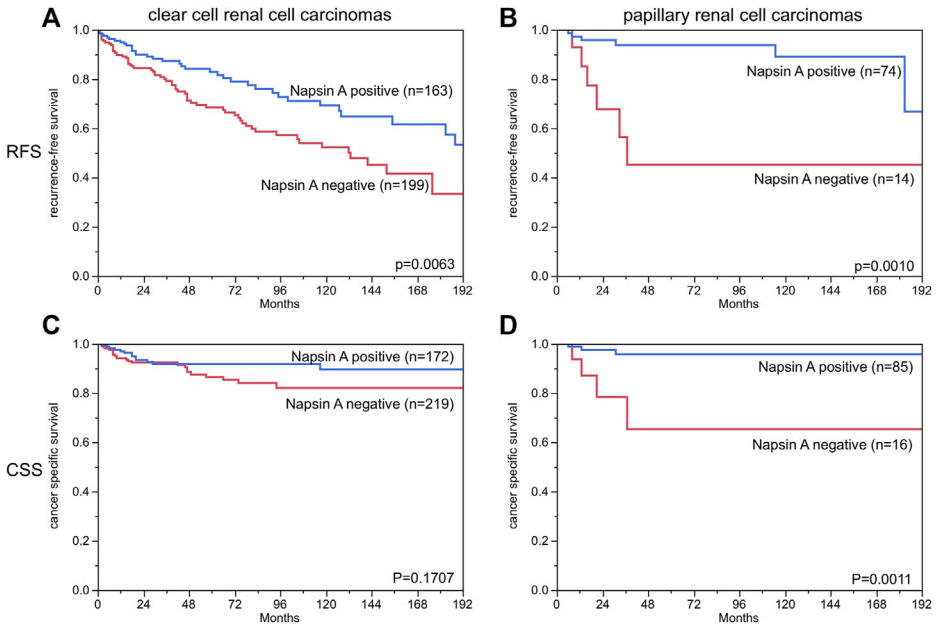

FIGURE 4 | Napsin A immunostaining and recurrence-free survival and cancer specific survival in patients with papillary and clear cell renal cell carcinoma. Weak, moderate and strong staining are combined as "positive". (RFS = recurrence free survival, CSS = cancer specific survival). *The numbers do not add to the total number of tumors with clinical follow-up data, since only cases with evaluable Napsin A staining are included.

TABLE 2 | Univariable and multivariable Cox regression analyses.

Parameter	Univariable cox regression analyses				Multivariable cox regression analyses			
	Clear cell renal cell carcinoma		Papillary renal cell carcinoma		Clear cell renal cell carcinoma		Papillary renal cell carcinoma	
	Ep: RFS *p* value	Ep: CSS *p* value	Ep: RFS *p* value	Ep: CSS *p* value	Ep: RFS *p* value	Ep: CSS *p* value	Ep: RFS *p* value	Ep: CSS *p* value
ISUP	<0.0001	<0.0001	0.0015	—	0.2421	0.2241	0.8549	0.8419
Fuhrmann	<0.0001	<0.0001	0.0032	0.3023	0.4526	0.5251	0.8993	0.8670
Thoenes	<0.0001	<0.0001	0.0012	0.0377	0.2295	0.0852	0.2735	0.2806
UICC	<0.0001	<0.0001	<0.0001	<0.0001	0.0550	0.2512	0.0413	1.0000
Tumor stage (pT)	<0.0001	<0.0001	<0.0001	0.0001	0.3931	0.1097	0.0539	0.1933
Lymph node metastasis (pN)	<0.0001	0.0158	0.0046	0.0090	0.3122	0.8636	0.0559	1.0000
Napsin A	0.0061	0.1670	0.0061	0.0083	0.4835	0.3929	0.4313	0.3871

Abbreviations: CSS, Cancer specific survival; EP, endpoint; RFS, Recurrence-free survivial.

between cancer cells [3]. Our finding of 71.7% Napsin A positive clear cell ovarian carcinomas while none of 521 serous high grade carcinomas were Napsin A positive further corroborates the previously suggested diagnostic utility of Napsin A IHC for the distinction of these tumors [27]. A limitation of our study is the absence of large cell carcinomas of the lung which have not been included on the tissue microarray.

To differentiate adenocarcinoma from the lung from pulmonary metastases of extrapulmonary origin and to support a pulmonary origin of metastases from unknown primary tumors is another major application of Napsin A IHC. The virtual limitation of Napsin A expression to few cancer types makes Napsin A highly useful marker for assessing the site of origin of cancers. It is a potential pitfall, however, that several cancer types, that often metastasize to the lung belong to the exclusive group of potentially Napsin A positive cancers, such as renal cell carcinoma, urothelial cancer, colorectal carcinoma and clear cell carcinomas of the ovary and the endometrium. Approximately one third of patients with renal cell carcinoma present with metastatic disease, in most cases metastasis to the lung [72]. Therefore, a biopsy of a mass in the lung could, on the basis of Napsin A positivity, be misdiagnosed as a primary adenocarcinoma of the lung. Several case reports have indeed reported such unfortunate cases [73–75].

FIGURE 5 | Graphical representation of Napsin A data from this study (marked with a cross) in comparison with the previous literature (marked with a dot). In order to simplify the figure the percentage of weak, moderate and strong staining was merged. Yellow crosses are used for tumor entities with 10–50 evaluable cases and green crosses are used for tumor entities with >50 evaluable cases. Red dots are used for studies from previous studies involving 1–9 cases, yellow dots for studies involving 10–50 cases and green dots for studies involving >50 cases. All studies are quoted in the list of references.

All our data are based on the analysis of TMA spots measuring 0.6 mm in diameter. TMAs are thus highly suited to model the diagnostic situation in small biopsies such as bronchial biopsies where the tumor cell content is comparably small. That we observed a similarly high rate of Napsin A positivity (85%) as found by most other studies using larger tissue samples [16, 24, 49, 50, 52, 58, 59, 61, 63] suggests a low rate of Napsin A expression heterogeneity in adenocarcinomas. It is well possible, that the analysis of larger specimen would result in somewhat higher positivity rate in squamous cell carcinomas than the 0% in our study. This might either be due to a higher risk of entrapped normal Napsin A positive macrophages or pneumocytes mimicking Napsin A positivity or to true focal expression in tumor cells. In this context, it is of note, that the only study comparing immunostaining data obtained on TMAs vs. findings in corresponding large sections with patient prognosis as the study endpoint found a superiority of TMA data. Although the large section analysis of more than 500 breast

cancers had identified almost twice as many p53 positive cases (40%) than each of four different TMAs containing one spot each per tumor (20% each), all four TMAs–but not the large section data - identified a strong prognostic impact of p53 positivity [76]. Torhorst et al [76] concluded from their data that either staining artifacts or clinically irrelevant focal p53 alterations were responsible for their unexpected results.

In this study, the prognostic role of Napsin A expression was evaluated in renal cell carcinomas because this tumor cohort included significant numbers of Napsin A positive and negative cases. The most noticeable result of this analysis is the dependency of the study outcome on the selected antibody dilution. While significant differences in outcome were not visible at a dilution of 1:400, the number of positive cases increased at a dilution of 1:135 and significant differences became visible. The reason for decreased prognosis in renal cell carcinomas with a Napsin A expression loss is unclear. Previous studies analyzing drug resistance in lung cancer cells suggested that Napsin A expression may inhibit epithelial-mesenchymal transition (EMT) [77, 78], which apart from being a mechanism for resistance to chemotherapy could play a role in tumor progression. However, many physiological functions of renal tubular cells are no longer required in renal tumors. It is thus also possible, that the loss of physiological Napsin A expression is a bystander phenomenon occurring as a result of a general dedifferentiation of tumor cells during cancer progression and which does not exert cancer-relevant effects on cell function. There is only a small number of previous studies analyzing the prognostic value of Napsin A expression in cancer. Multiple studies had suggested that Napsin A expression may be a predictor for prolonged overall survival in adenocarcinoma of the lung [55, 60, 79, 80]. In another study Fadare et al [71], did not find associations of Napsin A expression and survival or clinicopathological features in clear cell carcinomas of the endometrium. Considering, that the prognostic impact of Napsin A expression was rather weak and only visible at a high antibody concentration that already resulted in considerable background staining, we do not anticipate a major role of Napsin A analysis for kidney cancer prognosis assessment.

CONCLUSION

These results provide a comprehensive overview on Napsin A expression in human cancers and a systematic comparison with previous studies. The data also show that a reduced or lost Napsin A expression is linked to tumor dedifferentiation in renal cell carcinomas.

DATA AVAILABILITY STATEMENT

The raw data supporting the conclusions of this article will be made available by the authors, without undue reservation.

ETHICS STATEMENT

The usage of archived diagnostic leftover tissues for manufacturing of TMAs and their analysis for research purposes as well as patient data analysis have been approved by local laws (HmbKHG, §12,1) and by the local Ethics Committee (Ethics Commission Hamburg, WF-049/09). All work has been carried out in compliance with the Helsinki Declaration. Written informed consent for participation was not required for this study in accordance with the national legislation and the institutional requirements.

AUTHOR CONTRIBUTIONS

SW, JB, GS, and SM designed the study, and drafted the manuscript. SW, MK, and SM performed IHC analysis and scoring. MK, RS, CHM, and JB performed statistical analysis. AL, FB, DH, KM, CF, CB, RU, WW, SS, EB, DD, RK, AM, and TK participated in data interpretation, and helped to draft the manuscript.

CONFLICT OF INTEREST

The Institute of Pathology of the UKE receives royalties on the sale of Napsin A clone MSVA-112 from MS Validated Antibodies GmbH (owned by a family member of GS).

ACKNOWLEDGMENTS

We are grateful to Melanie Witt, Inge Brandt, Sünje Seekamp, and Maren Eisenberg for excellent technical support.

SUPPLEMENTARY MATERIAL

The Supplementary Material for this article can be found online at: https://www.por-journal.com/articles/10.3389/pore.2021.613099/full#supplementary-material.

REFERENCES

1. Hirano T, Franzén B, Uryu K, Okuzawa K, Alaiya A, Vanky F, et al. Detection of polypeptides associated with the histopathological differentiation of primary lung carcinoma. *Br J Cancer* (1995) 72(4):840–8. doi:10.1038/bjc.1995.422
2. Tatnell PJ, Powell DJ, Hill J, Smith TS, Tew DG, and Kay J. Napsins: new human aspartic proteinases. *FEBS Lett* (1998) 441(1):43–8. doi:10.1016/s0014-5793(98)01522-1
3. Ordóñez NG. Napsin A expression in lung and kidney neoplasia. *Adv Anat Pathol* (2012) 19(1):66–73. doi:10.1097/PAP.0b013e31823e472e
4. Mori K, Ogawa Y, Tamura N, Ebihara K, Aoki T, Muro S, et al. Molecular cloning of a novel mouse aspartic protease-like protein that is expressed abundantly in the kidney. *FEBS Lett* (1997) 401(2-3):218–22. doi:10.1016/s0014-5793(96)01473-1
5. Hirano T, Auer G, Maeda M, Hagiwara Y, Okada S, Ohira T, et al. Human tissue distribution of TA02, which is homologous with a new type of aspartic

proteinase, napsin A. *Jpn J Cancer Res* (2000) 91(10):1015–21. doi:10.1111/j.1349-7006.2000.tb00879.x

6. Xu B, Abourbih S, Sircar K, Kassouf W, Aprikian A, Tanguay S, et al. Diagnostic and prognostic role of immunohistochemical expression of napsin-A aspartic peptidase in clear cell and papillary renal cell carcinoma. *Appl Immunohistochem Mol Morphol* (2014) 22(3):206–12. doi:10.1097/PAI.0b013e31828ef24e
7. Iwamoto M, Nakatani Y, Fugo K, Kishimoto T, and Kiyokawa T. Napsin A is frequently expressed in clear cell carcinoma of the ovary and endometrium. *Hum Pathol* (2015) 46(7):957–62. doi:10.1016/j.humpath.2015.03.008
8. Brasch F, Ochs M, Kähne T, Guttentag S, Schauer-Vukasinovic V, Derrick M, et al. Involvement of napsin A in the C- and N-terminal processing of surfactant protein B in type-II pneumocytes of the human lung. *J Biol Chem* (2003) 278(49):49006–14. doi:10.1074/jbc.M306844200
9. Mori K, Shimizu H, Konno A, and Iwanaga T. Immunohistochemical localization of napsin and its potential role in protein catabolism in renal proximal tubules. *Arch Histol Cytol* (2002) 65(4):359–68. doi:10.1679/aohc.65.359
10. Guan S, Wu Y, Zhang Q, and Zhou J. TGF-β1 induces CREB1-mediated miR-1290 upregulation to antagonize lung fibrosis *via* Napsin A. *Int J Mol Med* (2020) 46(1):141–8. doi:10.3892/ijmm.2020.4565
11. Wu J, Zhang Y, Ding T, Cheng R, Gong W, Guo Y, et al. Napsin A expression in subtypes of thyroid tumors: comparison with lung adenocarcinomas. *Endocr Pathol* (2020) 31(1):39–45. doi:10.1007/s12022-019-09600-6
12. Surrey LF, Frank R, Zhang PJ, and Furth EE. TTF-1 and napsin-A are expressed in a subset of cholangiocarcinomas arising from the gallbladder and hepatic ducts. *Am J Surg Pathol* (2014) 38(2):224–7. doi:10.1097/PAS.0000000000000138
13. Stoll LM, Johnson MW, Gabrielson E, Askin F, Clark DP, and Li QK. The utility of napsin-A in the identification of primary and metastatic lung adenocarcinoma among cytologically poorly differentiated carcinomas. *Cancer Cytopathology* (2010) 118(6):441–9. doi:10.1002/cncy.20108
14. Argani P, Hicks J, De Marzo AM, Albadine R, Illei PB, Ladanyi M, et al. Xp11 translocation renal cell carcinoma (RCC): extended immunohistochemical profile emphasizing novel RCC markers. *Am J Surg Pathol* (2010) 34(9):1295–303. doi:10.1097/PAS.0b013e3181e8ce5b
15. Velez MJ, Thomas CL, Stratton J, Bergfeld W, and Weaver J. The utility of using immunohistochemistry in the differentiation of metastatic, cutaneous clear cell renal cell carcinoma and clear cell hidradenoma. *J Cutan Pathol* (2017) 44(7):612–5. doi:10.1111/cup.12946
16. El-Maqsoud NMRA, Tawfiek ER, Abdelmeged A, Rahman MFA, and Moustafa AAE. The diagnostic utility of the triple markers Napsin A, TTF-1, and PAX8 in differentiating between primary and metastatic lung carcinomas. *Tumor Biol* (2016) 37(3):3123–34. doi:10.1007/s13277-015-3964-3
17. Zhu B, Rohan SM, and Lin X. Immunoexpression of napsin A in renal neoplasms. *Diagn Pathol* (2015) 10:4. doi:10.1186/s13000-015-0242-z
18. Bishop JA, Sharma R, and Illei PB. Napsin A and thyroid transcription factor-1 expression in carcinomas of the lung, breast, pancreas, colon, kidney, thyroid, and malignant mesothelioma. *Hum Pathol* (2010) 41(1):20–5. doi:10.1016/j.humpath.2009.06.014
19. Kim M-Y, Go H, Koh J, Lee K, Min H-S, Kim M-A, et al. Napsin A is a useful marker for metastatic adenocarcinomas of pulmonary origin. *Histopathology* (2014) 65(2):195–206. doi:10.1111/his.12383
20. Ye J, Findeis-Hosey JJ, Yang Q, McMahon LA, Yao JL, Li F, et al. Combination of napsin A and TTF-1 immunohistochemistry helps in differentiating primary lung adenocarcinoma from metastatic carcinoma in the lung. *Appl Immunohistochem Mol Morphol* (2011) 19(4):313–7. doi:10.1097/PAI.0b013e318205b059
21. Chevarie-Davis M, Riazalhosseini Y, Arseneault M, Aprikian A, Kassouf W, Tanguay S, et al. The morphologic and immunohistochemical spectrum of papillary renal cell carcinoma. *Am J Surg Pathol* (2014) 38(7):887–94. doi:10.1097/PAS.0000000000000247
22. Turner BM, Cagle PT, Sainz IM, Fukuoka J, Shen SS, and Jagirdar J. Napsin A, a new marker for lung adenocarcinoma, is complementary and more sensitive and specific than thyroid transcription factor 1 in the differential diagnosis of primary pulmonary carcinoma: evaluation of 1674 cases by tissue microarray. *Arch Pathol Lab Med* (2012) 136(2):163–71. doi:10.5858/arpa.2011-0320-OA
23. Chernock RD, El-Mofty SK, Becker N, and Lewis JS, Jr. Napsin A expression in anaplastic, poorly differentiated, and micropapillary pattern thyroid carcinomas. *Am J Surg Pathol* (2013) 37(8):1215–22. doi:10.1097/PAS.0b013e318283b7b2
24. Kadivar M, and Boozari B. Applications and limitations of immunohistochemical expression of "Napsin-A" in distinguishing lung adenocarcinoma from adenocarcinomas of other organs. *Appl Immunohistochem Mol Morphol* (2013) 21(3):191–5. doi:10.1097/PAI.0b013e3182612643
25. Leskela S, Romero I, Cristobal E, Pérez-Mies B, Rosa-Rosa JM, Gutierrez-Pecharroman A, et al. The frequency and prognostic significance of the histologic type in early-stage ovarian carcinoma. *Am J Surg Pathol* (2020) 44(2):149–61. doi:10.1097/PAS.0000000000001365
26. Rao LKF, and Gilbertson JR. Longitudinal engagement of pathology residents. *Am J Clin Pathol* (2014) 142(6):748–54. doi:10.1309/AJCPWJ61RERWEDIK
27. Kandalaft PL, Gown AM, and Isacson C. The lung-restricted marker napsin A is highly expressed in clear cell carcinomas of the ovary. *Am J Clin Pathol* (2014) 142(6):830–6. doi:10.1309/AJCP8WO2EOIAHSOF
28. Li Q, Zeng X, Cheng X, Zhang J, Ji J, Wang J, et al. Diagnostic value of dual detection of hepatocyte nuclear factor 1 beta (HNF-1β) and napsin A for diagnosing ovarian clear cell carcinoma. *Int J Clin Exp Pathol* (2015) 8(7):8305–10.
29. Rekhi B, Deodhar KK, Menon S, Maheshwari A, Bajpai J, Ghosh J, et al. Napsin A and WT 1 are useful immunohistochemical markers for differentiating clear cell carcinoma ovary from high-grade serous carcinoma. *APMIS* (2018) 126(1):45–55. doi:10.1111/apm.12784
30. Lim D, Ip PPC, Cheung ANY, Kiyokawa T, and Oliva E. Immunohistochemical comparison of ovarian and uterine endometrioid carcinoma, endometrioid carcinoma with clear cell change, and clear cell carcinoma. *Am J Surg Pathol* (2015) 39(8):1061–9. doi:10.1097/PAS.0000000000000436
31. Fadare O, Zhao C, Khabele D, Parkash V, Quick CM, Gwin K, et al. Comparative analysis of Napsin A, alpha-methylacyl-coenzyme A racemase (AMACR, P504S), and hepatocyte nuclear factor 1 beta as diagnostic markers of ovarian clear cell carcinoma: an immunohistochemical study of 279 ovarian tumours. *Pathology* (2015) 47(2):105–11. doi:10.1097/PAT.0000000000000223
32. Lee S, Piskorz AM, Le Page C, Mes Masson A-M, Provencher D, Huntsman D, et al. Calibration and optimization of p53, WT1, and napsin A immunohistochemistry ancillary tests for histotyping of ovarian carcinoma. *Int J Gynecol Pathol* (2016) 35(3):209–21. doi:10.1097/PGP.0000000000000251
33. Roy M, Jain D, Yadav R, Mathur SR, and Iyer VK. TTF-1 and napsin-A are not markers for biliary phenotype. *Am J Surg Pathol* (2015) 39(12):1742–4. doi:10.1097/PAS.0000000000000551
34. Yamashita Y, Nagasaka T, Naiki-Ito A, Sato S, Suzuki S, Toyokuni S, et al. Napsin A is a specific marker for ovarian clear cell adenocarcinoma. *Mod Pathol* (2015) 28(1):111–7. doi:10.1038/modpathol.2014.61
35. Tennstedt P, Köster P, Brüchmann A, Mirlacher M, Haese A, Steuber T, et al. The impact of the number of cores on tissue microarray studies investigating prostate cancer biomarkers. *Int J Oncol* (2012) 40(1):261–8. doi:10.3892/ijo.2011.1216
36. Büscheck F, Fraune C, Simon R, Kluth M, Hube-Magg C, Möller-Koop C, et al. Aberrant expression of membranous carbonic anhydrase IX (CAIX) is associated with unfavorable disease course in papillary and clear cell renal cell carcinoma. *Urol Oncol Semin Original Invest* (2018) 36(12):e19–531. doi:10.1016/j.urolonc.2018.08.015
37. Eichenauer T, Bannenberg DC, Kluth M, Wittmer C, Büscheck F, Möller K, et al. 8p deletions in renal cell carcinoma are associated with unfavorable tumor features and poor overall survival. *Urol Oncol Semin Original Invest* (2020) 38(2):e13–43. doi:10.1016/j.urolonc.2019.09.024
38. Eichenauer T, Simmendinger L, Kluth M, Chirico V, Luebke AM, Höflmayer D, et al. Chromosomal deletion of 9p21 is linked to poor patient prognosis in papillary and clear cell kidney cancer. *Urol Oncol Semin Original Invest* (2020) 38(6):e1–605. doi:10.1016/j.urolonc.2020.02.022

39. Eichenauer T, Simmendinger L, Fraune C, Mandelkow T, Blessin NC, Kluth M, et al. High level of EZH2 expression is linked to high density of CD8-positive T-lymphocytes and an aggressive phenotype in renal cell carcinoma. *World J Urol* (2020) 39:481. doi:10.1007/s00345-020-03200-4
40. Büscheck F, Fraune C, Simon R, Kluth M, Hube-Magg C, Möller-Koop C, et al. Prevalence and clinical significance of VHL mutations and 3p25 deletions in renal tumor subtypes. *Oncotarget* (2020) 11(3):237–49. doi:10.18632/oncotarget.27428
41. Büscheck F, Fraune C, Kluth M, Lennartz M, Simon R, Hube-Magg C, et al. A non-diploid DNA status is linked to poor prognosis in renal cell cancer. *World J Urol* (2020) 39:829. doi:10.1007/s00345-020-03226-8
42. Eichenauer T, Shadanpour N, Kluth M, Göbel C, Weidemann S, Fraune C, et al. Chromosome 17p13 deletion is associated with an aggressive tumor phenotype in clear cell renal cell carcinoma. *World J Surg Onc* (2020) 18(1):128. doi:10.1186/s12957-020-01902-y
43. Zenali MJ, Weissferdt A, Solis LM, Ali S, Tang X, Mehran RJ, et al. An update on clinicopathological, immunohistochemical, and molecular profiles of colloid carcinoma of the lung. *Hum Pathol* (2015) 46(6):836–42. doi:10.1016/j.humpath.2014.10.032
44. Dejmek A, Naucler P, Smedjeback A, Kato H, Maeda M, Yashima K, et al. Napsin A (TA02) is a useful alternative to thyroid transcription factor-1 (TTF-1) for the identification of pulmonary adenocarcinoma cells in pleural effusions. *Diagn Cytopathol* (2007) 35(8):493–7. doi:10.1002/dc.20667
45. Bian T, Zhao J, Feng J, Zhang Q, Qian L, Liu J, et al. Combination of cadherin-17 and SATB homeobox 2 serves as potential optimal makers for the differential diagnosis of pulmonary enteric adenocarcinoma and metastatic colorectal adenocarcinoma. *Oncotarget* (2017) 8(38):63442–52. doi:10.18632/oncotarget.18828
46. Mukhopadhyay S, and Katzenstein A-LA. Subclassification of non-small cell lung carcinomas lacking morphologic differentiation on biopsy specimens. *Am J Surg Pathol* (2011) 35(1):15–25. doi:10.1097/PAS.0b013e3182036d05
47. Kadota K, Nitadori J-i., Rekhtman N, Jones DR, Adusumilli PS, and Travis WD. Reevaluation and reclassification of resected lung carcinomas originally diagnosed as squamous cell carcinoma using immunohistochemical analysis. *Am J Surg Pathol* (2015) 39(9):1170–80. doi:10.1097/PAS.0000000000000439
48. Ezzat NE, Tahoun NS, and Ismail YM. The role of S100P and IMP3 in the cytologic diagnosis of pancreatic adenocarcinoma. *J Egypt Natl Cancer Inst* (2016) 28(4):229–34. doi:10.1016/j.jnci.2016.10.002
49. Aulakh KS, Chisholm CD, Smith DA, and Speights VO. TTF-1 and napsin A do not differentiate metastatic lung adenocarcinomas from primary esophageal adenocarcinomas: proposal of a novel staining panel. *Arch Pathol Lab Med* (2013) 137(8):1094–8. doi:10.5858/arpa.2012-0305-OA
50. Ueno T, Linder S, and Elmberger G. Aspartic proteinase napsin is a useful marker for diagnosis of primary lung adenocarcinoma. *Br J Cancer* (2003) 88(8):1229–33. doi:10.1038/sj.bjc.6600879
51. Inamura K, Satoh Y, Okumura S, Nakagawa K, Tsuchiya E, Fukayama M, et al. Pulmonary adenocarcinomas with enteric differentiation. *Am J Surg Pathol* (2005) 29(5):660–5. doi:10.1097/01.pas.0000160438.00652.8b
52. Hirano T, Gong Y, Yoshida K, Kato Y, Yashima K, Maeda M, et al. Usefulness of TA02 (napsin A) to distinguish primary lung adenocarcinoma from metastatic lung adenocarcinoma. *Lung Cancer* (2003) 41(2):155–62. doi:10.1016/s0169-5002(03)00194-6
53. Wu J, Chu PG, Jiang Z, and Lau SK. Napsin A expression in primary mucin-producing adenocarcinomas of the lung. *Am J Clin Pathol* (2013) 139(2):160–6. doi:10.1309/AJCP62WJUAMSZCOM
54. Rossi G, Cavazza A, Righi L, Sartori G, Bisagni A, Longo L, et al. Napsin-A, TTF-1, EGFR, and ALK status determination in lung primary and metastatic mucin-producing adenocarcinomas. *Int J Surg Pathol* (2014) 22(5):401–7. doi:10.1177/1066896914527609
55. Piljic Burazer M, Mladinov S, Capkun V, Kuret S, and Glavina Durdov M. The utility of thyroid transcription factor 1 (TTF-1), napsin A, excision repair cross-complementing 1 (ERCC1), anaplastic lymphoma kinase (alk) and the epidermal growth factor receptor (egfr) expression in small biopsy in prognosis of patients with lung adenocarcinoma - a retrograde single-center study from Croatia. *Med Sci Monit* (2017) 23:489–97. doi:10.12659/msm.899378
56. Ye J, Hameed O, Findeis-Hosey J, Fan L, Li F, McMahon L, et al. Diagnostic utility of PAX8, TTF-1 and napsin A for discriminating metastatic carcinoma from primary adenocarcinoma of the lung. *Biotech Histochem* (2012) 87(1):30–4. doi:10.3109/10520295.2011.591838
57. Nishino M, Hoang MP, Della Pelle P, Morales-Oyarvide V, Huynh TG, Mark EJ, et al. Napsin A/p40 antibody cocktail for subtyping non-small cell lung carcinoma on cytology and small biopsy specimens. *Cancer Cytopathology* (2016) 124(7):472–84. doi:10.1002/cncy.21707
58. Cadioli A, Rossi G, Costantini M, Cavazza A, Migaldi M, and Colby TV. Lung cancer histologic and immunohistochemical heterogeneity in the era of molecular therapies. *Am J Surg Pathol* (2014) 38(4):502–9. doi:10.1097/PAS.0000000000000154
59. Suzuki A, Shijubo N, Yamada G, Ichimiya S, Satoh M, Abe S, et al. Napsin A is useful to distinguish primary lung adenocarcinoma from adenocarcinomas of other organs. *Pathol - Res Pract* (2005) 201(8-9):579–86. doi:10.1016/j.prp.2005.05.010
60. Yang X, Liu Y, Lian F, Guo L, Wen P, Liu XY, et al. Lepidic and micropapillary growth pattern and expression of Napsin A can stratify patients of stage I lung adenocarcinoma into different prognostic subgroup. *Int J Clin Exp Pathol* (2014) 7(4):1459–68.
61. Jin L, Liu Y, Wang X, and Qi X. Immunohistochemical analysis and comparison of napsin A, TTF1, SPA and CK7 expression in primary lung adenocarcinoma. *Biotech Histochem* (2018) 93(5):364–72. doi:10.1080/10520295.2018.1444790
62. Vidarsdottir H, Tran L, Nodin B, Jirström K, Planck M, Jönsson P, et al. Immunohistochemical profiles in primary lung cancers and epithelial pulmonary metastases. *Hum Pathol* (2019) 84:221–30. doi:10.1016/j.humpath.2018.10.009
63. Zhang P, Han Y-P, Huang L, Li Q, and Ma D-L. Value of napsin A and thyroid transcription factor-1 in the identification of primary lung adenocarcinoma. *Oncol Lett* (2010) 1(5):899–903. doi:10.3892/ol_00000160
64. Koh J, Go H, Kim M-Y, Jeon YK, Chung J-H, and Chung DH. A comprehensive immunohistochemistry algorithm for the histological subtyping of small biopsies obtained from non-small cell lung cancers. *Histopathology* (2014) 65(6):868–78. doi:10.1111/his.12507
65. Kriegsmann K, Cremer M, Zgorzelski C, Harms A, Muley T, Winter H, et al. Agreement of CK5/6, p40, and p63 immunoreactivity in non-small cell lung cancer. *Pathology* (2019) 51(3):240–5. doi:10.1016/j.pathol.2018.11.009
66. Bulutay P, Akyurek N, and Memis L. Clinicopathological and prognostic significance of the EML4-ALK translocation and IGFR1, TTF1, napsin A expression in patients with lung adenocarcinoma. *Tjpath* (2020) 37(1):7–71. doi:10.5146/tjpath.2020.01503
67. Kushitani K, Amatya VJ, Okada Y, Katayama Y, Mawas AS, Miyata Y, et al. Utility and pitfalls of immunohistochemistry in the differential diagnosis between epithelioid mesothelioma and poorly differentiated lung squamous cell carcinoma. *Histopathology* (2017) 70(3):375–84. doi:10.1111/his.13073
68. Ordóñez NG. A word of caution regarding napsin A expression in squamous cell carcinomas of the lung. *Am J Surg Pathol* (2012) 36(3):396–401. doi:10.1097/PAS.0b013e31823b13e2
69. Zhang Y, Zheng D, Li Y, Pan Y, Sun Y, and Chen H. Comprehensive investigation of clinicopathologic features, oncogenic driver mutations and immunohistochemical markers in peripheral lung squamous cell carcinoma. *J Thorac Dis* (2017) 9(11):4434–40. doi:10.21037/jtd.2017.10.43
70. Zannoni GF, Santoro A, Angelico G, Spadola S, Arciuolo D, Valente M, et al. Clear cell carcinoma of the endometrium: an immunohistochemical and molecular analysis of 45 cases. *Hum Pathol* (2019) 92:10–7. doi:10.1016/j.humpath.2019.06.005
71. Fadare O, Desouki MM, Gwin K, Hanley KZ, Jarboe EA, Liang SX, et al. Frequent expression of napsin A in clear cell carcinoma of the endometrium. *Am J Surg Pathol* (2014) 38(2):189–96. doi:10.1097/PAS.0000000000000085
72. Flanigan RC, Campbell SC, Clark JI, and Picken MM. Metastatic renal cell carcinoma. *Curr Treat Options Oncol* (2003) 4(5):385–90. doi:10.1007/s11864-003-0039-2
73. Kubo T, Hirohashi Y, Fujita H, Sugita S, Kikuchi Y, Shinkawa T, et al. Occult ovarian clear-cell carcinoma diagnosed as primary adenocarcinoma of the lung: a case report of a diagnostic pitfall for clinicians and pathologists. *Respir Med Case Rep* (2018) 25:306–8. doi:10.1016/j.rmcr.2018.10.013
74. Jain D, Mallick SR, Singh V, Singh G, Mathur SR, and Sharma MC. Napsin A expression in anaplastic lymphoma kinase-positive diffuse large B-cell

lymphoma: a diagnostic pitfall. *Appl Immunohistochem Mol Morphol* (2016) 24(5):e34–e40. doi:10.1097/PAI.0000000000000289

75. Ito T, Nakanishi K, and Goto H. A case of napsin A-positive metastatic lung cancer originating from the colon. *Surg Case Rep* (2017) 3(1):114. doi:10.1186/s40792-017-0389-9
76. Torhorst J, Bucher C, Kononen J, Haas P, Zuber M, Köchli OR, et al. Tissue microarrays for rapid linking of molecular changes to clinical endpoints. *Am J Pathol* (2001) 159(6):2249–56. doi:10.1016/S0002-9440(10)63075-1
77. Zhou L, Lv X, Yang J, Zhu Y, Wang Z, and Xu T. Napsin A is negatively associated with EMT-mediated EGFR-TKI resistance in lung cancer cells. *Mol Med Rep* (2018) 18(2):1247–52. doi:10.3892/mmr.2018.9075
78. Zhou L, Lv X, Yang J, Zhu Y, Wang Z, and Xu T. Overexpression of Napsin A resensitizes drug-resistant lung cancer A549 cells to gefitinib by inhibiting EMT. *Oncol Lett* (2018) 16(2):2533–8. doi:10.3892/ol.2018.8963
79. Lee JG, Kim S, and Shim HS. Napsin A is an independent prognostic factor in surgically resected adenocarcinoma of the lung. *Lung Cancer* (2012) 77(1):156–61. doi:10.1016/j.lungcan.2012.02.013
80. Ma Y, Fan M, Dai L, Kang X, Liu Y, Sun Y, et al. The expression of TTF-1 and Napsin A in early-stage lung adenocarcinoma correlates with the results of surgical treatment. *Tumor Biol* (2015) 36(10):8085–92. doi:10.1007/s13277-015-3478-z

Pathology & Oncology Research

frontiers

ORIGINAL RESEARCH
published: 22 April 2021
doi: 10.3389/pore.2021.613264

Beneficial Effect of Lenalidomide-Dexamethason Treatment in Relapsed/Refractory Multiple Myeloma Patients: Results of Real-Life Data From 11 Hungarian Centers

Gergely Varga[1]†, András Dávid Tóth[1], Virág Réka Szita[1], Zoltán Csukly[2], Apor Hardi[2], Júlia Gaál-Weisinger[3], Zsolt Nagy[3], Elvira Altai[4], Annamária Rencsik[4], Márk Plander[5], Tamás Szendrei[5], Krisztina Kórád[6], Gáspár Radványi[6], János Rottek[7], Beáta Deák[7], Erika Szaleczky[7], Tamás Schneider[7], Zoltán Kohl[8], Szabolcs Kosztolányi[8], Hussain Alizadeh[8], Zsuzsanna Lengyel[9], Szabolcs Modok[9], Zita Borbényi[9], Szilvia Lovas[10], László Váróczy[10], Árpád Illés[10], Péter Rajnics[11], Tamás Masszi[1] and Gábor Mikala[2]*

[1]Department of Internal Medicine and Haematology, Semmelweis University, Budapest, Hungary, [2]National Institute for Hematology and Infectious Diseases, Department of Hematology and Stem Cell Transplantation, South Pest Central Hospital, Budapest, Hungary, [3]Department of Internal Medicine and Oncology, Semmelweis University, Budapest, Hungary, [4]Veszprém-Csolnoky Ferenc County Hospital, Hematology, Veszprém, Hungary, [5]Markusovszky University Teaching Hospital, Szombathely, Hungary, [6]Borsod-Abaúj- Zemplén Central County University Teaching Hospital, Miskolc, Hungary, [7]National Institute of Oncology, Budapest, Hungary, [8]1st Department of Internal Medicine, University of Pécs, Pécs, Hungary, [9]2nd Department of Medicine and Cardiology Center, University of Szeged, Szeged, Hungary, [10]Department of Hematology, Institute for Medicine, Clinical Center, University of Debrecen, Debrecen, Hungary, [11]Somogy County Kaposi Mór Teaching Hospital, Kaposvár, Hungary

OPEN ACCESS

Edited by:
Gabor Cserni,
University of Szeged, Hungary

***Correspondence:**
Gergely Varga
vargager@gmail.com

†**ORCID**:
orcid.org/0000-0001-6875-056X

Received: *01 October 2020*
Accepted: *01 April 2021*
Published: *22 April 2021*

Citation:
Varga G, Dávid Tóth A, Réka Szita V, Csukly Z, Hardi A, Gaál-Weisinger J, Nagy Z, Altai E, Rencsik A, Plander M, Szendrei T, Kórád K, Radványi G, Rottek J, Deák B, Szaleczky E, Schneider T, Kohl Z, Kosztolányi S, Alizadeh H, Lengyel Z, Modok S, Borbényi Z, Lovas S, Váróczy L, Illés Á, Rajnics P, Masszi T and Mikala G (2021) Beneficial Effect of Lenalidomide-Dexamethason Treatment in Relapsed/Refractory Multiple Myeloma Patients: Results of Real-Life Data From 11 Hungarian Centers. Pathol. Oncol. Res. 27:613264. doi: 10.3389/pore.2021.613264

In Hungary, the cost of lenalidomide-based therapy is covered only for relapsed multiple myeloma (MM) patients, therefore lenalidomide is typically used in the second-line either as part of a triplet with proteasome inhibitors or as a doublet. Lenalidomide-dexamethasone is a standard treatment approach for relapsed/refractory MM, and according to recent large randomized clinical trials (RCT, the standard arm of POLLUX, ASPIRE, TOURMALINE), the progression-free survival (PFS) is expected to be approximately 18 months. We surveyed ten Hungarian centers treating MM and collected data of 278 patients treated predominantly after 2016. The median age was 65 years, and patients were distributed roughly equally over the 3 international staging system groups, but patients with high risk cytogenetics were underrepresented. 15.8% of the patients reached complete response, 21.6% very good partial response, 40.6% partial response, 10.8% stable disease, and 2.5% progressed on treatment. The median PFS was unexpectedly long, 24 months, however only 9 months in those with high risk cytogenetics. We found interesting differences between centers regarding corticosteroid type (prednisolone, methylprednisolone or dexamethasone) and dosing, and also regarding the choice of anticoagulation, but the outcome of the various centers were not different. Although the higher equivalent steroid dose resulted in more complete responses, the median PFS of those having lower corticosteroid dose and methylprednisolone were not inferior

compared to the ones with higher dose dexamethasone. On multivariate analysis high risk cytogenetics and the number of prior lines remained significant independent prognostic factors regarding PFS ($p < 0.001$ and $p = 0.005$). Our results show that in well-selected patients Lenalidomide-dexamethasone can be a very effective treatment with real-world results that may even outperform those reported in the recent RCTs. This real world information may be more valuable than outdated RCT data when treatment options are discussed with patients.

Keywords: myeloma, lenalidomide, relapsed, real life, treatment

INTRODUCTION

Lenalidomide in combination with dexamethasone (Rd) has been widely used in relapsed/refractory multiple myeloma (R/R MM) for more than a decade and is now the backbone of most three and four-drug combinations for both newly diagnosed and relapsed myeloma. Nevertheless, it is difficult to tell exactly what to expect currently when lenalidomide is used as a doublet in relapsed patients. Based on the results of two pivotal randomized clinical trials (MM-009 and MM-010), the Food and Drug Administration approved Rd for the treatment of MM patients who have received at least one prior line of therapy in 2006 [1–3], however, the landscape has changed immensely since then, with lenalidomide being increasingly used in the first-line setting. As the treated cohort changed, so did the outcome, as demonstrated nicely by some recent randomized clinical trials (RCTs, e.g. POLLUX, ASPIRE, TOURMALINE), where Rd was used in the control arm with progression-free survivals (PFS) significantly longer than in the aforementioned trials [4–6].

As lenalidomide-based therapy is only funded for relapsed patients in Hungary, most patients receiving second-line therapy are lenalidomide-naïve, and thus treated with either Rd or an Rd based triplet. There are however still many open questions regarding its optimal use: whether we can use Rd rather than a triplet without significantly compromising our patients' outcome, and what results we may expect from this protocol.

In this study, we approached all Hungarian hematology facilities treating MM patients with a questionnaire about their use of Rd in the routine clinical setting, collecting data with regards to patient characteristics and associated treatment outcome and compared it with results from the initial phase 3 clinical trials as well as with the control arm of some recent RCTs of Rd backbone triplets.

PATIENTS AND METHODS

Patients

Eleven Hungarian centers responded to our query, supplying data about 283 patients treated with Rd over the course of the last 10 years from 2010–19, however only eight patients were started on Rd before 2015, eight in 2015, all ther others after 2015, as the need for individual funding applications had held back its widespread use until then. Post autologous stem cell transplantation (ASCT) lenalidomide maintenance was not used in this group of patients as it was not funded until 2018. Patients treated with Rd in the first line, or with Rd used in a triplet were excluded, we collected data about later "add-on" use of third drugs. Prognostic markers such as ISS and fluorescence *in situ* hybridization (FISH) have been collected as well as the response according to the International Myeloma Working Group (IMWG) criteria and progression-free and overall survivals (OS) [7, 8]. High-risk FISH result was defined as t (4; 14), t (14; 16) and/or del (17p), per the published IMWG guideline [9], the threshold for del (17p) was 5%.

Statistical Analysis

The primary endpoint was PFS and secondary outcome measures were overall response rate and OS. PFS was measured from the start of treatment to the date of disease progression or death. The overall response rate was defined as the collective proportion of pts with complete response (CR), very good partial remission (VGPR), partial remission (PR), or minimal response (MR) as their best response. OS was defined as the time from the start of treatment to the date of death. Comparisons of dichotomous variables were performed by Fisher's exact test. Continuous variables were compared by Mann–Whitney or Kruskal–Wallis tests. PFS and OS were estimated by Kaplan–Meier analysis, baseline clinical characteristics were evaluated for predictive significance by multivariate Cox regression. The analyses were carried out using the SPSS (version 20.0; SPSS, Chicago, IL) software package.

RESULTS

Patient Characteristics

We analyzed the data of 283 patients treated with Rd at 11 centers. An overview of patient characteristics is presented in **Table 1**. The median age of the patients at diagnosis (65 years) was typical for the Hungarian myeloma cohort, however, the age at Rd initiation (70 years) was higher than that of the typical relapsed patient in clinical trials. The number of patients with known high-risk features (high ISS, HR FISH, extramedullary disease, and renal failure) was lower in each category than expected. HR FISH included t (4; 14), t (14; 16) and del (17p); 24 additional patients had amplification of chromosome 1q21. The performed prognostic tests varied widely between centers, with some doing FISH routinely while others not, also taking into account that plasma cell selection had not universally been routine before 2018.

TABLE 1 | Patients' characteristics.

Total number/male/female	283/140/143
Median and mean age at diagnosis in years (range)	65.2/64.1 (28.2–86.3)
Median and mean age at Rd initiation in years (range)	70.2/68.4 (36.1–90)
Heavy chain IgG, A, LC, non-secretory (%)	62.9/22.4/12.1/1.4
Light chain kappa, lambda (%)	66.9/31.6
ISS at diagnosis (ISS 1/2/3%; missing 45)	30.4/37.1/32.5
FISH (SR/HR %; missing 100)	87.5/12.5
ISS pre Rd (ISS 1/2/3%; missing 110)	36.6/40.0/23.4
Extramedullary disease pre Rd (%)	9.1
Renal failure (GFR <30 ml/min, %)	12.8
Median prior lines (range)	2 (1–8)
Prior thal/bor/len (%)	65.6/92.4/3.2
Prior ASCT (%)	46.5
Steroid: dex, methylpred (%)	62.7, 37.3
Median weekly dex eqvivalent[a] corticosteroid dose (<20 mg/20 mg/40 mg %)	14.7/36.8/48.5

[a]*1 mg dexamethasone is roughly equivalent to 5 mg methylprednisolone.*

Abbreviations: ASCT, autologous stem cell transplantation; bor, bortezomib; dex, dexamethasone; FISH, fluorescence in situ *hybridization; ISS, international staging system; len, lenalidomide; methylpred, methylprednisolone; Rd, lenalidomide-dexamethasone; thal, thalidomide.*

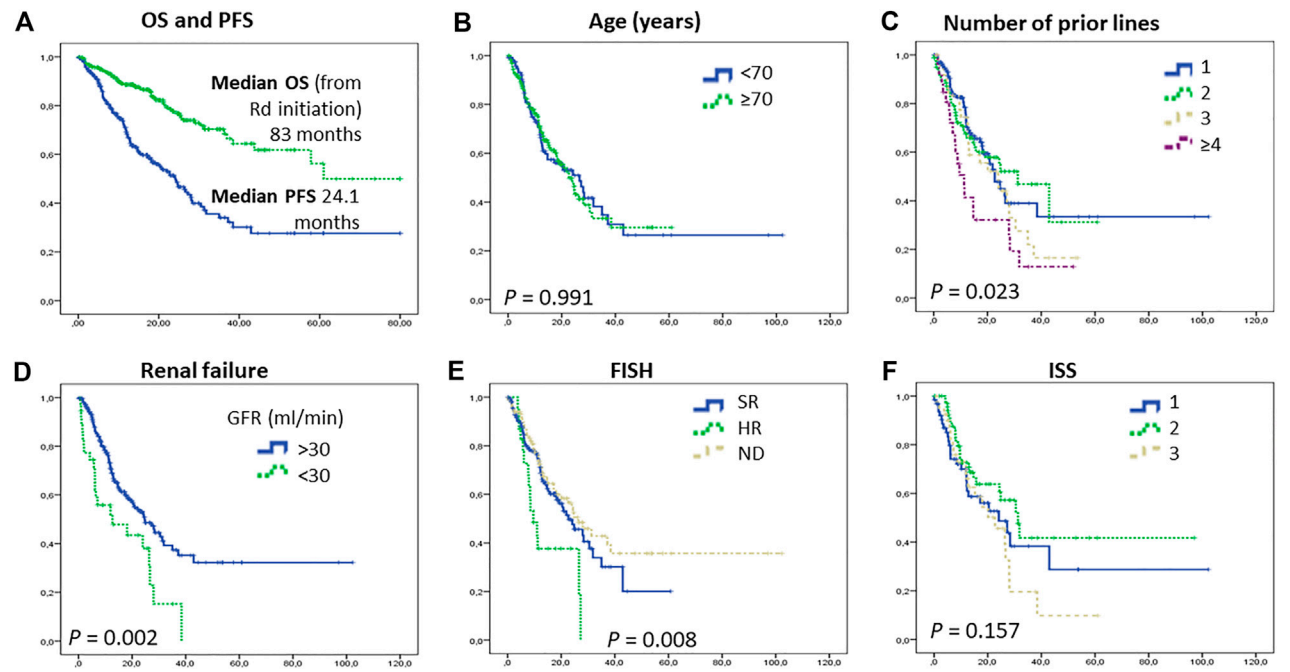

FIGURE 1 | Survival of patients. Overall and progression-free survival of the whole cohort **(A)**; Progression-free survival according to Age **(B)**, number of prior lines **(C)**, renal function **(D)**, FISH **(E)**, and ISS **(F)**. Both PFS and OS have exceeded what was expacted based on the pivotal randomized clinical trials [2]. Patients with renal failure and high risk cytogenetics were benefited less from Rd treatment. Abrreviations: FISH, fluorescence *in situ* hybridization; GFR, glomerular filtration rate; ISS, international staging system; OS, overall survival; PFS, progression free survival; Rd, lenalidomide-dexamethason.

Response

Out of the 259 patients who had response assessment, 20.5% had CR, 25.9% VGPR, 36.7% PR, 14.5% SD and only 2.4% PD. ISS, HR cytogenetics did not affect the best response (data not shown). Similarly, patients with renal failure had a comparable response rate to those without, while patients with extramedullary disease had a trend to have less than PR (26.1 vs. 13.1%, $p = 0.09$). Unsurprisingly, the chance of reaching a good response declined with more than 3 prior lines (data not shown), however, previous exposure to thalidomide, bortezomib, lenalidomide, or ASCT did not affect the response.

Addition of 3rd Drug

An interesting sub-analysis looked into the 54 patients where the treating physician escalated the therapy with the addition of a third drug after a median of two months due to suboptimal response (PD 7.8%, SD 41.2%, PR 41.2%). Keeping in mind that with Rd as a doublet you can expect a deepening response at this

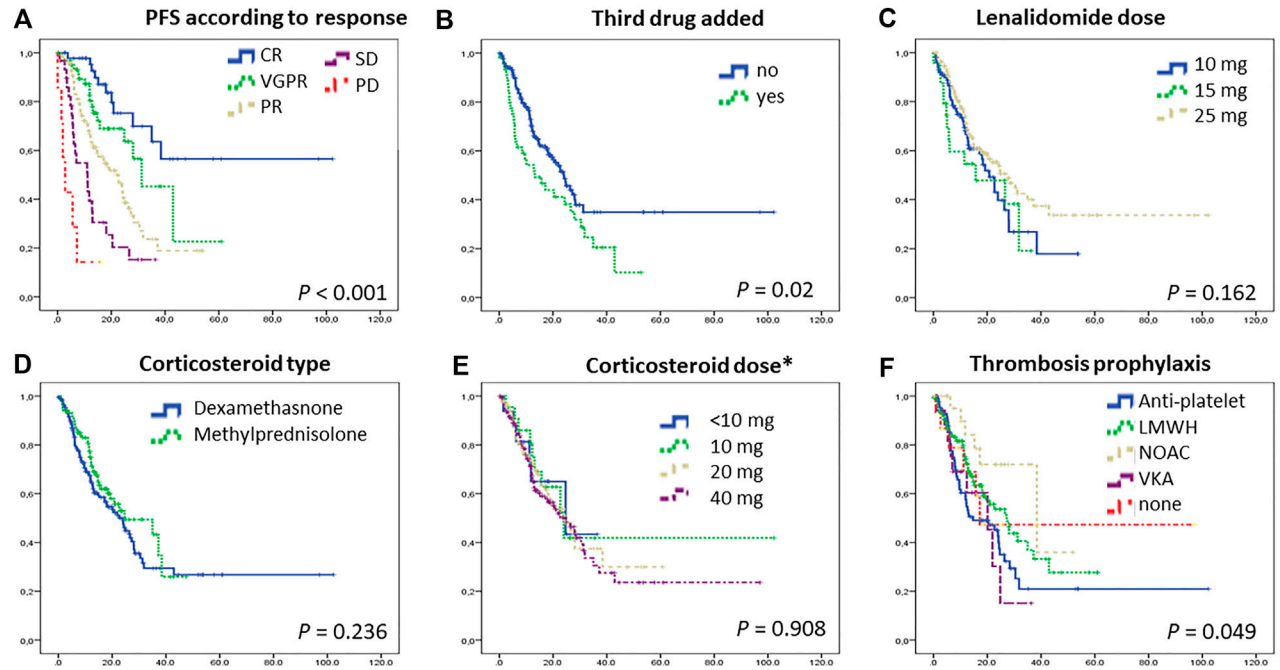

FIGURE 2 | Progression-free survival according to response **(A)**, whether a third drug was added **(B)**, lenalidomide dose **(C)**, cordicosteroid type **(D)** and dose **(E)**, and thromboprophylaxis type **(F)**. Patients with deeper responses had longer PFS. In some cases with suboptimal response, a third drug (usually bortezomib) was added to Rd, but the outcome of these patients remained inferior compared to others. Importantly, the corticosteroid type (dexamethasone or methylprednisolone-a frequently used replacement of dexamethasone in Hungary) and dose did not have an effect on PFS. Abrreviations: CR, complete response; LMWH, low-molecular-weight heparin; NOAC, novel oral anticoagulants; PD, progressive disease; PFS, progression free survival; PR, partial response; Rd, lenalidomide-dexamethason; SD, stable disease; VGPR, very good partial response; VKA, vitamin K antagonists. *dexamethasone (5 mg methylprednisolone is equivalent with 1 mg dexamethasone).

stage too, some of these patients experienced an upgrade of their initial response after the third drug was added (PR patients: 35% CR, 30% VGPR, 35% PR; SD patients 14.3% CR, 19% VGPR, 28.6% PR, 38.1% SD; PD patients 25% VGPR, 75% PD). The third drug was bortezomib in 21, cyclophosphamide in 3, bendamustine in 3, carfilzomib in 2, daratumumab in 5, and ixazomib in 20 cases (this latter probably due to its availability in a compassionate use program).

Survival

The median progression-free survival (PFS) of the whole group was 24.3 months, the overall survival (OS) calculated from the start of the Rd protocol 83.0 months (**Figure 1A**). The PFS was similar in patients above and below 70 years of age (22.7 and 26.3 months, $p = 0.36$, **Figure 1B**), the survival of patients with 1, 2 and 3 prior therapies was similar, however above 3 lines the PFS was significantly worse (1 line 22.7, 2 lines 31.7, 3 lines 24.0 months, 4 or more lines 11.3 months, $p = 0.023$, **Figure 1C**). There was no difference between the PFS and OS patients treated in different centers (data not shown).

Patients with renal failure prior to Rd initiation had a worse outcome (PFS 12.7 vs. 24.6 months, $p = 0.002$), Those with high-risk FISH also had a significantly worse PFS (8.4 vs. 22.7 months, $p = 0.008$). Interestingly a significant sized cohort of patients with unknown FISH had a similar outcome to those with standard-risk (26.3 months); most likely showing the treating physicians' more active approach to biopsy patients progressing aggressively and a more laid-back attitude to those behaving suggesting standard risk. ISS assessed at treatment initiation did not predict the PFS duration that was 24.1, 31.3, and 22.7 months in the ISS 1, 2, and 3 groups, respectively (**Figures 1D–F**). Characteristically, those with a good response to treatment had a significantly better PFS (**Figure 2A**).

When all the pre-Rd prognostic variables (age, ISS,FISH, renal failure, the number of prior lines) and treatment characteristics (lenalidomide dose, steroid type and dose) were entered to Cox multivariate analysis, only FISH and the number of prior lines remained significant independent factors ($p < 0.001$ and $p = 0.005$).

Those patients whose original response was considered suboptimal, and therefore a third drug was added, fared worse compared to others (**Figure 2B**). However if those with ixazomib addition (as part of a compassionate use program available at the period) were examined separately, that group had actually a superior PFS.

If the group that has an unexpectedly long (>18 months) survival is examined separately, that cohort has fewer patients with IgA M-protein, less with light chain only MM, marginally more ISS 1 and less ISS 3 patients ($p = 0.065$). From the FISH point of view, 30.6% of the standard risk patients were in this group, while only 17.4% of the high risk. Similarly, from those with 1q amplification, only 15.4% were in this group, while 35.2% of those without were. Renal failure, prior therapy, steroid type, and dose did not play a role here, and interestingly, the response reached at either 2- or 6-months time points did not affect this.

TABLE 2 | Adverse events. As reported by the treating physcians, number of occurances and proportion of occurances, no gradings were collected. 283 patitent were treated in total, 69 has one or more adverse events reported.

Adverse event	Number of cases and relative proportion (%)
Bone marrow suppression	29 (10.3)
Gastrointestinal	10 (3.5)
Infection	8 (2.8)
Neuropathy	7 (2.5)
Deep vein thrombosis	6 (2.1)
Skin reaction	5 (1.8)
Cardiovascular	2 (0.7)
Fatigue	2 (0.7)
Orthostatic hypotension	2 (0.7)
Vasculitis	1 (0.3)
Acute myocardial infarction	1 (0.3)
Intolerance	1 (0.3)
Periorbital edema	1 (0.3)
Suicide	1 (0.3)

Lenalidomide Dosing

Lenalidomide dose was adjusted for renal function and age, and physicians used several dosing patterns including 25 mg every other day, 15 mg, and 10 mg daily, however, 55% of the patients in this study had 25 mg lenalidomide, daily (21/28 days, though the treatment holiday period was frequently longer than the standard 7 days, data not shown). The PFS did not differ significantly between these dosing subgroups (**Figure 2C**).

Steroid Type and Dosing

An interesting part of our real-world analysis was the comparison of the two types of corticosteroids used by Hungarian centers. In Hungary, dexamethasone is often replaced with methylprednisolone in daily routine as oral dexamethasone has not been marketed and therefore had to be purchased via hospital pharmacies, whereas methylprednisolone is an oral prescription drug available in several different formats. Even still, almost two-thirds of the patients were treated with oral dexamethasone, a minority with intravenous dexamethasone, and slightly more than one third with oral methylprednisolone. The weekly dose was 40 mg dexamethasone in the majority, but lower than that in a significant group. Calculated to the respective equivalent dexamethasone dose, some patients had as low as 4 mg weekly (5.9%), others 10 mg (8.1%), however, the majority had either 20 mg (36.8%) or 40 mg (48.5%). Dose adjustments during therapy were not collected. The preference of corticosteroid type and dose varied according to the treating center. Interestingly, neither the type nor the dose seemed to significantly affect the outcome (**Figures 2D,E**).

Type of Thrombosis Prophylaxis

The nature of our data collection did not allow us to readily identify the reasoning behind the choice of thromboprophylaxis in a given patient, but we could notice different trends between the treating centers: some seemed to use antiplatelet therapy in younger patients and anticoagulation (low molecular weight heparin, novel anticoagulants or vitamin K antagonists) in older ones, whereas other centers had a rather uniform preference toward one or another type. In terms of PFS, those on novel anticoagulants had a marginally longer PFS, but this was probably more of an association with better renal function rather than a true causality ($p = 0.049$, **Figure 2F**).

Adverse Events

Table 2 shows the adverse events (AEs), as reported. Grading is not included as it was not uniformly provided by the treating centers. The number of AEs here is lower compared to prospective clinical trials, not unusual in retrospective patient chart-type data collections. Only 6 cases of deep vein thromboses were reported, 4 in low-molecular-weight heparin treated patients, and 2 in those taking aspirin. The other common AEs were bone marrow suppression, infections, and diarrhea, none of them requiring permanent treatment discontinuation.

DISCUSSION

While real-life results of oncology drugs are typically inferior when compared to RCTs, in this case, we found the opposite. According to the later published pooled analysis of the long term survival of the two similarly designed pivotal Rd trials (MM-009 and MM-010), the PFS was only 11.1 months, which of course compared very favorably to the placebo + dexamethason control arm (4.6 months) [1–3]. The patients of these pivotal trials were mostly treated by 2 or more lines of treatment, but only a minority had prior bortezomib (7.6%), and less than half had thalidomide exposure (36%). One could expect that in a novel-agent-naïve population a new drug could work even better, although the opposite is possible as well if the predominantly chemo-treated population was already damaged by ineffective chemotherapy courses giving rise to more resistant clones.

The level of supportive care has also increased significantly since then, probably further contributing to the improved results. Firstly, thromboembolic events were significantly more common in patients treated with lenalidomide plus dexamethasone in the absence of prophylactic anticoagulation which was not recommended at the time. In a later study, IOM-0810 a greater percentage of patients was anticoagulated, but this was still not a mandatory measure [10].

Another important difference is the corticosteroid use. At the time when the pivotal trials were designed, 40 mg oral dexamethasone on days 1–4, 9–12, and 17–20 of each 28-days cycle was recommended. This rather high dose was later proven to be more toxic than the now-standard lower doses [11]. These data resulted in the new and universally approved standard dose of weekly 40 mg (20 mg in more elderly patients). Even more contemporary results advocate further dose reduction of lenalidomide and complete abolition of dex after 9 cycles of upfront Rd treatment [12]. As our results demonstrated, in day to day practice the treating physicians do utilize an even wider range of corticosteroid types and doses depending on patients' performance status. Importantly, this did not seem to adversely impact the outcome, raising the question of whether it is justified to use 40 mg uniformly in everyone as some centers do, or whether dose adjustment is more appropriate.

The other datasets we can compare our findings to are the standard arm of the recent RCTs using Rd backbones to test the

addition of daratumumab (POLLUX, [4], carfilzomib (ASPIRE, [5], or ixazomib (TOURMALINE, [6], which reported PFS as 17.5, 17.6 and 14.7 months respectively, which are again shorter than what our real-world analysis showed. The explanation ought to lie in the obvious difference in patient characteristics: in the RCTs, patients were randomized to have Rd instead of the triplet, whereas off-trial the treating physician could freely select patients with disease of lower perceived risk to receive the doublet treatment. It was outside of the scope of this analysis to review what other treatments were utilized at the time by the centers, but based on the low patient numbers with high-risk cytogenetics in our cohort (this was around 25% in the three RCTs quoted above, and not stated in the pivotal MM-009 and MM-010 trials) we can speculate that high-risk patients had either bortezomib based protocols or other triplets, instead of the Rd doublet.

A cohort of patients with a suboptimal initial result had a 3rd drug added to enhance the effect of the Rd protocol after a median of 2 months. It is difficult to assess in retrospect what exactly the trigger for the upgrade was, but certainly, these patients fared worse compared to the rest, proving that when Rd seems to fail, Rd backbone triplets may not be the best salvage options.

In summary, our results confirmed that Rd remains a very effective treatment in well-selected patients, mostly those who are lenalidomide-naïve and do not show high-risk features. During the COVID-19 pandemic choosing an all-oral combination can be a good alternative to the more expensive, in part intravenous triplets which do require frequent hospital visits exposing the patients to potential encounters with others, spreading the infection.

DATA AVAILABILITY STATEMENT

The original contributions presented in the study are included in the article/Supplementary Material, further inquiries can be directed to the corresponding author.

ETHICS STATEMENT

Ethical review and approval was not required for the study on human participants in accordance with the local legislation and institutional requirements. Written informed consent for participation was not required for this study in accordance with the national legislation and the institutional requirements.

AUTHOR CONTRIBUTIONS

All authors listed have made a substantial, direct, and intellectual contribution to the work and approved it for publication.

CONFLICT OF INTEREST

The authors declare that the research was conducted in the absence of any commercial or financial relationships that could be construed as a potential conflict of interest.

REFERENCES

1. Dimopoulos M, Spencer A, Attal M, Prince HM, Harousseau J-L, Dmoszynska A, et al.Lenalidomide Plus Dexamethasone for Relapsed or Refractory Multiple Myeloma. *N Engl J Med* (2007) 357:2123–32. doi:10.1056/nejmoa070594
2. Dimopoulos MA, Chen C, Spencer A, Niesvizky R, Attal M, Stadtmauer EA, et al.Long-term Follow-Up on Overall Survival from the MM-009 and MM-010 Phase III Trials of Lenalidomide Plus Dexamethasone in Patients with Relapsed or Refractory Multiple Myeloma. *Leukemia* (2009) 23:2147–52. doi:10.1038/leu.2009.147
3. Weber DM, Chen C, Niesvizky R, Wang M, Belch A, Stadtmauer EA, et al.Lenalidomide Plus Dexamethasone for Relapsed Multiple Myeloma in North America. *N Engl J Med* (2007) 357:2133–42. doi:10.1056/nejmoa070596
4. Dimopoulos MA, Oriol A, Nahi H, San-Miguel J, Bahlis NJ, Usmani SZ, et al.Daratumumab, Lenalidomide, and Dexamethasone for Multiple Myeloma. *N Engl J Med* (2016) 375:1319–31. doi:10.1056/nejmoa1607751
5. Stewart AK, Rajkumar SV, Dimopoulos MA, Masszi T, Špička I, Oriol A, et al.Carfilzomib, Lenalidomide, and Dexamethasone for Relapsed Multiple Myeloma. *N Engl J Med* (2015) 372:142–52. doi:10.1056/nejmoa1411321
6. Moreau P, Masszi T, Grzasko N, Bahlis NJ, Hansson M, Pour L, et al.Oral Ixazomib, Lenalidomide, and Dexamethasone for Multiple Myeloma. *N Engl J Med* (2016) 374:1621–34. doi:10.1056/nejmoa1516282
7. Durie BGM, Harousseau JL, Harousseau J-L, Miguel JS, Bladé J, Barlogie B, et al.International Uniform Response Criteria for Multiple Myeloma. *Leukemia* (2006) 20:1467–73. doi:10.1038/sj.leu.2404284
8. Kyle RA, and Rajkumar SVCriteria for Diagnosis, Staging, Risk Stratification and Response Assessment of Multiple Myeloma. *Leukemia* (2008) 23:3–9. doi:10.1038/leu.2008.291
9. Palumbo A, Avet-Loiseau H, Oliva S, Lokhorst HM, Goldschmidt H, Rosinol L, et al.Revised International Staging System for Multiple Myeloma: A Report from International Myeloma Working Group. *Jco* (2015) 33:2863–9. doi:10.1200/jco.2015.61.2267
10. Knauf W, Aldaoud A, Losem C, Mittermueller J, Neise M, Niemeier B, et al.Lenalidomide Plus Dexamethasone for Patients with Relapsed or Refractory Multiple Myeloma: Final Results of a Non-interventional Study and Comparison with the Pivotal Phase 3 Clinical Trials. *Leuk Res* (2018) 68: 90–7. doi:10.1016/j.leukres.2018.03.008
11. Rajkumar SV, Jacobus S, Callander NS, Fonseca R, Vesole DH, Williams ME, et al.Lenalidomide Plus High-Dose Dexamethasone versus Lenalidomide Plus Low-Dose Dexamethasone as Initial Therapy for Newly Diagnosed Multiple Myeloma: an Open-Label Randomised Controlled Trial. *Lancet Oncol* (2010) 11:29–37. doi:10.1016/s1470-2045(09)70284-0
12. Larocca A, Salvini M, Gaidano G, Cascavilla N, Baldini L, Glietta M, et al.Sparing Steroids in Elderly Intermediate Fit Newly Diagnosed Multiple Myeloma Patients Treated with a Dose/schedule Adjusted RD-R vs. Continuous RD: Results of RV-MM-PI-0752 Phase III Randomized Study: PF586. *Hema Sphere* (2019) 3(S1):244. . Abstract retrieved from EHA Library. 06/14/19; 266385. doi:10.1097/01.HS9.0000560632.24271.d7

Pathology & Oncology Research

frontiers

REVIEW
published: 03 May 2021
doi: 10.3389/pore.2021.1609802

Hypoxia Signaling in Cancer: From Basics to Clinical Practice

Anna Sebestyén[1], *László Kopper*[1], *Titanilla Dankó*[1] *and József Tímár*[2]*

[1]1st Department of Pathology and Experimental Cancer Research, Semmelweis University, Budapest, Hungary, [2]2nd Department of Pathology, Semmelweis University, Budapest, Hungary

Cancer hypoxia, recognized as one of the most important hallmarks of cancer, affects gene expression, metabolism and ultimately tumor biology-related processes. Major causes of cancer hypoxia are deficient or inappropriate vascularization and systemic hypoxia of the patient (frequently induced by anemia), leading to a unique form of genetic reprogramming by hypoxia induced transcription factors (HIF). However, constitutive activation of oncogene-driven signaling pathways may also activate hypoxia signaling independently of oxygen supply. The consequences of HIF activation in tumors are the angiogenic phenotype, a novel metabolic profile and the immunosuppressive microenvironment. Cancer hypoxia and the induced adaptation mechanisms are two of the major causes of therapy resistance. Accordingly, it seems inevitable to combine various therapeutic modalities of cancer patients by existing anti-hypoxic agents such as anti-angiogenics, anti-anemia therapies or specific signaling pathway inhibitors. It is evident that there is an unmet need in cancer patients to develop targeted therapies of hypoxia to improve efficacies of various anti-cancer therapeutic modalities. The case has been opened recently due to the approval of the first-in-class HIF2α inhibitor.

Keywords: cancer, hypoxia, angiogenesis, metabolism, therapy

INTRODUCTION

One of the most typical macroscopic pathologic characteristics of malignant tumors is the presence of bleeding and necrosis (**Figure 1**). This is due to the fact that growth of normal tissues manifests in harmony with vascularization while in case of cancer, tumor growth is driven by activated oncogenes irrespective of permissive vascular supply. Necrotic tumor tissue does not present much harm to the host organism, but the hypoxic part of the tumor tissue and the hypoxic tumor cells are usually the major drivers of tumor progression [1–3].

There is a difference in the oxygenation/physoxia of various normal tissues (4–10% O_2) due to the differential blood supply and tolerance to hypoxia. The most oxygenized tissues are renal cortex, liver, breast and pancreatic tissues, while the least oxygenized ones are brain, lung and intestinal mucosa (**Table 1**). As compared to normal tissues, oxygenation levels are much lower in cancers, even in the most vascularized tumors the O_2 rate is only 2% (lung cancer), but in most cases it is much lower, especially, for pancreatic cancers, where this rate is the lowest (0.3%) [1].

OPEN ACCESS

Edited by:
Andrea Ladányi, National Institute of Oncology, Hungary

***Correspondence:**
József Tímár
jtimar@gmail.com

Received: *09 March 2021*
Accepted: *14 April 2021*
Published: *03 May 2021*

Citation:
Sebestyén A, Kopper L, Dankó T and Tímár J (2021) Hypoxia Signaling in Cancer: From Basics to Clinical Practice. Pathol. Oncol. Res. 27:1609802. doi: 10.3389/pore.2021.1609802

Abbreviations: EPO, erythropoietin; ESA, erythropoiesis stimulating agent; FDG-PET, fluoro-deoxy-glucose positron emission tomography; FMISO, fluoromisonidasole; HBO, hyperbaric O2; Hgb, hemoglobin; HIF, hypoxia inducible factor; HRE, HIF-responsive element; OXPHOS, oxidative phosphorylation, ROS, reactive oxygen species; TCA, tricarboxylic acid cycle; VEGF, vascular endothelial growth factor; VHL, von Hippel Lindau.

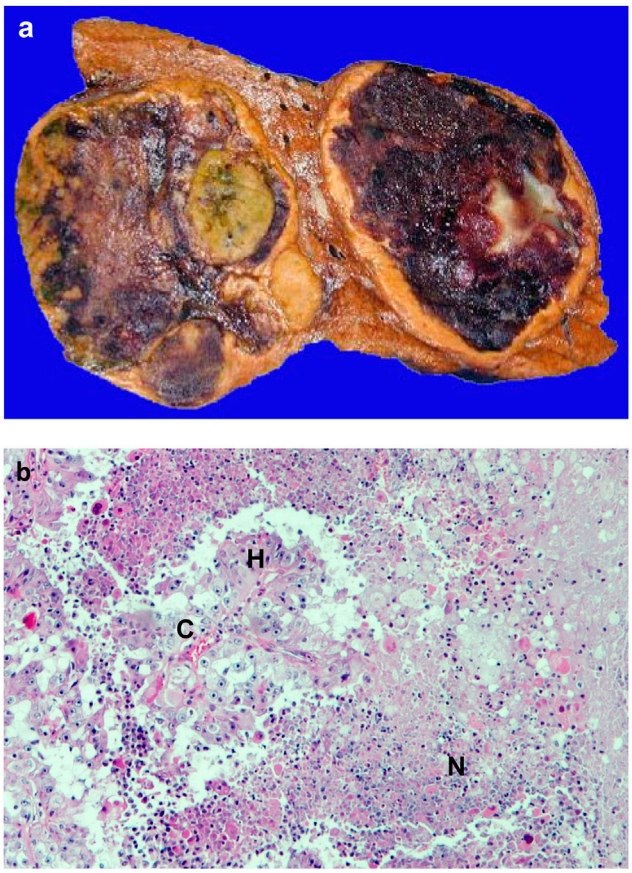

FIGURE 1 | Necrosis in cancer. **(A)**. Macroscopic picture of hemorrhagic necrosis in liver cancer; **(B)**. Microscopic picture of necrosis in renal cell cancer (HE staining). C = capillary, H = hypoxic area, N = necrotic area.

TABLE 1 | Comparison of oxygenation levels in cancer and host tissues. [1].

Cancer	% O_2	Host tissue	% O_2
Lung cancer	2.2	Renal cortex	9.5
Rectal adenocarcinoma	1.8	Breast tissue	8.5
Glial tumors	1.7	Pancreatic tissue	7.5
Breast adenocarcinoma	1.5	Liver	7.3
Renal cell cancer	1.3	Lung	5.6
Cervical squamous cell cancer	1.2	Uterine cervix	5.5
Hepatocellular cancer	0.8	Brain	4.6
Pancreatic adenocarcinoma	0.3	Rectal tissue	3.9

For individual references see [1].

Hypoxia has various forms: acute, chronic, toxic and systemic ones. In cancers, toxic form of hypoxia is not significant. Acute hypoxia is perfusion hypoxia while chronic hypoxia is characterized as diffusion hypoxia, indicating various pathomechanisms behind. Systemic hypoxia in cancer patients is also a frequent event. Collectively, cancer hypoxia usually is a combination of acute, chronic and systemic forms of hypoxia,

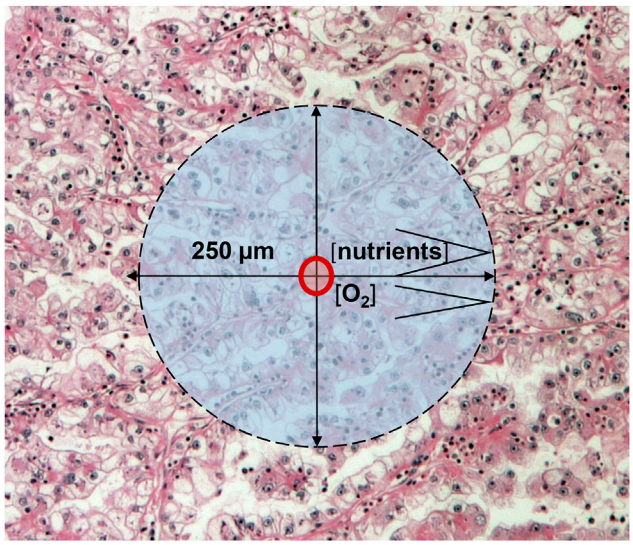

FIGURE 2 | Schematic presentation of cancer growth beyond 1 mm^3: oxygen and nutrient diffusion distances.

which not only drives tumor progression, but also a leading cause of resistance to various therapeutic modalities [3–6].

Below we will provide an overview about the causes of cancer hypoxia and the induced cellular responses; and additionally, we will also summarize the metabolic and immunological consequences. At the end, current therapeutic approaches to overcome cancer hypoxia will be summarized.

PATHOMECHANISM OF CANCER HYPOXIA

According to Folkman's theory, a tissue (including cancer) which growth beyond 2–3 mm^3 requires new blood vessels [2]. We now know that oxygen and nutrient supplies are considered to be optimal in a 250-µm radius of capillaries in various tissues, accordingly a >1 mm^3 tumor tissue can survive without new vessels (**Figure 2**). Since cancer growth exceeds that size, cancer progression/development is driven not by the presence of blood vessels but the immanent oncogenic mechanisms. In cancers, it is almost inevitable that hypoxia would develop which can be due to: 1) compressed intratumoral vessels [3], 2) abnormal newly developed intratumoral capillaries [4], or 3) the systemic hypoxia in the host. Acute hypoxia without resolution leads to the development of necrosis in case of extremely low O_2 levels which is not normalized rapidly at that area. However, chronic hypoxia is the most typical form of hypoxia in tumor tissues [5]. Meanwhile, acute and chronic hypoxia are combined in frequently in cancer tissues leading to central tumor necrosis and surrounded by hypoxic areas (**Figure 1B**). Chronic hypoxia may induce physiological responses in tumor tissue, but in case of genetic changes of the signaling pathway components, this response could be profoundly different [6].

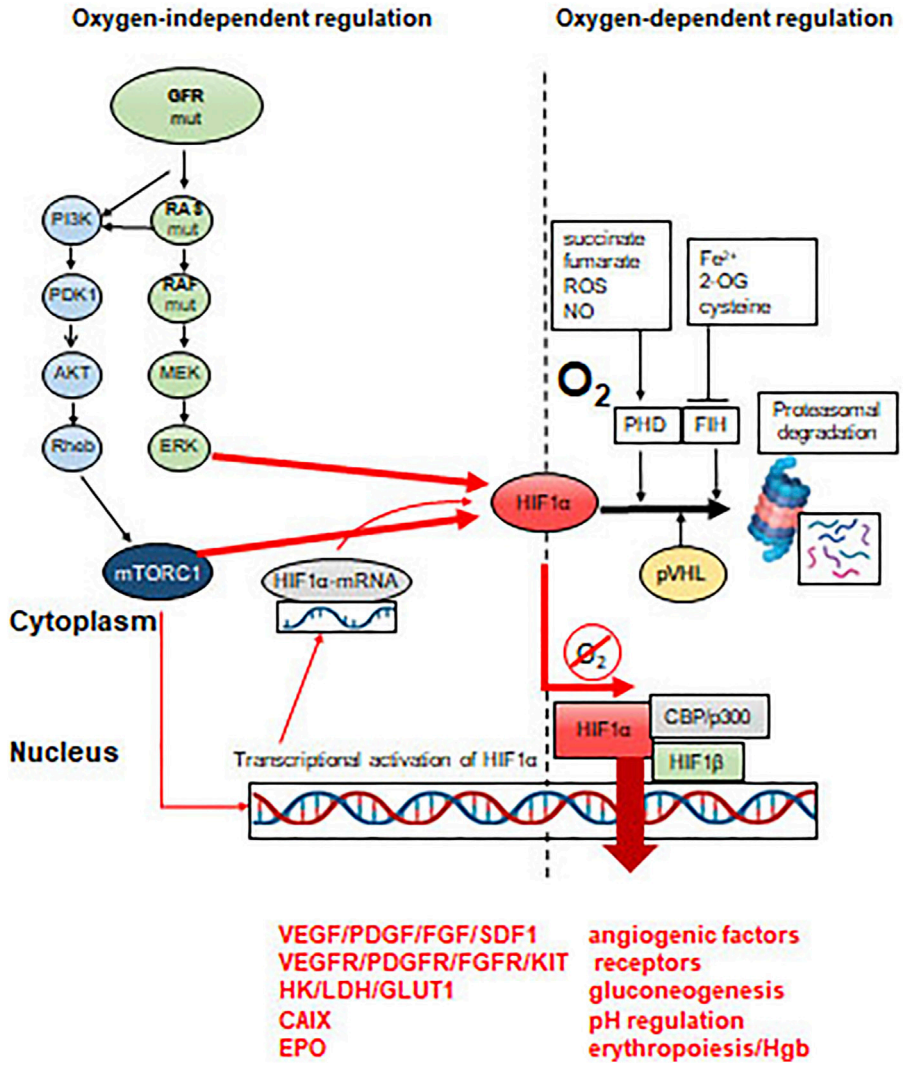

FIGURE 3 | Molecular mechanisms of activation of HIFα transcription factors. HRE = hypoxia-responsive element in the promoter region of specific genes. Effect of constitutive oncogenic activation on HIFα. Proteasomal degradation is inhibited by mTOR or ERK activity, even in the presence of sufficient oxygen levels.

OXYGEN-DEPENDENT HIF ACTIVATION

In (cancer) cells there are two O_2 sensors: the prolyl-hydroxylases (PHD1-3) and the asparaginyl-hydroxylase (FIH), characterized by different O_2 affinities (low: PHD, high: FIH). Accordingly, PHD activity is decreasing linearly with lowered O_2 levels, while FIH activity would decrease only at very low O_2 levels. A unique role of the oxygen sensors is to hydroxylate HIFα transcription factors. At high O_2 levels, hydroxylases label HIFα proteins for VHL, which recognizes these forms and send them for proteasomal degradation by recruiting ubiquitin ligases (**Figure 3**). In this way HIFα proteins are characterized by the shortest half-life among cellular proteins. HIF proteins are α/β heterodimer transcription factors where the expression of the HIFβ partner is constitutional, but it is inactive as a monomer. This powerful transcription factor system is under strict regulatory control: at normoxia, prolyl-hydroxylation ensures protein degradation, while aryl-hydroxylation results in functional inactivation due to the inhibition of coactivator bindings (p300/CBP). Low O_2 levels stabilize HIFα proteins which accumulate and translocate to the nucleus. In parallel, it also activates the expression of certain genes which are involved in adaptation to hypoxic conditions [5, 7] (**Figure 3**).

TABLE 2 | Classical HIF1A regulated genes based on key publications [6, 9].

ADM	CDKN1A	FLT1	LDHA	PKM	TPI1
AK3	CITED2	GAPDH	MDR1/ABCB1	SERPINE1	VEGFA
ALDOA	CP	HK1/2	NOS2	SLCA1/3	
ALDOC	EDN1	HMOX1	P4HA2	TF	
BNIP3	ENO1	IGF2	PFKL	TFRC	
CAIX	EPO	IGFBP1/2/3	PGK1	TGFB3	

There are 216 genes in the human genome which contain HIF-responsive elements (HRE) in their promoters [6, 8, 9] However, the list of classical HIF regulated genes is much shorter (~40) [9]. (**Table 2**). These target genes are responsible for the cellular responses to hypoxia or the accommodation to chronic hypoxia. Meanwhile, the best-known HIF-target genes are angiogenic factors (e.g. VEGF, FGF, PDGF, ANGP1/2 and SDF1), angiogenic factor receptors (VEGFR2/KDR, VEGFR1, KIT) or the O_2 transport capacity regulator, EPO [6]. Those genes which are involved in hypoxia-induced metabolic adaptation are equally important (see later). HIF1α and HIF2α have different target gene profiles, but their regulation and accordingly their roles can be different in cancer progression.

It is a unique consequence of cellular hypoxia that the induced metabolic changes result in production of reactive oxygen species (ROS) which can induce DNA damages, similar to other mutagens. Since under hypoxia the function of DNA repair enzymes can be downregulated, there is a risk of further accumulation of DNA mutations in oxygen-deprived conditions [10].

The vital role of HIF transcription factors is reflected by the fact that their mutations are very rare in cancers: at low frequency, HIF1α mutation can be detected in renal cell cancer [11], while HIF2α mutation results in the development of a rare tumor, paraganglioma [12]. Mutations of HIF regulators–such as VHL, even in the form of germline ones (von-Hippel Lindau syndrome)–are much more frequent in cancers [13]. The consequences of the constitutive HIF activation during development can be observed in VHL syndrome where hemangioblastomas, neuroendocrine tumors of the pancreas and adrenal gland may develop beside the characteristic renal cell cancer. Accordingly, the genetic prototype of HIF-deregulated cancer is the sporadic renal cell carcinoma, where the incidence of the loss of function mutation of VHL is 50%, resulting in an angiogenesis-dependent tumor [14].

Detection of hypoxia in human tumors is a challenge due to the fact that tissue fixation can alter HIF- and hypoxic target protein detections, moreover, native specimens with preserved O_2 supply are not readily available. Meanwhile HIFα detection in combination with CAIX, GLUT1 or VEGF can help to overcome this problem [15]. Especially, the combination of mRNA and protein detection of HIF1/2α and their targets could be useful. Using such a combined approach in metastatic renal cell cancer, it was possible to demonstrate that high HIF1α and low HIF2α expressions or a "HIF-index" are poor prognostic factors, when CAIX, GLUT1 and GAPDH overexpressions follow this prognostic trend [16].

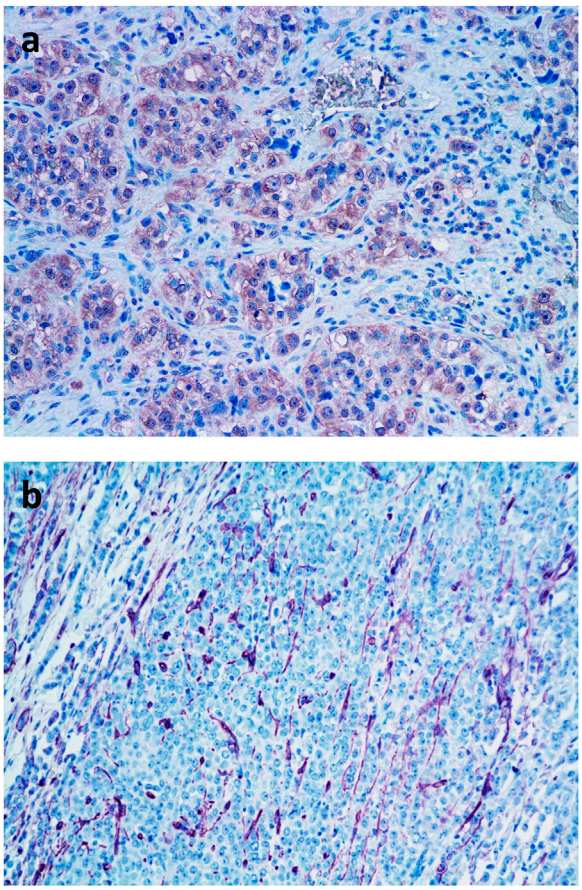

FIGURE 4 | Demonstration of intratumoral microvasculature in breast cancer. **(A)**. Detection of VEGF in tumor cells by immunohistochemistry (pink color); **(B)**. Neo-angiogenesis in breast cancer tissue: demonstration of intratumoral blood vessels by immunohistochemical labeling of CD31 positive endothelial cells (pink color) BAR = 100 μm.

OXYGEN-INDEPENDENT HIF ACTIVATION: "PSEUDOHYPOXIA"

Mutations of growth factor receptors or members of their respective signaling pathways are characteristics for many different cancer types: EGFR mutations in lung adenocarcinoma, HER2 amplifications in breast and gastric cancers, RAS mutations in lung and colorectal cancers, BRAF mutations in melanoma, thyroid or GI-tract cancers or mutations of the lipid kinase signaling pathway members (PI3KCA, AKT) in various cancer types [17]. One of the common functional consequence of these activating mutations is the extreme activity of mTORC1, resulting in constitutive protein synthesis and/or stabilization/functional activation of HIFα. On the other hand, HIFα stabilization can also be the consequence of the increased activity of the RAS-MEK-ERK signaling pathway [18]. Connection among tumor hypoxia, increased HIFα activity and tumor progression is a dogma today [6]. In hypoxic tumor cells, HIF activates several HRE genes that are essential for migration, invasion and metastasis: for example, autocrine motility factor and its receptor (AMF and AMFR); MET oncoprotein, receptor for scatter factor (paracrine regulators); CXCR4 chemokine receptor, matrix metalloproteinases such as MMP2/9 and collagen network remodeling lysil- and prolyl-hydroxylases (LOX and P4HA). The increased migratory activity of hypoxic tumor cells is also due to the activation of the RhoA/ROCK1 signaling pathway leading to cytoskeletal remodeling [6, 18, 19].

VASCULARIZATION OF HYPOXIC CANCER TISSUE

During chronic inflammation or tissue necrosis in the regenerating normal tissues, development of novel capillary network takes place in the form of neo-angiogenesis. This process is fundamentally different from the embryonic development of blood vessels, called vasculogenesis, referring to the fact that in the developing tumor tissues there was no vasculature previously. This later process is based on the mobilization of angiogenic precursors which migrate from bone marrow to developing tissues. In the new location, these cells differentiate into endothelial cells which than form new vasculature in cooperation with mesenchymal cells [20]. In cancer tissues, hypoxia or oncogenic activation of the HIF pathway induces the expression of genes involved in angiogenesis (VEGF, PDGF, SDF) to increase the blood supply and O_2 level. The production of large amount of angiogenic factors and/or cytokines by tumor tissues can also support the migration of these precursors from the bone marrow into the tumor tissue. However, the contribution of vasculogenesis to the vascularization of tumor tissue is minimal in humans [21].

It is much more characteristic in tumor tissues that the production of angiogenic factors/cytokines induces "regeneratory"-type of neo-angiogenesis. In this case, the new capillaries are derived from pre-existing peritumoral capillary network in the form of sprouting (**Figure 4**). Tumor-induced neo-angiogenesis is initiated by local production of VEGF, PDGF, FGF, TGFβ, TNFα, and ANG2. This type of neo-angiogenesis occurs at the venous site of the capillary network [20]. It is still widely accepted that these new capillaries are growing into the developing tumor tissue [2, 20]. However, it is much more common that the tumor-induced novel peritumoral capillary network is incorporated into the tumor tissue by vessel cooption [20, 22, 23]. Furthermore, this reparative neo-angiogenesis takes place in a host tissue specific manner in various tumors [24, 25].

It is more and more evident that reparative neo-angiogenesis is not the most common mechanism to provide blood supply for tumor tissues. Experimental and clinicopathological data demonstrated that the vessel-cooption (incorporation of preexisting vessels) is the most conventional form of vascularization of primary and metastatic tumor tissues. The capillary density of certain tissues (e.g. lung, liver) is sufficiently high, fulfilling the requirement of 1-mm^3 size for tumor growth [2, 20, 23]. Drivers of this type of vascularization are tumor-derived cytokines involved in endothelial cell survival such as angiopoetins and VEGF [23–25]. There is another non-neoangiogenic form of blood supply of tumor tissues (especially in brain tumors or brain metastases), the glomeruloid vasculogenesis/angiogenesis [20, 26], where the preexisting capillaries are remodeled into novel chaotic, tortuous capillary loops. Major drivers of this remodeling are the extremely high local concentrations of VEGF, FGF and PDGF complemented by CSF1, SDF1 and SCF1.

There is a fundamental alteration of gene expression regulation in cancer cells which can provide stem cell properties. This aberrant regulation can result in the loss of linage-specific gene expressions and acquiring new ones. The best-known example of this alteration is the epithelial-mesenchymal transition (EMT) [27]. But there are other forms of such transitions (mimicries) such as 1) neurogenic mimicry, expression of neurogenic genes in non-neural cell types, mostly epithelial cells; 2) megakaryocytic mimicry, expression of megakaryocyte-specific genes in non-bone marrow cell types [28]; or 3) vasculogenic mimicry, [29–31] expression of endothelial genes in non-angioblastic cells, also driven by chronic hypoxia and/or constitutive HIFα expression. If tumor cells express endothelial genes, it can result in the development of novel phenotypic features, communication ability between endothelial cells of the preexisting capillaries and tumor cells which form capillary lumina connected to the blood capillaries [30, 31].

It is of note, that vascularization of tumor tissue is cancer-type specific and greatly depends on the host tissue. Accordingly, it can be different in metastases as compared to primary tumors [24, 25].

Microvessel density of tumor tissues are usually high and it is expected that the blood supply of tumors is also optimal. In contrast to this presumption, tumor tissue is hypoxic. One reason of the poor blood supply is that the interstitial pressure is increased in tumor tissues resulting in the collapse of tumoral capillaries [3]. Another feature of the tumoral blood vessels (newly developed or incorporated) is that their structure is abnormal, the endothelial lumen is leaky and/or the supportive pericytes are missing [4]. In this way, a vicious cycle develops: the hypoxic tumor becomes angiogenic and tries to develop or coopt more capillaries, but this do not lead to higher O_2 levels; on the contrary, tumor tissue hypoxia is stabilized. According to **Table 1**, the best oxygenized tumor is lung cancer closely followed by breast and rectal cancers. However, kidney cancer is characterized by the highest microvessel density followed by lung or breast cancers [32], suggesting that there is no direct connection between vascularization and oxygenation of cancer tissues.

Even if tumor tissue would be optimally vascularized, systemic hypoxia could also lead to tumor tissue hypoxia in cancer patients. There are several causes for systemic hypoxia such as bleeding, hemolysis (hemolytic anemia), bone marrow infiltration by tumor cells, bone marrow depletion by chemo- or radiotherapy, nephrotoxicity of chemotherapy, chronic obstructive lung disease or cardiac failure. Accordingly, systemic causes of tumor tissue hypoxia are outstanding features of malignant tumors [33].

METABOLIC CONSEQUENCES OF TUMOR HYPOXIA

Biological oxidative processes (oxidative phosphorylation) can be termed as the bioenergetically optimal energy productions in cellular metabolism. In hypoxic or pseudo-hypoxic conditions, cancer cells with rapid proliferation capacity require high energy and nutrient supply, and the related bioenergetic pathways have

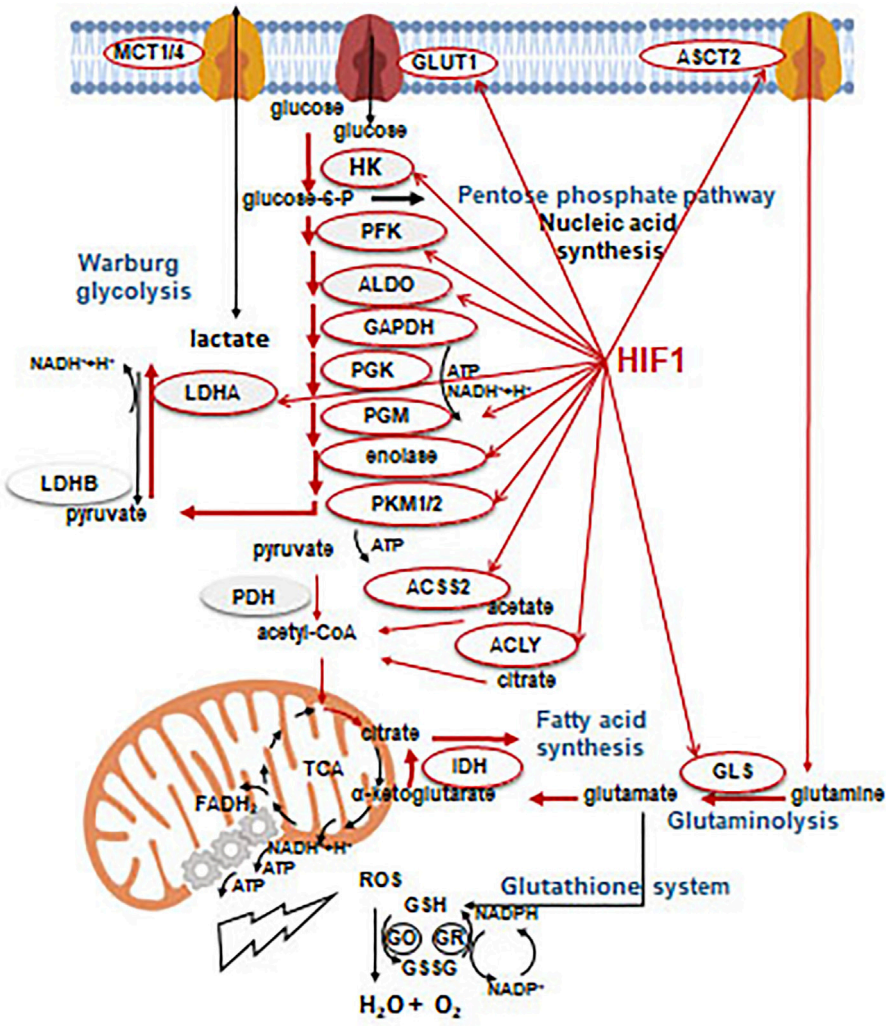

FIGURE 5 | Effects of HIF1α on the metabolic rearrangement. Without going into details, enzymes and processes which can be controlled and/or associated with glycolytic phenotype during metabolic rearrangement by HIF1α (regulation). Beside the effects on HIF1α targets involved in metabolic, glycolytic rearrangement (narrow red arrow), the most frequent and significant metabolic shifts (thick red arrow) are also presented in the figure.

to be re-wired [5]. In hypoxic microenvironment, HIF activation results in the accumulation of lactic acid (as a consequence of anaerobic glycolysis) which is a characteristic metabolic feature of the majority of tumors. Furthermore, in cancer cells independently of the oxygen concentration changes, the erobic glycolytic phenotype (Warburg effect–aerobic glycolysis) can also be found [34].

It has been well-known since the early 2000s, that the HIF1α stabilization and the elevated HIF1α protein levels are characteristic for ~50% of tumor cells under normoxia [35]. As a consequence, the productions of several glycolytic enzymes or transporters increase in malignant cells, e.g. the gene expressions of glucose transporter (GLUT1-3) or pyruvate-dehydrogenase-kinase 1 (PDK1), pyruvate kinase isoform 2 (PKM2) are elevated. These contribute to the conversion of pyruvate to lactate. In addition, entering acetyl-CoA into the tricarboxylic acid cycle (TCA) can be inhibited, leading to decreased mitochondrial respiration and oxygen consumption. In parallel, glutamine or other intermediates of various metabolic processes can fuel TCA with anaplerosis [3], e.g. the increase in glutaminase expression, glutaminolysis or influencing protein and lipid metabolism (**Figure 5**).

HIF1α-mediated metabolic rearrangement can also contribute to other microenvironmental alterations since lactate production and acidification are important oncogenic features. Based on these, the most important oncogenic impact of HIF1 activation is necessarily the angiogenic effect. HIF1α has a comparable importance in maintaining the proliferation demands for rapid metabolic rearrangements [34]. In tumor microenvironment, the energy and nutrient demand of tumor cells can dominate but the tissue oxygenation could also affect the metabolism of stromal cells. In non-transformed cells of well-oxygenated tissues and even in tumor cells which are located near to blood vessels, an oxidative phenotype, the reverse utilization of lactic acid (reverse

Warburg effect) can be observed [36]. The evolving metabolic symbiosis can guarantee the optimal utilization of energy resources at tissue level [37].

The most important differences in metabolic machinery of tumors and their normal equivalents are mutations of key genes, and the related signaling pathways which drive continuously high metabolic activity for proliferation. This can be emerged concomitantly with proper net lactic acid overproduction and metabolic flexibility [38, 39]. It is also known that certain tumors can have differences in basic metabolic processes e.g. alterations in anaplerotic mechanisms of TCA (e.g. lipid metabolic alterations or autophagy). Even certain oncogenic mutations result in oncometabolite production [40]. Tumor growth induces activation of several additional early or late stress responses i.e. elevation of ROS supporting hypoxia, extracellular acidification to maintain optimal energy level in nutrient or oxygen deprivation. Simultaneously, other metabolic adaptation mechanisms can induce the activation of antioxidant processes in cancer cells. Glutathione system is one of the important antioxidant cellular programs. Glutathione reductase neutralizes H_2O_2 with glutathione derived from cysteine, glutamate and glycine. In a further step, NADPH, as a cofactor of glutathione oxidase, converts glutathione. Thioredoxin system, as an additional alternative, can reduce the H_2O_2 level by the use of NADPH. In summary, NADPH has a remarkable role not only in biosynthetic processes but also in buffering ROS levels [41] (**Figure 5**). The balance of ROS-regulating capacities is also an important element of metabolic changes, which foster hypoxic processes. Recently, alterations in several tumor-specific factors have been characterized in the regulation of ROS generation such as NRF2 or SLC7A.

mTOR kinase is an important regulatory element of signaling network and metabolism has special and context-dependent role in hypoxia-related cellular events. The two different mTOR complexes have critical functions in cellular homeostasis by sensing and synthesizing intra- and extracellular conditions [42]. Moreover, mTORC1 influences the protein expression level of several onco-proteins such as HIF1α at post-transcriptional, translational level. However, the production of HIF1α requires mTORC1 activity, additionally, post-translational degradation of the protein regulated directly and quickly by O_2 level [43]. Therefore, mTOR hyperactivity provides stabilization of HIF1α protein and other regulatory failures contributing to the HIF1α stabilization in pseudohypoxic tumor tissues [44]. Moreover, other cellular stresses (nutrient deprivation, DNA damage responses, low energy level and "real" cellular hypoxia) could reduce mTORC1 activity and slow down the tumor proliferation/growth. This situation rewires cellular metabolic processes e.g. reduces oxygen consumption and/or induces autophagy [45] leading slower metabolic activity and forces cellular survival mechanisms with balanced bioenergetics [46]. They could give an opportunity to restore cellular homeostasis and mTORC1 activity maintaining pseudohypoxia in tumor cells.

Considering the fundamental regulatory changes of certain tumors (mutations of oncogenes/tumor suppressors in signaling) and their metabolic consequences or the expected effects of currently available treatments, novel therapeutic options could be introduced to target and inhibit metabolic adaptation mechanisms. The importance of the latter is that hypoxia-induced metabolic processes (e.g. in case of anti-angiogenic treatments) have to be taken into account since using inhibitors of metabolic adaptation regulators (such as mTOR) or other enzymes, metabolic catastrophe, synthetic lethality could be induced in cancer cells [47, 48].

IMMUNOLOGIC CONSEQUENCES OF TUMOR HYPOXIA

Antitumoral immune responses are affected by (tumor) tissue hypoxia [40]. Antitumoral innate immune responses are mediated by NK cells and macrophages. It is important that macrophages are sensitive to hypoxia and instead of the M1/antitumoral polarization in normoxia, under such circumstances they obtain M2/immunosuppressive phenotype [49]. Furthermore, HIF activation in hypoxia enhances immune suppressive effects of myeloid-derived suppressor cells [50]. On the other hand, NK cells remain active against tumor cells in hypoxia [51].

Hypoxia fundamentally affects the acquired immune responses to tumors as well. One of the main immunosuppressive cytokine in the hypoxic microenvironment is VEGF [52]. In hypoxia, VEGF promotes $CD4^+$ T-cell differentiation into T-regulatory cells, suppressing the emerging immunoreactions. Hypoxia modulates immune checkpoint inhibitory molecules on infiltrating cells and tumor cells by inducing PDL1 expression. In $CD8^+$ cytotoxic T-cells, hypoxia also induces CTLA-4 receptor, another checkpoint regulator [53]. In lung cancer, it was demonstrated that cancer cells overexpress PDL1 at the border of necrotic tumor while the infiltrating cells express PD1 and activate immunosuppressive mechanisms [54]. For an effective antitumoral response, the density of immune effector cells is an important parameter. It was shown in skin melanoma that increased tumoral vascular density is associated with increased macrophage and T-cell density [55].

CLINICAL IMAGING OF TUMOR HYPOXIA

It is a longstanding goal in experimental cancer research and clinical oncology to develop reliable markers to measure pO_2 levels in cancer tissues or to detect hypoxia. It is an invasive approach to use polarographic oxygen electrodes to measure pO_2 levels in cancer tissues. On the other hand, there are immunohistochemical techniques to asses tissue hypoxia in biopsies. This is also an invasive technique since it requires to inject exogenous hypoxia marker into the tumor tissue before resection such as pimonidazol or a derivative, EF5. It is a less reliable approach to use endogenous hypoxia markers such as HIF1α or GLUT1 immunohistochemistry. The problem here is that not only hypoxia can induce the expression of those marker genes but also various genetic changes of the tumor which cause overexpression of the markers independent of the hypoxia.

Accordingly, non-invasive techniques have been developed and tested clinically. One approach is to use magnetic resonance imaging such as blood-oxygen level dependent imaging (BOLD) able to monitor tissue perfusion. On the other hand, nuclear magnetic resonance spectroscopy can be used to measure increased lactate or decreased ATP levels in cancer tissues: unfortunately, the sensitivity and resolution of these techniques are very low. The gold standard technology to measure tumor tissue pO_2 levels is PET using $^{15}O_2$. However, the short half-life of this marker prevents the widespread use of this technology. Meanwhile PET is the technology which can be used to asses tumor tissue hypoxia. The first marker was 2-nitroimidazole and (^{18F})FMISO later it was developed further into ^{123}I-tracers. It is an alternative to use reduced chelated metals such as ^{60}Cu-compound ATSM although their sensitivity is lower as compared to FMISO. Last but not least, FDG-PET can also be used to assess the glycolysis and increased glucose transport in cancer tissues. Although the specificity of FDG-PET is lower compared to FMISO. The parallel use of the two technologies give the best assessment of tumor tissue hypoxia in clinical situations [56, 57].

MODULATION OF EFFICACY OF CHEMO- AND RADIOTHERAPY BY TUMOR HYPOXIA

One major modality of cancer treatments is the cytotoxic chemotherapy. However, in a significant proportion of cases, tumors are resistant or acquire resistance during therapy. Chemotherapy resistance depends on genetic and epigenetic factors among which tissue hypoxia is a significant factor. In hypoxia, tumor cells intend to leave cell cycle, and the apoptotic processes are inhibited–these result in decreased sensitivity to cell proliferation blocking cytotoxic agents. Furthermore, in cancer cells, hypoxia induces drug transporter proteins promoting their chemoresistance. At first, in hypoxia HIF1α induces MDR1/ABCB1 efflux transporter resulting in resistance to chemotherapeutics which are its substrates (like doxorubicin)–this mechanism is quite universal among various cancer types [58]. On the other hand, in hypoxia oxygenic stress response is activated by NRF2, which activates HIF1α, but more importantly an array of multidrug resistance genes such as *MDR1/ABCB1, MRP1/ABCC1* and *BCRP/ABCG2* resulting in resistance to a variety of other chemotherapeutics [59, 60].

Furthermore, tumor tissue is characterized by perfusion hypoxia due to the abnormal structure of the intratumoral blood vessels which are also incompetent delivering cytotoxic drugs. Even some chemotherapeutics require O_2 for optimal effects [1, 61]. It is of note, chemotherapy resistance can be predicted by the expression of HIF1α in some types of squamous cancers [1].

Other major therapeutic modality of cancers is radiotherapy, however, it requires optimal normoxic conditions [62]. Oxygen enhancement ratio refers to the enhancement of the therapeutic effect of irradiation due to the presence of oxygen. Ionizing radiation induces DNA damages by free radicals which are stabilized by ROS. In hypoxia, ROS production is decreased and intracellular SH-containing molecules (glutathione and cysteine) "repair" DNA damages by back-reducing free radicals in DNA. Hypoxia-induced cell cycle arrest and apoptosis resistance (by BCL2 overexpression) decrease the sensitivity of tumor tissue to irradiation. HIF1α overexpression in oral cancer is a negative predictive factor for radiotherapy [63]. For the maximal efficacy of radiotherapy, it is important to induce endothelial cell apoptosis as well. However, the elevated VEGF level promotes endothelial cell survival in hypoxic microenvironment. Accordingly, the alteration of tumoral microvessel density upon irradiation is a sensitive prognostic factor for radiotherapy efficacy [64]. Meanwhile these effects of hypoxia are unique to X-ray irradiation and much less pronounced in other radiotherapy modalities. On the other hand, fractionated irradiation improved the antitumoral effects due to the better timing of irradiation for the reoxygenization period in the tumor tissue.

ANTI-ANGIOGENIC THERAPY OF CANCER

It has been considered that the inhibition of tumor-induced angiogenesis could have potential antitumoral effects [1]. Considering widespread effects of hypoxia, it would be irrational to deepen hypoxia further in tumor tissues. Overall, anti-angiogenic drugs have been developed and this therapy became the fourth modality following chemo-, radiotherapy and surgery. There are two major groups of anti-angiogenic drugs, the anti-VEGF agents (mostly antibodies) and small molecular inhibitors of VEGFR [65, 66] (**Table 3**). Although in preclinical models these drugs were able to decrease tumoral microvessel densities – this has never been demonstrated at clinical circumstances. Later on, it was turned out that all these agents are able to normalize the malfunctioning tumoral blood vessels [67] by improving tumor tissue perfusion and decreasing hypoxia.

On the other hand, these agents are not effective in monotherapy except for renal cell cancer. This cancer is multidrug resistant, it genetically depends on HIF activation and characterized by extreme VEGF production. This genetic hypoxia dependence is due to the frequent loss of function mutations of VHL [13]. In any other cancer types, anti-angiogenic dugs are effective only in combination with chemo- and/or radiotherapy i.e. increasing the efficacy of cytotoxic therapies by decreasing tissue hypoxia. It is another fact that anti-angiogenic drugs are not effective in combinations with other targeted therapies, with the exception of *EGFR*-mutant lung adenocarcinoma where EGFR inhibitors can be effectively combined with anti-VEGF antibody [68].

It is an equally important question whether anti-angiogenic agents can be effective in cancers where the driver oncogene induces constitutive HIF activation. In case of colorectal cancers, chemotherapy in combination with anti-VEGF antibody is similarly effective in *KRAS*-mutant and wild-type tumors [69]. On the contrary, in case of lung adenocarcinoma, chemotherapy

TABLE 3 | Clinical use of antiangiogenic drugs [33, 34].

	Drug type	Molecular target	Clinical use
Ligand inhibitors			
Bevacizumab	Monoclonal antibody	VEGF-A	RCC, GBL, OEC, CRC, LUAD, CeC, BC
Ziv-Aflibercept	Recombinant peptide	VEGF-A/B, PlGF, VEGF-C/D	CRC
Receptor inhibitor (ECD)			
Ramucirumab	Monoclonal antibody	VEGFR2	CRC, LUAD, GaC
Kinase inhibitors			
Sunitinib	Small molecular inhibitor	VEGFR1/2/3 PDGFRβ, KIT, RET	RCC
Sorafenib	"	VEGFR1/2/3 PDGFR, KIT, RET, RAF	RCC, HCC
Pazopanib	"	VEGFR1/2, FGFR, KIT	RCC, STS
Axitinib	"	VEGFR1/2/3	RCC
Regorafenib	"	VEGFR, PDGFR, FGFR, TIE2, RAF, KIT	CRC, HCC
Cabozantinib	"	VEGFR, TIE2, MET, RET	RCC, HCC

BC, breast cancer; CeC, cervical cancer; CRC, colorectal cancer; ECD, extracellular domain; GaC, gastric cancer; GBL, glioblastoma; HCC, hepatocellular carcinoma; LUAD, lung adenocarcinoma; OEC, ovarian epithelial cancer; RCC, renal cell cancer; STS, soft tissue sarcoma.

combination with anti-VEGF antibody is effective in *KRAS* wild-type tumors exclusively [70].

It is a further issue if the efficacy of anti-angiogenic agents depends on the type of tumor vascularization or not. Looking into the indications of these anti-angiogenic agents [65, 66] (**Table 3**), there are tumors where 1) neo-angiogenesis is predominant (renal, breast and colorectal cancers), 2) vessel cooption is characteristic (glioblastoma, lung adenocarcinoma) and 3) unique vascularization form can be observed (liver or esophageal cancers).

However, similar to almost all cancer treatment forms, anti-angiogenic therapy also leads to emergence of resistance. One possible cause of anti-angiogenic therapy resistance is the switch of the angiogenic phenotype: VEGF to PDGF in renal cell cancer, VEGF to FGF in squamous cancers, VEGF to Bv8 peptide in glioblastoma, VEGF to TGFβ in hepatocellular cancer [71], and VEGF to apelin in lung or breast cancers [72]. Similar to other therapeutic modalities, efficacy of anti-angiogenic agents is also dependent on the optimal perfusion of the tumor tissue [73].

EFFECT OF HYPOXIA ON THE EFFICACY OF IMMUNOTHERAPY

If hypoxia affects antitumoral immune responses, it is justified to propose that hypoxia may affect immunotherapy as well [74]. Unfortunately, there are scanty experimental data in this respect, however, clinical developments may help to answer this important question. It can be reasonable to propose that in case of a tumor type where anti-angiogenic therapy is effective, it can be further improved by immunotherapy. It has become evident, that only certain patients and tumors respond well to immunotherapy. This can also suggests to combine immunotherapy with anti-angiogenic agents to decrease hypoxia and VEGF levels in such cases. It is also an important consideration that a fraction of anti-angiogenic agents are "dirty" (not highly specific) VEGFR inhibitors which affect other receptors, crucially important in the normal function of anti-tumoral T-cells. Accordingly, consideration of "pure" (more specific) VEGFR blockers may have a higher chance for clinical efficacy. In case of renal cell cancer, anti-angiogenic monotherapy is the basis of tumor management. The development of combination strategies with immunotherapy was clinically very effective [75] leading to FDA approval of several combinations with multikinase inhibitors (**Table 4**). Immunotherapy and anti-angiogenic treatment combination also approved recently in lung adenocarcinoma [76] and hepatocellular carcinoma [77] (**Table 4**). Furthermore, in various cancer types such as colorectal, ovarian or breast cancers, anti-angiogenic treatment (anti-VEGF antibody) and anti-PD1 antibody therapies are approved individually, accordingly it is expected that such combinations will also be a part of clinical management of patients soon.

THERAPY OF SYSTEMIC HYPOXIA

The primary cause of systemic hypoxia in cancer patients is anemia (low Hgb levels), accordingly it has to be managed to improve efficacies of other therapeutic modalities. However, targeted therapy has to be applied even in case of systemic hypoxia. There are three therapeutic options for anemia: iron supply, transfusion and erythropoiesis stimulating agents (ESA). Unfortunately, transfusion and ESA administration have a severe adverse effect which is thromboembolism. Iron deficient anemia is a frequent cause for cancer patient's anemia; therefore, beside determination of the Hgb levels, it is necessary to determine Se-ferritin levels and saturation. In case of absolute iron deficiency, iron administration is necessary, in case of relative iron deficiency, iron supply have to be completed with ESA [78, 79]. It is important to mention that beside severe possible side effects of ESA, this treatment may have other important biological effects: normalization of tumoral blood vessels improving drug perfusion [80] or promoting efficacy of radiotherapy [81], asx observed in preclinical models. However, it is assumed that correction of systemic hypoxia may not be equally effective in tumors where the O_2-independent HIF activation takes place.

TABLE 4 | Approved combinatorial therapies of anti-angiogenic agents and immune checkpoint inhibitors.

Tumor	Anti-PD1 Ab	Anti-PDL1 Ab	Anti-VEGF Ab	Anti-angiogenic TKi	Combination approval
LUAD	—	Atezolizumab	Bevacizumab	—	+
HCC	—	Atezolizumab	Bevacizumab	—	+
RCC	Pembrolizumab	—	—	Axitinib	+
	Nivolumab	—	—	Axitinib	+
	—	Avelumab	—	Cabozantinib	+

Ab, antibody; HCC, hepatocellular carcinoma; LUAD, lung adenocarcinoma; RCC, renal cell carcinoma; TKi, tyrosine kinase inhibitor.

TABLE 5 | Targeted therapies of HIF in cancer.

Mechanism	Target	Agent	Preclinical	Clinical	Tumor Type
HIFα RNA expression	HIF1α	Antisense	+	–	Various
	HIF2α	sh-RNA	+	–	Various
	HIF1α	$ZnSO_4$	+	–	Melanoma
HIFα protein synthesis	HIF1α	Digoxin	+	–	Various
	HIF2α	2-ME	+	–	Various
		Topotecan	+	–	Various
HIFα stabilization	HIFα	HSP-90 inhibitor	+	+	BRC
	mTOR	Everolimus	+	+	RCC
		Temsirolimus	+	+	BRC
Direct HIFα inhibitors	HIF1α	Acryflavine	+	–	Various
		YC-1	+	–	Various
	HIF2α	PT2385	+	+	Various
	HIF2α	MK6482	+	+	VHL syndrome related tumors
DNA binding	HRE	Echinomycin	+	–	Various

BRC, breast cancer; HIF, hypoxia-inducible factor; HRE, HIF-responsive element; RCC, renal cell cancer; sh-RNA, short hairpin RNA; VHL, von-hippel lindau.
Grey shade: FDA approvals.

MOLECULAR THERAPY OF HYPOXIA

It was shown above that hypoxia signaling in cancer is a key regulatory pathway affecting several aspects of cancer biology offering an obvious target for intervention. It would be an indirect approach to disconnect hypoxia signaling since the effector of the O_2-independent oncogenic driver-driven pathway is mTOR (**Table 5**; **Figure 3**). In this respect, it has to be mentioned that the first mTOR inhibitor therapies were introduced into the clinic long time ago in case of *VHL*-mutation dependent renal cell cancer (everolimus and tensirolimus), and more recently in case of breast cancer recently [82].

In experimental models, it was possible to downregulate HIF1/2α by antisense oligos or sh-RNA [83]. In human melanoma preclinical models, $ZnSO_4$ administration was able to downregulate HIF1α expression selectively which had antitumoral and antimetastatic effects [84]. The other approach is to target HIF protein synthesis using digoxin [83], 2-methoxy-estradiol [85] or topotecan [83]. According to preclinical models, these agents could be effective, however, there are no available clinical data. Stabilization of HIFα can be suspended by HSP-90 inhibitor *in vivo* [86].

Of note, the HIF complex-induced binding to HRE regions in promoters of various genes can be achieved by echinomycin [87]. However, the ultimate goal have to be the development of small molecule HIF inhibitors. *In vitro*, acriflavin [83] or YC-1 [88] can directly bind to HIF1α; although they have shown some preclinical activity, the clinical development was discontinued. However, small molecule HIF2α inhibitors, PT2977/MK6482 and PT2385 have been developed recently and tested in clinical trials [89]. MK6482 was used clinically in VHL syndrome related renal cell cancer with promising activity [90]. Based on these results, MK6482 became the first FDA-approved HIF2α inhibitor.

Anti-hypoxia therapies have already been introduced in case of radiotherapy using hyperbaric O_2 (HBO), which could have some activity in squamous cancers of the head and neck [91]. It is another clinical approach to combine accelerated radiotherapy with nicotinamide and carbogen (ARCON) of which research reached phase-III [92] but did not resulted in clinical acceptance. Another clinically active therapeutic option is "chemical anti-hypoxia" by the use of doranidazole or nimorazol in lung cancer radiotherapy [93] which are used more widely nowadays due to the success of the DAHANCA 5–85 trial. Generation of intratumoral O_2 is also feasible to improve the efficacy of radiotherapy by using bioactive albumin-MnO_2 nanoparticles [94]. The imminent question concerning all these approaches is whether any of these could be exploited in case of other anticancer therapeutic modalities such as chemotherapy, targeted therapy, anti-angiogenic therapy or immunotherapy.

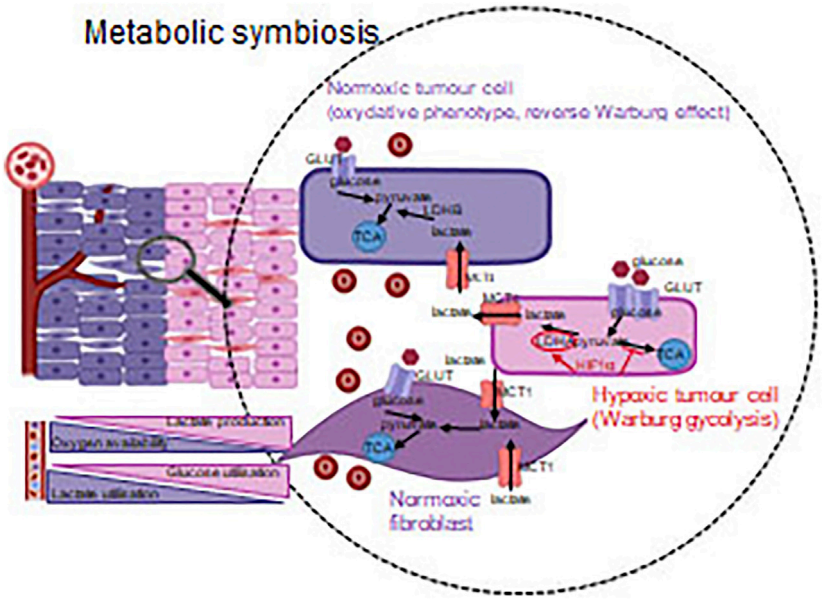

FIGURE 6 | Metabolic symbiosis–optimizing the available energy sources. Tumorous and other non-tumorous cells derived from microenvironment utilize the nutrients in harmony with the oxygen concentration (via the regulating role of HIF1α). Accordingly, not only the glycolysis, but also the reverse Warburg effect–in a well-oxygenated environment–provide adaptation capacity/opportunity for cancerous cells.

METABOLIC THERAPY

During tumor progression, angiogenic and metabolic effects of HIF activation are in a complex relation, and crosstalk among the related signaling machineries can be important. Metabolic adaptation can be observed in case tumor cells survive the consequences of anti-angiogenetic or anti-HIF1α treatments. This phenomenon can be illustrated with the example of metabolic symbiosis and heterogeneity [95]. Tumor cells in the tissue context, optimize and balance the utilization of the available energy resources to maintain their continuous proliferation even in stress conditions. In oxygenated environment, tumorous or even normal cells can consume the excreted metabolites of other cells located in the stroma. As an example, lactate produced during "lactic glycolysis" of hypoxic or pseudo-hypoxic cells can be utilized in this manner [37] (**Figure 6**). Metabolic plasticity and tissue co-operation are important factors of the tumor resistance to various therapies. Metabolic adaptation also has a remarkable role in maintaining/supporting the survival of the so-called cancer stem- or dormant cells [96, 97].

All of these provide an opportunity for therapeutic exploitation of targeting metabolic symbiosis, which can also lead to the introduction of novel therapeutic options in anti-angiogenic combination treatments. It was observed that the activity pattern of mTOR shows intratumoral heterogeneity as a consequence of anti-angiogenic therapies. This finding calls the attention to the master regulatory role of mTOR kinase in developing therapy resistance [98]. Several clinical trials of renal carcinoma, glioma, neuroendocrine and gastrointestinal cancers are ongoing, involving mTOR inhibitors in combination with anti-angiogenic treatments, however, the results may vary between tumor types [99–102]. Beside mTOR inhibitors, additional opportunities can be found for the inhibition of metabolic adaptation and symbiosis. The uptake and the release of extracellular metabolites and their transporters can also be inhibited in these metabolic alterations. Moreover, various metabolite transporter proteins–involving monocarboxylate transporters (MCTs), which contribute to lactate transport–can also be tested as a part of anti-angiogenic treatment combination [38, 39, 103, 104].

Autophagy can be induced by certain treatments or microevironmental effects in relation to metabolic adaptation and resistance [45]. It can either result in apoptosis of cancer cells or provide appropriate bioenergetic background for cellular survival. Autophagy activation can be observed in case of anti-angiogenic therapies. It is not surprising that autophagy inhibiting/inducing factors could be associated with anti-tumor effects in certain combinational treatments. Autophagy-targeted therapies and the combinatorial effect of anti-angiogenic treatments were confirmed among experimental conditions e.g. in lung carcinomas [105].

As a further metabolic mechanism, mitochondrial oxidation cannot be neglected as a potential therapeutic target (i.e. metabolic phenotype of cancer stem cells or tumor cells in an oxygenized environment). The anti-diabetic drug, complex I inhibitor (OXPHOS) metformin and phenformin (AMPK activator) can inhibit mitochondrial electron transport chain. Based on certain studies, their combination with chemotherapy could be effective, but it could significantly enhance the effect of anti-angiogenic therapy (bevacizumab) without increasing the severity of side effects (e.g. in metastatic NSCLC) [105–107].

Other studies also call the attention to metabolism-targeting agents in combinations, which highlights that these could potentially enhance the impact of sensitizing strategies and accordingly, mTOR inhibitors could inhibit tumor progression as having a complex modifying role on metabolism [108–113].

Treatments (including anti-angiogenic ones) targeting metabolic adaptation mechanisms and influencing metabolic symbiosis administered in combination could cause metabolic catastrophe in cancer tissue adaptation machinery. These could also help the development of traditional targeted or anti-angiogenic therapy combinations. However, tumor heterogeneity, similarly to immunoediting mechanisms, always has to be considered in experimental model systems [114, 115]. Significant differences could be obtained by studying *in vitro* and *in vivo* models or clinical tumor specimens. Therefore, the administration of metabolic inhibitors has to be verified a priori of clinical trials, and appropriate biomarkers have to be discovered to use them in a "targeted" or precision manner.

CONCLUSION

Our knowledge in the past decades enormously increased abut the mechanism and detriemental consequences of tumor hypoxia. Fortunately, these information led to development several new therapeutic modalities and started to transform the use of existing therapies. However, the tumor hypoxia issue must be developed into a core aspect of cancer management from diagnosis through treatment to effective cure.

AUTHOR CONTRIBUTIONS

AS, writing, table composition, figure composition: LK, concept: TD, writing, editing, figure composition: JT, concept, writing, correcting.

FUNDING

This work was supported by National Research, Development and Innovation Office, Hungary, 507 (K-135540-TJ, FK-128404-SA).

CONFLICT OF INTEREST

The authors declare that the research was conducted in the absence of any commercial or financial relationships that could be construed as a potential conflict of interest.

REFERENCES

1. Muz B, de la Puente P, Azab F, and Azab AK. The Role of Hypoxia in Cancer Progression, Angiogenesis, Metastasis, and Resistance to Therapy. *Hp* (2015) 3:83–92. doi:10.2147/HP.S93413
2. Folkman J. Tumor Angiogenesis: Therapeutic Implications. *N Engl J Med* (1971) 285:1182–6. doi:10.1056/NEJM197111185210810.1056/nejm197108122850711
3. Heldin C-H, Rubin K, Pietras K, and Östman A. High Interstitial Fluid Pressure - an Obstacle in Cancer Therapy. *Nat Rev Cancer* (2004) 4:806–13. doi:10.1038/nrc1456
4. Siemann DW. The Unique Characteristics of Tumor Vasculature and Preclinical Evidence for its Selective Disruption by Tumor-Vascular Disrupting Agents. *Cancer Treat Rev* (2011) 37:63–74. doi:10.1016/j.ctrv.2010.05.001
5. Lee P, Chandel NS, and Simon MC. Cellular Adaptation to Hypoxia through Hypoxia Inducible Factors and beyond. *Nat Rev Mol Cel Biol* (2020) 21:268–83. doi:10.1038/s41580-020-0227-y
6. Semenza GL. HIF-1 and Tumor Progression: Pathophysiology and Therapeutics. *Trends Mol Med* (2002) 8:s62–s67. doi:10.1016/s1471-4914(02)02317-1
7. Pugh CW, and Ratcliffe PJ. New Horizons in Hypoxia Signaling Pathways. *Exp Cel Res* (2017) 356:116–21. doi:10.1016/j.yexcr.2017.03.008
8. Ortiz-Barahona A, Villar D, Pescador N, Amigo J, and del Peso L. Genome-wide Identification of Hypoxia-Inducible Factor Binding Sites and Target Genes by a Probabilistic Model Integrating Transcription-Profiling Data and In Silico Binding Site Prediction. *Nucl Acid Res* (2010) 38:2332–45. doi:10.1093/nar/gkp1205
9. SEMENZA. (2021), Available at: www. gsea-msigdb.org/gsea/msigdb/cards/SEMENZA_HIF1A_TARGETS (Accessed 09. 03, 2021).
10. Kaplan AR, and Glazer PM. Impact of Hypoxia on DNA Repair and Genome Integrity. *Mutagenesis* (2020) 35:61–8. doi:10.1093/mutage/gez019
11. Morris MR, Hughes DJ, Tian YM, Ricketts CJ, Gentle D, Serrano-Fernandez P, et al. Mutation Analysis of Hypoxia-Inducible Factors HIF1α and HIF2α in Renal Carcinoma. *Anticancer Res* (2009) 29:4337–43.
12. Pang Y, Gupta G, Jha A, Yue X, Wang H, Huynh TT, et al. Nonmosaic Somatic HIF2A Mutations Associated with Late Onset Polycythemia-paraganglioma Syndrome: Newly Recognized Subclass of Polycythemia-paraganglioma Syndrome. *Cancer* (2019) 125:1258–66. doi:10.1002/cncr.31839
13. Gläsker S, Vergauwen E, Koch CA, Kutikov A, and Vortmeyer AO. Von Hippel-Lindau Disease: Current Challenges and Future Prospects. *Ott* (2020) Vol. 13:5669–90. doi:10.2147/OTT.S190753
14. Dizman N, Philip EJ, and Pal SK. Genomic Profiling in Renal Cell Carcinoma. *Nat Rev Nephrol* (2020) 16:435–51. doi:10.1038/s41581-020-0301-x
15. Macklin PS, Yamamoto A, Browning L, Hofer M, Adam J, and Pugh CW. Recent Advances in the Biology of Tumour Hypoxia with Relevance to Diagnostic Practice and Tissue-based Research. *J Pathol* (2020) 250:593–611. doi:10.1002/path.5402
16. Szendrői A, Szász AM, Kardos M, Tőkés AM, Idan R, Szűcs M, et al. Opposite Prognostic Roles of HIF1α and HIF2α Expressions in Bone Metastatic Clear Cell Renal Cell Cancer. *Oncotarget* (2016) 7:42086–98. doi:10.18632/oncotarget.9669
17. Aoki M, and Fujishita T. Oncogenic Roles of the PI3K/AKT/mTOR axis. *Curr Top Microbiol Immunol* (2017) 407:153–89. doi:10.1007/82_2017_6
18. Semenza GL. The Hypoxic Tumor Microenvironment: A Driving Force for Breast Cancer Progression. *Biochim Biophys Acta (Bba) - Mol Cel Res* (2016) 1863:382–91. doi:10.1016/j.bbamcr.2015.05.036
19. Tátrai E, Bartal A, Gacs A, Paku S, Kenessey I, Garay T, et al. Cell Type-dependent HIF1 α-mediated Effects of Hypoxia on Proliferation, Migration and Metastatic Potential of Human Tumor Cells. *Oncotarget* (2017) 8:44498–510. doi:10.18632/oncotarget.17806
20. Döme B, Hendrix MJC, Paku S, Tóvári J, and Tímár J. Alternative Vascularization Mechanisms in Cancer. *Am J Pathol* (2007) 170:1–15. doi:10.2353/ajpath.2007.060302
21. Döme B, Tímár J, Dobos J, Mészáros L, Rásó E, Paku S, et al. Identification and Clinical Significance of Circulating Endothelial Progenitor Cells in Human Non-small Cell Lung Cancer. *Cancer Res* (2006) 66:7341–7. doi:10.1158/0008-5472.CAN-05-4654

22. Döme B, Paku S, Somlai B, and Tímár J. Vascularization of Cutaneous Melanoma Involves Vessel Co-option and Has Clinical Significance. *J Pathol* (2002) 197:355–62. doi:10.1002/path.1124
23. Bridgeman VL, Vermeulen PB, Foo S, Bilecz A, Daley F, Kostaras E, et al. Vessel Co-option Is Common in Human Lung Metastases and Mediates Resistance to Anti-angiogenic Therapy in Preclinical Lung Metastasis Models. *J Pathol* (2017) 241:362–74. doi:10.1002/path.4845
24. Dezső K, Bugyik E, Papp V, László V, Döme B, Tóvári J, et al. Development of Arterial Blood Supply in Experimental Liver Metastases. *Am J Pathol* (2009) 175:835–43. doi:10.2353/ajpath.2009.090095
25. Szabó V, Bugyik E, Dezso K, Ecker N, Nagy P, Tímár J, et al. Mechanism of Tumour Vascularization in Experimental Lung Metastases. *J Pathol* (2015) 235:384–96. doi:10.1002/path.4464
26. Döme B, Tımár J, and Paku S. A Novel Concept of Glomeruloid Body Formation in Experimental Cerebral Metastases. *J Neuropathol Exp Neurol* (2003) 62:655–61. doi:10.1093/jnen/62.6.655
27. Inan S, and Hayran M. Cell Signaling Pathways Related to Epithelial Mesenchymal Transition in Cancer Metastasis. *Crit Rev Oncog* (2019) 24: 47–54. doi:10.1615/CritRevOncog.2018029509
28. Tímár J, Tóvári J, Rásó E, Mészáros L, Bereczky B, and Lapis K. Platelet-mimicry of Cancer Cells: Epiphenomenon with Clinical Significance. *Oncology* (2005) 69:185–201. doi:10.1159/000088069
29. Manoitis AJ, Folberg R, Hess A, Seftor EA, Gardner LMG, Pe'er J, et al. Vascular Channel Formation by Human Melanoma Cells: Role in Vasculogenic Mimicry. *Am J Pathol* (1999) 155:739–52. doi:10.1016/S0002-9440(10)65173-5
30. Tímár J, and Tóth J. Tumor Sinuses - Vascular Channels. *Pathol Oncol Res* (2000) 6:83–6. doi:10.1007/BF03032354
31. Hendrix MJC, Seftor EA, Hess AR, and Seftor REB. Vasculogenic Mimicry and Tumour-Cell Plasticity: Lessons from Melanoma. *Nat Rev Cancer* (2003) 3:411–21. doi:10.1038/nrc1092
32. Lőrincz T, Tímár J, and Szendrői M. Alterations of Microvascular Density in Bone Metastases of Adenocarcinomas. *Pathol Oncol Res* (2004) 10:149–53. doi:10.1007/BF03033743
33. Gilreath JA, Stenehjem DD, and Rodgers GM. Diagnosis and Treatment of Cancer-Related Anemia. *Am J Hematol* (2014) 89:203–12. doi:10.1002/ajh.23628
34. Parks SK, Cormerais Y, and Pouysségur J. Hypoxia and Cellular Metabolism in Tumour Pathophysiology. *J Physiol* (2017) 595:2439–50. doi:10.1113/JP273309
35. Robey IF, Lien AD, Welsh SJ, Baggett BK, and Gillies RJ. Hypoxia-Inducible Factor-1α and the Glycolytic Phenotype in Tumors. *Neoplasia* (2005) 7: 324–30. doi:10.1593/neo.04430
36. Faubert B, Solmonson A, and DeBerardinis RJ. Metabolic Reprogramming and Cancer Progression. *Science* (2020) 368:eaaw5473. doi:10.1126/science.aaw5473
37. Yoshida GJ. Metabolic Reprogramming: the Emerging Concept and Associated Therapeutic Strategies. *J Exp Clin Cancer Res* (2015) 34:11. doi:10.1186/s13046-015-0221-y
38. Danhier P, Bański P, Payen VL, Grasso D, Ippolito L, Sonveaux P, et al. Cancer Metabolism in Space and Time: Beyond the Warburg Effect. *Biochim Biophys Acta (Bba) - Bioenerg* (2017) 1858:556–72. doi:10.1016/j.bbabio.2017.02.001
39. Moldogazieva NT, Mokhosoev IM, and Terentiev AA. Metabolic Heterogeneity of Cancer Cells: An Interplay between HIF-1, GLUTs, and AMPK. *Cancers* (2020) 12:862. doi:10.3390/cancers12040862
40. Sarkadi B, Mészáros K, Krencz I, Canu L, Krokker L, Zakariás S, et al. Glutaminases as a Novel Target for SDHB-Associated Pheochromocytomas/Paragangliomas. *Cancers* (2020) 12:599. doi:10.3390/cancers12030599
41. Payen VL, Zampieri LX, Porporato PE, and Sonveaux P. Pro- and Antitumor Effects of Mitochondrial Reactive Oxygen Species. *Cancer Metastasis Rev* (2019) 38:189–203. doi:10.1007/s10555-019-09789-2
42. Liu GY, and Sabatini DM. mTOR at the Nexus of Nutrition, Growth, Ageing and Disease. *Nat Rev Mol Cel Biol* (2020) 21(4):183–203. doi:10.1038/s41580-019-0199-y
43. He L, Gomes AP, Wang X, Yoon SO, Lee G, Nagiec MJ, et al. mTORC1 Promotes Metabolic Reprogramming by the Suppression of GSK3-dependent Foxk1 Phosphorylation. *Mol Cel* (2018) 70(5):949–60. doi:10.1016/j.molcel.2018.04.024
44. Li W, Petrimpol M, Molle KD, Hall MN, Battegay EJ, and Humar R. Hypoxia-induced Endothelial Proliferation Requires Both mTORC1 and mTORC2. *Circ Res* (2007) 100(1):79–87. doi:10.1161/01.RES.0000253094.03023.3f
45. Daskalaki I, Gkikas I, and Tavernarakis N. Hypoxia and Selective Autophagy in Cancer Development and Therapy. *Front Cel Dev. Biol.* (2018) 6:104. doi:10.3389/fcell.2018.00104
46. Mutvei AP, Nagiec MJ, Hamann JC, Kim SG, Vincent CT, and Blenis J. Rap1-GTPases Control mTORC1 Activity by Coordinating Lysosome Organization with Amino Acid Availability. *Nat Commun* (2020) 11(1): 1416. doi:10.1038/s41467-020-15156-5
47. Parks SK, and Pouysségur J. Targeting pH Regulating Proteins for Cancer Therapy-Progress and Limitations. *Semin Cancer Biol* (2017) 43:66–73. doi:10.1016/j.semcancer.2017.01.007
48. Li S, Topatana W, Juengpanich S, Cao J, Hu J, Zhang B, et al. Development of Synthetic Lethality in Cancer: Molecular and Cellular Classification. *Sig Transduct Target Ther* (2020) 5(1):241. doi:10.1038/s41392-020-00358-6
49. Díaz-Bulnes P, Saiz ML, López-Larrea C, and Rodríguez RM. Crosstalk between Hypoxia and ER Stress Response: a Key Regulator of Macrophage Polarization. *Front Immunol* (2020) 10:2951. doi:10.3389/fimmu.2019.02951
50. Vetsika E-K, Koukos A, and Kotsakis A. Myeloid-Derived Suppressor Cells: Major Figures that Shape the Immunosuppressive and Angiogenic Network in Cancer. *Cells* (2019) 8:1647. doi:10.3390/cells8121647
51. Taylor CT, and Colgan SP. Regulation of Immunity and Inflammation by Hypoxia in Immunological Niches. Nat Rev *Immunol* (2017) 17:774–85. doi:10.1038/nri.2017.103
52. Kaur S, Chang T, Singh SP, Lim L, Mannan P, Garfield SH, et al. CD47 Signaling Regulates the Immunosuppressive Activity of VEGF in T Cells. *J.I.* (2014) 193:3914–24. doi:10.4049/jimmunol.1303116
53. Petrova V, Annicchiarico-Petruzzelli M, Melino G, and Amelio I. The Hypoxic Tumour Microenvironment. *Oncogenesis* (2018) 7:10. doi:10.1038/s41389-017-0011-9
54. Reiniger L, Téglási V, Pipek O, Rojkó L, Glasz T, Vágvölgyi A, et al. Tumor Necrosis Correlates with PD-L1 and PD-1 Expression in Lung Adenocarcinoma. *Acta Oncologica* (2019) 58:1087–94. doi:10.1080/0284186X.2019.1598575
55. Kiss J, Tímár J, Somlai B, Gilde K, Fejős Z, Gaudi I, et al. Association of Microvessel Density with Infiltrating Cells in Human Cutaneous Malignant Melanoma. *Pathol Oncol Res* (2007) 13:21–31. doi:10.1007/BF02893437
56. Serganova I, Humm J, Ling C, and Blasberg R. Tumor Hypoxia Imaging: Fig. 1. *Clin Cancer Res* (2006) 12:5260–4. doi:10.1158/1078-0432.CCR-06-0517
57. Krohn KA, Link JM, and Mason RP. Molecular Imaging of Hypoxia. *J Nucl Med* (2008) 49:129S–148S. doi:10.2967/jnumed.107.045914
58. Scotto KW. Transcriptional Regulation of ABC Drug Transporters. *Oncogene* (2003) 22:7496–511. doi:10.1038/sj.onc.1206950
59. Jin X, Gong L, Peng Y, Li L, and Liu G. Enhancer-bound Nrf2 Licenses HIF-1α Transcription under Hypoxia to Promote Cisplatin Resistance in Hepatocellular Carcinoma Cells. *Aging* (2020) 13:364–75. doi:10.18632/aging.202137
60. Belisario DC, Kopecka J, Pasino M, Akman M, De Smaele E, Donadelli M, et al. Hypoxia Dictates Metabolic Rewiring of Tumors: Implications for Chemoresistance. *Cells* (2020) 9:2598. doi:10.3390/cells9122598
61. Cosse J-P, and Michiels C. Tumour Hypoxia Affects the Responsiveness of Cancer Cells to Chemotherapy and Promotes Cancer Progression. *Acamc* (2008) 8:790–7. doi:10.2174/187152008785914798
62. Koshinani HM, Afshar S, and Najafi R. Hypoxia: a Double-Edged Sword in Cancer Therapy. *Cancer Invest* (2016) 34:536–45. doi:10.1080/07357907.2016.1245317
63. Aebersold DM, Burri P, Beer KT, Laissue J, Djonov V, Greiner RH, et al. Expression of Hypoxia Inducible Factor-Alpha: a Novel Predictive, Prognostic Parameter in the Radiotherapy of Oropharyngeal Cancer. *Cancer Res* (2001) 61:2911–6.
64. Lövey J, Lukits J, Remenár E, Koronczay K, Kásler M, Németh G, et al. Antiangiogenic Effects of Radiotherapy but Not Initial Microvessel Density

Predict Survival in Inoperable Oropharyngeal Squamous Cell Carcinoma. *Strahlenther Onkol* (2006) 182:149–56. doi:10.1007/s00066-006-1447-6
65. Jászai J, and Schmidt M. Trends and Challenges in Tumor Anti-angiogenic Therapies. *Cells* (2019) 8:1102. doi:10.3390/cells8091102
66. Garcia J, Hurwitz HI, Sandler AB, Miles D, Coleman RL, Deurloo R, et al. Bevacizumab (Avastin) in Cancer Treatment: A Review of 15 Years of Clinical Experience and Future Outlook. *Cancer Treat Rev*. (2020). 86. p. 102017. doi:10.1016/j.ctrv.2020.102017
67. Martin JD, Seano G, and Jain RK. Normalizing Function of Tumor Vessels: Progress, Opportunities, and Challenges. *Annu Rev Physiol* (2019) 81:505–34. doi:10.1146/annurev-physiol-020518-114700
68. Chen Z, Wei J, Ma X, and Yu J. Efficacy of EGFR-TKIs with or without Angiogenesis Inhibitors in Advanced Non-small-cell Lung Cancer: A Systematic Review and Meta-Analysis. *J Cancer* (2020) 11:686–95. doi:10.7150/jca.34957
69. Sun D-c., Shi Y, Wang Y-r., Lv Y, Yan H, Mao H, et al. KRAS Mutation and Primary Tumor Location Do Not Affect Efficacy of Bevacizumab-Containing Chemotherapy in Stagae IV Colorectal Cancer Patients. *Sci Rep* (2017) 7:14368. doi:10.1038/s41598-017-14669-2
70. Ghimessy AK, Gellért A, Schlegl E, Hegedüs B, Rásó E, Barbai T, et al. KRAS Mutations Predict Response and Outcome in Advanced Lung Adenocarcinoma Patients Receiving First-Line Bevacizumab and Platinum-Based Chemotherapy. *Cancers* (2019) 11:1514. doi:10.3390/cancers11101514
71. Haibe Y, Kreidieh M, El Hajj H, Khalifeh I, Mukherji D, Temraz S, et al. Resistance Mechanisms to Anti-angiogenic Therapies in Cancer. *Front Oncol* (2020) 10:221. doi:10.3389/fonc.2020.00221
72. Uribesalgo I, Hoffmann D, Zhang Y, Kavirayani A, Lazovic J, Berta J, et al. Apelin Inhibition Prevents Resistance and Metastasis Associated with Anti-angiogenic Therapy. *EMBO Mol Med* (2019) 11:e9266. doi:10.15252/emmm.201809266
73. Török S, Rezeli M, Kelemen O, Végvári A, Watanabe K, Sugihara Y, et al. Limited Tumor Tissue Drug Penetration Contributes to Primary Resistance against Angiogenesis Inhibitors. *Theranostics* (2017) 7:400–12. doi:10.7150/thno.16767
74. Fukumura D, Kloepper J, Amoozgar Z, Duda DG, and Jain RK. Enhancing Cancer Immunotherapy Using Antiangiogenics: Opportunities and Challenges. *Nat Rev Clin Oncol* (2018) 15:325–40. doi:10.1038/nrclinonc.2018.29
75. Rassy E, Flippot R, and Albiges L. Tyrosine Kinase Inhibitors and Immunotherapy Combinations in Renal Cell Carcinoma. *Ther Adv Med Oncol* (2020) 12:175883592090750. doi:10.1177/1758835920907504
76. Gubens MA, and Davies M. NCCN Guidelines Updates: New Immunotherapy Strategies for Improving Outcomes in Non-small Cell Lung Cancer. *J Natl Compr Canc Netw* (2019) 17:574–8. doi:10.6004/jnccn.2019.5005
77. Hilmi M, Neuzillet C, Calderaro J, Lafdil F, Pawlotsky J-M, and Rousseau B. Angiogenesis and Immune Checkpoint Inhibitors as Therapies for Hepatocellular Carcinoma: Current Knowledge and Future Research Directions. *J Immunotherapy Cancer* (2019) 7:333. doi:10.1186/s40425-019-0824-5
78. Gaspar BL, Sharma P, and Das R. Anemia in Malignancies: Pathogenetic and Diagnostic Considerations. *Hematology* (2015) 20:18–25. doi:10.1179/1607845414Y.0000000161
79. Bohlius J, Bohlke K, Castelli R, Djulbegovic B, Lustberg MB, Martino M, et al. Management of Cancer-Associated Anemia with Erythropoiesis-Stimulating Agents: ASCO/ASH Clinical Practice Guideline Update. *Jco* (2019) 37:1336–51. doi:10.1200/JCO.18.02142
80. Tóvári J, Gilly R, Rásó E, Paku S, Bereczky B, Varga N, et al. Recombinant Human Erythropoietin α Targets Intratumoral Blood Vessels, Improving Chemotherapy in Human Xenograft Models. *Cancer Res* (2005) 65:7186–93. doi:10.1158/0008-5472.CAN-04-2498
81. Lövey J, Bereczky B, Gilly R, Kenessey I, Rásó E, Simon E, et al. Recombinant Human Erythropoietin Alpha Improves the Efficacy of Radiotherapy of a Human Tumor Xenograft, Affecting Tumor Cells and Microvessels. *Strahlenther Onkol* (2008) 184:1–7. doi:10.1007/s00066-008-1745-2
82. Zou Z, Tao T, Li H, and Zhu X. mTOR Signaling Pathway and mTOR Inhibitors in Cancer: Progress and Challenges. *Cell Biosci* (2020) 10:31. doi:10.1186/s13578-020-00396-1
83. Karakhasev S, and Reginato MJ. Progress toward Overcoming Hypoxia-Induced Resistance to Solid Tumor Therapy. *Cancer Management Res* (2015) 7:253–64. doi:10.2147/CMAR.S58285
84. Burián Z, Ladányi A, Barbai T, Piurkó V, Garay T, Rásó E, et al. Selective Inhibition of HIF1α Expression by ZnSO4 Has Antitumoral Effects in Human Melanoma. *Pathol Oncol Res* (2020) 26:673–9. doi:10.1007/s12253-018-00573-1
85. Mabjeesh NJ, Escuin D, LaVallee TM, Pribluda VS, Swartz GM, Johnson MS, et al. 2ME2 Inhibits Tumor Growth and Angiogenesis by Disrupting Microtubules and Dysregulating HIF. *Cancer Cell* (2003) 3:363–75. doi:10.1016/s1535-6108(03)00077-1
86. Modi S, Stopeck A, Linden H, Solit D, Chandarlapaty S, Rosen N, et al. HSP90 Inhibition Is Effective in Breast Cancer: A Phase II Trial of Tanespimycin (17-AAG) Plus Trastuzumab in Patients with HER2-Positive Metastatic Breast Cancer Progressing on Trastuzumab. *Clin Cancer Res* (2011) 17:5132–9. doi:10.1158/1078-0432.CCR-11-0072
87. Kong D, Park EJ, Stephen AG, Calvani M, Cardellina JH, Monks A, et al. Echinomycin, a Small-Molecule Inhibitor of Hypoxia-Inducible Factor-1 DNA-Binding Activity. *Cancer Res* (2005) 65:9047–55. doi:10.1158/0008-5472.CAN-05-1235
88. Yeo E-J, Chun Y-S, Cho Y-S, Kim J, Lee J-C, Kim M-S, et al. YC-1: A Potential Anticancer Drug Targeting Hypoxia-Inducible Factor 1. *JNCI J Natl Cancer Inst* (2003) 95:516–25. doi:10.1093/jnci/95.7.516
89. Courtney KD, Infante JR, Lam ET, Figlin RA, Rini BI, Brugarolas J, et al. Phase I Dose-Escalation Trial of PT2385, a First-In-Class Hypoxia-Inducible Factor-2α Antagonist in Patients with Previously Treated Advanced Clear Cell Renal Cell Carcinoma Antagonist in Patients with Previously Treated Advanced Clear Cell Renal Cell Carcinoma. *Jco* (2018) 36:867–74. doi:10.1200/JCO.2017.74.2627
90. Jonasch E, Donskov F, Iliopoulos O, Rathmell WK, Narayan V, Maughan BL, et al. Phase II Study of the Oral HIF-2α Inhibitor MK-6482 for Von Hippel-Lindau Disease-Associated Renal Cell Carcinoma. *Jco* (2020) 38:5003. doi:10.1200/JCO.2020.38.15_suppl.5003
91. Overgaard J. Hypoxic Modification of Radiotherapy in Squamous Cell Carcinoma of the Head and Neck - A Systematic Review and Meta-Analysis. *Radiother Oncol* (2011) 100:22–32. doi:10.1016/j.radonc.2011.03.004
92. Janssen GO, Rademakers SE, Terhaard CH, Doornaert PA, Bijl HP, van der Ende P, et al. Accelerated Radiotherapy with Carbogen and Nicotinamide for Laryngeal Cancer: Results of a Phase III Randomized Trial. *J Clin Oncol* (2012) 30:1777–83. doi:10.1200/JCO.2011.35.9315
93. Thompson D, Yang H, Baines H, Miles E, Bolton S, West C, et al. NIMRAD - a Phase III Trial to Investigate the Use of Nimorazole Hypoxia Modification with Intensity-Modulated Radiotherapy in Head and Neck Cancer. *Clin Oncol (R Coll Radiol* (2014) 26:344–7. doi:10.1016/j.clon.2014.03.003
94. Barker HE, Paget JTE, Khan AA, and Harrington KJ. The Tumour Microenvironment after Radiotherapy: Mechanisms of Resistance and Recurrence. *Nat Rev Cancer* (2015) 15:409–25. doi:10.1038/nrc3958
95. Jiménez-Valerio G, and Casanovas O. Angiogenesis and Metabolism: Entwined for Therapy Resistance. *Trends Cancer* (2017) 3:10–8. doi:10.1016/j.trecan.2016.11.007
96. Peiris-Pagès M, Martinez-Outschoorn UE, Pestell RG, Sotgia F, and Lisanti MP. Cancer Stem Cell Metabolism. *Breast Cancer Res* (2016) 18:55. doi:10.1186/s13058-016-0712-6
97. Liang L, Hui K, Hu C, Wen Y, Yang S, Zhu P, et al. Autophagy Inhibition Potentiates the Anti-angiogenic Property of Multikinase Inhibitor Anlotinib through JAK2/STAT3/VEGFA Signaling in Non-small Cell Lung Cancer Cells. *J Exp Clin Cancer Res* (2019) 38:71. doi:10.1186/s13046-019-1093-3
98. AllenMiéville EP, Miéville P, Warren CM, Saghafinia S, Li L, Peng M-W, et al. Metabolic Symbiosis Enables Adaptive Resistance to Anti-angiogenic Therapy that Is Dependent on mTOR Signaling. *Cel Rep* (2016) 15:1144–60. doi:10.1016/j.celrep.2016.04.029
99. Vallet S, Pahernik S, Höfner T, Tosev G, Hadaschik B, Duensing S, et al. Efficacy of Targeted Treatment beyond Third-Line Therapy in Metastatic Kidney Cancer: Retrospective Analysis from a Large-Volume Cancer Center.

Clin Genitourinary Cancer (2015) 13(3):e145–e152. doi:10.1016/j.clgc.2014.12.012

100. Wick W, Platten M, Wick A, Hertenstein A, Radbruch A, Bendszus M, et al. Current Status and Future Directions of Anti-angiogenic Therapy for Gliomas. *Neuro Oncol* (2016) 18(3):315–28. doi:10.1093/neuonc/nov180
101. Galdy S, Cella CA, Spada F, Murgioni S, Frezza AM, Ravenda SP, et al. Systemic Therapy beyond First-Line in Advanced Gastric Cancer: An Overview of the Main Randomized Clinical Trials. *Crit Rev Oncology/Hematology* (2016) 99:1–12. doi:10.1016/j.critrevonc.2015.09.004
102. Grozinsky-Glasberg S, Lines KE, Avniel-Polak S, Bountra C, and Thakker RV. Preclinical Drug Studies in MEN1-Related Neuroendocrine Neoplasms (MEN1-NENs). *Endocr Relat Cancer* (2020) 27(9):R345–R355. doi:10.1530/ERC-20-0127
103. Yoshida GJ. The Harmonious Interplay of Amino Acid and Monocarboxylate Transporters Induces the Robustness of Cancer Cells. *Metabolites* (2021) 11(1):27. doi:10.3390/metabo11010027
104. Benej M, Svastova E, Banova R, Kopacek J, Gibadulinova A, Kery M, et al. CA IX Stabilizes Intracellular pH to Maintain Metabolic Reprogramming and Proliferation in Hypoxia. *Front Oncol* (2020) 10:1462. doi:10.3389/fonc.2020.01462
105. Marrone KA, Zhou X, Forde PM, Purtell M, Brahmer JR, Hann CL, et al. A Randomized Phase II Study of Metformin Plus Paclitaxel/Carboplatin/Bevacizumab in Patients with Chemotherapy-Naïve Advanced or Metastatic Nonsquamous Non-Small Cell Lung Cancer. *Oncol* (2018) 23:859–65. doi:10.1634/theoncologist.2017-0465
106. Markowska A, Sajdak S, Markowska J, and Huczyński A. Angiogenesis and Cancer Stem Cells: New Perspectives on Therapy of Ovarian Cancer. *Eur J Med Chem* (2017) 142:87–94. doi:10.1016/j.ejmech.2017.06.030
107. Petővári G, Dankó T, Krencz I, Hujber Z, Rajnai H, Vetlényi E, et al. Inhibition of Metabolic Shift Can Decrease Therapy Resistance in Human High-Grade Glioma Cells. *Pathol Oncol Res* (2020) 26:23–33. doi:10.1007/s12253-019-00677-2
108. Felkai L, Krencz I, Kiss DJ, Nagy N, Petővári G, Dankó T, et al. Characterization of mTOR Activity and Metabolic Profile in Pediatric Rhabdomyosarcoma. *Cancers* (2020) 12:1947. doi:10.3390/cancers12071947
109. Petővári G, Dankó T, Tőkés AM, Vetlényi E, Krencz I, Raffay R, et al. *In situ* metabolic Characterisation of Breast Cancer and its Potential Impact on Therapy. *Cancers* (2020) 9:2492. doi:10.3390/cancers12092492
110. Rotundo MS, Galeano T, Tassone P, and Tagliaferri P. mTOR Inhibitors, a New Era for Metastatic Luminal HER2-Negative Breast Cancer? A Systematic Review and a Meta-Analysis of Randomized Trials. *Oncotarget* (2016) 7(19):27055–66. doi:10.18632/oncotarget.7446
111. Wu K, Sun XQ, Wang CQ, Gao TX, Sun P, Wang Y, et al. Metronomic Combination Chemotherapy Using Everolimus and Etoposide for the Treatment of non-Hodgkin Lymphoma. *Cancer Med* (2019) 8(10):4688–98. doi:10.1002/cam4.2364
112. Hue-Fontaine L, Lemelin A, Forestier J, Raverot G, Milot L, Robinson P, et al. Metformin and Everolimus in Neuroendocrine Tumours: A Synergic Effect?. *Clin Res Hepatol Gastroenterol* (2020) 44(6):954–60. doi:10.1016/j.clinre.2020.02.011
113. Ariaans G, Jalving M, Vries EGEd., and Jong Sd. Anti-tumor Effects of Everolimus and Metformin Are Complementary and Glucose-dependent in Breast Cancer Cells. *BMC Cancer* (2017) 17(1):232. doi:10.1186/s12885-017-3230-8
114. Moore EC, Cash HA, Caruso AM, Uppaluri R, Hodge JW, Van Waes C, et al. Enhanced Tumor Control with Combination mTOR and PD-L1 Inhibition in Syngeneic Oral Cavity Cancers. *Cancer Immunol Res* (2016) 4(7):611–20. doi:10.1158/2326-6066.CIR-15-0252
115. Ramesh A, Natarajan SK, Nandi D, and Kulkarni A. Dual Inhibitors-Loaded Nanotherapeutics that Target Kinase Signaling Pathways Synergize with Immune Checkpoint Inhibitor. *Cel Mol Bioeng* (2019) 12(5):357–73. doi:10.1007/s12195-019-00576-1

Pathology & Oncology Research

frontiers

ORIGINAL RESEARCH
published: 03 May 2021
doi: 10.3389/pore.2021.643146

Cell Cycle Regulatory Protein Expression in Multinucleated Giant Cells of Giant Cell Tumor of Bone: do They Proliferate?

*Mate E. Maros[1,2,3], Peter Balla[1], Tamas Micsik[1], Zoltan Sapi[1], Miklos Szendroi[4], Holger Wenz[3], Christoph Groden[3], Ramses G. Forsyth[5], Piero Picci[6] and Tibor Krenacs[1]**

[1]1st Department of Pathology and Experimental Cancer Research, Semmelweis University, Budapest, Hungary, [2]Department of Biomedical Informatics at the Center for Preventive Medicine and Digital Health, Mannheim, Germany, [3]Department of Neuroradiology, Medical Faculty Mannheim, University of Heidelberg, Mannheim, Germany, [4]Department of Orthopedics, Semmelweis University, Budapest, Hungary, [5]Department of Anatomic Pathology and Experimental Pathology, University Ziekenhuis, Brussels, Belgium, [6]Laboratory of Experimental Oncology, Istituto Ortopedico Rizzoli, Bologna, Italy

Cells of the monocyte macrophage lineage form multinucleated giant cells (GCs) by fusion, which may express some cell cycle markers. By using a comprehensive marker set, here we looked for potential replication activities in GCs, and investigated whether these have diagnostic or clinical relevance in giant cell tumor of bone (GCTB). GC rich regions of 10 primary and 10 first recurrence GCTB cases were tested using immunohistochemistry in tissue microarrays. The nuclear positivity rate of the general proliferation marker, replication licensing, G1/S-phase, S/G2/M-phase, mitosis promoter, and cyclin dependent kinase (CDK) inhibitor reactions was analyzed in GCs. Concerning Ki67, moderate SP6 reaction was seen in many GC nuclei, while B56 and Mib1 positivity was rare, but the latter could be linked to more aggressive (p = 0.012) phenotype. Regular MCM6 reaction, as opposed to uncommon MCM2, suggested an initial DNA unwinding. Early replication course in GCs was also supported by widely detecting CDK4 and cyclin E, for the first time, and confirming cyclin D1 upregulation. However, post-G1-phase markers CDK2, cyclin A, geminin, topoisomerase-2a, aurora kinase A, and phospho-histone H3 were rare or missing. These were likely silenced by upregulated CDK inhibitors $p15^{INK4b}$, $p16^{INK4a}$, $p27^{KIP1}$, p53 through its effector $p21^{WAF1}$ and possibly cyclin G1, consistent with the prevention of DNA replication. In conclusion, the upregulation of known and several novel cell cycle progression markers detected here clearly verify early replication activities in GCs, which are controlled by cell cycle arresting CDK inhibitors at G1 phase, and support the functional maturation of GCs in GCTB.

Keywords: giant cell tumor of bone, giant cells, Ki-67, cyclin D1, p53, p21 (CDKN1A) WAF1, cyclin G1

OPEN ACCESS

Edited by:
Anna Sebestyén, Semmelweis University, Hungary

****Correspondence:***
Tibor Krenacs
krenacst@gmail.com

Received: *17 December 2020*
Accepted: *01 April 2021*
Published: *03 May 2021*

Citation:
Maros ME, Balla P, Micsik T, Sapi Z, Szendroi M, Wenz H, Groden C, Forsyth RG, Picci P and Krenacs T (2021) Cell Cycle Regulatory Protein Expression in Multinucleated Giant Cells of Giant Cell Tumor of Bone: do They Proliferate?. Pathol. Oncol. Res. 27:643146. doi: 10.3389/pore.2021.643146

INTRODUCTION

There are two major ways of forming multinucleate giant cells i.e. acytokinetic cell division and cell fusion [1]. Proliferating neoplastic cells, e.g. Reed-Sternberg cells in Hodgkin's lymphoma or multinucleated tumor cells in soft tissue, e.g. myxofibro- and osteosarcomas are resulted from incomplete cell division as a result of their cytoskeleton vulnerability e.g. of the contractile ring [2].

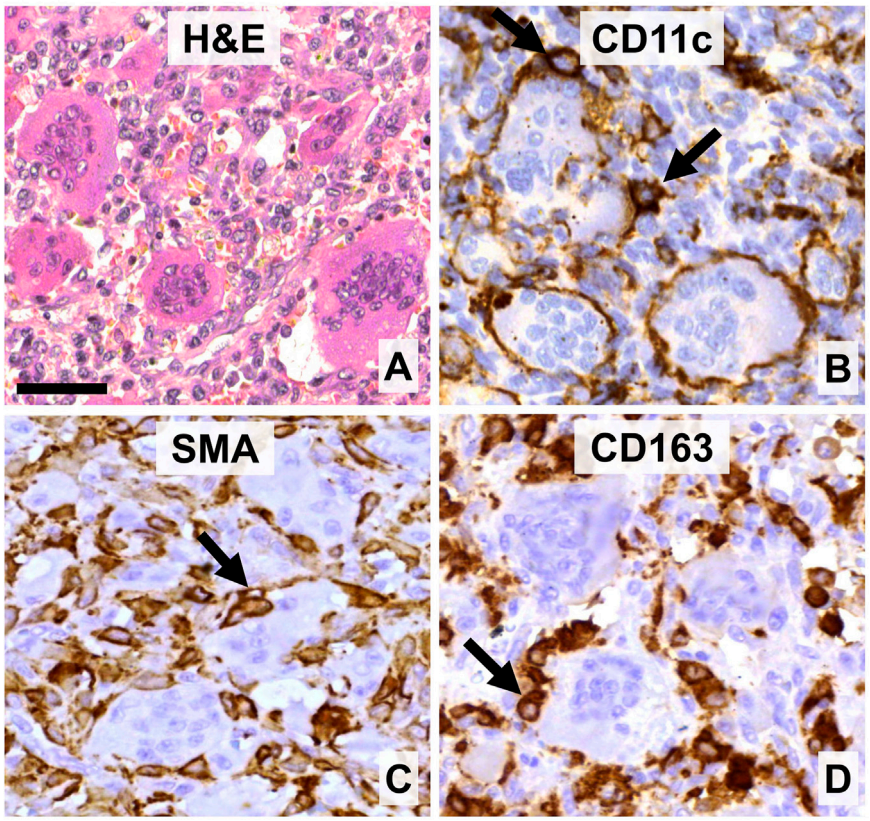

FIGURE 1 | The main cell components of giant cell tumor of bone. **(A)** Multinucleated giant cells (GCs) of different sizes are intermingled with mononuclear and red blood cells (hematoxylin-eosin staining, **(**H&E**)**. **(B)** GCs and their monocytic precursors are positive for CD11c. **(C)** Neoplastic stromal cells can be positive for smooth muscle actin (SMA). **(D)** Histiocytes and monocytic GC precursors but not GCs express CD163 scavenger receptor. Arrows show immunopositive cells intimate association with GCs. DAB (brown) immunoperoxidase reactions **(B–D)**. Scale bar: 50 μm for all images.

On the contrary, inflammatory multinucleated giant cells (GC), such as osteoclast-type giant cells, Langhans-type granuloma giant cells and foreign body giant cells are formed by fusion of cells of the monocyte-macrophage lineage [3].

By testing the expression of cell cycle phase progression associated markers in the mononuclear cells of GCTB, we recently showed that cases with elevated post-G1-phase cell fraction, indicating accelerated cell cycle progression, may predict shorter progression free survival (PFS) [4]. We also recognized that GC nuclei may show diverse proportion of immunoreactions not only for the earlier detected cyclin D and $p21^{WAF1}$ [5, 6], and cell cycle control proteins, but also for some cell cycle licensing and promoter markers, which had not been noticed before, despite GCs are considered to be of reactive, osteoclastic phenotype [7]. Therefore, here we studied the expression of a comprehensive set of cell cycle regulatory proteins to see if GCs in GCTB are still show replicative activity and if it has a clinico-pathological relevance.

GCTB is an osteolytic, locally destructive bone lesion, which, besides GCs, is made up mainly of mononuclear monocytic cells which act as precursors for GCs, and of neoplastic stromal cells (**Figure 1**). The proliferating, neoplastic stromal cells, generally carrying H3F3A G34W mutation [8], are the major drivers of osteoclastogenesis and pathological bone resorption [9, 10]. They produce canonical (RANKL/M-CSF) and non-canonical (e.g., LIGHT, TNFα, IL-6 or vascular endothelial growth factor–VEGF) growth factors and hypoxia inducible factors 1α and 2α [14], which can either directly or through autocrine activation promote osteoclastogenesis and osteolysis [11, 12]. We have shown earlier that besides the replication activity of neoplastic stromal cells, their elevated epidermal growth factor receptor (EGFR) signaling and deregulated gap junction connexin43 expression and channel functions, can contribute to GCTB progression, mediated by GCs [4, 13, 14].

In the present study, we tested the expression of cell cycle regulatory proteins in GC nuclei, including 3 clones for the general proliferation marker Ki67; the DNA replication licensing factors MCM2 and MCM6; the G1-S phase marker cyclin D1 and its complexing partner CDK4/6; the early (CDK2 and cyclin A) and late (topoisomerase 2–TOP2) post-G1 phase markers; and the G2-M-phase markers (aurora kinase A–AURKA, and phospho-histone-H3–pHH3) [15]. Furthermore, the DNA replication inhibitor geminin, the cyclin dependent kinase inhibitors $p15^{INK4b}$, $p16^{INK4a}$, $p21^{WAF1}$ and $p27^{KIP1}$; as well as the oncosuppressor retinoblastoma and p53 [16], and the unpaired

TABLE 1 | Clinicopathological features of the study cohort.

Number of patients	20
Number of surgical cases	20
Progression groups	Nr. Enneking's/Campanacci's grade
Primary	10 L 3 A 5 Ag 2
1st recurrent cases	10 L 2 A 4 Ag 4
Median age (at case diagnosis)	30.8 years (range: 13.7–75.6 years)
Sex (female, %)	13 (65)
Sex ratio	0.54:1 (m/f) or 1:1.85 (f/m)
Survival	
Median recurrence survival	58.1 months (range:5.5–159.5, IQR: 18.9–79.2)
Number of progression events	12
Localization	Total (%)
Upper limb	5 (25)
Lower limb	13 (65)
Central (Sacrum + Spine or Pelvis)	2 (10)
Treatment types	Total (%)
Curettage	12 (60)
Resection or Amputation or Excision	6 (30)
Radiotherapy	2 (10)

GCTB, giant cell tumor of bone; L, latent; A, active; Ag, aggressive; LQ/UQ, lower/upper quartile

cyclin G1 [17, 18] proteins were also examined. We aimed to profile cell cycle activity in GCs and see if it is different between primary and recurrent GCTB.

MATERIALS AND METHODS

Study Cohort

This study was performed on immunostained 2 mm diameter, 70 sample tissue microarray (TMA) sections of formalin-fixed and paraffin-embedded samples of GCTB cases, which were diagnosed between 1994–2005 at the Institute of Rizzoli, Bologna (IOR), Italy (ethical approval: IOR 13351/5-28-2008 and Semmelweis University: 87/2007) [9,10]. A stratified random sample of 10 primary tumors (P) and 10 first recurrences (1-Rec) were selected from our previously published single-center retrospective study [9]. The clinicopathological characteristics of the selected cohort are presented in **Table 1**. Briefly, of the 20 patients, 12 progression events were registered (60%) during follow-up. During the study period 12 progression events were registered. Eight-eight patients (40%) were continuously disease free or had local recurrences respectively, 2 (10%) were alive with disease at last follow-up while malignant transformation and stroke both with consecutive fatal outcomes occurred in 1-1 patients (5%).

Immunohistochemistry

Following routine dewaxing, the antigen retrieval of TMA sections was done in an electric pressure cooker (Avair, Bitalon, Pecs, Hungary) using 0.01 M Tris–0.1 M EDTA (TE) at ~105°C for 30 min. Mouse or rabbit monoclonal primary antibody clones, or rabbit polyclonal immunoglobulins were incubated overnight (16 h) at room temperature. These included anti-Ki67 Mib1 (1:100; Dako, Glostrup, Denmark), B56 (1:100; Histopathology, Pecs, Hungary), SP6 (1:600); anti-MCM2 (CRCT2.1, 1:200) and -MCM6 (1:600, PA5-79649); anti-cyclin D1 (SP4, 1:200), -CDK2 (1:300, 2B6), -CDK4 (1:300, DCS31 + 35), -cyclin E (13A3, 1:20), -cyclin G (11C8, 1:100), -cyclin A (6E6, 1:500), -topoisomerase 2 (Ki-S1, 1:200), -aurora kinase A (1G4, 1:80; Cell Signaling, Danvers, MA, United States), -pHH3Ser10 (K872.3, 1:100); -p53 (DO7, 1:100), -retinoblastoma (1F8, 1:100), -$p15^{INK4b}$ (15P06, 1:200), -$p16^{INK4a}$ (JC8, 1:200), -$p21^{WAF1}$ (SX118, 1:100), and -geminin (EM6, 1:150; Leica-NovoCastra, Newcastle Upon-Tyne, United Kingdom), -p53 (DO7, 1:200, Leica-NovoCastra; and BP53–12, 1:100), and -retinoblastoma (51B7, 1:100) immunoglobulins (IgGs). Except where otherwise indicated, all antibodies were from Thermo-Fisher LabVision (Fremount, CA, United States). Then, the NovoLink polymer peroxidase kit (Leica-NovoCastra) was used as a detection system for 60 min. Immunoreactions were revealed by using DAB Quatro kit (Thermo-Fisher) for 3–5 min under microscopic control and the sections were coverslip mounted after hematoxylin nuclear conterstaining. For double immunofluorescence (C) mouse Ki67 (Mib1, green) and rabbit cyclin D1 (SP4, red) antibodies, were detected simultaneously using Alexa Fluor 488 goat anti-mouse IgG (1:200, green; code: A11001), Alexa Fluor 564 goat anti-rabbit IgG (1:200, red; code: A11035). The immunostained TMA sections were digitalized with the Pannoramic® Scan II System and analyzed using its CaseViewer software (3DHISTECH, Budapest, Hungary).

Evaluation of the Immunoreactions

After setting up and agreeing on the evaluation criteria with the project leader (TK), systematic assessment was done by an independent assessor (MEM) blinded to all clinical- and other cell cycle marker expression data in three different osteoclast/giant cell rich high-power fields (HPF; 80x) in each case (overall ~1000 regions of interest) [4]. All nuclear positivity, which was obvious compared to adjacent negative cells showing only hematoxylin staining, was counted. Additional cytoplasmic staining was considered only for $p16^{INK4a}$ on a four-grade Likert scale (0-negative, 1-weak, 2-moderate, 3-strong). The number of GCs (N_{GC}), GC nuclei (N_{GC_nuclei}) and respective cell cycle marker positive GC nuclei ($N_{GC\_nuclei+}$) were recorded and averaged for each case. To robustly estimate N_{GC} and N_{GC_nuclei} in a surgical specimen, their values were averaged over all tested cell cycle markers for each case, respectively. As $N_{GC\_nuclei+}$ values are dependent on multiple factors e.g. the position of the TMA core within the specimen, N_{GC} and properties of the CC marker, their absolute values showed substantial variances and were not necessarily comparable across different immunostainings. Therefore, we normalized these values by calculating their ratio for each staining ($N_{GC\_nuclei+}/N_{GC\_nuclei}$) to allow for more stable and direct comparisons across cell cycle markers.

Statistical Analyses

All analyses were performed with the R statistics program (v.3.6.3, R Core Team 2020, Vienna Austria; RStudio IDE v.

TABLE 2 | Ratios of cell cycle marker positive GC nuclei in primary and first recurrent GCTB.

Type of material	Marker	Ratio of positive GC nuclei				Statistic (W)	*p*	$p^{\star}_{Bonferroni}$ (n = 14)	p_{adj}
		Median	IQR	min	Max				
P	CDK2	0.031	0.055	0	0.111	72	0.10	0.0036	n.s.
1-Rec	CDK2	0.004	0.012	0	0.078				
P	CDK4	0.325	0.642	0	0.95	28	0.72	0.0036	n.s.
1-Rec	CDK4	0.412	0.193	0.043	0.826				
P	Cyclin A	0	0	0	0	40	0.17	0.0036	n.s.
1-Rec	Cyclin A	0	0	0	0.006				
P	Cyclin D1	0.941	0.13	0.694	0.994	66	0.25	0.0036	n.s.
1-Rec	Cyclin D1	0.874	0.152	0.462	0.981				
P	Cyclin G1	1	0.018	0.868	1	21	0.091	0.0036	n.s.
1-Rec	Cyclin G1	0.956	0.053	0.333	0.967				
P	Geminin	0	0	0	0.005	3	**0.045**	0.0036	n.s
1-Rec	Geminin	0.015	0.017	0	0.061				
P	Ki67 B56	0.027	0.045	0	0.096	22	0.32	0.0036	n.s.
1-Rec	Ki67 B56	0.047	0.017	0.007	0.118				
P	Ki67 Mib1	0	0.012	0	0.048	17	**0.012**	0.0036	n.s.
1-Rec	Ki67 Mib1	0.034	0.039	0	0.172				
P	Ki67 SP6	0.955	0.054	0	1	13	1	0.0036	n.s.
1-Rec	Ki67 SP6	0.75	0.958	0.012	1				
P	MCM2	0.021	0.072	0	0.118	13.5	0.52	0.0036	n.s.
1-Rec	MCM2	0.051	0.158	0	0.225				
P	MCM6	0.5	0.544	0.174	1	20	0.15	0.0036	n.s.
1-Rec	MCM6	0.209	0.265	0.061	0.438				
P	$p15^{INK4b}$	0.773	0.162	0.447	0.967	13	1	0.0036	n.s
1-Rec	$p15^{INK4b}$	0.884	0.942	0	1				
P	$p16^{INK4a}$	0.032	0.045	0	0.233	10	0.69	0.0036	n.s.
1-Rec	$p16^{INK4a}$	0.026	0.312	0.009	1				
P	$p21^{WAF1}$	0.818	0.162	0.264	1	32	0.31	0.0036	n.s.
1-Rec	$p21^{WAF1}$	0.902	0.082	0.392	1				

Bold p-values for geminin and Ki67 Mib1 indicate non-adjusted statistical significance.

1.2.5033, Boston, MA, United States). Non-normally distributed variables were displayed as median, range and interquartile range (IQR). Categorical variables were reported as proportions. The Jonckheere–Terpstra test was used to investigate the overall difference between Enneking's/Campanacci's grading (i.e. latent, active and aggressive), GC count and GC nuclear positivity. We used the nonparametric Wilcoxon-Mann-Whitney *U* test for two samples comparing the mean rank of N_{GC}, N_{GC_nuclei}, and $N_{GC\_nuclei+}$ as well as their ratios between primary and recurrent samples [19]. Uni- and multivariate Cox proportional hazards models of time-to-first-event analyses were performed to explore possible associations between $N_{GC\_nuclei+}$ and progression free survival (PFS) [4]. Figures were generated with the ggplot2 library using colorblind-friendly palettes. *p*-values were adjusted for multiple testing to counteract type 1 error inflation using the conservative Bonferroni correction. Adjusted *p*-values ($p^{\star}$) <0.05 were considered significant.

RESULTS

General Proliferation Markers in Giant Cells

Based on the potential importance of GC functions in GCTB progression, which may be linked to proliferation, first we counted the number and nuclear density of GCs. Though, neither the overall average GC number (N_{GC}; W = 59, p = 0.53) nor the average number of GC nuclei (N_{GC_nuclei}; W = 49, p = 0.97) showed statistical difference between P and 1-Rec GCTB cases, there was a trend of inverse relationship between the radiological grade (latent: L; active: A; aggressive: Ag) of GCTB and the overall average N_{GC} ($W_{L\_vs\_Ag}$ = 30, $p_{L\_vs\_Ag}$ = 0.065; $W_{A\_vs\_Ag}$ = 37, $p_{A\_vs\_Ag}$ = 0.11) and N_{GC_nuclei} ($W_{L\_vs\_A}$ = 29, $p_{L\_vs\_A}$ = 0.093). The distribution of the ratio of cell cycle marker positive GC nuclei in primary and 1-Rec GCTB cases is summarized in **Table 2**.

Of the 3 clones for the general proliferation marker protein Ki67, both mouse monoclonals (Mib1 and B56) showed occasional positive reaction in a few GC nuclei (**Figure 2A,B**). Interestingly, weak to moderate Mib1 reaction generally appeared also in the cytoplasm of GCs. Unexpectedly, the rabbit monoclonal SP6 reacted in many GC nuclei, however, weaker than in the adjacent proliferating mononuclear cells (**Figure 2C**). Of note, strong SP6 nuclear staining in GCs was at similar frequency as with Mib1 or B56. Of the replication licensing complex proteins, MCM2 was detected also only occasionally in a few GC nuclei (**Figure 2D**), as opposed to MCM6 which was seen frequently, but also weaker in the large (>40 nuclei) GCs, than in the small (<10–15 nuclei) ones or in the mononuclear cells (**Figure 2E**). Though Mib1 positive nuclei in GCs were markedly higher (W = 17, p = 0.012) in 1-Rec than in P cases (**Figure 2F**), it did not reach significance after adjusting for multiple testing ($p^{\star}$ = 0.0036). Also, neither B56 (p = 0.32) and SP6 (p = 1.0) Ki67 clones, nor MCM2 (p = 0.52) and MCM6 (p = 0.15) positive GC nuclei showed statistically different frequency between P and 1-Rec cases (see also in **Table 2**).

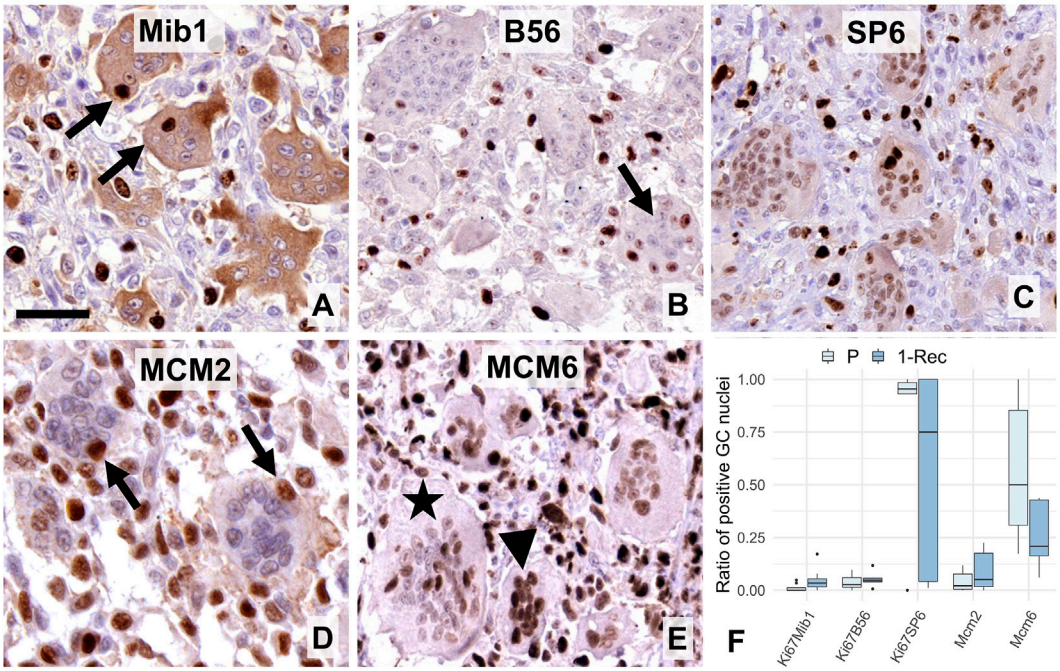

FIGURE 2 | Expression of "general" proliferation markers i.e. Ki67 **(A–C)** and MCM-complex proteins **(D–E)** in multinucleated GCs. Mib1 **(A)** and B56 **(B)** antibodies showed occasional nuclear immunoreactions (arrows), while the SP6 clone resulted in usually weaker, but a widespread Ki67 positivity in GCs. Cytoplasmic Mib1 positivity in GCs was validated by negativity in several mononuclear cells. MCM2 reaction (arrows) was also rare in GCs **(D)**, while that of MCM6 was rather frequent **(E)** and obviously more pronounced in smaller (arrowhead), than larger GCs (asterisk). Scale bar represents 40 μm on A, 50 μm on **(B,C,E)**, and 30 μm on **(D)**. Boxplot of the ratio of immunopositive GC nuclei vs. all GC nuclei **(F)** in primary (P) and first recurrent (1-Rec) GCTB cases.

G1/S-phase Progression Markers in Giant Cells

Concerning early G1-S phase regulation associated markers, weak to moderate cyclin dependent kinase 4/6 (CDK4/6) reactions were seen in around half of the GC nuclei (**Figure 3A**), while the vast majority of their nuclei showed moderate to strong reaction with the complexing partner cyclin D1 (**Figure 3B**). The intensity of the reactions and the rate of positive nuclei for cyclin D1 showed inverse relationship with the size and nuclear density of GCs (**Figure 3C**). Compared to CDK4/6, much less CDK2 positive nuclei were seen in GCs (**Figure 3D**). However, its complexing partner cyclin E, though it was not systematically counted, was widely detected in GC nuclei as a moderate reaction (**Figure 3E**), so as cyclin G1 (**Figure 3F**). Though average frequency of cyclin G1 in GCs showed a non-significant trend (W = 21. $p = 0.091$) toward P cases, CDK4 (W = 28, $p = 0.72$), cyclin D1 (W = 66, $p = 0.25$) and CDK2 (W = 72, $p = 0.10$) values did not differ statistically between primary and 1-Rec cases (**Figure 3G**).

Post G1-phase Markers and Cell Cycle Inhibitors in Giant Cells

Cyclin A, the S-G2-M transition partner of CDK2, was practically not detected (**Figure 4A**) in GCs, while the cell cycle repressor geminin (**Figure 4B**) only at very low frequency, although it appeared more often in 1-Rec cases (W = 3, $p = 0.045$/n.s.). Topoisomerase 2a (**Figure 4C**), responsible for genome organization in S-phase and chromatid segregation in mitosis, was not detected. Also, as expected from these, both the G2-M phase associated aurora kinase A and pHH3 (the latter primarily labels metaphase cells), were missing from GCs. The latter was also very rare even in the mononuclear cell fraction. Boxplots of quantitative analyses for some of these markers are shown in (**Figure 4D**).

In line with these, all CDK inhibitors tested including $p15^{INK4b}$, $p16^{INK4a}$, $p21^{WAF1}$ and $p27^{KIP1}$ were detected widely in GC nuclei (**Figures 5A–D**). $p16^{INK4a}$ showed the least nuclear positivity but showed widespread cytoplasmic reaction, while $p21^{WAF1}$ was strongly detected practically in most GC nuclei. Fitting into this pattern, the majority of GC nuclei were immunopositive over a wide range of intensities when using either the DO7 (**Figure 5E**) or BP53–12 antibody clones (not shown) specific for the p53; or when retinoblastoma antibody was used (**Figure 5F**). However, none of the systematically analyzed CDK inhibitors including $p15^{INK4b}$ (W = 13, $p = 1.0$), $p16^{INK4a}$ (W = 10, $p = 0.69$) and $p21^{WAF1}$ (W = 32, $p = 0.31$) showed differential expression between primary and 1-Rec samples (**Figures 5G,H**).

Explorative Survival Analyses

Explorative univariate Cox proportional hazards analyses revealed that the increased average number of Ki67 Mib1 positive GC nuclei (HR = 1.1, 95% CI: 1–1.2, $p_{non\text{-}adj} = 0.041$)

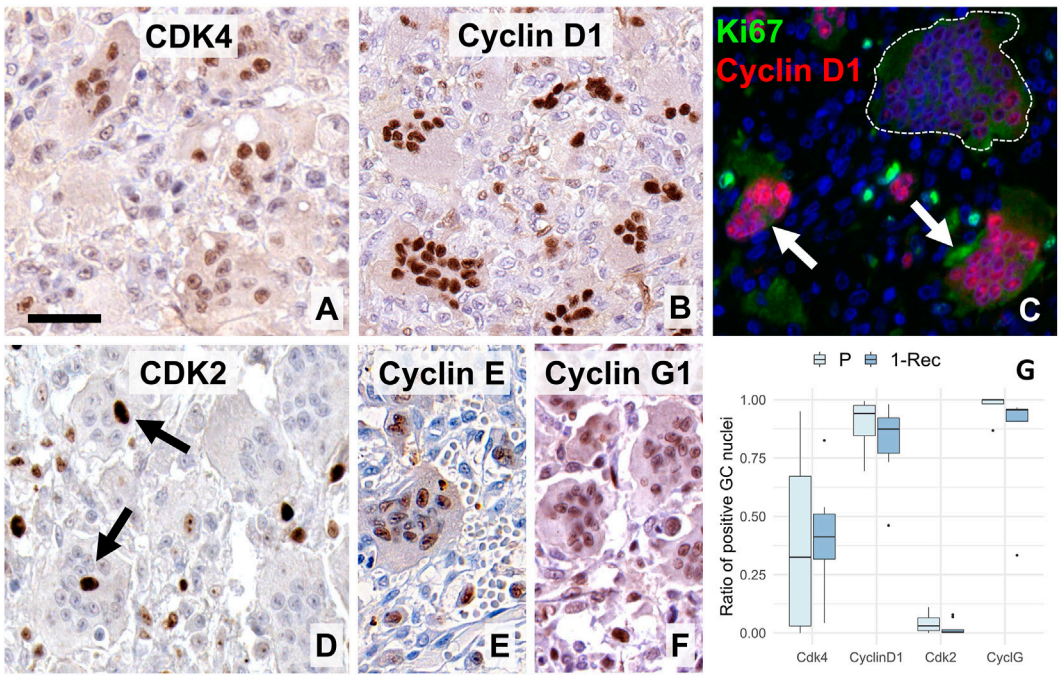

FIGURE 3 | Expression of early G1-S-phase promoting cell cycle markers in giant cells (GC). Many nuclei were positive for the CDK 4/6 **(A)** and almost all were strongly stained for its complexing partner cyclin D1 **(B)**. Double immunofluorescence **(C)** for Ki67 (Mib1, green) and cyclin D1 (SP4, red) showed strong cyclin D1 positivity in smaller GCs (white arrow) but only very faint and missing reaction in a large, aged GC (within white broken line). CDK2 **(D)** was rarely detected in GCs (arrows), as opposed to the widespread expression of cyclin E **(E)** and cyclin G1 **(F)**. Scale bar: 40 μm for **(A,C,D)**; and 50 μm for **(B,E,F)** images. Boxplots of the ratio of immunopositive GC nuclei vs. all GC nuclei **(G)** for some of these markers in primary (P) and first recurrence (1-Rec) GCTB.

was significantly associated with shorter PFS while no other marker showed relevant associations with PFS.

DISCUSSION

In GCTB, GCs need continuous supply of precursors to fuse, progressively form and resorb bone. They are under the influence of growth factors including receptor activator for NFκB ligand (RANKL) and macrophage colony stimulating factor (M-CSF) and their substitutes e.g. interleukins 6, 11 and 8, and TNFα; as well as VEGF, placental growth factor (PlGF), hepatocyte growth factor (HGF) and FLt-3 ligand, respectively, some of which can induce proliferation [11, 20, 21]. Earlier studies by others showed the widespread expression of cyclin D1 [5, 6, 22–24] cyclin D3 [5] and $p21^{WAF1}$ [6], less p16 and scarce Ki67 [22] in GCs. Still, these data were insufficient to declare replication activity in GCs. In our present work, in addition to confirming previous observations, we revealed further cell cycle promoters, which can verify [23] an early cell cycle course in GCs. However, the effect of the generally detected cell cycle licensing MCM6, and the cell cycle promoters CDK4 and cyclin E, are likely neutralized in GCs by the upregulation CDK inhibitors $p15^{INK4b}$, $p16^{INK4a}$, $p27^{KIP1}$ and the p53 induced $p21^{WAF1}$, consistent with a cell cycle arrest at the late G1 phase. The potential emergence and links among the markers of this study during the cell cycle are drafted in **Figure 6**.

The general proliferation marker Ki67, which has been involved in heterochromatin organization, the inhibition of p21-mediated G1/S-phase checkpoint activation and in the formation of mitotic perichromosomal protein sheet, can be detected throughout the replication cycle [25]. So far, only one study reported a weak Ki67 Mib1 staining in <5% of GCs in only 3 out of 29 (10%) GCTB samples. Of the 3 Ki67 clones we investigated in GCs, both Mib1 and B56 showed a low ratio of nuclear positivity (<10%) while SP6 demonstrated a wide range with >75% median. The specificity of the moderate intensity SP6 reaction in GCs was validated by the clear negativity of some adjacent mononuclear cells. Though Ki67 expression peaks at G2/M-phases, the protein is only gradually eliminated from newly divided cells, therefore, its amount may also reflect the time the cell spent in quiescence [26]. Accordingly, the markedly higher ratio of positive GC nuclei in 1-Rec vs. primary cases, and its association with shorter PFS in our explorative survival analysis may also indicate accelerated dynamics of GC formation in the advanced cases. The cytoplasmic Mib1 staining in GCs shown also by others [27] is likely to be related to its metabolic elimination by the ubiquitin proteasome system [28]. The differential occurrence of the Ki67 clones can be partly related to the slower degradation of the epitope region recognized by SP6 compared to the others. However, further signs in this study suggested that this may also be linked with an initial replication activity.

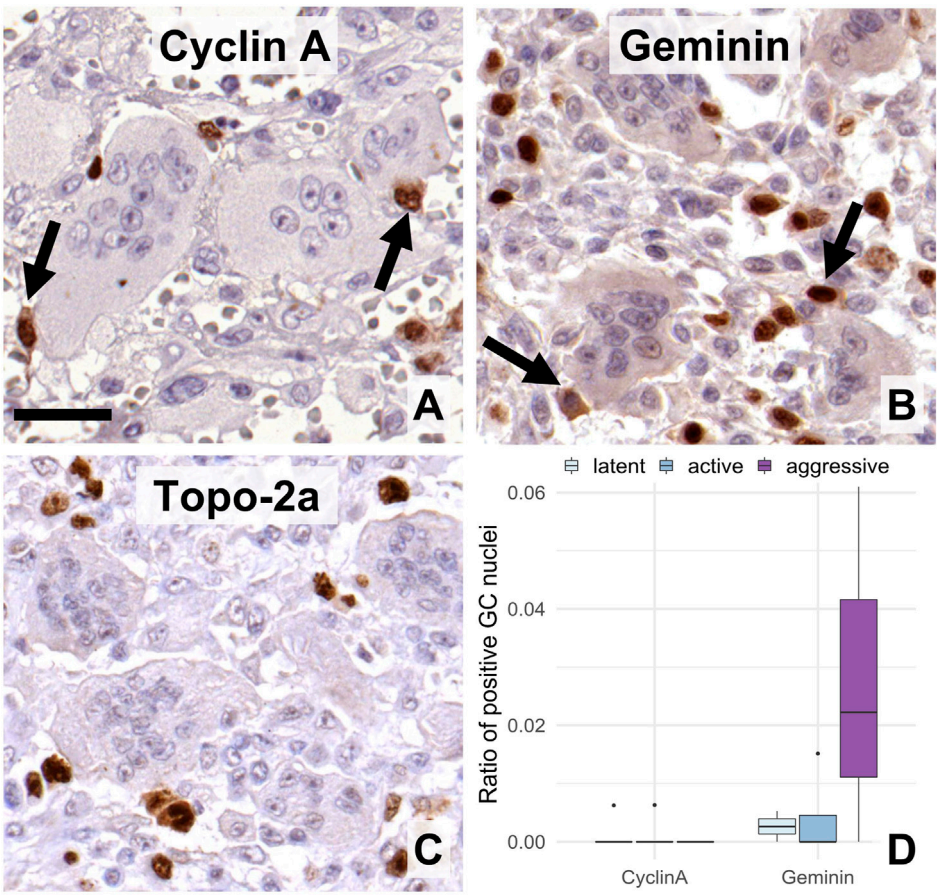

FIGURE 4 | Expression of post-G1 (S-G2-M)-phase cell cycle markers in GC. Cyclin A **(A)**, geminin **(B)**, and topoisomerase-2a **(C)** were practically detected only in the mononuclear cells. Arrows show immunopositive mononuclear cells of close association with multinucleated GCs. Scale bar: 30 μm for all images. Very rare geminin positive cells were somewhat more frequent in agressive grade tumors vs. the other groups (**(D)**, boxlot).

Members of the MCM2-7 helicase complex, which can also be detected all over the cycle, unwind double-stranded DNA and allow the controlled licensing of DNA for duplication [16]. However, while MCM6 complexed with MCM4 and MCM7 is involved in relaxing DNA to single strands, the MCM2 subunit (MCM3, and MCM5 too), has potential inhibitory role on this function [29]. Our widespread detection of MCM6 with moderate intensity but only occasional occurrence of MCM2 in GC nuclei, may reflect the initiation of DNA unwinding in GCs.

Cyclin-dependent serine/threonine kinases complex with their regulatory subunit cyclins to phosphorylate retinoblastoma and promote the transition of different phases during cell cycle progression [30]. Here, we revealed the widespread emergence not only of the previously detected cyclin D1 [5, 6], but also its partner CDK4 in the earliest G1-S phase promoter complex. This complex not only can inactivate retinoblastoma but also support the activation of the next G1-S-phase promoter cyclin E-CDK2 complex through reducing mitochondrial metabolism to prevent cyclin E degradation [31]. In agreement with this, we regularly detected cyclin E in GCs, however, only very rarely found its complexing partner CDK2 in GC nuclei, indicating a late G1-phase arrested cell cycle. At the same time, cyclin D1-CDK4/6 complex can also support cell growth e.g. through mTORC1 activation [32], and high cyclin D1 levels can assist in metabolic substrate utilization toward mitochondrial amino acid production [31], which propose a role for cyclin D1 also in GC growth and differentiation. Furthermore, cyclin D1 overexpression in GCs may also be required for multinucleation [5], as it enhanced the number of nuclei e.g. in cardiomyocytes [33] and was detected primarily in giant trophoblasts rather than in diploid ones [34].

In agreement with earlier studies, in GCs we also revealed the widespread expression of $p21^{WAF1}$, the universal CDK inhibitor [35]. However, despite $p21^{WAF1}$ is considered to block cyclin D1-CDK4/6 complex and CDK2 activities, paradoxically it may also be important for CDK4/6 complex assembly [36] and for the nuclear export of cyclin D1 [37, 38]. These might explain our frequent detection of CDK4 but not the CDK2, and the high levels of the CDK4 partner cyclin D1 in GC nuclei. $P21^{WAF1}$ is an important effector of the cell cycle control functions of p53 [39]. Before us, p53 expression had been noticed only incidentally in one publication [40]. Here, we detected p53 in the majority of GC nuclei using 2 different antibody clones (DO7 and BP53–12 respectively) to give, for the first time, clear evidence that GCs

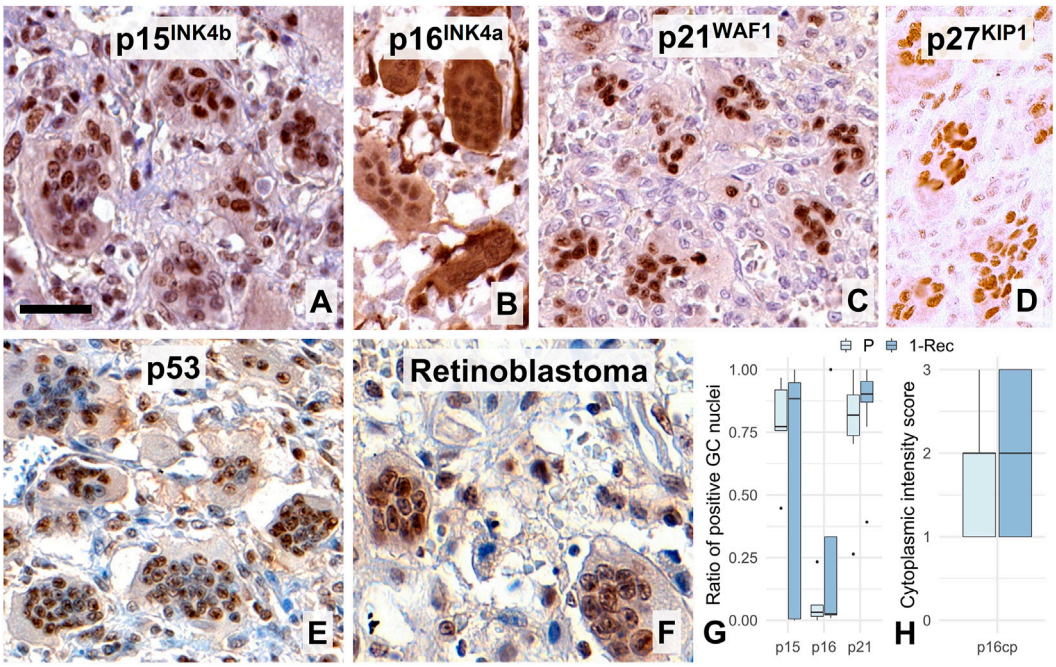

FIGURE 5 | Widespread nuclear immunoreactions for the cell cycle control inhibitor markers $p15^{INK4b}$ **(A)**, $p16^{INK4a}$ (B, where cytoplasmic reaction was frequent), $p21^{WAF1}$, **(C)**, $p27^{KIP1}$ **(D)**, p53 (DO7, **E)**, and retinoblastoma **(F)** proteins in multinucleated giant cell nuclei. Scale bar represents 40 μm on **(A)**, 50 μm on **(B–E)**, and 30 μm on **(F)**. Boxplots of the ratio of immunopositive GC nuclei vs. all GC nuclei for some of these markers **(G)**; and for the cytoplasmic $p16^{INK4a}$ reaction **(H)** in primary (P) and first recurrence (1-Rec) GCTBs.

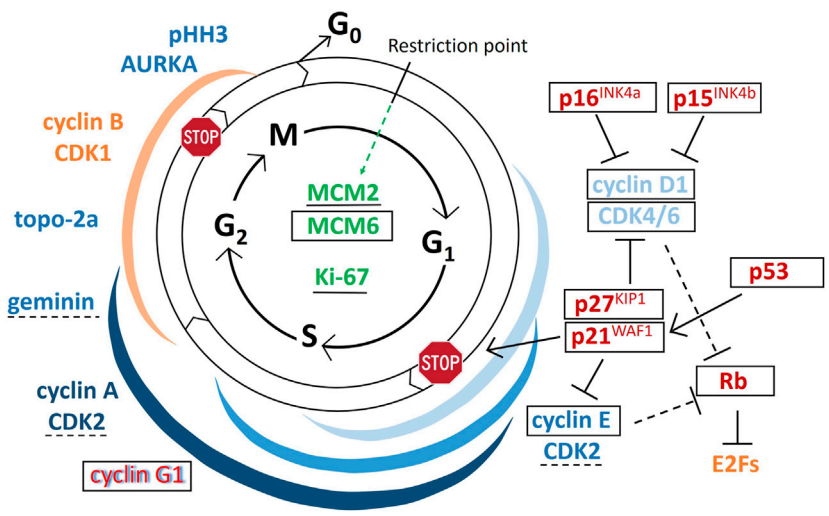

FIGURE 6 | Draft on the emergence and potential role of regulatory proteins during the cell cycle. Arrows indicate activating functions while "T" signs show inhibitory functions. Markers in green can be detected throughout the cycle, those in blue support, while those in red inhibit cell cycle progression; red letters with blue shadow at cyclin G1 indicate binary functions; and the markers in yellow are important but not tested in this study. In GCTB giant cells, the markers that are framed in black were widely detected, those underlined with continuous line were occasionally found, those underlined using broken lines are found very rarely, while those which are not labeled either of these ways, were practically not detected within GCs. Colored ribbons show the rough expression duration of the matching-colored cyclin-cyclin dependent kinase complexes.

upregulate this important "guardian" of the genome. Cytoskeletal stress, which may occur during multinucleation in GCs, can induce p53 upregulation and activate $p21^{WAF1}$ for blocking S-phase entry at G1-checkpoint [39]. The p53-dependent G1 arrest of multinucleated tetraploid cells has been previously described [41] and p53 activity with the

contribution of $p21^{WAF1}$ can also drive this process even further to result in cellular senescence [42]. We also noticed the general upregulation of $p27^{KIP1}$ in GCs, which in normal cells is primarily linked to controlling the cell cycle through inhibiting both cyclin E-CDK2 and cyclin D1-CDK4/6 activities [43]. Both $p21^{WAF1}$ and $p27^{KIP1}$ play essential roles also in GC functions as shown by the osteopetrotic phenotype in mice with deleted genes encoding these proteins [44]. In GCTB, arresting of the potential cell cycle activities and inducing senescence are required for GC maturation involving the production of key proteases cathepsin K and MMP-9 for pathological bone resorption [45].

As a p53 target, cyclin G1 has been involved in both supporting cell cycle arrest and in driving the S-G2-M-transition [17]. As a supposed oncogene cyclin G1 may activate the MDM2 oncoprotein by recruiting Ser/Thr protein phosphatase 2A (PP2A), which dephosphorylates MDM2 to inhibit and degrade p53 [17, 18, 46]. We detected cyclin G1 in most GC nuclei with a non-significant trend toward higher values in primary vs. 1-Rec GCTB cases. This may rather support its role in cell cycle arrest than as a promoter of replication in GCs which are reactive, non-malignant cells. However, it is also possible, that cyclin G1 upregulation is a rebound effect to control p53 overexpression and prevent apoptosis induction [17, 18, 46]. The permanently elevated cyclin D1 levels in functionally active GCs, but its disappearance from oversized (>40 nuclei), aged GCs may also be consistent with the protective function of cyclin D1 [17, 46].

Besides $p21^{WAF1}$ and $p27^{KIP1}$, the upregulation of other CDK inhibitors, particularly targeting CDK4 and CDK6 proteins including $p15^{INK4b}$ and $p16^{INK4a}$, further support the cell cycle related activity in GCs [47]. Both $p15^{INK4b}$ and $p16^{INK4a}$ are also likely to contribute to G1-phase cell cycle arrest [48, 49], while $p16^{INK4a}$ may also be linked to cellular senescence induction supporting either the full functional differentiation or the aged-cell decay in GCs [50]. Cell cycle arrest by CDK inhibitors was also reflected by retinoblastoma upregulation in GCs. In line with these findings, practically none of the S-G2-M phase markers including cyclin A, the later complexing partner of CDK2, the cell cycle repressor geminin, the G2-M phase transition associated cyclin B, or the M-phase related AURKA and pHH3 were detected within GCs [16]. This pattern is consistent with the full functional maturation of GCs. The S-G2 phase marker positive mononuclear cells which had no discernible cytoplasmic boarders with GCs, were likely to be monocytes close to or within the fusion process (**Figures 4A,B**). In support of this, a subpopulation of CD14+/CD33 + monocytes was shown to proliferate in response to M-CSF and form pre-osteoclasts when primed with RANKL [51]. Then pre-osteoclasts loose CD33 expression and fuse with more monocytic cells [52] and the proliferating monocytes form significantly more GCs than the rest of the monocytic pool [51].

Despite silenced, the early signs of replication proved here, may reflect the generation dynamics and age-related activity of GCs. *In vitro* data confirm an inverse correlation between GC size and resorption activity at mild acidic conditions [53]. This is in line with data showing elevated recurrence potential in GCTB cases, which dominantly contain GCs of <15 nuclei compared to those carrying larger ones [18]. In the present study, the average size and nuclear density of GCs also revealed an inverse trend with the clinicoradiological grade of GCTB. Furthermore, the cyclin D1 and MCM6 reactions in GCs were obviously stronger and more frequent in small sized (~<15 nuclei) than in larger GCs, particularly when nuclear numbers were ~>40. These are also in agreement with our earlier finding of the significantly lower average size of GCs in recurrent GCTB cases where the growth related EGFR protein level was elevated in the mononuclear stromal cells, the major drivers of GC formation and activity [13]. All these support the view that smaller sized GCs are the younger, dynamically forming populations, which may show more signs of early replication than the aged, functionally less active oversized GCs (~>40 nuclei).

Dissecting the replication cycle into major cells fractions through the immunohistochemical detection of nuclear proteins which regulate or control different phases of replication, may allow accurate assessment of cell proliferation dynamics *in situ*. Using a marker set, selected carefully from the list we described here, can serve cell cycle analysis for diagnostic, prognostic and predictive purposes in any pathological process particularly in cancer.

CONCLUSION

Though multinucleated GCs in GCTB are thought to be of reactive phenotype formed by fusion of cells of the monocyte macrophage lineage, they had been occasionally shown to express cell proliferation related markers. By using a comprehensive marker set, here we revealed, for the first time in GCs, the general upregulation of cell cycle promoting markers MCM6, CDK4 and cyclin E, indicating primary DNA unwinding and G1-S-phase promoting activities. We also confirmed the earlier published widespread expression of cyclin D1, which all, unequivocally demonstrated an early replication activity in GCs. This, however, was silenced by the widespread expression of CDK inhibitors $p15^{INK4b}$, $p16^{INK4a}$, $p27^{KIP1}$ and p53 induced $p21^{WAF1}$ resulting in cell cycle arrest at the G1 checkpoint, confirmed by the missing production of post-G1-phase faction markers. The complex interplay among these elements under the influence of external growth and differentiation factors is required for the functional maturation and bone resorbing activity of GCs in GCTB.

DATA AVAILABILITY STATEMENT

The original contributions presented in the study are included in the article/Supplementary Material, further inquiries can be directed to the corresponding authors.

ETHICS STATEMENT

The studies involving human participants were reviewed and approved by the Institute of Rizzoli (IOR), Bologna, Italy (ethical approval no.: IOR 13351/5-28-2008), and Semmelweis University, Budapest, Hungary (ethical approval no.: 87/2007). Written informed consent to participate in this study was provided by the participants' legal guardian/next of kin.

AUTHOR CONTRIBUTIONS

Conceived and designed the experiments: TK and MM. Performed the experiments: MM, PB, and PP. Analyzed the data: MM, TK, HW, and PP. Performed statistical analyses: MM; Contributed reagents/materials/analysis tools: PP, ZS, MS, RF, CG, and TK. Wrote the paper: MM and TK. Diagnosed GCTB cases and advised the study: ZS, MS, and RF. Supervised the study: TK. All authors critically reviewed the manuscript and approved the final version.

FUNDING

This study was performed within the framework of EuroBoNet, an EU FP6 funded Network of Excellence Program (LSHC-CT-2006-018814). The founders had no influence on study design, data collection, analysis and decision to publish, or preparation of the manuscript.

CONFLICT OF INTEREST

MM reports non-related funding from the German Ministry for Education and Research (MI-I 01ZZ1801E) and non-related consultancy for Siemens Healthineers and SmartReporting GmbH. The authors declare that the research was conducted in the absence of any commercial or financial relationships that could be construed as a potential conflict of interest.

REFERENCES

1. Chambers TJMultinucleate Giant Cells. *J Pathol* (1978) 126(3):125–48. doi:10.1002/path.1711260302
2. Ariizumi T, Ogose A, Kawashima H, Hotta T, Umezu H, and Endo NMultinucleation Followed by an Acytokinetic Cell Division in Myxofibrosarcoma with Giant Cell Proliferation. *J Exp Clin Cancer Res* (2009) 28:44. doi:10.1186/1756-9966-28-44
3. Vignery AMacrophage Fusion. *J Exp Med* (2005) 202(3):337–40. doi:10.1084/jem.20051123
4. Maros ME, Schnaidt S, Balla P, Kelemen Z, Sapi Z, Szendroi M, et al.*In situ* cell Cycle Analysis in Giant Cell Tumor of Bone Reveals Patients with Elevated Risk of Reduced Progression-free Survival. *Bone* (2019) 127:188–98. doi:10.1016/j.bone.2019.06.022
5. Kauzman A, Li SQ, Bradley G, Bell RS, Wunder JS, and Kandel RCyclin Alterations in Giant Cell Tumor of Bone. *Mod Pathol* (2003) 16(3):210–8. doi:10.1097/01.MP.0000057235.65327.40
6. Kandel R, Li SQ, Bell R, Wunder J, Ferguson P, Kauzman A, et al.Cyclin D1 and P21 Is Elevated in the Giant Cells of Giant Cell Tumors. *J Orthop Res* (2006) 24(3):428–37. doi:10.1002/jor.20036
7. Maggiani F, Forsyth R, Hogendoorn PCW, Krenacs T, and Athanasou NAThe Immunophenotype of Osteoclasts and Macrophage Polykaryons. *J Clin Pathol* (2011) 64(8):701–5. doi:10.1136/jcp.2011.090852
8. Behjati S, Tarpey PS, Presneau N, Scheipl S, Pillay N, Van Loo P, et al.Distinct H3F3A and H3F3B Driver Mutations Define Chondroblastoma and Giant Cell Tumor of Bone. *Nat Genet* (2013) 45(12):1479–82. doi:10.1038/ng.2814
9. Szendrői MGiant-cell Tumour of Bone (GCT). In: G Bentley, editor. *European Surgical Orthopaedics and Traumatology*. Berlin, Germany: Springer (2014). p. 4037–54.
10. Cowan RW, and Singh GGiant Cell Tumor of Bone: A Basic Science Perspective. *Bone* (2013) 52(1):238–46. doi:10.1016/j.bone.2012.10.002
11. Knowles HJ, and Athanasou NAAcute Hypoxia and Osteoclast Activity: a Balance between Enhanced Resorption and Increased Apoptosis. *J Pathol* (2009) 218(2):256–64. doi:10.1002/path.2534
12. Knowles HJ, and Athanasou NACanonical and Non-canonical Pathways of Osteoclast Formation. *Histol Histopathol* (2009) 24:337. doi:10.14670/HH-24.337
13. Balla P, Moskovszky L, Sapi Z, Forsyth R, Knowles H, Athanasou NA, et al.Epidermal Growth Factor Receptor Signalling Contributes to Osteoblastic Stromal Cell Proliferation, Osteoclastogenesis and Disease Progression in Giant Cell Tumour of Bone. *Histopathology* (2011) 59(3):376–89. doi:10.1111/j.1365-2559.2011.03948.x
14. Balla P, Maros ME, Barna G, Antal I, Papp G, Sapi Z, et al.Prognostic Impact of Reduced Connexin43 Expression and Gap Junction Coupling of Neoplastic Stromal Cells in Giant Cell Tumor of Bone. *PLoS One* (2015) 10(5):e0125316. doi:10.1371/journal.pone.0125316
15. Satyanarayana A, and Kaldis PMammalian Cell-Cycle Regulation: Several Cdks, Numerous Cyclins and Diverse Compensatory Mechanisms. *Oncogene* (2009) 28(33):2925–39. doi:10.1038/onc.2009.170
16. Williams GH, and Stoeber KThe Cell Cycle and Cancer. *J Pathol* (2012) 226(2):352–64. doi:10.1002/path.3022
17. Kimura SH, and Nojima HCyclin G1 Associates with MDM2 and Regulates Accumulation and Degradation of P53 Protein. *Genes Cells* (2002) 7(8):869–80. doi:10.1046/j.1365-2443.2002.00564.x
18. Gordon E, Ravicz J, Liu S, Chawla S, and Hall FCell Cycle Checkpoint Control: The Cyclin G1/Mdm2/p53 axis Emerges as a Strategic Target for Broad-Spectrum Cancer Gene Therapy - A Review of Molecular Mechanisms for Oncologists. *Mol Clin Onc* (2018) 9(2):115–34. doi:10.3892/mco.2018.1657
19. Wenz H, Maros ME, Meyer M, Förster A, Haubenreisser H, Kurth S, et al.Image Quality of 3rd Generation Spiral Cranial Dual-Source CT in Combination with an Advanced Model Iterative Reconstruction Technique: A Prospective Intra-individual Comparison Study to Standard Sequential Cranial CT Using Identical Radiation Dose. *PLoS One* (2015) 10(8):e0136054. doi:10.1371/journal.pone.0136054
20. Knowles H, and Athanasou NHypoxia-inducible Factor Is Expressed in Giant Cell Tumour of Bone and Mediates Paracrine Effects of Hypoxia on Monocyte-Osteoclast Differentiation via Induction of VEGF. *J Pathol* (2008) 215(1):56–66. doi:10.1002/path.2319
21. Knowles HJ, and Athanasou NACanonical and Non-canonical Pathways of Osteoclast Formation. *Histol Histopathol* (2009) 24(3):337–46. doi:10.14670/HH-24.337
22. Choi JW, Lee JH, Kim YS, and Kim YSFrequent Upregulation of Cyclin D1 and p16INK4a Expression with Low Ki-67 Scores in Multinucleated Giant Cells. *Pathobiology* (2011) 78(4):233–7. doi:10.1159/000327359
23. Matsubayashi S, Nakashima M, Kumagai K, Egashira M, Naruke Y, Kondo H, et al.Immunohistochemical Analyses of β-catenin and Cyclin D1 Expression in Giant Cell Tumor of Bone (GCTB): A Possible Role of Wnt Pathway in GCTB Tumorigenesis. *Pathol - Res Pract* (2009) 205(9):626–33. doi:10.1016/j.prp.2009.02.011
24. Lujic N, Sopta J, Kovacevic R, Stevanovic V, and Davidovic RRecurrence of Giant Cell Tumour of Bone: Role of P53, Cyclin D1, β-catenin and Ki67. *Int Orthopaedics (Sicot)* (2016) 40(11):2393–9. doi:10.1007/s00264-016-3292-2
25. Sun X, and Kaufman PDKi-67: More Than a Proliferation Marker. *Chromosoma* (2018) 127(2):175–86. doi:10.1007/s00412-018-0659-8

26. Sales Gil R, and Vagnarelli PKi-67: More Hidden behind a 'Classic Proliferation Marker'. *Trends Biochem Sci* (2018) 43(10):747–8. doi:10.1016/j.tibs.2018.08.004
27. Ismail FW, Shamsudin AM, Wan Z, Daud SM, and Samarendra MSKi-67 Immuno-Histochemistry Index in Stage III Giant Cell Tumor of the Bone. *J Exp Clin Cancer Res* (2010) 29:25. doi:10.1186/1756-9966-29-25
28. Miller I, Min M, Yang C, Tian C, Gookin S, Carter D, et al.Ki67 Is a Graded Rather Than a Binary Marker of Proliferation versus Quiescence. *Cell Rep* (2018) 24(5):1105–12.e5. doi:10.1016/j.celrep.2018.06.110
29. Vijayraghavan S, and Schwacha AThe Eukaryotic Mcm2-7 Replicative Helicase. *Subcell Biochem* (2012) 62:113–34. doi:10.1007/978-94-007-4572-8_7
30. Malumbres MCyclin-dependent Kinases. *Genome Biol* (2014) 15(6):122. doi:10.1186/gb4184
31. Pestell RGNew Roles of Cyclin D1. *Am J Pathol* (2013) 183(1):3–9. doi:10.1016/j.ajpath.2013.03.001
32. Romero-Pozuelo J, Figlia G, Kaya O, Martin-Villalba A, and Teleman AACdk4 and Cdk6 Couple the Cell-Cycle Machinery to Cell Growth via mTORC1. *Cell Rep* (2020) 31(2):107504. doi:10.1016/j.celrep.2020.03.068
33. Soonpaa MH, Koh GY, Pajak L, Jing S, Wang H, Franklin MT, et al.Cyclin D1 Overexpression Promotes Cardiomyocyte DNA Synthesis and Multinucleation in Transgenic Mice. *J Clin Invest* (1997) 99(11):2644–54. doi:10.1172/JCI119453
34. Palazon LS, Davies TJ, and Gardner RLTranslational Inhibition of Cyclin B1 and Appearance of Cyclin D1 Very Early in the Differentiation of Mouse Trophoblast Giant Cells. *Mol Hum Reprod* (1998) 4(11):1013–20. doi:10.1093/molehr/4.11.1013
35. Georgakilas AG, Martin OA, and Bonner WMp21: A Two-Faced Genome Guardian. *Trends Mol Med* (2017) 23(4):310–9. doi:10.1016/j.molmed.2017.02.001
36. Cheng M, Olivier P, Diehl JA, Fero M, Roussel MF, Roberts JM, et al.The p21Cip1 and p27Kip1 CDK `inhibitors' Are Essential Activators of Cyclin D-dependent Kinases in Murine Fibroblasts. *EMBO J* (1999) 18(6):1571–83. doi:10.1093/emboj/18.6.1571
37. Alt JR, Cleveland JL, Hannink M, and Diehl JAPhosphorylation-dependent Regulation of Cyclin D1 Nuclear Export and Cyclin D1-dependent Cellular Transformation. *Genes Dev* (2000) 14(24):3102–14. doi:10.1101/gad.854900
38. Alt JR, Gladden AB, and Diehl JAp21Cip1 Promotes Cyclin D1 Nuclear Accumulation via Direct Inhibition of Nuclear Export. *J Biol Chem* (2002) 277(10):8517–23. doi:10.1074/jbc.M108867200
39. Hafner A, Bulyk ML, Jambhekar A, and Lahav GThe Multiple Mechanisms that Regulate P53 Activity and Cell Fate. *Nat Rev Mol Cell Biol* (2019) 20(4):199–210. doi:10.1038/s41580-019-0110-x
40. Yalcinkaya U, Ugras N, Kabul S, Ocakoglu G, and Bilgen MSPrognostic Value of P53 Protein Expression in Giant Cell Tumor of Bone. *pjp* (2015) 4(4):389–96. doi:10.5114/pjp.2015.57252
41. Ganem NJ, and Pellman DLimiting the Proliferation of Polyploid Cells. *Cell* (2007) 131(3):437–40. doi:10.1016/j.cell.2007.10.024
42. Rieder CL, and Maiato HStuck in Division or Passing through. *Dev Cell* (2004) 7(5):637–51. doi:10.1016/j.devcel.2004.09.002
43. Wander SA, Zhao D, and Slingerland JMp27: A Barometer of Signaling Deregulation and Potential Predictor of Response to Targeted Therapies: Figure 1. *Clin Cancer Res* (2011) 17(1):12–8. doi:10.1158/1078-0432.Ccr-10-0752
44. Sankar U, Patel K, Rosol TJ, and Ostrowski MCRANKL Coordinates Cell Cycle Withdrawal and Differentiation in Osteoclasts Through the Cyclin-Dependent Kinase Inhibitors p27KIP1and p21CIP1. *J Bone Miner Res* (2004) 19(8):1339–48. doi:10.1359/JBMR.040321
45. Lindeman JHN, Hanemaaijer R, Mulder A, Dijkstra PDS, Szuhai K, Bromme D, et al.Cathepsin K Is the Principal Protease in Giant Cell Tumor of Bone. *Am J Pathol* (2004) 165(2):593–600. doi:10.1016/S0002-9440(10)63323-8
46. Okamoto K, Li H, Jensen MR, Zhang T, Taya Y, Thorgeirsson SS, et al.Cyclin G Recruits PP2A to Dephosphorylate Mdm2. *Mol Cell* (2002) 9(4):761–71. doi:10.1016/s1097-2765(02)00504-x
47. Sherr CJ, and Roberts JMCDK Inhibitors: Positive and Negative Regulators of G1-phase Progression. *Genes Dev* (1999) 13(12):1501–12. doi:10.1101/gad.13.12.1501
48. Carnero A, Hudson JD, Hannon GJ, and Beach DHLoss-of-function Genetics in Mammalian Cells: the P53 Tumor Suppressor Model. *Nucleic Acids Res* (2000) 28(11):2234–41. doi:10.1093/nar/28.11.2234
49. Hudson JD, Shoaibi MA, Maestro R, Carnero A, Hannon GJ, and Beach DHA Proinflammatory Cytokine Inhibits P53 Tumor Suppressor Activity. *J Exp Med* (1999) 190(10):1375–82. doi:10.1084/jem.190.10.1375
50. Dimri GP, Hara E, and Campisi JRegulation of Two E2F-Related Genes in Presenescent and Senescent Human Fibroblasts. *J Biol Chem* (1994) 269(23):16180–6. doi:10.1016/s0021-9258(17)33990-x
51. Lari R, Kitchener PD, and Hamilton JAThe Proliferative Human Monocyte Subpopulation Contains Osteoclast Precursors. *Arthritis Res Ther* (2009) 11(1):R23. doi:10.1186/ar2616
52. Forsyth RG, De Boeck G, Baelde JJ, Taminiau AH, Uyttendaele D, Roels H, et al.CD33+ CD14− Phenotype Is Characteristic of Multinuclear Osteoclast-like Cells in Giant Cell Tumor of Bone. *J Bone Mineral Res* (2009) 24(1):70–7. doi:10.1359/jbmr.080905
53. Orriss IR, and Arnett TRRodent Osteoclast Cultures. *Methods Mol Biol* (2012) 816:103–17. doi:10.1007/978-1-61779-415-5_8

Pathology & Oncology Research

frontiers

ORIGINAL RESEARCH
published: 03 May 2021
doi: 10.3389/pore.2021.622855

Evaluation of Protein Purification Techniques and Effects of Storage Duration on LC-MS/MS Analysis of Archived FFPE Human CRC Tissues

*Sophia C. Rossouw[1], Hocine Bendou[1], Renette J. Blignaut[2], Liam Bell[3], Jonathan Rigby[4] and Alan Christoffels[1]**

[1]South African Medical Research Council Bioinformatics Unit, South African National Bioinformatics Institute, University of the Western Cape, Bellville, South Africa, [2]Department of Statistics and Population Studies, University of the Western Cape, Bellville, South Africa, [3]Centre for Proteomic and Genomic Research, Observatory, Cape Town, South Africa, [4]Division of Anatomical Pathology, Department of Pathology, Faculty of Health Sciences, University of Stellenbosch, National Health Laboratory Service, Tygerberg Hospital, Cape Town, South Africa

To elucidate cancer pathogenesis and its mechanisms at the molecular level, the collecting and characterization of large individual patient tissue cohorts are required. Since most pathology institutes routinely preserve biopsy tissues by standardized methods of formalin fixation and paraffin embedment, these archived FFPE tissues are important collections of pathology material that include patient metadata, such as medical history and treatments. FFPE blocks can be stored under ambient conditions for decades, while retaining cellular morphology, due to modifications induced by formalin. However, the effect of long-term storage, at resource-limited institutions in developing countries, on extractable protein quantity/quality has not yet been investigated. In addition, the optimal sample preparation techniques required for accurate and reproducible results from label-free LC-MS/MS analysis across block ages remains unclear. This study investigated protein extraction efficiency of 1, 5, and 10-year old human colorectal carcinoma resection tissue and assessed three different gel-free protein purification methods for label-free LC-MS/MS analysis. A sample size of n = 17 patients per experimental group (with experiment power = 0.7 and $\alpha = 0.05$, resulting in 70% confidence level) was selected. Data were evaluated in terms of protein concentration extracted, peptide/protein identifications, method reproducibility and efficiency, sample proteome integrity (due to storage time), as well as protein/peptide distribution according to biological processes, cellular components, and physicochemical properties. Data are available *via* ProteomeXchange with identifier PXD017198. The results indicate that the amount of protein extracted is significantly dependent on block age ($p < 0.0001$), with older blocks yielding less protein than newer blocks. Detergent removal plates were the most efficient and overall reproducible protein purification method with regard to number of peptide and protein identifications, followed by the MagReSyn® SP3/HILIC method (with on-bead enzymatic digestion), and lastly the acetone precipitation and formic acid resolubilization method. Overall, the results indicate that long-term storage of FFPE tissues (as measured by methionine oxidation) does not considerably interfere with retrospective proteomic analysis ($p > 0.1$). Block age mainly

OPEN ACCESS

Edited by:
Andrea Ladányi, National Institute of Oncology (NIO), Hungary

***Correspondence:**
Alan Christoffels
alan@sanbi.ac.za

Received: *29 October 2020*
Accepted: *01 March 2021*
Published: *03 May 2021*

Citation:
Rossouw SC, Bendou H, Blignaut RJ, Bell L, Rigby J and Christoffels A (2021) Evaluation of Protein Purification Techniques and Effects of Storage Duration on LC-MS/MS Analysis of Archived FFPE Human CRC Tissues. Pathol. Oncol. Res. 27:622855. doi: 10.3389/pore.2021.622855

affects initial protein extraction yields and does not extensively impact on subsequent label-free LC-MS/MS analysis results.

Keywords: formalin-fixed paraffin-embedded proteomics, acetone precipitation and formic acid resolubilization, detergent removal plates, SP3/HILIC-on-bead-digestion, mass spectrometry, LC-MS/MS

INTRODUCTION

Tissues from biopsies, resections and/or surgery are routinely taken from patients as a treatment option and/or to facilitate more accurate diagnosis. The current universal tissue preservation method of choice is formalin-fixation and paraffin-embedment, to avoid tissue auto-proteolysis and putrefaction, and to allow tissue specimens to be analyzed and examined at a later stage [1–4]. Formalin-fixation is also considered to be a superior preservative, since formaldehyde quickly and easily penetrates and fixes tissues because of its small molecular size, it causes minimal tissue shrinkage and distortion, and produces exceptional staining results in histopathology [4–6]. The formalin-fixed, paraffin-embedded (FFPE) method of tissue preservation also allows for the indefinite room temperature storage of FFPE blocks, thereby removing much of the cost and difficulty associated with fresh-cryopreserved tissue storage. The technique involves the immersion and incubation of tissues in formaldehyde solution, which is then replaced with alcohol (ethanol) in a dehydration step. Dehydration of the sample is achieved by removing all the water from the sample *via* ethanol incubation and subsequent alcohol clearing with xylene incubation. The xylene is then replaced by molten paraffin, which infiltrates the sample. The final step involves paraffin-embedding and hardening of the sample, which involves embedment of the specimen into liquid embedding material such as wax. Samples are then stored and archived for future use [1, 3, 4].

The protein profiling of FFPE tissues has immense potential for biomarker discovery and validation. Tumor tissue represents the ideal biological material for cancer proteomics studies and biomarker discovery, since tumor-specific protein markers are typically present at elevated concentrations in patient biopsy tissue [4, 7]. Pathology institutes routinely process and store patient biopsy and/or surgery tissue samples and therefore most pathology archives consist of thousands of FFPE blocks, which often comprise recent as well as decade-old blocks. These repositories contain numerous varieties of patient tissue specimens, including rare malignancies together with metadata such as patient medical records, which contain information about diagnosis, survival, and response to therapy. Due to this and the fact that FFPE samples are easily stored and obtainable, many recent proteomics, genomics and immunohistochemical studies have focused on improving methods for analysis of FFPE tissue [4, 8, 9]. However, the effect of long-term storage, at resource-limited institutions in developing countries, on extractable protein quantity/quality has not yet been investigated. In addition, the optimal sample preparation techniques required for accurate, reproducible results from label-free LC-MS/MS analysis across block ages remains unclear.

[10] found no significant difference in protein identifications from FFPE kidney tissue (normal and tumor) samples that were stored up to 10 years. In addition, some top-down proteomic studies have found no significant difference in protein yields between younger and older FFPE blocks [11], whereas others have found a significant decrease in protein yield as block age increases [12, 13]. The main detrimental pre-analytical factor appears to be tissue fixation time, with longer periods (>24 h) leading to significant decreases in protein yield and number of proteins identified *via* LC-MS/MS [13–15]. During the completion of this study [16], published their work in which they used tandem mass tag labeling and high pH fractionation to evaluate the impact of storage time on FFPE ovarian adenocarcinoma specimens (as old as 32 years) and found an overall decline in identifiable peptides and phosphopeptides due to the formalin fixation process but no further decline/degradation due to storage duration. Even though the aforementioned studies focused on storage duration/block age, to our knowledge there is no evidence to demonstrate the outcome of different protein purification techniques on older samples. There remains a need to provide empirical evidence for the impact of storage duration and conditions within the context of a resource-limited environment, such as the Anatomical Pathology department at Tygerberg Hospital (Western Cape, South Africa).

Due to formalin-induced protein cross-linking, strong detergents such as sodium dodecyl sulfate (SDS) are required for total tissue solubilization and protein extraction from FFPE tissues [17–19]. However, SDS binds to amino acids and thereby changes the protein spatial conformational structure. This, in turn, inhibits proteases, such as trypsin, from accessing protein cleavage sites (which have become distorted through SDS binding) and also inhibits protease activity by changing enzyme conformational structure (through SDS binding). In addition, SDS alters the chromatographic separation of peptides and also interferes with electrospray ionization (ESI) mass spectrometry by dominating mass spectra and significantly suppressing analyte ion signals since it is readily ionizable and present in greater abundances than individual peptide ions. For these reasons, SDS must be completely depleted from a sample before enzymatic digestion and LC-ESI MS/MS analysis [17–20]. However, SDS removal with minimal sample loss is a challenging task and several gel-free approaches have been proposed over the years. These approaches include incorporating the use of detergent removal plates (DRP), protein precipitation with organic solvents, such as the acetone precipitation and formic acid resolubilization (APFAR) method [18, 20, 21], and/or methods using hydrophilic interaction liquid chromatography (HILIC) and magnetic resin (such as the Single-Pot Solid-

TABLE 1 | Information of the FFPE specimens selected for analysis.

Patient number	Block age (years)	Patient age (years)	Gender	Diagnosis	Grade	Stage	Location
1	1	75	M	Adenocarcinoma	Low-grade	IIA	Left colon
2	1	81	M	Adenocarcinoma	Low-grade	IIA	Left colon
3	1	68	F	Adenocarcinoma	Low-grade	IIA	Left colon
4	1	42	M	Adenocarcinoma	Low-grade	IVA	Left colon
5	1	80	F	Adenocarcinoma	Low-grade	I	Left colon
6	1	79	M	Adenocarcinoma	Low-grade	IIA	Left colon
7	1	49	M	Adenocarcinoma	Low-grade	IIA	Left colon
8	1	40	F	Adenocarcinoma	Low-grade	IIA	Left colon
9	1	56	M	Adenocarcinoma	Low-grade	IIA	Left colon
10	1	79	F	Adenocarcinoma	Low-grade	IIA	Left colon
11	1	64	F	Adenocarcinoma	Low-grade	IIA	Left colon
12	1	53	M	Adenocarcinoma	Low-grade	IIIB	Left colon
13	1	78	M	Adenocarcinoma	Low-grade	IIA	Left colon
14	1	51	F	Adenocarcinoma	Low-grade	IIIB	Left colon
15	1	31	M	Adenocarcinoma	Low-grade	IIIB	Left colon
16	1	73	F	Adenocarcinoma	Low-grade	IIIB	Left colon
17	1	54	F	Adenocarcinoma	Low-grade	IIIC	Left colon
18	5	51	F	Adenocarcinoma	Low-grade	IIA	Left colon
19	5	56	F	Adenocarcinoma	Low-grade	IIIB	Left colon
20	5	86	M	Adenocarcinoma	Low-grade	IIA	Left colon
21	5	59	M	Adenocarcinoma	Low-grade	IIC	Left colon
22	5	67	M	Adenocarcinoma	Low-grade	IIA	Left colon
23	5	82	M	Adenocarcinoma	Low-grade	IIA	Left colon
24	5	49	F	Adenocarcinoma	Low-grade	IIIB	Left colon
25	5	54	M	Adenocarcinoma	Low-grade	IIA	Left colon
26	5	58	M	Adenocarcinoma	Low-grade	IIC	Left colon
27	5	44	F	Adenocarcinoma	Low-grade	I	Left colon
28	5	50	M	Adenocarcinoma	Low-grade	IIA	Left colon
29	5	74	F	Adenocarcinoma	Low-grade	IIA	Left colon
30	5	54	M	Adenocarcinoma	Low-grade	IIA	Left colon
31	5	47	F	Adenocarcinoma	Low-grade	IIIA	Left colon
32	5	55	M	Adenocarcinoma	Low-grade	IIIB	Left colon
33	5	83	M	Adenocarcinoma	Low-grade	IIA	Left colon
34	5	60	M	Adenocarcinoma	Low-grade	IIA	Left colon
35	10	69	M	Adenocarcinoma	Low-grade	IIIB	Left colon
36	10	47	F	Adenocarcinoma	Low-grade	IIA	Left colon
37	10	58	F	Adenocarcinoma	Low-grade	IIA	Left colon
38	10	83	M	Adenocarcinoma	Low-grade	IIA	Left colon
39	10	57	F	Adenocarcinoma	High-grade	IIA	Right colon
40	10	46	F	Adenocarcinoma	High-grade	IIA	Right colon
41	10	77	F	Adenocarcinoma	Low-grade	IIA	Left colon
42	10	63	F	Adenocarcinoma	Low-grade	IIA	Left colon
43	10	67	M	Adenocarcinoma	Low-grade	IIIB	Left colon
44	10	50	F	Adenocarcinoma	Low-grade	IIA	Left colon
45	10	42	M	Adenocarcinoma	Low-grade	IIA	Left colon
46	10	71	F	Adenocarcinoma	Low-grade	IIA	Left colon
47	10	70	M	Adenocarcinoma	Low-grade	IIA	Left colon
48	10	69	M	Adenocarcinoma	Low-grade	IIA	Left colon
49	10	62	F	Adenocarcinoma	Low-grade	IIA	Right colon
50	10	78	M	Adenocarcinoma	Low-grade	IIIB	Left colon
51	10	33	M	Adenocarcinoma	Low-grade	IIA	Left colon

Phase-enhanced Sample Preparation (SP3) method) [22] in the sample processing workflow prior to LC-MS/MS analysis.

One of the aims of this study was to methodically characterize the effects of storage time (over 1, 5, and 10 years) on the quality of data produced *via* label-free LC-MS/MS analysis of FFPE tissue blocks from a resource-limited pathology archive, to dispel any notions that these samples may be inferior for whatever reason so that they can be utilized with confidence in any future studies. In addition, three different gel-free protein purification methods (APFAR, DRP and MagReSyn® SP3/HILIC) for label-free LC-MS/MS analysis were also assessed across all block ages. These protein purification methods were published within the last 5 years, and their comparative analysis have not been carried out to our knowledge and this study provides experimental data for this assessment together with statistical support. Furthermore, the best suited method for analyzing archived colorectal carcinoma (CRC) FFPE tissue was determined with regards to peptide and protein identifications, reproducibility, digestion efficiency, and any method-based protein selection bias.

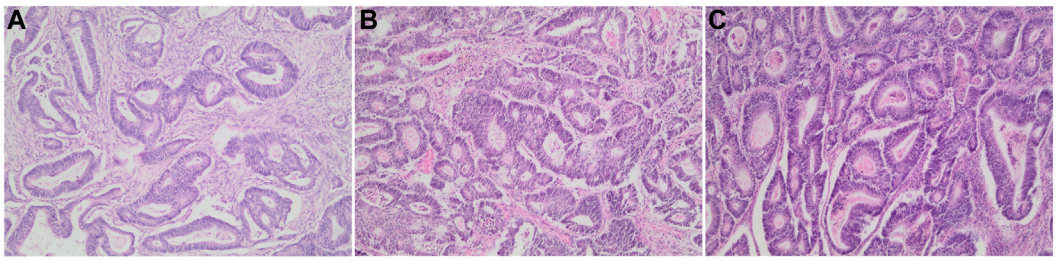

FIGURE 1 | Colonic adenocarcinoma resection tissue samples. Representative H&E stained sections of patient cases/block ages analyzed in this study. **(A)** 1-year-old block. **(B)** 5-year-old block, and **(C)** 10-year-old block at ×100 magnification.

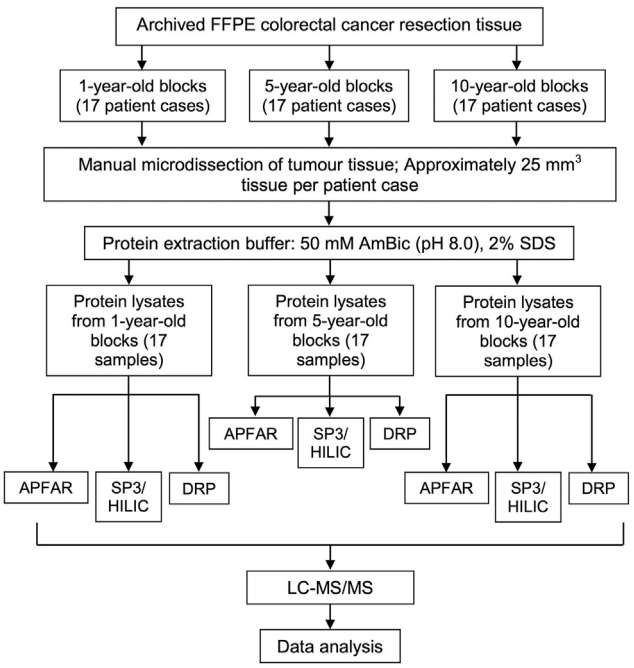

FIGURE 2 | Experimental design and workflow used to evaluate the effects of block age and different sample processing methods. FFPE human colorectal carcinoma resection tissues from 17 patients per block age (1, 5, and 10-year old blocks) were cut and tumor areas were manually micro-dissected for analysis. From each patient, tissue sections, which corresponded to approximately 25 mm^3 tissue per patient/sample, were cut per sample. Protein was extracted and quantified, after which each patient sample was split in three, for subsequent sample processing by either the APFAR, DRP, or SP3/HILIC methods. Resultant peptides were analyzed *via* LC-MS/MS and data analysis was performed on all sample MS/MS spectra.

MATERIALS AND METHODS

FFPE Human Colorectal Carcinoma Resection Samples

FFPE tissue blocks, which consist of human CRC resection samples, were obtained from the Anatomical Pathology department at Tygerberg Hospital (Western Cape, South Africa) after obtaining ethics approval from the Biomedical Science Research Ethics Committee (BMREC) of the University of the Western Cape, as well as the Health Research Ethics Committee (HREC) of Stellenbosch University. The FFPE blocks were anonymized prior to processing. The 1-year-old blocks were archived since approximately 2016 (when the tissue was resected), 5-year-old blocks were archived since 2012, and 10-year-old blocks were archived since 2007 (experiments/protein extractions were performed in 2017/2018). Tissue processing and fixation times/conditions and storage conditions are unknown, since specimens were retrospectively collected. Seventeen patient cases, per block age, were reviewed and selected (**Table 1**). Using protein identification results from a pilot study (unpublished results), an overall F-test for one-way ANOVA determined that the sample size (n = 17) per group/block age resulted in a calculated power of 0.7 (α = 0.05).

Patients diagnosed with colorectal adenocarcinoma, after H&E staining, were reviewed by a pathologist to ensure tissue quality and comparability (**Figure 1**). The selected slides had carcinomas with more than 90% viable tumor nuclei.

Protein Extraction and Quantification

For each selected patient case (n = 17 per experimental condition), a number of 25 µm sections, which were equivalent to 25 mm^3 of manually micro-dissected FFPE tumor tissue per sample, were cut and mounted onto generic glass microscopy slides. Sections were air dried and processed for protein extraction as is shown in **Figure 2** (five batches of samples, with randomized selection and inclusion of samples from each of the different storage times, were processed for protein extraction.) The method used for sample processing and protein extraction was modified from the protocols used by [23, 24]. Briefly, tissue sections (mounted on glass slides) were heated on a heating block (65°C for 5 min), to melt the paraffin wax, followed by tissue deparaffinization consisting of two consecutive incubations in xylene (Sigma-Aldrich, United States) for 2.5 min and 1.5 min each respectively, at room temperature. Tissue sections were then rehydrated by successive incubations in absolute ethanol (Merck, Germany), 70% (v/v) ethanol, and twice with distilled water, for 1 min each at room temperature. The tissues were collected in protein LoBind microcentrifuge tubes (Eppendorf, Germany) by scraping the tissue off the glass slides using a clean sterile scalpel blade. Protein extraction buffer (50 mm Ammonium bicarbonate (AmBic) (pH 8.0) (Sigma-Aldrich, United States), 2% (w/v) SDS

(Sigma-Aldrich, United States) was added to the samples at a volume of approximately 20 µl protein extraction buffer per mm^3 of tissue (approximately 25 mm^3 tissue per sample). Samples were mixed by vortexing and incubated at 99°C in a heating block with agitation set at 600 RPM for 1 h, after which the samples were cooled/placed on ice before centrifugation at 16,000 x g and 18°C for 20 min to pellet the cell debris. The clarified lysates of each sample was transferred to new protein LoBind microcentrifuge tubes and an aliquot taken for protein yield determination. All samples were stored at −80°C until further processing. For protein yield determination, the total protein extracted from the FFPE tissues were quantified using the Pierce™ BCA Protein Assay Kit (Pierce Biotechnology, Thermo Fisher Scientific, United States) according to manufacturer's instructions. The samples were subsequently processed by the DRP, APFAR [18, 20, 21] and/or MagReSyn® SP3/HILIC magnetic bead digestion method [25]; ReSyn Biosciences, South Africa), prior to LC-MS/MS analysis (**Figure 2**).

Protein Purification Methods

Detergent Removal Plates Method

Detergent removal was carried out using detergent removal spin plates (Pierce Biotechnology, Thermo Fisher Scientific, United States) according to the manufacturer's instructions. Briefly, a detergent removal plate was placed on top of a wash plate and the shipping solution spun out at 1,000 x g for 2 min. The resin bed was equilibrated with 300 µl of 50 mm Triethylammonium bicarbonate (TEAB) and spun through as before, and this was repeated twice. Thereafter, 100 µg of protein was loaded onto the columns and incubated at room temperature for 2 min before spinning through at 1,000 x g for 2 min into the sample collection plate. Samples were then transferred to protein Lobind tubes and dried down by vacuum centrifugation. Once dried, samples were resuspended in 30 µl of 50 mm TEAB.

Acetone Precipitation and Formic Acid Resolubilization Method

A total of 100 µg protein was transferred to each protein Lobind microcentrifuge tube and precipitated by addition of four volumes of ice cold acetone (Sigma-Aldrich, United States) followed by overnight incubation at −20°C. Samples were then centrifuged at 21,000 x g for 15 min at 4°C. The supernatant was discarded and the pellet washed with ice cold acetone. This process was repeated for a total of three pelleting steps. Thereafter, the pellets were air-dried and subsequently solubilized by resuspension in 50 mm TEAB.

In-Solution Digestion

In-solution digestion was carried out on samples processed by the APFAR and DRP methods. The protein was reduced by the addition of 0.1 volumes of 100 mm tris(2-carboxyethyl) phosphine (TCEP) (Sigma-Aldrich, United States) to each sample followed by incubation at 60°C for 1 h. Alkylation was accomplished by addition of 0.1 volumes of 100 mm methyl methanethiosulphonate (MMTS) (Sigma-Aldrich, United States), which was prepared in isopropanol (Sigma-Aldrich, United States), to each sample and subsequent incubation at room temperature for 15 min. Protein digestion was accomplished by addition of 1:50 (trypsin: final protein ratio) trypsin (Promega, United States) in a solution with 50 mm TEAB, and overnight incubation at 37°C. Samples were dried down and resuspended in 0.1% trifluoroacetic acid (TFA) (Sigma-Aldrich, United States) prior to clean-up *via* Zip-Tip (Sigma-Aldrich, United States), after which the samples were again dried down and resuspended in a final volume of 12 µl liquid chromatography (LC) loading buffer (0.1% formic acid (FA) (Sigma-Aldrich, United States), 2% Acetonitrile (ACN) (Burdick and Jackson, United States).

MagReSyn® SP3/HILIC Method With On-Bead Digestion

In preparation for the SP3/HILIC magnetic bead workflow, MagReSyn® HILIC beads (ReSyn Biosciences, South Africa) were aliquoted into a new tube and the shipping solution removed. Beads were then washed with 250 µl wash buffer (15% ACN, 100 mm Ammonium acetate (Sigma-Aldrich, United States) pH 4.5) for 1 min then resuspended in loading buffer (30% ACN, 200 mm Ammonium acetate, pH 4.5). The rest of the process, described hereafter, was performed using a Hamilton MassSTAR robotics liquid handler (Hamilton, Switzerland). A total of 50 µg of protein from each sample was transferred to a protein LoBind plate (Merck, Germany). Protein was reduced with 10 mm TCEP (Sigma-Aldrich, United States) and incubated at 60°C for 1 h. Samples were cooled to room temperature and alkylated with 10 mm MMTS (Sigma-Aldrich, United States) at room temperature for 15 min. MagReSyn® HILIC magnetic beads were added at an equal volume to that of the sample and a ratio of 5:1 total protein. The plate was incubated at room temperature on a shaker at 900 RPM for 30 min for binding of protein to beads. After binding, the beads were washed four times with 500 µl of 95% ACN for 1 min each. For digestion, trypsin (Promega, United States) made up in 50 mm TEAB was added at a ratio of 1:10 total protein, and the plate was incubated at 37°C on the shaker for 4 h. After digestion, the supernatant containing the peptides was removed and dried down. The samples were then resuspended in LC loading buffer [0.1% FA (Sigma-Aldrich, United States), 2% ACN (Burdick & Jackson, United States)].

Label–Free LC–MS/MS Analysis

LC-MS/MS analysis was conducted with a Q-Exactive quadrupole-Orbitrap mass spectrometer (Thermo Fisher Scientific, United States) coupled with a Dionex Ultimate 3,000 nano-UPLC system. All samples run by LC-MS/MS were in a randomized order. Peptides were dissolved in a solution of 0.1% FA and 2% ACN and loaded on a C18 trap column (PepMap100, 300 µm × 5 mm × 5 µm). Samples were trapped onto the column and washed for 3 min before the valve was switched and peptides eluted onto the analytical column as described hereafter. A gradient of increasing organic proportion was used for peptide separation - chromatographic separation was performed with a Waters nanoease (Zenfit) M/Z Peptide CSH C18 column (75 µm × 25 cm × 1.7 µm) and the solvent

system employed was solvent A [0.1% FA in LC water (Burdick and Jackson, United States)] and solvent B (0.1% FA in ACN). The multi-step gradient for peptide separation was generated at 300 nl/min as follows: time change 5 min, gradient change: 2–5% solvent B, time change 40 min, gradient change 5–18% solvent B, time change 10 min, gradient change 18–30% solvent B, time change 2 min, gradient change 30–80% solvent B. The gradient was then held at 80% solvent B for 10 min before returning it to 2% solvent B and conditioning the column for 15 min. All data acquisition was obtained using Proxeon stainless steel emitters (Thermo Fisher, United States). The mass spectrometer was operated in positive ion mode with a capillary temperature of 320°C. The applied electrospray voltage was 1.95 kV. The mass spectra were acquired in a data-dependent manner using Xcalibur™ software version 4.2 (Thermo Fisher, United States) (Details of data acquisition parameters are shown in **Supplementary Table S1**).

Peptide and Protein Identification

Raw data containing centroid MS/MS spectra were converted into mgf (Matrix Science, United Kingdom) files using msconvert from the Proteo-Wizard software suite [12]. Peak lists obtained from MS/MS spectra were identified using X! Tandem (version X!Tandem Vengeance 2015.12.15.2) [26], MS Amanda (version 2.0.0.9706) [27] and MS-GF+ (version 2018.04.09) [28]. The search was conducted using SearchGUI (version 3.3.3) [29]. Protein identification was conducted against a concatenated target/decoy [30] version of the *Homo sapiens* (20,341, >99.9%) [with *Sus scrofa* (1, <0.1%)] complement of the UniProtKB [31] human reviewed Swiss-Prot proteome (one trypsin *Sus scrofa* sequence was also obtained from UniProtKB), downloaded on May 21, 2018 (**Supplementary Data Sheet S1**). The decoy sequences were created by reversing the target sequences in SearchGUI. The identification settings were as follows: Trypsin, Specific, with a maximum of 2 missed cleavages; 10.0 ppm as MS1 and 0.02 Da as MS2 tolerances; fixed modifications: Methylthio of C (+45.987,721 Da), variable modifications: Oxidation of M (+15.994,915 Da), Deamidation of N and Q (+0.984,016 Da); fixed modifications during refinement procedure: Methylthio of C (+45.987,721 Da), variable modifications during refinement procedure: Acetylation of protein N-term (+42.010565 Da), Pyrolidone from E (--18.010565 Da), Pyrolidone from Q (--17.026549 Da), Pyrolidone from carbamidomethylated C (--17.026549 Da). All algorithms specific settings are listed in the certificate of analysis available in **Supplementary Data Sheet S1**. Peptides and proteins were inferred from the spectrum identification results using PeptideShaker version 1.16.40 [32]. Peptide Spectrum Matches (PSMs), peptides and proteins were validated at a 1% False Discovery Rate (FDR) estimated using the decoy hit distribution (example of an annotated MS/MS spectrum for a peptide is shown in **Supplementary Image S1**). All validation thresholds are listed in the certificate of analysis (**Supplementary Data Sheet S1**). Post-translational modification localizations were scored using the D-score [33] and the phosphoRS score [34] with a threshold of 95.0 as implemented in the compomics-utilities package [35] (example of post-translational modification localizations for a peptide is shown in **Supplementary Image S2**).

Data and Statistical Analyses

Qualitative and quantitative data were exported from PeptideShaker and parsed using in-house scripts and graphs generated in Jupyter lab (using Pandas, NumPy, and Matplotlib Python packages), as well as Microsoft® Excel. Additional statistical analyses were performed using SAS® university edition and SAS® Studio version 3.8 (results of the statistical tests that were performed are listed in **Supplementary Table S2**). To determine if sample distributions were normal, a Kolmogorov–Smirnov or Shapiro–Wilk test was performed, with D denoting the test statistic for the Kolmogorov–Smirnov test and W denoting the test statistic for the Shapiro–Wilk test. For normal distributions, comparison of means across 3 (or more) groups was performed using the parametric ANOVA procedure, with F (F-ratio) denoting the test statistic. The Kruskal–Wallis nonparametric test for medians was used when data were from a non-normal distribution, and H denotes the test statistic. For all statistical reporting, the test statistic value is given along with the degrees of freedom (in brackets after the test statistic symbol) and *p*-value. Post hoc statistical analyses were performed on significant results using Bonferroni or Dunn's test [36]; Elliott and Hynan, 2011).

Spectrum counting abundance indexes were estimated using the Normalized Spectrum Abundance Factor (NSAF) [37] adapted for better handling of protein inference issues and peptide detectability. The NSAF method followed here involves counting the number of spectra attributed to each protein in the result set, which is subsequently normalized to a relative abundance [29, 37, 38]. In the PeptideShaker implementation, this count is then normalized for the length of the protein, the presence of shared peptides, as well as redundant peptides [29, 38]. The spectrum counting indexes were exported from PeptideShaker and parsed using in-house scripts. The NSAF values were multiplied by the lowest factor calculated for each pair of conditions compared, in order to deal with integers and facilitate comparisons. These NSAF values were then used to estimate the extent of differential protein abundance by calculating the Pearson's correlation coefficient (PCC), for each pair of conditions compared, to assess the relationship/level of correlation between samples. PCC graphs were generated in Jupyter lab using Pandas, NumPy, and Matplotlib Python packages. Principal component analysis (PCA) was performed for each patient case/sample's list of identified proteins and corresponding NSAF values, with Jupyter lab, using Pandas, NumPy, Scikit-learn, Seaborn and Matplotlib Python packages.

The physicochemical properties of the identified peptides, including the hydropathicity (Kyte-Doolittle scale), molecular weight, and isoelectric point were calculated for each sample using the Protein property analysis software (ProPAS) version 1.1 [39].

Venny version 2.1.0 [40] was used to generate Venn diagrams to visualize the consistency of peptide identifications between samples.

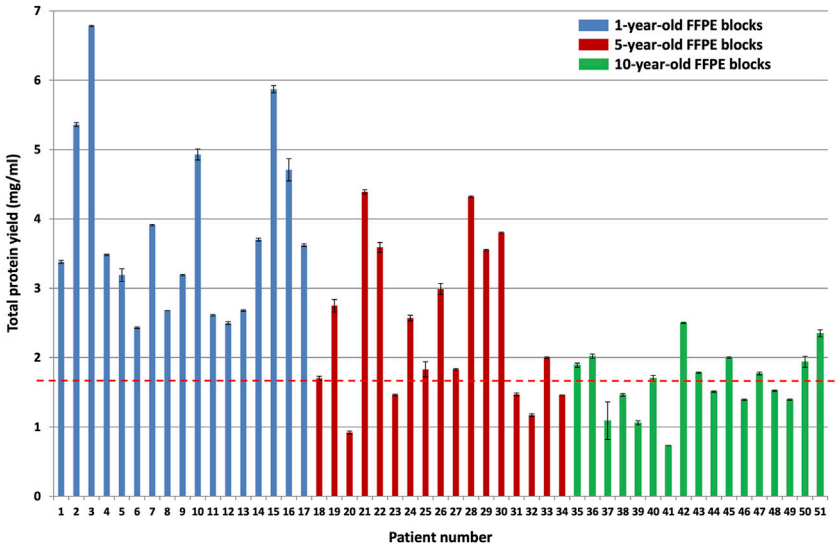

FIGURE 3 | BCA total protein quantitation assay results for the different block ages. Protein was extracted from approximately 25 mm^3 patient tumor tissue using 500 µl protein extraction buffer per sample ($n = 17$ patients per group, $p < 0.0001$). The blue bars indicate protein yield from 1-year-old FFPE blocks, the red bars indicate protein yield from 5-year-old FFPE blocks, and the green bars indicate protein yield from 10-year-old FFPE blocks. The red dotted line indicates the average protein yield obtained from the 10-year-old FFPE blocks, which is 1.65 mg/ml protein.

Protein annotations regarding subcellular localization were retrieved from Ensembl[1] using GOSlim UniProtKB-GOA[2] to minimize the number of terms retrieved. Hypergeometric testing was used to calculate the significance of gene ontology terms.

Inkscape Version 0.92.4 (5da689c313, 2019–01-14) (https://www.inkscape.org) was used to combine multiple graphs into single figures, add color and/or patterns and increase figure resolution.

Data Sharing Information

The mass spectrometry proteomics data [41] have been deposited to the ProteomeXchange Consortium [42] *via* the PRIDE [43] partner repository with the dataset identifier PXD017198 and DOI: 10.6019/PXD017198.

Default PeptideShaker protein reports for each sample and quality controls are listed in **Supplementary Tables S3–S5**.

RESULTS AND DISCUSSION

The objectives of this study were to evaluate three different sample processing methods (the APFAR or DRP methods followed by in-solution digestion, or the SP3/HILIC method with magnetic bead-based digestion) as well as the effect of storage time (FFPE tissue block age) on protein extraction efficiency and reproducibility. Subsequent proteomic analysis by label-free LC-MS/MS evaluated the proteome coverage, proportion of missed cleavages, and enrichment/selection bias based on sample processing method used.

Protein Extraction and Quantification

The BCA total protein quantitation assay results of all samples (after protein was extracted from approximately 25 mm^3 patient tumor tissue using 500 µl of protein extraction buffer per sample) are shown in **Figure 3**.

A Kruskal–Wallis test was conducted to examine the differences in protein yield between block ages (**Supplementary Table S2**). Protein yield was significantly affected by block age ($H(2) = 23.92$, $p < 0.0001$), as seen in **Figure 3**. Based on Dunn's post hoc testing results, there is evidence that the distribution of protein yields are significantly different for 1-year-old blocks vs 10-year-old blocks and for 1-year-old blocks vs 5-year-old blocks, but not for 5-year-old blocks vs 10-year-old blocks (results and conclusions are shown in **Supplementary Table S2**).

The 10-year-old FFPE tissues generated overall lower protein yields (an average of 1.65 ± 0.04 mg/ml) compared to the 5-year-old FFPE tissues, which generated an average of 2.46 ± 0.03 mg/ml protein, and the 1-year-old FFPE tissues, which generated an average of 3.82 ± 0.03 mg/ml protein. This corresponds to approximately 825 µg, 1,230 µg, and 1910 µg protein extracted from the 10, 5 and 1-year-old FFPE tissues, respectively, by using approximately 25 mm^3 tissue per sample [14]. were able to extract 300–400 µg (0.14 mg/ml) protein from 1.18 mm^3 FFPE colon adenoma tissue (of 60 µm thickness and 5 mm diameter), which is approximately 4 times higher. However, they noted a suppressive effect of formalin-fixation on protein yield estimates, using the BCA assay. This effect occurs because the amino acids that contribute to the reduction of copper are also

[1]www.ensembl.org

[2]www.ebi.ac.uk/GOA

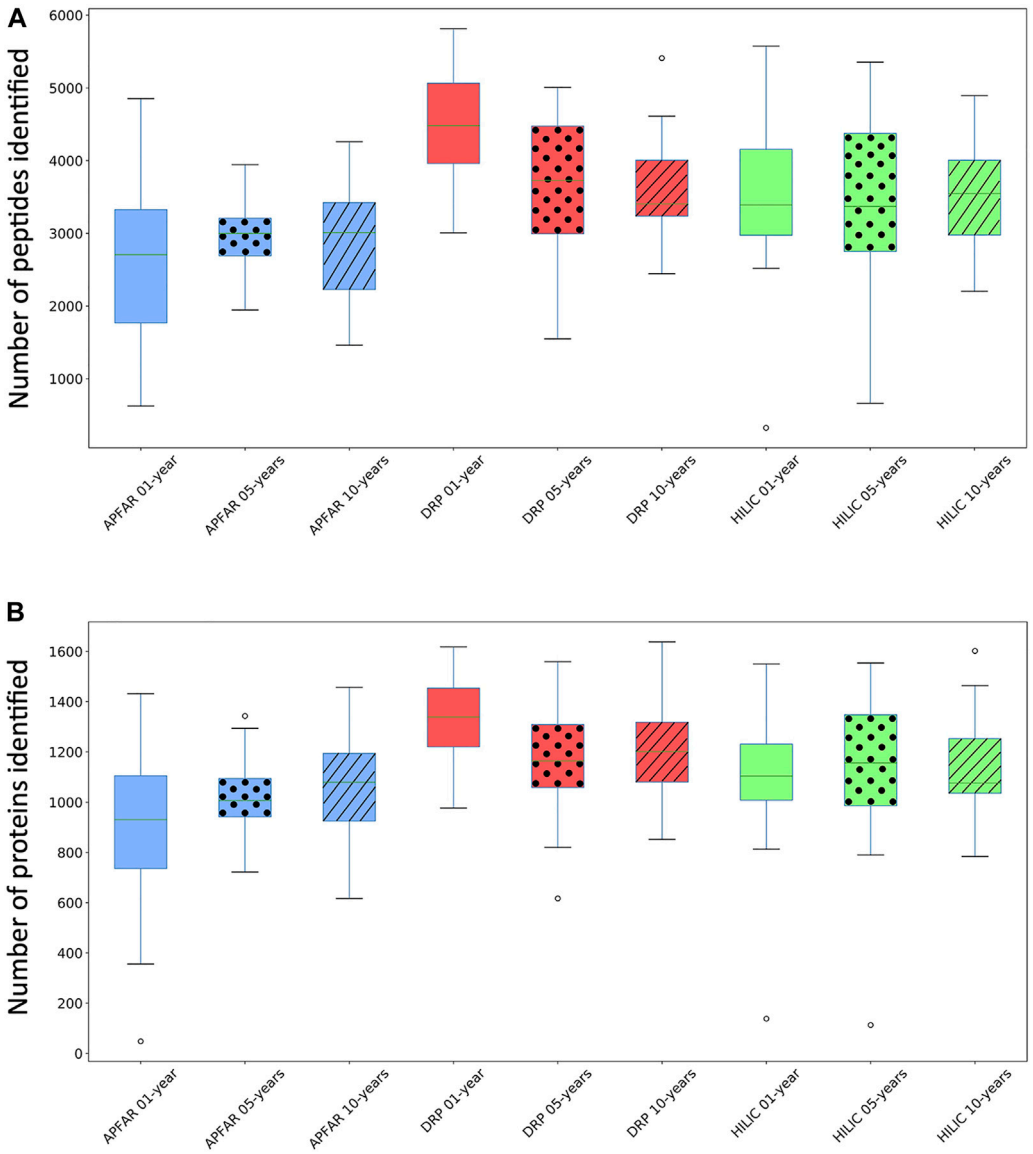

FIGURE 4 | Comparison of the number of peptides and proteins identified for the different protein purification methods for each block age. **(A)** Box and whiskers plots of the number of peptides identified (for all 17 patient cases) per block age ($p < 0.03$ for 1 and 10-year-old blocks), and protein purification method ($p = 0.0125$ for DRP). **(B)** Box and whiskers plots of the number of proteins identified (for all 17 patient cases) per block age ($p = 0.0002$ for 1-year-old blocks) and protein purification method ($p > 0.05$ for all methods). Blue boxplots refer to APFAR samples; Red boxplots refer to DRP samples; Green boxplots refer to SP3/HILIC samples. For all boxplots, 5-year-old samples are represented by dots; 10-year-old samples are represented by diagonal lines.

susceptible to reactions with formaldehyde. Therefore, they empirically determined a correction factor for protein yield estimates of FFPE tissues (using the BCA assay) by comparing it to freshly frozen colon adenoma tissue replicates' protein yields. They then used this correction factor to measure the amount of protein generated from their FFPE samples. Since we are not comparing fresh tissues to FFPE tissues, we did not determine the correction factor of our dataset and we report the protein yield estimates only. In addition [44], also extracted higher protein yields at 100 mg/ml protein from 0.1 mm^3 FFPE colonic adenoma tissue and [13] extracted 2.76 mg/ml protein from approximately 1-year-old and 1.48 mg/ml protein from approximately 21-year-old (1.5 mm^3) FFPE colon carcinoma tissue. On the other hand [45], extracted less protein than reported here, with 250 µg protein from approximately 18 mm^3 FFPE colon carcinoma tissues that were stored for less than 5 years. Therefore, the amount of protein extracted here falls within the published ranges for FFPE colon tissue.

Although approximately 25 mm^3 of manually microdissected tumor tissue per sample was used for protein extraction, and the volume of protein extraction buffer kept constant at 500 µl per sample, the total amount of extractable protein and protein yield

TABLE 2 | Known proteins deregulated in colon cancer.

					% Occurrence within 17 patient samples								
					APFAR			DRP			HILIC		
Main accession	Gene name	Protein name	MW (kDa)	Comments	1 year old	5 year old	10 year old	1 year old	5 year old	10 year old	1 year old	5 year old	10 year old
O95994	AGR2	Anterior gradient protein 2 homologue	19.97	Downregulated in CRC [47]	88	100	94	94	100	94	100	94	100
Q13951	CBFB	Core-binding factor subunit beta	21.49	Frequently overexpressed in CRC [48]	12	41	24	35	35	47	0	12	6
P08174	CD55; DAF	Complement decay-accelerating factor	41.37	Upregulated in CRC [49]	0	0	6	0	0	0	0	0	0
P10645	CHGA	Chromogranin-A	50.66	Downregulated in CRC [50]	29	29	18	18	18	18	24	18	18
A8K7I4	CLCA1	Calcium-activated chloride channel regulator 1	100.16	Regulator of calcium channels, frequently downregulated in CRC [51]	59	53	41	59	59	47	53	53	47
Q96KP4	CNDP2	Cytosolic non-specific dipeptidase	52.84	Overexpressed in CRC [52]	82	88	94	100	88	100	94	94	100
P07148	FABP1	FABP1 protein	14.20	Downregulated in CRC [47]	100	100	71	94	100	88	94	100	88
Q9Y6R7	FCGBP	IgGFc-binding protein	571.64	Downregulated in CRC [47]	76	94	82	76	94	76	82	88	82
P56470	LGALS4	Galectin-4	35.92	Downregulated in CRC [47]	100	100	100	100	100	100	94	100	100
P09429	HMGB1	High mobility group protein B1	24.88	Overexpression in CRC correlates with poor prognosis [53]	76	88	76	100	100	94	94	82	94
P01042	KNG1	Kininogen-1	71.91	Frequently overexpressed in CRC [54]	29	41	53	53	59	82	29	47	65
Q9UHB6	LIMA1	LIM domain and actin-binding protein 1	85.17	Downregulated in CRC [47]	0	0	6	0	0	24	6	6	0
P15941	MUC-1	Mucin-1	122.03	Frequently overexpressed in CRC, marker of poor prognosis [55]	0	6	12	6	6	12	0	6	6
Q02817	MUC-2	Mucin-2	539.96	Downregulation correlates with proliferation markers and with poor prognosis [55, 56]	59	59	76	71	65	71	65	71	76
P06748	NPM1	Nucleophosmin	32.55	Protein involved in carcinogenesis, overexpressed in CRC [57, 58]	100	100	100	100	100	100	100	100	100
Q6UX06	OLFM4	Olfactomedin-4	57.24	Protein overexpressed in CRC [54]	29	18	29	35	24	29	29	24	29
Q9Y617	PSAT1	Phosphoserine aminotransferase	40.40	Upregulated in CRC [59]	0	0	6	18	12	12	18	12	18
P53992	Sec24C	Protein transport protein Sec24C	118.25	Overexpressed in early CRC stages, while downregulated in advanced CRC stages [54]	0	0	0	0	6	6	6	0	0
P36952	SERPIN B5	Serpin B5	42.07	Upregulated in CRC [60]	29	6	29	35	6	29	29	6	29
P10599	TXN	Thioredoxin	11.73	Frequently overexpressed in CRC [61]	94	100	100	94	100	100	94	94	94

still differed among the patient samples within the same block ages (**Figure 3**). Similar variations in protein yields were also observed by [13] and is also noted in FFPE protein extraction protocols, such as the [46] manual, which explains that protein yield obtained from FFPE protein lysates may vary between samples due to variance in pre-analytical factors such as tissue handling and inconsistencies/differences in the formalin-fixation and paraffin-embedment protocol, which affects how well proteins will be preserved. They recommend increasing the amount of starting material/tissue if the quality of protein preservation in the FFPE sample is questionable [46].

The Effect of Block Age and Protein Purification Methods on Peptide and Protein Identification

The efficiency and reproducibility for each protein purification method, as well as the effect of storage time/block age, at both peptide and protein level, was assessed with regards to proteome coverage (number of peptides and proteins identified) (**Figures 4A,B**) and known protein biomarkers (proteins deregulated in colon cancer) from the literature, which were also identified in the data (**Table 2**).

Average results for all samples (**Figure 4**) show that, overall, the DRP method performed the best with the highest overall peptide and protein identifications, followed by the SP3/HILIC method. The APFAR method generated the lowest numbers of peptide and protein identifications (Results are shown in **Supplementary Table S6**).

One-way ANOVA or Kruskal–Wallis tests were conducted (results and conclusions are listed in **Supplementary Table S2**) to determine if the number of identified peptides and proteins were significantly different between block ages, as well as for each protein purification method.

Statistical analyses comparing protein purification method performance per block age indicated the following: For the 1-year-old blocks, based on post hoc Bonferroni (Dunn) t tests, the DRP method differs significantly ($F(2) = 12.78$, $p < 0.0001$, $\alpha = 0.05$) with regards to validated peptide identifications, however there was no significant difference between the numbers of validated peptides identified for the APFAR and SP3/HILIC methods. Based on Dunn's post hoc testing results, there is also evidence that the distribution of validated protein identifications (for 1-year old blocks) are significantly different ($p = 0.0002$) for DRP vs APFAR processing, but not for DRP vs HILIC and APFAR vs HILIC protein purification methods. With regards to validated peptide and protein identifications, there is no significant difference ($p > 0.05$) between protein purification methods for 5-year old blocks. For the 10-year old blocks, based on post hoc Bonferroni (Dunn) t tests, the DRP and APFAR methods differ significantly ($F(2) = 3.78$, $p = 0.0299$, $\alpha = 0.05$) with regards to validated peptide identifications, however there is no significant difference between the APFAR and SP3/HILIC and the DRP and SP3/HILIC methods.

Statistical analyses comparing the differences between block ages (effect of block age on the number of peptide/protein identifications) within each protein purification method indicated the following: Both the APFAR and SP3/HILIC methods performed most consistently across block ages, with no significant difference between 1, 5 and 10-year-old blocks [APFAR method: $F(2,48) = 0.88$, $p = 0.42$ for peptides identified and $H(2) = 2.28$, $p = 0.32$ for proteins identified; SP3/HILIC method: $F(2,48) = 0.03$, $p = 0.97$ for peptides identified and $H(2) = 0.101$, $p = 0.95$ for proteins identified]. Only the DRP method showed a significant difference between the block ages with regard to numbers of peptides identified [$F(2) = 4.81$, $p = 0.0125$, $\alpha = 0.05$], with a significant difference between 1 and 5-year-old blocks, as well as 1 and 10-year-old blocks, but no significant difference between 5 and 10-year-old blocks. In addition, no significant difference was detected for the number of proteins identified [$F(2,48) = 2.53$, $p = 0.09$].

The protein purification methods that did not show any significant differences between block ages, are in accordance with the findings of other studies [10, 14]. [14] also assessed the effect of storage time/block age on FFPE colon adenoma tissue samples (stored for 1, 3, 5, or 10 years), using isoelectric focusing to fractionate peptides before LC-MS/MS analysis. They found no significant difference between the numbers of proteins identified for each block age and concluded that long-term storage of FFPE colon adenoma tissues did not compromise the samples. In general, the proteome coverage reported here (for all the block ages and protein purification methods) falls within the range of several other studies of proteomic analysis of FFPE tissue [3, 14, 62, 63], with higher identification numbers reported by other studies [10, 44, 64, 65]. **Table 2** shows known proteins that are deregulated in colon cancer that were also identified in the data. The % occurrence of these proteins within each group of 17 patients per experimental condition was calculated and shows that there are no observable differences due to block age. However, the DRP method shows overall higher % occurrence of these protein biomarkers, compared to the other protein purification methods.

The Effect of Block Age and Protein Purification Methods on Peptide-Level Reproducibility

The qualitative reproducibility for each sample and experimental condition was also measured in terms of peptide identification overlap (shown in **Supplementary Image S3**), calculated from the peptide sequences identified in each sample and experimental condition, irrespective of peptide abundance.

Supplementary Image S3A illustrates that the APFAR method showed the highest peptide overlap/common peptides (46.5%) between samples of different block ages. This was followed by the SP3/HILIC method, with 45.4% peptide overlap, and the lowest peptide overlap was seen for the DRP method at 43%. Overall, there was no substantial difference between uniquely identified peptides of the different block ages (ranging from 11.3% to 13.2%) for the APFAR and SP3/HILIC methods. However, the 1-year-old blocks processed with the DRP method had the highest percentage of uniquely identified peptides at 20.4%.

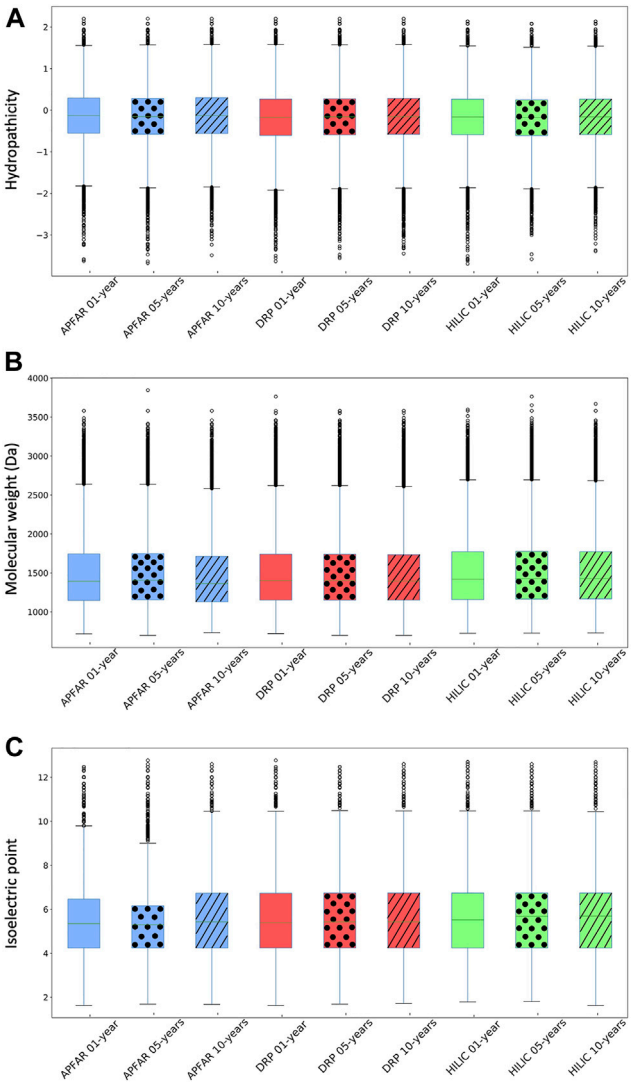

FIGURE 5 | Physicochemical properties of identified peptides for all experimental conditions (n = 17 patients per group). **(A)** Hydropathicity based on GRAVY scoring matrix. **(B)** Molecular weight (MW). **(C)** Isoelectric point (pI). Blue boxplots refer to APFAR samples; Red boxplots refer to DRP samples; Green boxplots refer to HILIC samples. For all boxplots, 5-year-old samples are represented by dots; 10-year-old samples are represented by diagonal lines.

The shared peptides for each protein purification method within a specific block age are shown in **Supplementary Image S3B**. The 10-year-old blocks showed the highest peptide overlap/common peptides (37.5%) between the different protein purification methods. This was followed by the 5-year-old blocks, with 36.7% peptide overlap, and the lowest peptide overlap was seen for the 1-year-old blocks at 33.3%. This could be due, in part, to similar proteins extracted from the older blocks (since formaldehyde-induced cross-linking continues with time), compared to more diverse sets of proteins extracted from the more recently preserved 1-year-old blocks [66]. Due to the continuation and extent of formaldehyde-induced protein cross-linking with time, the extraction of full-length proteins from older FFPE blocks is also more difficult [66]. In addition [67], were able to identify small proteins, without antigen retrieval and enzymatic digestion steps, *via* mass spectrometry imaging. They hypothesize that not all proteins, especially small proteins (with short amino acid sequences and low lysine content), react with formaldehyde to the same extent. However, larger proteins (with longer amino acid sequences and greater lysine content) were more challenging to detect *via* mass spectrometry, and therefore have a greater probability of being more extensively crosslinked by formaldehyde. On average, for all block ages and protein purification methods, the identified proteins were in the range of 40–60 kDa (data not shown). This therefore indicates that mostly low and medium molecular weight proteins were extracted from the FFPE tissues at all block ages.

Supplementary Image S3C shows that, when all the identified peptides for each block age is combined within a protein purification method, there is 34.1% overlapping peptides shared between the different methods. The DRP method had the highest percentage of uniquely identified peptides at 19.5%, followed by the SP3/HILIC method, with 15.8% unique peptides, and the lowest uniquely identified peptides was seen for the APFAR method at 9.9%.

Physicochemical Properties of Extracted and Processed Peptides

The effect of archival time/block age as well as protein purification method protein selection/enrichment bias was assessed with regards to peptide sequence physicochemical properties in **Figure 5**, which illustrates the peptide distribution according to hydropathicity, molecular weight and isoelectric point (pI). Kruskal–Wallis tests were conducted to determine if there were significant differences between experimental conditions (**Supplementary Table S2**).

Overall, a comparison of the majority (upper and lower quartiles) of all peptides of all experimental conditions shows that they share similar hydropathicity scales (**Figure 5A**). There is a significant difference ($p < 0.0001$) between the hydropathicity of peptides generated in all experimental conditions (**Supplementary Table S2**), however, the average relative hydropathicity of all the samples are negative (below zero), which indicates that the majority of peptides that were extracted and processed, by all three protein purification methods and across all block ages are hydrophilic [36, 68].

Figure 5B indicates that the molecular weight ranges of identified peptides are relatively constant across all samples and experimental conditions, with the majority >1000 Da and <2000 Da. There is a significant difference ($p < 0.0001$) between the molecular weights of peptides generated *via* the different protein purification methods for 1, 5 and 10-year old blocks. With regards to block age differences, there is no significant difference ($p = 0.26$) between the molecular weights of peptides generated *via* the DRP method, however there is a significant difference ($p < 0.05$) between the molecular weights of peptides generated using the APFAR and/or SP3/HILIC methods.

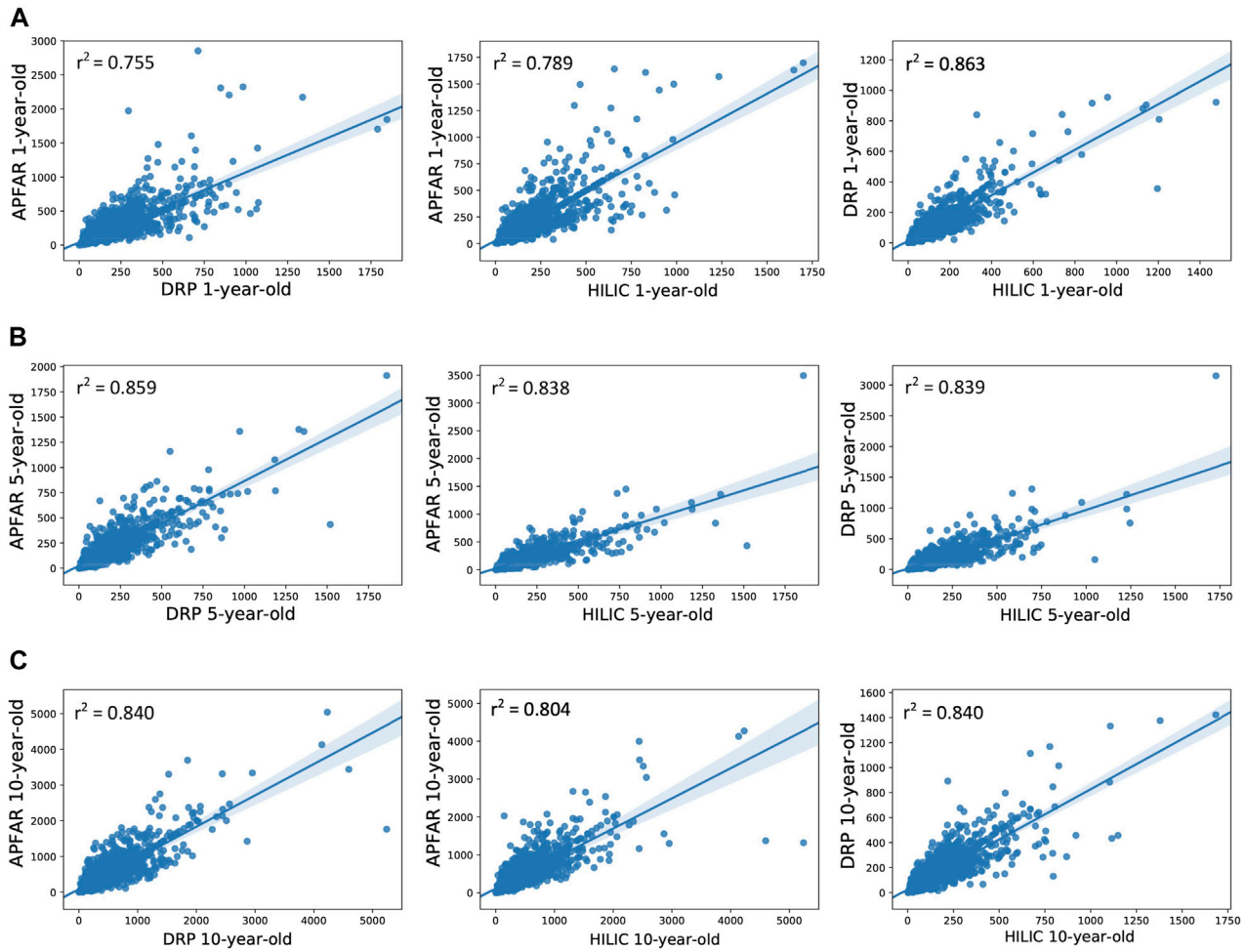

FIGURE 6 | Correlation of protein abundance between all protein purification methods for each patient sample. **(A)** Correlation of protein abundance for all protein purification methods for 1-year-old blocks/samples (n = 17 patients per group). **(B)** Correlation of protein abundance for all protein purification methods for 5-year-old blocks/samples (n = 17 patients per group). **(C)** Correlation of protein abundance for all protein purification methods for 10-year-old blocks/samples (n = 17 patients per group). The Pearson correlation coefficients (r^2) are indicated on each plot and plot axes values are the normalized NSAF values for proteins present in both condition compared per plot.

There is a significant difference ($p < 0.0001$) between the pI ranges of peptides generated in all experimental conditions, however, the pI range values are relatively similar across all samples and experimental conditions, with the majority above pI 4 and below pI 7 (**Figure 5C**).

These results are in accordance with previous studies that used the APFAR and SP3/HILIC methods [20–22, 69].

The Effect of Block Age and Protein Purification Methods on Protein-Level Reproducibility

The quantitative reproducibility between experimental conditions were expressed as PCC dot plots (**Figure 6**), which were calculated based on the NSAF abundance values for identified proteins in each sample and experimental condition. PCA plots were also generated from this data to assess the variance between block ages and the protein purification methods (**Figure 7**).

Figure 6 shows the correlation of protein abundance for all protein purification methods for each block age. This illustrates that, for 1-year-old blocks, the DRP and SP3/HILIC methods yielded comparable relative protein abundances (PCC value of 0.863), whereas proteome composition correlation was lower for the AFFAR and DRP (PCC value of 0.755) as well as APFAR and SP3/HILIC (PCC value of 0.789) methods. Overall, the 5 and 10-year-old blocks show similar proteome composition correlation between the protein purification methods.

For 5-year-old blocks, the PCC values for the APFAR and SP3/HILIC, as well as DRP and SP3/HILIC methods are approximately equal, 0.838 and 0.839, respectively. The APFAR and DRP method has a higher PCC value of 0.859, indicating slightly higher correlation in proteome composition between these two protein purification methods.

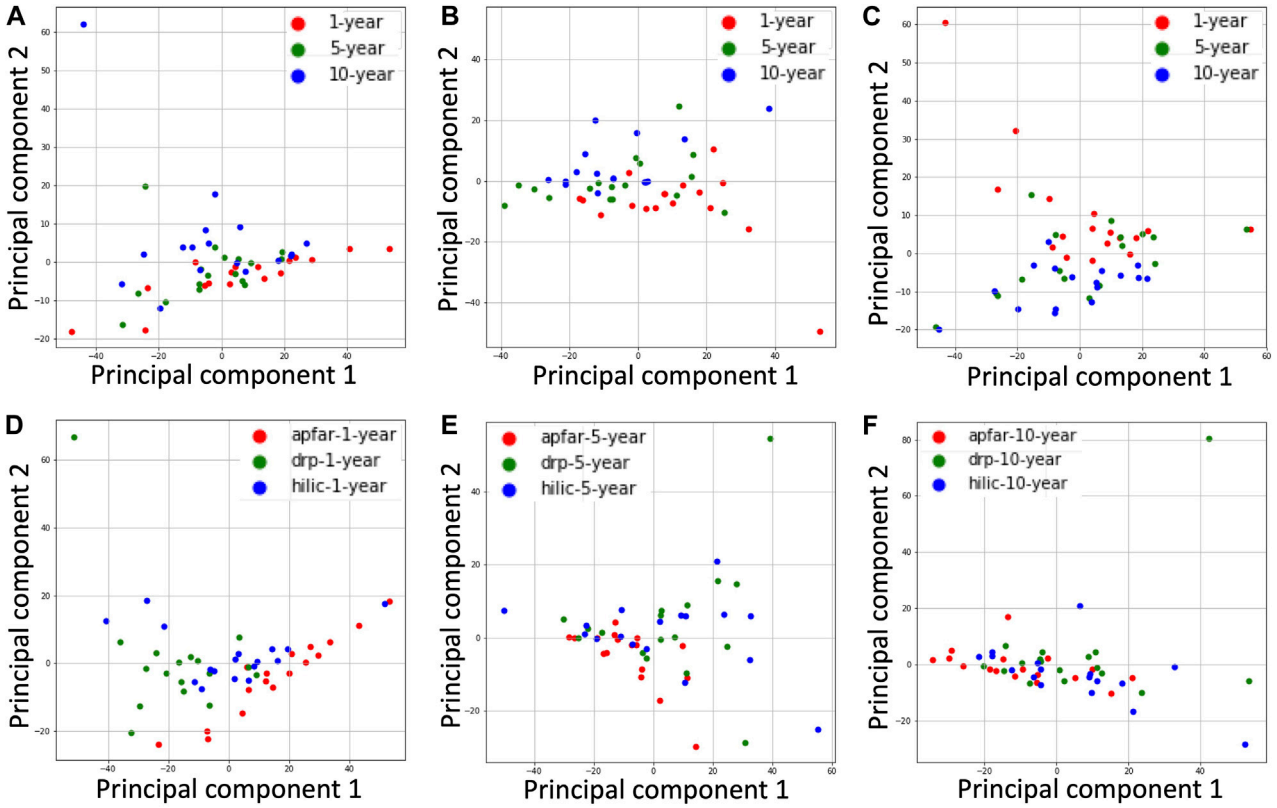

FIGURE 7 | PCA plots for all block ages and protein purification methods. The NSAF values for proteins identified from each patient case were normalized and dimensionality reduced by principal component analysis of the datasets. **(A)** PCA plot of all block age (1-year-old = red; 5-year-old = green; 10-year-old = blue) samples processed via the APFAR method. **(B)** PCA plot of all block age (1-year-old = red; 5-year-old = green; 10-year-old = blue) samples processed via the DRP method. **(C)** PCA plot of all block age (1-year-old = red; 5-year-old = green; 10-year-old = blue) samples processed via the HILIC method. **(D)** PCA plot of 1-year-old samples for all protein purification methods (APFAR = red; DRP = green; HILIC = blue). **(E)** PCA plot of 5-year-old samples for all protein purification methods (APFAR = red; DRP = green; HILIC = blue). **(F)** PCA plot of 10-year-old samples for all protein purification methods (APFAR = red; DRP = green; HILIC = blue).

For 10-year-old blocks, the PCC values for the APFAR and DRP as well as DRP and SP3/HILIC methods were the same. The APFAR and SP3/HILIC method has a lower PCC value of 0.804, indicating slightly lower correlation in proteome composition between these two protein purification methods. These results indicate that sample processing with the different methods introduces an observable bias with regard to proteome composition. This bias is also more pronounced for 1-year-old blocks, compared to older blocks.

PCA plots showing clusters of samples, based on their similarities, were generated for all block ages and protein purification methods (**Figure 7**). The samples that have similar expression profiles are clustered together. **Figures 7A–C** show the clustering of different block ages (1, 5, and 10 years) for each protein purification method, with the DRP method having the lowest variance (10.73%) between block ages, followed by the SP3/HILIC method (13.68%), and the APFAR method, which has the highest variance at 14.57%.

For the protein purification methods (**Figures 7D–F**), the 10-year-old blocks/samples shows the lowest variance between the different methods (11.4%), followed by the 5-year-old blocks/samples. This could be due, in part, to similar proteins extracted from the older blocks because the formaldehyde-induced protein cross-linking process is continual and becomes more extensive with time [66] (also noted and discussed in *The Effect of Block Age and Protein Purification Methods on Peptide-Level Reproducibility*). The 1-year-old blocks/samples (**Figure 7D**) shows the highest variance (15.86%) between the different methods.

GO Analysis of Identified Proteins

The effect of storage time/block age as well as the protein purification methods' protein selection biases were assessed with regards to the main biological processes and cellular components present within the identified proteins, using Gene Ontology (GO) annotation. The distribution of the percentages of proteins belonging to each GO term was plotted for GO terms that occurred at >15% frequency for all samples and experimental conditions (**Figure 8**).

Overall, similar GO profiles were obtained for all samples, therefore only the GO terms that showed some observable difference between experimental conditions were plotted. **Figure 8A** shows the percentage frequency at which the identified proteins (of all experimental conditions) occurs for

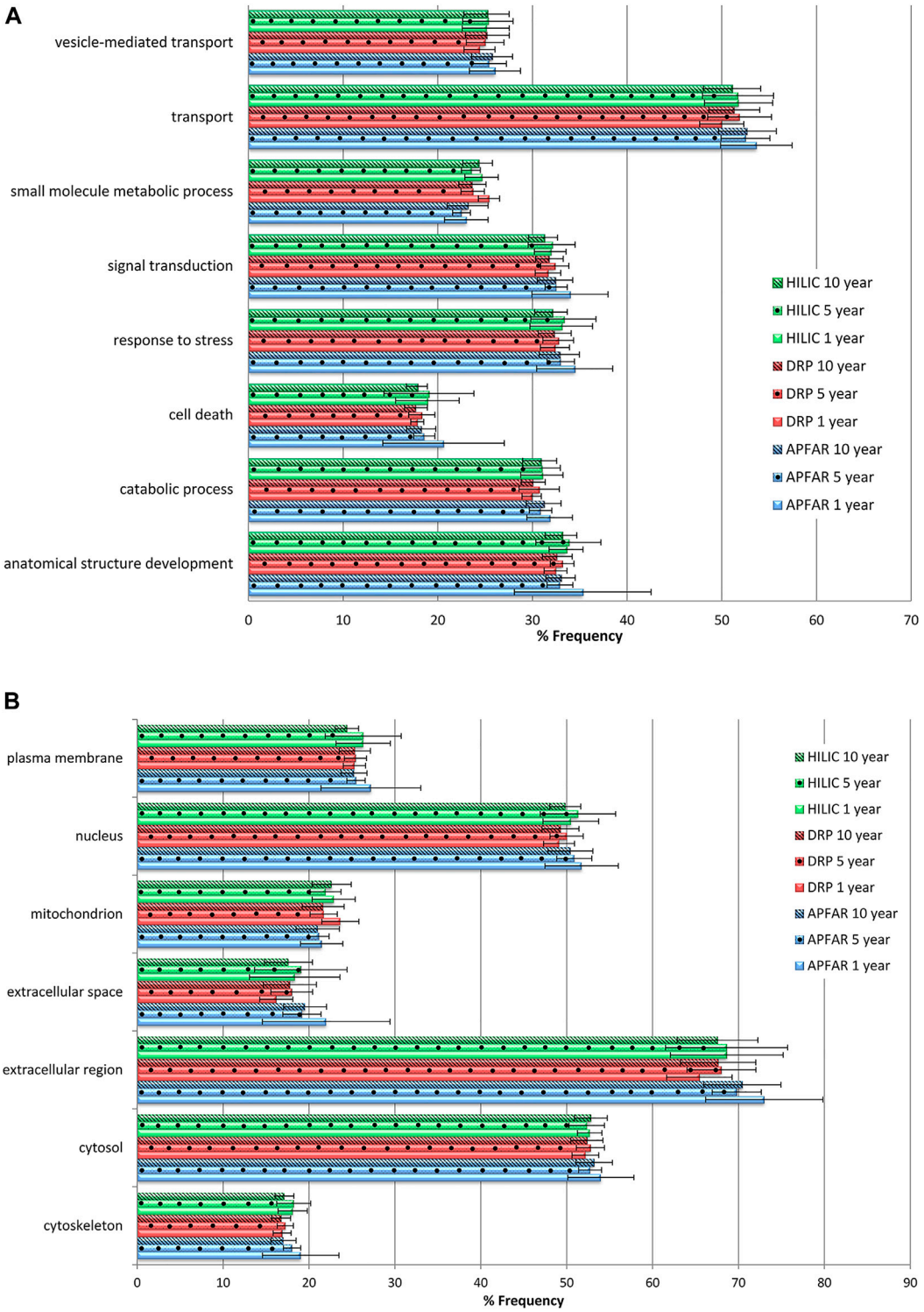

FIGURE 8 | Gene Ontology annotation profiles for proteins identified from all block ages and protein purification methods. **(A)** GO profiles according to biological processes. **(B)** GO profiles according to cellular components. The average proportions for all 17 patients per condition are shown with error bars indicating the standard deviation. Blue bars refer to APFAR samples; Red bars refer to DRP samples; Green bars refer to HILIC samples. For all samples, 5-year-old samples are represented by dots; 10-year-old samples are represented by diagonal lines.

each of the plotted GO terms for biological processes, and **Figure 8B** shows cellular components.

One-way ANOVA or Kruskal–Wallis tests were conducted (results are listed in **Supplementary Table S2**) to determine if there were any significant differences with regard to the % frequency of occurrence of GO terms between block ages, as well as for each protein purification method.

All GO terms (for all block ages and protein purification methods) occurred at >15% frequency for all samples and are clearly represented by **Figure 8**. Therefore all block ages and protein purification methods used in this study demonstrate more or less equivalent usability for proteomic analysis. Statistically significant differences were mainly observed for 1-year-old blocks processed *via* the APFAR and/or DRP methods. Overall, the HILIC method showed least bias across all GO terms plotted.

Statistical analyses for protein purification methods showed that some GO terms for 1-year-old blocks processed *via* the APFAR and DRP methods were significantly enriched ($p < 0.05$) for % frequency of occurrence when using the APFAR method. These GO terms were: catabolic process, cytoskeleton, extracellular region, extracellular space, mitochondrion and transport. The APFAR method differed significantly (depleted) ($p < 0.05$) from both the DRP and HILIC methods for 1 and 5-year-old blocks for % frequency of occurrence of the term "small molecule metabolic process".

Statistical analyses for the different block ages (processed *via* the DRP method) showed that the 1-year-old blocks are significantly enriched ($p < 0.05$) for GO terms "mitochondrion" and "small molecule metabolic process" when compared to the 5 and 10-year-old blocks. In addition, for samples processed *via* the HILIC method, only the 10-year-old blocks were significantly depleted ($p < 0.05$) for % frequency of occurrence of the term "plasma membrane" when compared to the 1 and 5-year-old blocks. For samples processed *via* the APFAR method, the 1-year-old blocks were significantly enriched ($p < 0.05$) whereas the 10-year-old blocks were significantly depleted ($p < 0.05$) with regard to the GO term "cytoskeleton".

Assessment of the Digestion Efficiency of the Protein Purification Methods for all Block Ages

To assess the reproducibility and digestion efficiency of the different protein purification methods, the percentages of missed cleavages across all samples were analyzed (shown in **Supplementary Image S4**). To successfully analyze FFPE tissues requires overcoming the issue of the formaldehyde cross-linking between molecules [2, 4, 6, 11]. The most important aspect to take into consideration for accurate protein extraction from FFPE tissues is the cleavage of these methylene bridges to allow for proper trypsin digestion. The methylene bridges prevent trypsin from reaching its cleavage sites. If the methylene bridges are not adequately cleaved, it will result in improperly digested, cross-linked peptides that will not produce correct MS results. Therefore, the effect of storage time/block age on trypsin digestion efficiency was also determined by comparing the percentage of missed cleavages across all block ages.

Supplementary Image S4 shows that overall, all protein purification methods and all block ages generated low numbers of missed cleavages. The APFAR method (**Supplementary Image S4A**) generated the lowest percentages of missed cleavages with ≥85% of all peptides for 1-year-old samples having no missed cleavages, and ≥90% of all peptides for 5 and 10-year-old samples having no missed cleavages. This was followed by the DRP method (**Supplementary Image S4B**), with ≥85% of all peptides (except for sample number DRP-9) for 1-year-old samples having no missed cleavages, and ≥85% of all peptides for 5 and 10-year-old samples having no missed cleavages (except for sample number DRP-34 of the 5-year-old cohort). The SP3/HILIC method (**Supplementary Image S4C**) had overall lower digestion efficiency with ≥80% of all peptides for 1 and 5-year-old samples having no missed cleavages, and ≥80% of all peptides for 10-year-old samples having no missed cleavages (except for samples HILIC-37 and HILIC-41).

The protein purification methods' digestion efficiency therefore does not appear to be only affected by the age of the sample, since older and newer blocks gave varying results depending on the processing method used [14]. found that after deparaffinization and rehydration, cross-linked proteins are efficiently digested with trypsin, without the need for additional specialized reagents, even under mild conditions typically used for fresh tissues. This is also observed here, since all block ages and protein purification methods used demonstrate sufficient trypsin activity/cleavage efficiency, with all samples showing low levels of missed cleavages. Generally, the percentage of missed cleavages of the present study was in the range of several other recent reports [69–71], with lower percentage of missed cleavages reported in [20].

Effects of Block Age and Protein Purification Methods on Sample Proteome Integrity

The oxidation of methionine is a major protein modification, which converts methionine to methionine sulfoxide, and targets the affected protein for degradation, both *in vivo* and *in vitro* [72]. Methionine oxidation is linked to processes relating to aging and pathology (*in vivo*) as well as *in vitro* conditions caused by protein purification, storage, light exposure, and exposure to free radicals generated in the presence of metals during LC-MS/MS analysis [72]. To determine the impact of long-term storage, the percentage of peptides containing methionine oxidation (out of the total number of peptides identified) was calculated for all block ages and protein purification methods (**Supplementary Image S5**).

Kruskal–Wallis tests were conducted to determine if the percentage of peptides containing methionine oxidation were significantly different between block ages for each protein purification method (**Supplementary Table S2**). No significant differences were found between 1, 5 and 10-year old blocks/

samples processed *via* the APFAR [H (2) = 1.23, $p = 0.54$], DRP [H (2) = 0.86, $p = 0.65$], or SP3/HILIC [H (2) = 3.38, $p = 0.18$] methods. **Supplementary Image S5** shows that for the 10-year-old blocks/samples the percentage of peptides with methionine oxidation are 8.77 ± 3.41%, 7.77 ± 2.41%, and 5.47 ± 2.13%, for APFAR, DRP and SP3/HILIC respectively. Similar percentages of peptides with methionine oxidation (7.65 ± 2.05% and 7.38 ± 2.15%) are observed for 1 and 5-year-old blocks/samples processed *via* the APFAR method. The same is seen for 1 and 5-year-old blocks/samples processed *via* the DRP method (7.24 ± 2.11% and 6.83 ± 1.69%). The SP3/HILIC method has lower percentages of peptides with methionine oxidation for all block ages, with 4.34 ± 1.36%, 4.43 ± 1.16% and 5.47 ± 2.13%, for 1, 5, and 10-year-old blocks/samples respectively. Therefore, the choice of sample preparation/protein purification method may contribute to methionine oxidation artifacts [72]. [73] found that methionine oxidation increases during enzymatic digestion, with the presence of residual metals in the digestion buffer, sample contact with metal surfaces, as well as chromatography separation.

The SP3/HILIC method's results are in agreement with results reported by [3] for newly preserved (<1-year-old) FFPE samples (processed using acetone precipitation and sodium hydroxide resolubilization for protein purification), which had methionine oxidation ratios of 3.9–4.5% for all identified peptides. In contrast [14], reported higher methionine oxidation levels and found that archived colon adenoma tissues displayed an increase in methionine oxidation with block age - from 16.8% after one year of storage, 18.2% for 5-year-old samples up to 25.2% after 10 years of storage.

CONCLUSION

Archived FFPE tissue repositories are precious sources of clinical material, often stored for decades, for clinical proteomic studies. Since these preserved blocks may be conveniently stored at ambient temperatures, it makes them easily accessible and cost effective. However, standardized protocols for the proteomic analysis of FFPE tissues have not been determined yet. In addition, the effect of block age and storage at resource-limited institutions, on protein quality remains unclear. We have demonstrated, using recently developed protein purification techniques (and FFPE human colorectal cancer resection tissues) that, overall, block age mainly affects protein yields during the protein extraction phase. Therefore, greater amounts of starting material are required for older blocks prior to LC-MS/MS analysis. Analyzed samples' peptide and protein identifications mainly differed according to the protein purification method used and not block age, which mainly impacted on tissue proteome composition.

This study is also of particular relevance, since it assessed the performance of three different protein purification techniques on tissues derived from samples stored over a long period of time (1–10 years). The comparative analyses of these methods, across different block ages, have not been carried out to our knowledge and therefore this study provides both experimental data for this assessment as well as statistical support. The different methods show differences in the number of peptides and proteins identified and sample proteome composition, differences in reproducibility in terms of peptide identification overlap, PCA variance, as well as protocol digestion efficiency. Overall, the DRP and SP3/HILIC methods performed the best, with the SP3/HILIC method requiring less protein (and therefore less starting material) than the other methods, therefore making it the most sensitive and efficient protein purification method.

These results are encouraging since they indicate that long-term storage of FFPE tissues does not significantly interfere with retrospective proteomic analysis. In addition, variations in pre-analytical factors (spanning a decade), such as tissue harvesting, handling, the fixation protocol used as well as storage conditions (at resource-limited institutions in developing countries), does not affect protein extraction and shotgun proteomic analysis to a significant extent.

DATA AVAILABILITY STATEMENT

The mass spectrometry proteomics data [41] generated and analyzed for this study can be found in the PRIDE [43] repository (http://www.ebi.ac.uk/pride/archive/) with the dataset identifier PXD017198 and DOI: 10.6019/PXD017198.

ETHICS STATEMENT

FFPE tissue blocks, which consisted of human colorectal resection samples, were retrospectively selected after obtaining ethics clearance from the Biomedical Science Research Ethics Committee (BMREC) of the University of the Western Cape (ethics reference number: BM17/7/15), and the Health Research Ethics Committee (HREC) of Stellenbosch University (ethics reference number: S17/10/203). The FFPE blocks were anonymized prior to processing and archived.

AUTHOR CONTRIBUTIONS

AC provided the funding for the project; AC, SR, LB, RB, and JR contributed conception and design of the study; JR reviewed and selected all samples; SR performed the protein extraction work and wrote the first draft of the manuscript; LB performed the mass spectrometry experiment; SR performed the data and statistical analyses with assistance from HB and RB. All authors contributed to manuscript revision, read and approved the final submitted version.

FUNDING

This work was supported by the South African Research Chairs Initiative of the Department of Science and Innovation and National Research Foundation of South Africa (Grant ID 64751).

CONFLICT OF INTEREST

The authors declare that the research was conducted in the absence of any commercial or financial relationships that could be construed as a potential conflict of interest.

ACKNOWLEDGMENTS

We thank Gerhard Walzl for making available laboratory bench space at the Stellenbosch University Immunology Group, and Andrea Gutschmidt at the Stellenbosch University Immunology Group for her technical assistance and support during the use of their laboratory space. We also thank Charles Gelderbloem and Yunus Kippie at the University of the Western Cape's Biotechnology and Pharmacology departments, respectively, for their technical assistance and support during the project.

SUPPLEMENTARY MATERIAL

The Supplementary Material for this article can be found online at: https://www.por-journal.com/articles/10.3389/pore.2021.622855/full#supplementary-material.

REFERENCES

1. Daniele L, D'Armento G, and Bussolati G. Preanalytical time interval (PATI) and fixation. In: G Stanta, editor. *Guidelines for molecular analysis in archive tissues*. Berlin: Springer-Verlag (2011). p. 5–11.
2. Avaritt NL, Shalin S, and Tackett AJ. Decoding the proteome in formalin-fixed paraffin-embedded (FFPE) tissues. *J Proteomics Bioinform* (2014) 7:e25. doi:10.4172/jpb.10000e25
3. Bronsert P, Weißer J, Biniossek ML, Kuehs M, Mayer B, Drendel V, et al. Impact of routinely employed procedures for tissue processing on the proteomic analysis of formalin-fixed paraffin-embedded tissue. *Prot Clin Appl* (2014) 8:796–804. doi:10.1002/prca.201300082
4. Gustafsson OJR, Arentz G, and Hoffmann P. Proteomic developments in the analysis of formalin-fixed tissue. *Biochim Biophys Acta (Bba) - Proteins Proteomics* (2015) 1854:559–80. doi:10.1016/j.bbapap.2014.10.003
5. Klockenbusch C, O'Hara JE, and Kast J. Advancing formaldehyde cross-linking towards quantitative proteomic applications. *Anal Bioanal Chem* (2012) 404:1057–67. doi:10.1007/s00216-012-6065-9
6. Magdeldin S, and Yamamoto T. Toward deciphering proteomes of formalin-fixed paraffin-embedded (FFPE) tissues. *Proteomics* (2012) 12:1045–58. doi:10.1002/pmic.201100550
7. Maes E, Valkenborg D, Mertens I, Broeckx V, Baggerman G, Sagaert X, et al. Proteomic analysis of formalin-fixed paraffin-embedded colorectal cancer tissue using tandem mass tag protein labeling. *Mol Biosyst* (2013) 9:2686–95. doi:10.1039/c3mb70177h
8. Tanca A, Abbondio M, Pisanu S, Pagnozzi D, Uzzau S, and Addis MF. Critical comparison of sample preparation strategies for shotgun proteomic analysis of formalin-fixed, paraffin-embedded samples: insights from liver tissue. *Clin Proteomics* (2014) 11(28):1–11. doi:10.1186/1559-0275-11-28
9. Shen K, Sun J, Cao X, Zhou D, and Li J. Comparison of different buffers for protein extraction from formalin-fixed and paraffin-embedded tissue specimens. *PLoS ONE* (2015) 10(11):e0142650. doi:10.1371/journal.pone.0142650
10. Craven RA, Cairns DA, Zougman A, Harnden P, Selby PJ, and Banks RE. Proteomic analysis of formalin-fixed paraffin-embedded renal tissue samples by label-free MS: assessment of overall technical variability and the impact of block age. *Proteomics Clin Appl* (2013) 7(3-4):273–82. doi:10.1002/prca.201200065
11. Fowler CB, O'Leary TJ, and Mason JT. Toward improving the proteomic analysis of formalin-fixed, paraffin-embedded tissue. *Expert Rev Proteomics* (2013) 10(4):389–400. doi:10.1586/14789450.2013.820531
12. Kessner D, Chambers M, Burke R, Agus D, and Mallick P. ProteoWizard: open source software for rapid proteomics tools development. *Bioinformatics* (2008) 24:2534–6. doi:10.1093/bioinformatics/btn323
13. Wolff C, Schott C, Porschewski P, Reischauer B, and Becker K-F. Successful protein extraction from over-fixed and long-term stored formalin-fixed tissues. *PLoS ONE* (2011) 6(1):e16353. doi:10.1371/journal.pone.0016353
14. Sprung RW, Brock JWC, Tanksley JP, Li M, Washington MK, Slebos RJC, et al. Equivalence of protein inventories obtained from formalin-fixed paraffin-embedded and frozen tissue in multidimensional liquid chromatography-tandem mass spectrometry shotgun proteomic analysis. *Mol Cel Proteomics* (2009) 8. doi:10.1074/mcp.m800518-mcp200
15. Tanca A, Pagnozzi D, Falchi G, Biosa G, Rocca S, Foddai G, et al. Impact of fixation time on GeLC-MS/MS proteomic profiling of formalin-fixed, paraffin-embedded tissues. *J Proteomics* (2011) 74:1015–21. doi:10.1016/j.jprot.2011.03.015
16. Piehowski PD, Petyuk VA, Sontag RL, Gritsenko MA, Weitz KK, Fillmore TL, et al. Residual tissue repositories as a resource for population-based cancer proteomic studies. *Clin Proteom* (2018) 15:26. doi:10.1186/s12014-018-9202-4
17. Wiśniewski JR, Zougman A, Nagaraj N, and Mann M. Universal sample preparation method for proteome analysis. *Nat Methods* (2009) 6(5):359–62. doi:10.1038/nmeth.1322
18. Botelho D, Wall MJ, Vieira DB, Fitzsimmons S, Liu F, and Doucette A (2010). Top-down and bottom-up proteomics of SDS-containing solutions following mass-based separation. *J Proteome Res*., 9, 2863–70. doi:10.1021/pr900949p
19. Pellerin D, Gagnon H, Dubé J, and Corbin F. Amicon-adapted enhanced FASP: an in-solution digestion-based alternative sample preparation method to FASP. *F1000Res* (2015) 4:140–18. doi:10.12688/f1000research.6529.1
20. Kachuk C, Stephen K, and Doucette A. Comparison of sodium dodecyl sulfate depletion techniques for proteome analysis by mass spectrometry. *J Chromatogr A* (2015) 1418:158–66. doi:10.1016/j.chroma.2015.09.042
21. Doucette AA, Vieira DB, Orton DJ, and Wall MJ. Resolubilization of precipitated intact membrane proteins with cold formic acid for analysis by mass spectrometry. *J Proteome Res* (2014) 13(12):6001–12. doi:10.1021/pr500864a
22. Hughes CS, Foehr S, Garfield DA, Furlong EE, Steinmetz LM, and Krijgsveld J. Ultrasensitive proteome analysis using paramagnetic bead technology. *Mol Syst Biol* (2014) 10(10):1–10. doi:10.15252/msb.20145625
23. Scicchitano MS, Dalmas DA, Boyce RW, Thomas HC, and Frazier KS. Protein extraction of formalin-fixed, paraffin-embedded tissue enables robust proteomic profiles by mass spectrometry. *J Histochem Cytochem* (2009) 57(9):849–60. doi:10.1369/jhc.2009.953497
24. Wiśniewski JR. Proteomic sample preparation from formalin fixed and paraffin embedded tissue. *J Vis Exp* (2013) 79:e50589. doi:10.3791/50589
25. Hughes CS, Sorensen PH, and Morin GB. A standardized and reproducible proteomics protocol for bottom-up quantitative analysis of protein samples using SP3 and mass spectrometry. In: V Brun and Y Coute´, editors. *Proteomics for biomarker discovery: methods and protocols, methods in molecular biology*. New York: Springer Nature (2019). p. 65–87. doi:10.1007/978-1-4939-9164-8_5
26. Craig R, and Beavis RC. TANDEM: matching proteins with tandem mass spectra. *Bioinformatics* (2004) 20(9):1466–7. doi:10.1093/bioinformatics/bth092
27. Dorfer V, Pichler P, Stranzl T, Stadlmann J, Taus T, Winkler S, et al. MS Amanda, a universal identification algorithm optimized for high accuracy tandem mass spectra. *J Proteome Res* (2014) 13:3679–84. doi:10.1021/pr500202e
28. Kim S, and Pevzner PA. MS-GF+ makes progress towards a universal database search tool for proteomics. *Nat Commun* (2014) 5:5277. doi:10.1038/ncomms6277

29. Vaudel M, Barsnes H, Berven FS, Sickmann A, and Martens L. SearchGUI: an open-source graphical user interface for simultaneous OMSSA and X!Tandem searches. *Proteomics* (2011) 11:996–9. doi:10.1002/pmic.201000595
30. Elias JE, and Gygi SP. Target-Decoy search strategy for mass spectrometry-based proteomics. *Methods Mol Biol* (2010) 604:55–71. doi:10.1007/978-1-60761-444-9_5
31. Apweiler R, Bairoch A, Wu CH, Barker WC, Boeckmann B, Ferro S, et al. UniProt: the universal protein knowledgebase. *Nucleic Acids Res* (2004) 32: 115D–119. doi:10.1093/nar/gkh131
32. Vaudel M, Burkhart JM, Zahedi RP, Oveland E, Berven FS, Sickmann A, et al. PeptideShaker enables reanalysis of MS-derived proteomics data sets. *Nat Biotechnol* (2015) 33(1):22–4. doi:10.1038/nbt.3109
33. Vaudel M, Breiter D, Beck F, Rahnenführer J, Martens L, and Zahedi RP. D-score: a search engine independent MD-score. *Proteomics* (2013) 13(6): 1036–41. doi:10.1002/pmic.201200408
34. Taus T, Köcher T, Pichler P, Paschke C, Schmidt A, Henrich C, et al. Universal and confident phosphorylation site localization using phosphoRS. *J Proteome Res* (2011) 10(12):5354–62. doi:10.1021/pr200611n
35. Barsnes H, Vaudel M, Colaert N, Helsens K, Sickmann A, Berven FS, et al. Compomics-utilities: an open-source Java library for computational proteomics. *BMC Bioinformatics* (2011) 12:70. doi:10.1186/1471-2105-12-70
36. Farias SE, Kline KG, Klepacki J, and Wu CC. Quantitative improvements in peptide recovery at elevated chromatographic temperatures from microcapillary liquid Chromatography–Mass spectrometry analyses of brain using selected reaction monitoring. *Anal Chem* (2010) 82(9):3435–40. doi:10.1021/ac100359p
37. Powell DW, Weaver CM, Jennings JL, McAfee KJ, He Y, Weil PA, et al. Cluster analysis of mass spectrometry data reveals a novel component of SAGA. *Mcb* (2004) 24:7249–59. doi:10.1128/mcb.24.16.7249-7259.2004
38. Vaudel M. MS2-based quantitation. In: C Bessant, editor. *New developments in mass spectrometry no. 5: proteome informatics*. Cambridge: The Royal Society of Chemistry (2017). p. 155–77. doi:10.1039/9781782626732-FP001
39. Wu S, and Zhu Y. ProPAS: standalone software to analyze protein properties. *Bioinformation* (2012) 8(3):167–9. doi:10.6026/97320630008167
40. Oliveros JC. *Venny. An interactive tool for comparing lists with Venn's diagrams* (2007). http://bioinfogp.cnb.csic.es/tools/venny/index.html (Accessed May 11, 2020).
41. Rossouw SC, Bendou H, Blignaut RJ, Bell L, Rigby J, and Christoffels A. Evaluation of protein purification techniques and effects of storage duration on LC-MS/MS analysis of archived FFPE human CRC tissues. In: *PRIDE database*. PXD017198 (2020). https://www.ebi.ac.uk/pride/archive/ (Accessed January 20, 2020).
42. Deutsch EW, Csordas A, Sun Z, Jarnuczak A, Perez-Riverol Y, Ternent T, et al. The ProteomeXchange Consortium in 2017: supporting the cultural change in proteomics public data deposition. *Nucleic Acids Res* (2017) 45(D1): D1100–D1106. doi:10.1093/nar/gkw936
43. Perez-Riverol Y, Csordas A, Bai J, Bernal-Llinares M, Hewapathirana S, Kundu DJ, et al. The PRIDE database and related tools and resources in 2019: improving support for quantification data. *Nucleic Acids Res* (2019) 47(D1):D442–D450. doi:10.1093/nar/gky1106
44. Wiśniewski JR, Duś K, and Mann M. Proteomic workflow for analysis of archival formalin-fixed and paraffin-embedded clinical samples to a depth of 10 000 proteins. *Proteomics Clin Appl* (2012) 7:1–9. doi:10.1002/prca.201200046
45. Baiwir T, Valladares-Ayerbes M, Haz-Conde M, Blanco M, Aparicio G, Fernández-Puente P, et al. A novel procedure for protein extraction from formalin-fixed paraffin-embedded tissues. *Proteomics* (2011) 11:2555–9. doi:10.1002/pmic.201000809
46. Agilent Technologies. *FFPE protein extraction solution protocol* (2009). Retrieved from https://www.chem-agilent.com/pdf/strata/400925.pdf (Accessed October 12, 2019).
47. Lee S, Bang S, Song K, and Lee I. Differential expression in normal-adenoma-carcinoma sequence suggests complex molecular carcinogenesis in colon. *Oncol Rep* (2006) 16(4):747–54. doi:10.3892/or.16.4.747
48. Andersen CL, Christensen LL, Thorsen K, Schepeler T, Sørensen FB, Verspaget HW, et al. Dysregulation of the transcription factors SOX4, CBFB and SMARCC1 correlates with outcome of colorectal cancer. *Br J Cancer* (2009) 100(3):511–23. doi:10.1038/sj.bjc.6604884
49. Mikesch J-H, Buerger H, Simon R, and Brandt B. Decay-accelerating factor (CD55): a versatile acting molecule in human malignancies. *Biochim Biophys Acta (Bba) - Rev Cancer* (2006) 1766(1):42–52. doi:10.1016/j.bbcan.2006.04.001
50. Helman LJ, Gazdar AF, Park JG, Cohen PS, Cotelingam JD, and Israel MA. Chromogranin A expression in normal and malignant human tissues. *J Clin Invest* (1988) 82(2):686–90. doi:10.1172/jci113648
51. Bustin SA, Li S-R, and Dorudi S. Expression of the Ca2+-activated chloride channel genes CLCA1 and CLCA2 is downregulated in human colorectal cancer. *DNA Cel Biol* (2001) 20(6):331–8. doi:10.1089/10445490152122442
52. Toiyama Y, Inoue Y, Yasuda H, Saigusa S, Yokoe T, Okugawa Y, et al. DPEP1, expressed in the early stages of colon carcinogenesis, affects cancer cell invasiveness. *J Gastroenterol* (2011) 46:153–63. doi:10.1007/s00535-010-0318-1
53. Yao X, Zhao G, Yang H, Hong X, Bie L, and Liu G. Overexpression of high-mobility group box 1 correlates with tumor progression and poor prognosis in human colorectal carcinoma. *J Cancer Res Clin Oncol* (2010) 136(5):677–84. doi:10.1007/s00432-009-0706-1
54. Quesada-Calvo F, Massot C, Bertrand V, Longuespée R, Blétard N, Somja J, et al. OLFM4, KNG1 and Sec24C identified by proteomics and immunohistochemistry as potential markers of early colorectal cancer stages. *Clin Proteom* (2017) 14(9). doi:10.1186/s12014-017-9143-3
55. Li A, Goto M, Horinouchi M, Tanaka S, Imai K, Kim YS, et al. Expression of MUC1 and MUC2 mucins and relationship with cell proliferative activity in human colorectal neoplasia. *Pathol Int* (2001) 51(11):853–60. doi:10.1046/j.1440-1827.2001.01291.x
56. Ogata S, Uehara H, Chen A, and Itzkowitz SH. Mucin gene expression in colonic tissues and cell lines. *Cancer Res* (1992) 52(21):5971–8.
57. Nozawa Y, Van Belzen N, Van der Made ACJ, Dinjens WNM, and Bosman FT. Expression of nucleophosmin/B23 in normal and neoplastic colorectal mucosa. *J Pathol* (1996) 178(1):48–52. doi:10.1002/(sici)1096-9896(199601)178:1<48::aid-path432>3.0.co;2-y
58. Yung BY. Oncogenic role of nucleophosmin/B23. Chang Gung Med *J* (2007) 30(4):285–93.
59. Vié N, Copois V, Bascoul-Mollevi C, Denis V, Bec N, Robert B, et al. Overexpression of phosphoserine aminotransferase PSAT1 stimulates cell growth and increases chemoresistance of colon cancer cells. *Mol Cancer* (2008) 7:14. doi:10.1186/1476-4598-7-14
60. Zheng H, Tsuneyama K, Cheng C, Takahashi H, Cui Z, Murai Y, et al. Maspin expression was involved in colorectal adenoma-adenocarcinoma sequence and liver metastasis of tumors. *Anticancer Res* (2007) 27(1A):259–65.
61. Powis G, Mustacich D, and Coon A. The role of the redox protein thioredoxin in cell growth and cancer. *Free Radic Biol Med* (2000) 29(3–4):312–22. doi:10.1016/s0891-5849(00)00313-0
62. Fu Z, Yan K, Rosenberg A, Jin Z, Crain B, Athas G, et al. Improved protein extraction and protein identification from archival formalin-fixed paraffin-embedded human aortas. *Prot Clin Appl* (2013) 7:217–24. doi:10.1002/prca.201200064
63. Gámez-Pozo A, Ferrer NI, Ciruelos E, López-Vacas R, Martínez FG, Espinosa E, et al. Shotgun proteomics of archival triple-negative breast cancer samples. *Prot Clin Appl* (2013) 7:283–91. doi:10.1002/prca.201200048
64. Wiśniewski JR, Ostasiewicz P, and Mann M. High recovery FASP applied to the proteomic analysis of microdissected formalin fixed paraffin embedded cancer tissues retrieves known colon cancer markers. *J Proteome Res* (2011) 10: 3040–9. doi:10.1021/pr200019m
65. Wiśniewski JR, Duś K, and Mann M. Proteomic workflow for analysis of archival formalin-fixed and paraffin-embedded clinical samples to a depth of 10 000 proteins. *Proteomics Clin Appl* (2013) 7:225–33. doi:10.1002/prca.201200046
66. Lemaire R, Desmons A, Tabet JC, Day R, Salzet M, and Fournier I. Direct analysis and MALDI imaging of formalin-fixed, paraffin-embedded tissue sections. *J Proteome Res* (2007) 6:1295–305. doi:10.1021/pr060549i
67. Paine MRL, Ellis SR, Maloney D, Heeren RMA, and Verhaert PDEM. Digestion-free analysis of peptides from 30-year-old formalin-fixed, paraffin-embedded tissue by mass spectrometry imaging. *Anal Chem* (2018) 90:9272–80. doi:10.1021/acs.analchem.8b01838

68. Kyte J, and Doolittle RF. A simple method for displaying the hydropathic character of a protein. *J Mol Biol* (1982) 157:105–32. doi:10.1016/0022-2836(82)90515-0
69. Moggridge S, Sorensen PH, Morin GB, and Hughes CS. Extending the compatibility of the SP3 paramagnetic bead processing approach for proteomics. *J Proteome Res* (2018) 17(4):1730–40. doi:10.1021/acs.jproteome.7b00913
70. Batth TS, Tollenaere MAX, Rüther PL, Gonzalez-Franquesa A, Prabhakar BS, Bekker-Jensen S, et al. Protein aggregation capture on microparticles enables multi-purpose proteomics sample preparation. *Mol Cell Proteomics* (2018) 18(5):1027–35. doi:10.1074/mcp.TIR118.001270
71. Hughes CS, Moggridge S, Müller T, Sorensen PH, Morin GB, and Krijgsveld J. Single-pot, solid-phase-enhanced sample preparation for proteomics experiments. *Nat Protoc* (2018) 14(1):1–18. doi:10.1038/s41596-018-0082-x
72. Liu H, Ponniah G, Neill A, Patel R, and Andrien B. Accurate determination of protein methionine oxidation by stable isotope labeling and LC-MS analysis. *Anal Chem* (2013) 85, 11705–9. doi:10.1021/ac403072w
73. Zang L, Carlage T, Murphy D, Frenkel R, Bryngelson P, Madsen M, et al. Residual metals cause variability in methionine oxidation measurements in protein pharmaceuticals using LC-UV/MS peptide mapping. *J Chromatogr B Analyt Technol Biomed Life Sci* (2012) 895-896, 71–6. doi:10.1016/j.jchromb.2012.03.016

GLOSSARY

ACN Acetonitrile
AmBic Ammonium bicarbonate
APFAR Acetone precipitation and formic acid resolubilization
BCA Bicinchoninic acid
CRC colorectal carcinoma
DRP detergent removal plates
ESI electrospray ionization
FA Formic acid
FDR False discovery rate
FFPE Formalin-fixed, paraffin-embedded
GO Gene ontology
H&E Hematoxylin and Eosin
HIAR Heat-induced antigen retrieval
HILIC Hydrophilic interaction liquid chromatography
LC Liquid chromatography
LC-MS/MS Liquid chromatography coupled to tandem mass spectrometry
LFQ Label-free quantitation
MMTS Methylmethanethiosulfonate
MS Mass spectrometry
NSAF Normalized spectrum abundance factor
PCA Principal component analysis
PCC Pearson's correlation coefficient
PSM Peptide Spectrum Match
PTM(s) Post-translational modification(s)
SDS Sodium dodecyl sulfate
SP3 Single-Pot Solid-Phase-enhanced Sample Preparation
TCEP Tris(2-carboxyethyl)phosphine
TEAB Triethylammonium bicarbonate
TFA Trifluoroacetic acid

Pathology & Oncology Research | frontiers

ORIGINAL RESEARCH
published: 06 August 2021
doi: 10.3389/pore.2021.1609900

Pathological Features in 100 Deceased Patients With COVID-19 in Correlation With Clinical and Laboratory Data

*L. M. Mikhaleva, A. L. Cherniaev, M. V. Samsonova, O. V. Zayratyants, L. V. Kakturskiy, O. A. Vasyukova, A. E. Birukov, A. S. Kontorshchikov, A. V. Sorokina and M. Y. Sinelnikov**

Research Institute of Human Morphology, Moscow, Russia

Background: Autopsies on COVID-19 deceased patients have many limitations due to necessary epidemiologic and preventative measures. The ongoing pandemic has caused a significant strain on healthcare systems and is being extensively studied around the world. Clinical data does not always corelate with post-mortem findings. The goal of our study was to find pathognomonic factors associated with COVID-19 mortality in 100 post-mortem full body autopsies.

Materials and Methods: Following necessary safety protocol, we performed 100 autopsies on patients who were diagnosed with COVID-19 related death. The macroscopic and microscopic pathologies were evaluated along with clinical and laboratory findings.

Results: Extensive coagulopathic changes are seen throughout the bodies of diseased patients. Diffuse alveolar damage is pathognomonic of COVID-19 viral pneumonia, and is the leading cause of lethal outcome in younger patients. Extrapulmonary pathology is predominantly seen in the liver and spleen. Intravascular thrombosis is often widespread and signs of septic shock are often present.

Conclusion: The described pathological manifestations of COVID-19 in deceased patients are an insight into the main mechanisms of SARS-CoV-2 associated lethal outcome. The disease bears no obvious bias in severity, but seems to be more severe in some patients, hinting at genetic or epigenetic factors at play.

Keywords: histological subtype, COVID-19, pathological features, large cohort, morphology

OPEN ACCESS

Edited by:
József Tímár,
Semmelweis University, Hungary

****Correspondence:***
M. Y. Sinelnikov
mikhail.y.sinelnikov@gmail.com

Received: *26 May 2021*
Accepted: *27 July 2021*
Published: *06 August 2021*

Citation:
Mikhaleva LM, Cherniaev AL, Samsonova MV, Zayratyants OV, Kakturskiy LV, Vasyukova OA, Birukov AE, Kontorshchikov AS, Sorokina AV and Sinelnikov MY (2021) Pathological Features in 100 Deceased Patients With COVID-19 in Correlation With Clinical and Laboratory Data. Pathol. Oncol. Res. 27:1609900. doi: 10.3389/pore.2021.1609900

INTRODUCTION

The ongoing SARS-CoV-2 outbreak has caused significant healthcare, social and mental difficulties [1]. On March 12th, 2020 the World Health Organization announced the outbreak a pandemic. More than 180 million cases of COVID-19 have now been registered by now in the world [2]. Lethality has been officially registered at 0.1–0.5% globally [2], yet many governments have been accused of artificially reducing both infection and lethality rates through falsification of data or underreporting [3,4]. Nevertheless, the toll of the ongoing SARS-CoV-2 pandemic has already brought significant social tension, healthcare straining and overall decrease in quality of life [5–7].

The pathological characteristics of COVID-19 pulmonary changes have been previously addressed, yet most studies present a small number of cases [8,9]. Several reports of pathological characteristics of extrapulmonary manifestations have also been reported [10–12].

The goal of our study was to assess the pathological features of COVID-19-related deaths during autopsy in a substantial cohort (100 cases). Our null hypothesis was that all cases of lethal outcome have similar associations and features, according to treatment modality and patient characteristics.

MATERIALS AND METHODS

Our study included clinical, laboratory and pathology findings collected from 100 deceased COVID-19 patients. Demographic, clinical data (including available patient history and comorbidities), computerized tomography (CT) results, macroscopic and microscopic assessment of pathological changes in the entire body was performed.

COVID-19 post-mortem verification. COVID-19 infection was confirmed in all patients by post-mortem PCR-testing (polymerize-chain reaction test) of biomaterial collected from the trachea, major bronchi and lungs. PCR-testing was performed for all patients, even when a COVID-19 diagnosis was already issued prior to lethal outcome.

Safety protocol. The autopsies were performed according to World Health Organization (WHO) and the Health Ministry of Russia recommendations. Pathologists and assistants worked in disposable full-body Taiwek suits, plastic safety glasses, two pairs of disposable gloves, class FPP3 inhalers, disposable aprons, shoelaces. Two staff members were allowed to be in the dissection room at any given time (a pathologist and a dissector). Brain examination was performed after manual skull sectioning. Electric sawing was not permitted. Following autopsy and tissue extraction, all instruments underwent disinfection in an antiseptic solution, all disposable utilities were utilized.

Pathological evaluation. Excised tissue fragments were fixed in 10% neutral formalin solution using the automatic histologic processor Leica ASP 300S (Germany). Paraffin filling was then performed using the Leica EG 1160 station (Germany). A Leica RM 2125 RTS (Germany) microtome was used to provide 3–4 μm thick slices. Hematoxylin and eosin, periodic acid-Schiff (PAS), and Alcian blue staining were performed using the Leica ST 5010 (Germany). Perls staining was used for histochemical detection of iron. The following organs were evaluated in all patients: brain; trachea and bronchi; lungs; bifurcation lymph nodes; heart; kidneys; spleen; liver.

Immunohistochemistry (IHC). Histological sections also underwent IHC evaluation. The produced 3–4 μm sections were placed on super adhesive slides (Trajan T7611), after which they were placed for 2 h into a thermostat (70°C). The staining was performed using double-stage avidin-biotin-peroxidase method with antigen unmasking solutions, polyclonal and monoclonal antigen use. IHC staining was performed using the Ventana BenchMark ULTRA IHC/ISH (United States) and Leica Bond-MAX (Germany). The following antibodies were used in our study: CD31 Mouse Monoclonal Antibody (clone JC70, ready-to-use), CK5/6 Mouse Monoclonal Antibody (clone D5/16B4, ready-to-use).

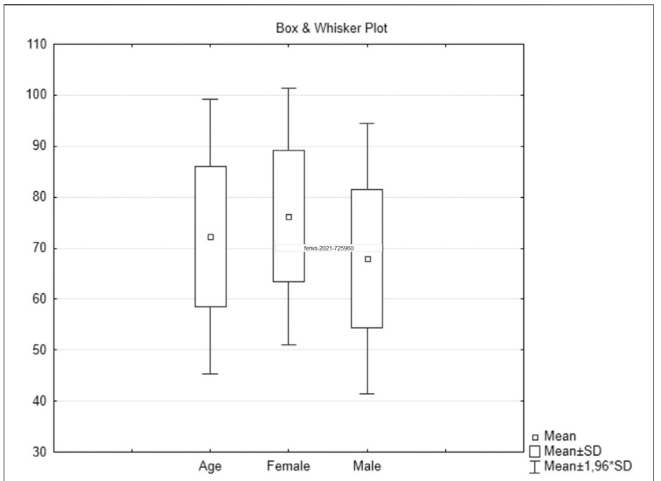

FIGURE 1 | COVID-19 related autopsy distribution by sex and age, mean ± standard deviation.

Microscopic evaluation. Microscopically the specimens were analyzed using the triocular Leica DMLB (Germany) microscope with a fully-compatible Leica DFC 420 (Germany) digital camera. Final image analysis was performed by ImageScope Color M software. Calibration was performed by an object-micrometer with 0.01 mm step.

During microscopic evaluation signs of respiratory distress syndrome (exudative and proliferative phases) were noted. The following parameters were analyzed: hyaline membrane structure, fibrin deposits, interalveolar bleeding, interalveolar edema, interstitial inflammation, cytopathic effects, granulation tissue (fibroblastic tissue), thrombi presence within vasculature, infarctions, neutrophilic groups, macrophages, lymphocytes, plasma cells, and siderophages within the tissue (and localization), squamous cell metaplasia and bronchial epithelium desquamation, squamous cell metaplasia and alveolar epithelium desquamation, macrophage presence within the alveoli, signs of viral presence (*via* cytopathic effect characterized by the formation of large cells of irregular shape with enlarged nuclei and coarse-grained chromatin, distinct nucleoli, with a perinuclear "halo" effect), myxoid edematous interstitial stroma presence, signs of aspiration, tissue necrosis. Pathological findings within the cohort are represented as mean and standard deviation.

Visual evaluation of the microscopic changes of other organs and tissues was also performed to identify pathologic changes. Organs showing signs of pathological change during autopsy were examined pathologically. Clinical indications and patient history were taken into account. All organs and systems underwent primary evaluation and were included in the study if pathological changes were noted.

Statistical evaluation. The significance of differences between sub-cohorts was determined using the independent *t*-test or the

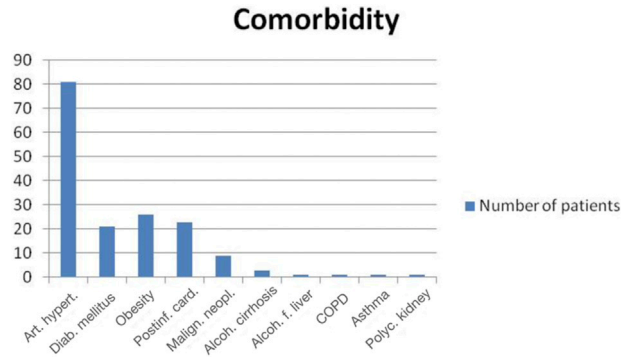

FIGURE 2 | Comorbidities in COVID-19 deceased patients [Art. hypert.—arterial hypertension (81/100), Diab. Mellitus—diabetes mellitus (21/100), Obesity (26/100), Postinf. card.–postinfarction cardiosclerosis (23/100), Malign. Neopl.—malignant neoplasms (8/100), Alcoh. cirrhosis—alcoholic cirrhosis of liver (3/100), Alcoh. f. liver—alcoholic fatty liver (1/100), COPD—chronic obstructive pulmonary disease (1/100), Asthma (1/100), Polyc. kidney—polycystic kidney (1/100)].

nonparametric Mann-Whitney *U*-test when variables were non-normally distributed. Comorbidity rates were compared using Pearson's chi-squared test or Fisher's exact test. Analysis of variance was performed to evaluate intergroup differences on each parameter with appropriate data. The minimal number of cases that needed to be included in this study was calculated using power analysis. Statistical data was calculated using RStudio software, version February 1, 1335 (RStudio, Inc., Boston, MA, United States). Results are presented as means ± standard deviation or as numbers and percentages, and statistical significance was set at p-values < 0.05.

RESULTS

Patient Characteristics

A total of 100 autopsies were performed (53 females, 47 males). The mean age of the deceased patients was 70.8 years (range: 45–95 years). Mean female age was 75.5 (range: 58–95 years). Mean male age was 67.5 (range: 45–92 years) (**Figure 1**). The mean duration of the disease until lethal outcome was 13.4 days (range: 2–48 days). The mean hospitalization duration was 7.48 days (range: 5–25 days).

Most of the deceased patients had aggravating conditions (**Figure 2**). Hypertensions was the most common comorbidity. 48% of patients had more than one comorbidity. Eight patients presented with malignancies: lung, breast, colon cancers, B-cell and T-cell lymphoma, cutaneous plasmacytoma (one case each), and chronic lymphocytic leukemia (two patients). Alcohol related hepatic micronodular cirrhosis was observed in three patients, one of which was diagnosed with the hepatocellular carcinoma. Hepatic steatosis without cirrhosis was noted once. Two deceased patients were diagnosed with COPD and bronchial asthma, one patient had a congenital polycystic kidney disease, and another one suffered from systemic amyloidosis with cardiac involvement.

Disseminated intravascular coagulation (DIC) syndrome was seen in 29 cases. It presented with serosal and mucosal hemorrhages (in 96% of cases) (**Figure 3H**), uncoagulated blood in the blood vessels and heart (in 79.3% of patients) and acute erosions within the gastrointestinal (GI) tract (in 44.8% of patients). Pulmonary thrombosis was found in 44.8% of patients effected by the DIC syndrome (13/29), Myocardial ischemic pathology was observed in 17.2% of patients (5/29), Intestinal gangrene was seen in 10.3% of patients (3/29) (**Figure 3I**). Gastrointestinal bleeding was noted in 10.3% of DIC cases (3/29).

Pulmonary Findings

Macroscopically, the pulmonary tissues of deceased patients showed signs of acute respiratory damage in the form of "shock lung" (varnish pulmonary surface with a dark-red or dark-cherry color, volume increase (from 1,100 to 2,860 g, mean volume is 1,659 g), and the pulmonary consolidation. Lung surface was airless, with a rubber density, dark-red or brown-red in color (**Figures 3A,B**). Pulmonary embolism was seen in 19 patients (**Figures 3A,C**). 31 patients showed signs of viral-bacterial pneumonia, and three patients developed mixed viral-bacterial-fungal pneumonia, confirmed by *in-vivo* microbiology assessment, mucus analysis and postmortem diagnosis.

Microscopic signs of diffuse alveolar damage (DAD) was seen as the morphologic equivalent of viral pneumonia, the signs of which were analyzed by a modification of T. Mauad et al. algorithm for pulmonary changes in influenza A (H1N1) patients (**Table 1**) [12].

In microscopic examination of the lungs pulmonary edema was found in 61 cases, hyaline membranes within alveolar walls and lumens was seen in 75 cases, alveolar epithelial plast-like desquamation in 67 patients. The cytopathic effect is seen as large alveolocytes with rubber chromatic nuclei and nucleoli presence, occasionally with a perinuclear "halo" and round-shape intracytoplasmic inclusions with signs of interstitial inflammation and occasional megakaryocytes: this phenomenon was seen in 55 cases. Among typical DAD findings vascular injuries were present: interalveolar capillary, vein and venular dilatation, interalveolar hemorrhages and arteriospasm were observed in 75 cases, although its severity varied from microscopic to vast pulmonary infarctions (31 cases) (**Figure 4**).

In the brain, both in the cortical and in the medulla and in the region of the basal nuclei, pronounced pericellular and perivascular edema, diapedesis and focal hemorrhages with saturation of adjacent brain tissue with blood were found. It is believed that violations of permeability of the blood-brain barrier and associated neural tissue damage are the result of the cytokine storm.

When examining the urogenital tract, with the exception of the kidneys, no specific changes were noted. In isolated cases, focal or confluent hemorrhages were revealed in the mucous membrane of the renal pelvis and ureters, as well as in the mucous membrane of the bladder, associated with systemic manifestations of DIC syndrome.

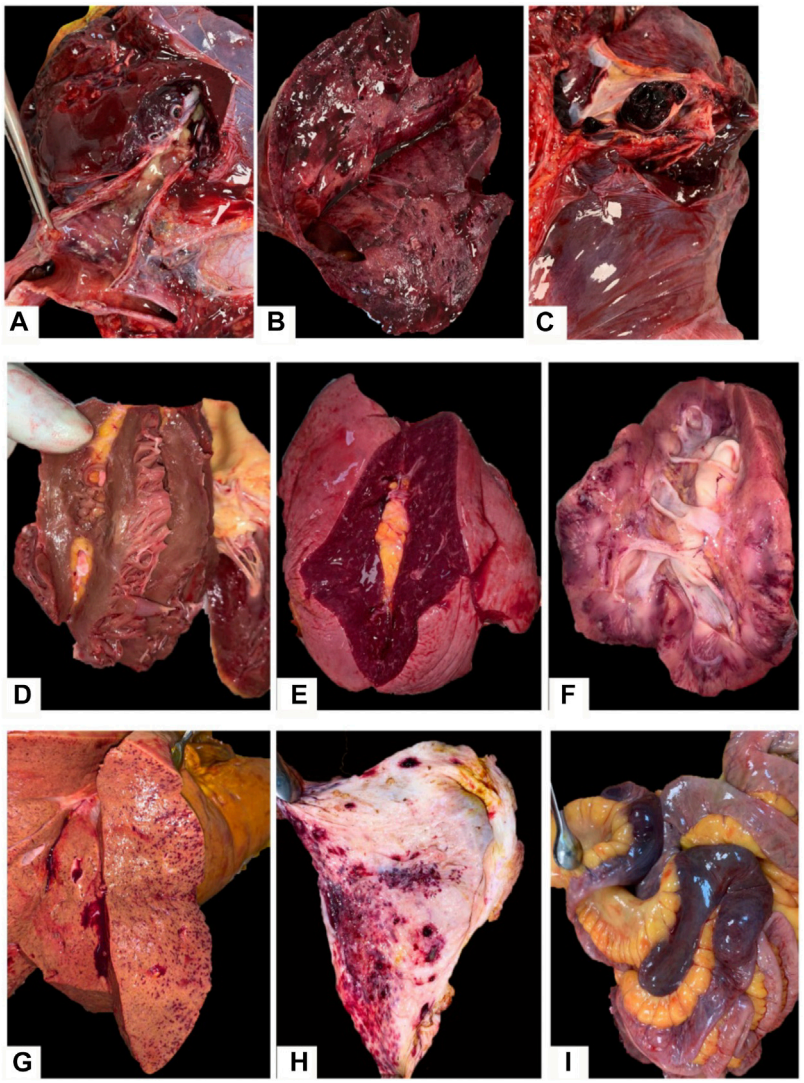

FIGURE 3 | Macroscopic findings in COVID-19 patients: **(A–C)**–pulmonary surface with a dark-red or dark-cherry color, volume increase and airless tissue, with a rubber density, dark-red or brown-red in color with pulmonary emboli detected in lung arteries lumens; **(D)**–left ventrical hypertrophia with pale ischemic metabolic focus; **(E)**—enlarged spleen with average pulp scraping; **(F)**—"shock" kidney with pale cortex and congested medullae with hemorrhages; **(G)**—liver tissue demonstrating fatty degeneration and congested vessels with focal hemorrhages; **(H)**–hemorrhages in the gastric mucosa in a COVID-19 patient complicated by DIC; **(I)**—segmental gangrene of the intestine in a COVID-19 patient complicated by DIC.

Edema and focal hemorrhages were found in the parotid glands, however, we did not find any changes in other salivary glands. Purulent tracheobronchitis was found in 34% of cases, hemorrhagic tracheobronchitis–in 10%, and mixed, purulent-hemorrhagic tracheobronchitis in 4 cases. These changes were most often associated with tracheal intubation and prolonged mechanical ventilation.

Red blood cell stasis with arterial fibrinous and organized thrombi were identified in 67 cases, the same findings were observed in veins in 48 cases. This is typical of fibrin cloths. The presence of alveolar siderophages, and siderophages were identified in bronchi and terminal bronchioles in 43 cases. Interalveolar and interstitial plasma cell and lymphocyte infiltration was found in 43 cases, although its severity varied. In 38 cases interstitial inflammation of the interalveolar septae was seen. 19 cases demonstrated a perivascular myxoid edematous stroma and similar stromal changes within the interalveolar septae. Terminal bronchiolar epithelial (n = 24) and alveolar (n = 37) squamous cell metaplasia, and its rare desquamation into the bronchi (n = 67) and alveoli in the form of plasts (n = 67) was common.

Vascular proliferation was identified in the form of multiple closely related thin-walled capillaries, confirmed by IHC staining with a CD31 marker (**Figures 5A–C**). Squamous cell metaplasia was characterized by a highly intensive membranous staining of epithelial cells in immunohistochemical processing by CK5-6 (**Figures 5D–F**). Based on morphologic findings, exudative (early) phase DAD was diagnosed in 45 cases. Proliferative

TABLE 1 | Microscopic changes in lungs.

Microscopic findings	Number of patients with the finding (N)
Hyaline membranes	75
Fibrin within the alveoli	54
Interalveolar hemorrhages	75
Siderophages within the alveoli	43
Interalveolar edema	61
Interstitial inflammation	38
Cytopathic effect	55
Granulation tissue	28
Pulmonary infarction	31
Arterial thrombi	67
Vein thrombi	48
Neutrophils in the bronchi/bronchioles/alveoli	29
Bronchial epithelium metaplasia	24
Bronchial epithelium desquamation	67
Alveolar epithelium metaplasia	37
Alveolar epithelium desquamation	67
Alveolar macrophages	56
Intercellular viral particles	0
Interstitial myxoid edematous stroma (alveolar walls, perivascular)	19
Aspiration	1
Plasma cells, lymphocytes within alveoli	43
Siderophages within the bronchi	12

(late) phase of DAD characterized by the fibrin deposits of different maturity within the alveoli and single terminal and respiratory bronchioles, also by polypoid fibroblastic tissue (granulation tissue) within the terminal bronchioles and alveoli was diagnosed in 45 cases. The exudative and productive phases of diffuse alveolar damage (mixed DAD phase) with signs of local interalveolar edema, hyaline membranes, desquamated alveolar epithelium combined with fibrin, alveolar fibroblastic component, alveolar and bronchial squamous cell metaplasia were found in 36 autopsy cases. In 31 cases, microscopic findings of bronchopneumonia, and in 3 cases viral-bacterial-mycotic pneumonia were identified, and it was proven by microbiological evaluation. In 1 case only a bacterial aspiration bronchopneumonia with no DAD criteria was identified, despite positive PCR testing.

Extrapulmonary Findings

Hemmoragic findings in the brain were found in seven cases (**Figure 6A**). Hepatomegaly and splenomegaly of ranging severity were identified in all COVID-19 autopsies. Heart weight varied from 250 to 700 g (mean = 452 g). The ventricular index in 81% of cases was less than 0.4, which testifies arterial hypertension. Postinfarction cardiosclerosis was observed in 23 patients (**Figure 6B**). Myocardial metabolic disorders were identified in 6 cases, five of which—in patients with DIC syndrome, which was interpreted as hemopoietic complications of COVID-19 infection in case an atherosclerotic plaque was absent within the coronary arteries (**Figure 3D**). Ischemic and hemorrhagic infarctions of the kidneys were identified in 2 cases, one of which was associated with DIC syndrome. "Shock kidneys" were noted in five autopsies, which demonstrated signs of acute renal failure (**Figure 3F**). Microscopically along with an arteriolonephrosclerosis (common finding in hypertensive patients), partial glomerular collapse, significant granular tubular epithelial dystrophy, renal tubular eosinophilic masses, tubular and interstitial necrosis and edema were commonly identified (**Figure 6C**).

The spleen varied in weight being 50–530 g (mean = 176 g). Splenic hyperplasia (over 190 g) with an notable pulp scraping was detected in 31 cases (**Figure 3E**). Increased splenic weight was more pronounced in patients with sings of septic shock. Microscopically a follicular reduction, splenic pulp unification with lymphocytes and multiple necrotic foci, and hemorrhages was noticed (**Figure 6E**). Focal hemorrphages as well as angiomatosis were also observed in bifurcation lymphnodes (**Figure 6F**). The livers had signs of droplet-like, middle-size and large droplet-like steatosis of ranging severity in all cases along with petechial hemorrhages (**Figures 3G**, **6D**).

Clinical correlation. In order to find significant difference between patient groups, we decided to evaluate the most common comorbid conditions in the deceased patients. These included arterial hypertension, obesity, ischemic heart disease and diabetes. The patients were categorized into eight groups according to combination of these comorbid conditions (**Table 2**). Analysis of variance showed that the mean respiration rate, C-reactive protein levels, heart mass, lung mass and CT severity grades were the only variables with significant differences. Specifically, patients with all four comorbidities had a significantly higher mean respiration rate. C-reactive protein levels were significantly greater in patients with comorbidities compared to those without. Interestingly, lung mass was greater in the group of patients with arterial hypertension, obesity and ischemic heart disease, compared to those without comorbid conditions. Pulmonary findings did not

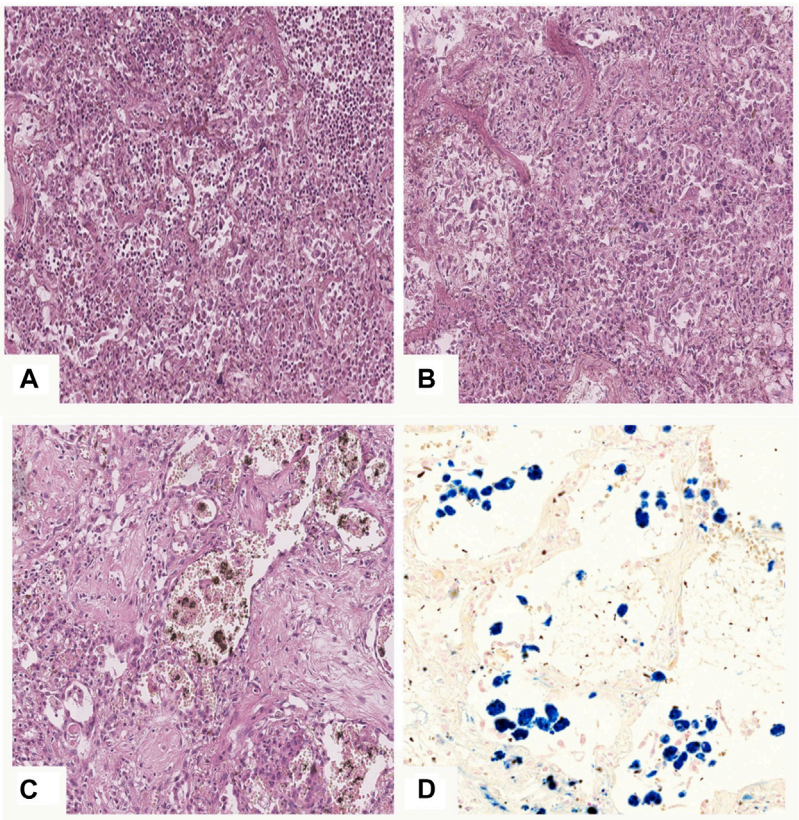

FIGURE 4 | Pulmonary microscopic findings in COVID-19 patients. **(A)**—DAD phase 1: hyaline membranes lining the alveoli, desquamation of alveolocytes, focus of leukocyte infiltration (upper right corner); **(B)**—DAD mixed phase—alongside hyaline membranes there are fibroblasts and granulation tissue present; **(C)**—DAD phase 2: fibrous tissue with single alveolar lumens detected, erythrocytes and hemosyderophages in the alveolar lumens; **(D)**—iron deposits in hemosyderophages in alveolar lumens. **(A–C)**—H&E stain, ×20; **(D)**—Perls' stain, ×20.

vary significantly in patients according to clinical findings (**Table 3**).

Further evaluation of clinical, laboratory and pathological correlates showed that patients with mean respiration rates of over 21 generally had lower C-reactive protein values ($p = 0.0316$) and showed signs of macrophage infiltration of alveoli more commonly ($p = 0.022$). Patients who were sick for over 14 days spent significantly more time on ventilation ($p = 0.001$), had lower SpO2 levels on admission ($p = 0.015$), commonly presented with granulation tissue ($p = 0.016$), neutrophil pulmonary infiltration ($p = 0.010$) and bronchial epithelial metaplasia ($p < 0.001$) than those who were sick for under 14 days. This suggests that granulation, neutrophil infiltration and epithelial changes are characteristic of disease progression.

Patients who passed away quicker (<7 days of hospitalization) were surprisingly younger ($p = 0.022$), had a higher heart mass ($p = 0.009$), shorter disease duration ($p < 0.0001$), spent less time on ventilation ($p < 0.0001$), had less venous thrombi ($p = 0.038$), less findings of epithelial desquamation ($p = 0.038$), myxoid edema ($p = 0.045$), plasmocytic infiltration ($p = 0.044$). Importantly, these findings did not show any significant variability in terms of comorbidity. Patients aged 70 and under were more often in DAD phase 1–2 ($p = 0.006$), while no other significant age related discrepancies were noted in both comorbidities, clinical and pathological status. Arterial thrombosis was more common in older patients ($p < 0.0001$), and was significantly associated with presence of siderophages in alveoli ($p = 0.0002$), interstitial pulmonary edema ($p = 0.011$), cytopathic effect ($p = 0.037$), pulmonary infarctions ($p = 0.016$) and presence of venous thrombi ($p < 0.0001$). C-reactive protein levels of over 200 were associated with increased macrophageal infiltration of alveoli ($p = 0.045$), reduced myxoid edema ($p = 0.016$) and were more common in patients with ischemic heart disease ($p = 0.009$).

DISCUSSION

Many publications regarding the safety and protocol for COVID-19 autopsies have been published [9–11,13,14]. Proper ventilation [9,15], full-body protection, breathing filters and other techniques have been recommended to assure isolation of the pathologist [9–11]. In some institutions pathologists follow a special in corpore technique [9], or a pinpoint ultrasound autopsy, while others prefer full or partial evisceration techniques [9–11]. Several institutions do not perform

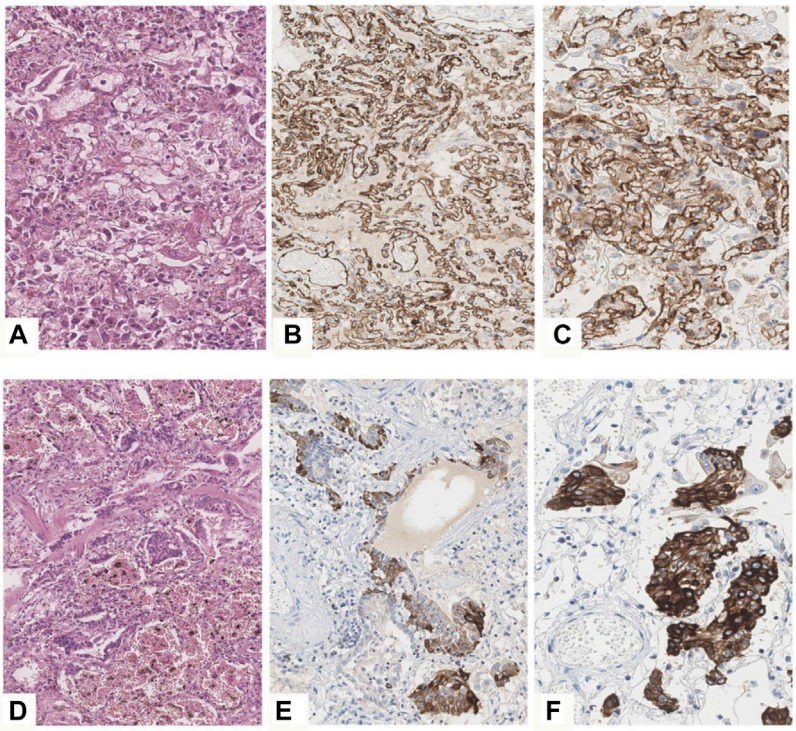

FIGURE 5 | DAD phase 2 in COVID-19 patiens. **(A–C)**—vascular proliferation in lungs. **(A)**—H&E, ×40, **(B,C)**—IHC with the CD31 marker, B×20, **(C)**—×40. **(D–F)**—squamous cell metaplasia of an alveolar epithelium and bronchi. **D**—H&E, ×20, **(E,F)**—IHC staining with the CK5-6 marker, **(E)**—×20, **(F)**—×40.

autopsies, favoring full-body post-mortem MRI scanning instead [16]. Such necessary limitations have been widely implemented [17–21]. In our study, we utilized a full-body isolation protocol, which allowed for complete pathological evaluation.

Numerous clinical studies showed the aggravating effects of comorbidities on COVID-19 prognosis [9,15,16,22–28]. Arterial hypertension, coronary artery disease, diabetes mellitus, obesity, malignant neoplasms and chronic pulmonary disease lead to increased lethality risk [6,9,15,16,26,29–35]. In our study, DAD was noted to be the main factor, influencing lethality in patients with existing comorbidities. More so, our revealed the presence of a mixed phase of diffuse alveolar damage with signs of both exudative and proliferative phases in COVID associated pathology, found a discrepancy between the duration of the disease and the phase of DAP (in some cases, the morphological picture of the exudative phase of DAP was observed later than 14 days from the onset of the disease, while in other cases, deposits of fibrin and granulation tissue were present already at 7 days from the onset of the disease). Our findings suggest that granulation, neutrophil infiltration and epithelial changes are characteristic of disease progression. Noting that the subjects of our study all succumb to the disease, it is important to note that these signs may be poop prognostic factors, indicating uncontrolled disease progression.

The limitations of our study involve the sample size: while being one of the largest cohorts reported, the subgroups were often too small for proper statistical evaluation. Furthermore, the lack of data on clinical background of some patients (due to the acute matter of the disease in previously unmonitored patients) posed limitations in analysis of risk factors and individual patterns. A single center analysis poses limitations regarding quality of care, which may vary elsewhere.

Diffuse alveolar damage has several distinct phases: an exudative phase (observed in 1–7 days of illness), followed by a proliferative phase (1–3 weeks since disease manifestation) and a fibrotic phase (if occurs, after 3 weeks). A combination of the proliferative and an exudative phase was seen in 36% of cases in our study, which is consistent with other findings [15,22,36,37]. A prolonging of the exudative phase may be associated with treatment, intervention ventilation and viral load factors. An Italian study showed that among 38 deceased patients hospitalized for 1–23 days, no one was diagnosed with the fibrotic stage of DAD, but rather with the exudative and early proliferative stages of DAD [15].

SARS-CoV-2 replicates mainly within Type II Alveolocytes due to ACE affinity [38,39]. However, Carsana et al. identified viral particles along the plasmalemma and inside the intracytoplasmic vacuoles of Type 1 and 2 Pneumocytes and alveolar macrophages [15]. Bacterial and mycotic pneumonia complicating SARS-CoV-2 infection have been discussed as factors influencing lethality and viral activity [9,15,16]. According to our data, a bacterial (31%) and a bacterial-mycotic (3%) flora was identified in the patients on prolonged artificial ventilation, which partially confirmed this hypothesis.

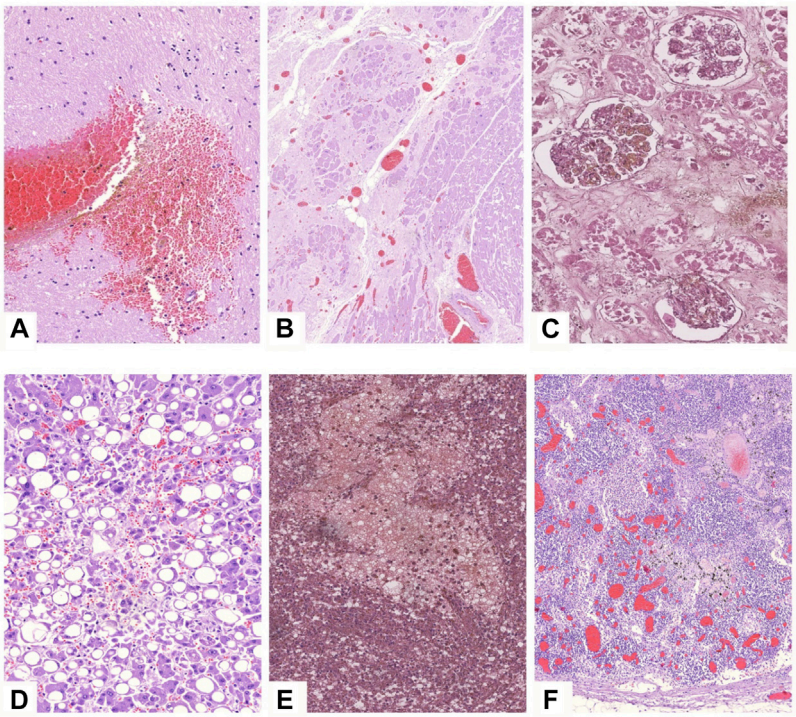

FIGURE 6 | Microscopic findings in other organs in COVID-19 patients. H&E stain. **(A)**—brain tissue demonstrating focal hemorrhage and pericellular edema, ×20; **(B)**—miocard sample with large postinfarction cardiosclerosis area, congested vessels and contracted cardiomyocytes, ×5; **(C)**—kidney specimen showing massive necrosis of tubular epithelium, ×20; **(D)**—steatosis of hepatocytes, congested vessels, ×20; **(E)**—focal hemorrhage in the spleen, ×20; **(F)**—reactive lymphadenitis with angiomatosis of bifurcation lymphnodes.

Vascular complications, including thromboembolic and hemorrhagic, are widely seen in post-mortem COVID-19 autopsies [40–44]. This is due to SARS-CoV-2 associated coagulopathic disorders (generalized thrombotic microangiopathy, vascular endothelial injury) [9,40]. We observed DIC in up to 31% of cases, presented as multiple vascular hemorrhages or thromboses in different locations, pulmonary artery and vein multiple obturating thromboses, including hemorrhagic pulmonary infarcts and extrapulmonary pathology.

According to our data, left ventricular hypertrophy, cardiomyocyte hypertrophy, cellular myocardial degeneration and arterial hypertension-related pathology were the most common findings in the heart, consistent with existing data [16,36,37]. IHC demonstrated that myocardial interstitial portion is mainly presented by macrophages and some amount of $CD4^+$ T-cells. $CD8^+$ T-cells and $CD20^+$ B-cells have not been identified. However, existing studies have not yet identified SARS-CoV-2 viral particles within the myocardium cells [36]. Lymphoplasmacytic infiltration was not identified by many researchers [37], the signs of myocarditis were also absent in our study. Myocardial senile amyloidosis was demonstrated in 1% of cases in our study, and was also noted by other researchers [9].

Several other studies have demonstrated lymphocytic infiltration of hepatic lobules, sinusoid dilatation, partial hepatocyte necrosis, yet were mainly associated with concomitant pathology (e.g., liver cirrhosis) [22,36,37]. Our findings show hepatocyte dystrophy and hepatic degeneration associated with direct COVID-19 associated damage. In our previous work owe showed COVID-19 lymph node damage consists of reduction of lymphoid follicles and expansion of the paracortical zone with reactive plasmacytosis, extrafollicular B-cell activation, sinus histiocytosis, signs of hemophagocytosis, formation of hyaline thrombi, diapedetic hemorrhages, and massive hemorrhages in individual nodes. An immunohistochemical study revealed the predominance of CD4 + T-helpers in the paracortical zone, depletion of cytotoxic CD8 + lymphocytes, an increase in the number of both lymphocytes expressing the PD-1 suppressor protein and activated lymphocytes expressing the CD30 activation antigen. CD123-positive plasmacytoid dendritic cells secreting type 1 interferon were found in a significant amount in the lumen of the sinuses and in the paracortical zone [45].

Damage to the kidneys in COVID-19 presents with arteriolonephrosclerosis along with nephritis, collapse glomerulopathy, tubular epithelium dystrophy with protein exudate, cylinders within enlarged tubules and fibrin thrombi within capillaries [22,36]. Tubular necrosis and renal infarctions, associated with septic conditions, were seen in 2 cases in our study. Splenic enlargement due to sepsis, major follicular reduction, lymphatic infiltration, necrosis and

TABLE 2 | Comparison of clinical data between patients with common comorbid conditions (AH, arterial hypertension; OB, obesity; DM, diabetes mellitus; ICD, ischemic heart disease).

Cat	A	B	C	D	E	F	G	H	
Comorbidity	**Arterial hypertension only (*n* = 33)**	**Arterial hypertension and Obesity (*n* = 8)**	**AH + OB + DM + ICD (*n* = 2)**	**AH + OB + DM (*n* = 9)**	**AH + DM (*n* = 7)**	**AH + ICD (*n* = 17)**	**AH + OB + ICD (*n* = 3)**	**None (*n* = 15)**	***p*-value (ANOVA)**
Age	71.73 ± 14.14	73.38 ± 16.28	68.50 ± 4.95	71.67 ± 13.37	72.71 ± 11.53	72.53 ± 13.63	86.67 ± 6.43	69.07 ± 12.81	0.656
Time from hospitalization to death (days)	8.12 ± 5.07	6.13 ± 7.90	12.50 ± 4.95	6.36 ± 3.38	7.57 ± 4.86	6.94 ± 4.44	13.33 ± 10.69	7.33 ± 4.69	0.430
Disease duration (symptom onset to death)	14.46 ± 6.19	11.38 ± 10.14	14.50 ± 6.36	11.11 ± 4.37	15.29 ± 6.32	14.06 ± 3.19	20.67 ± 23.67	11.20 ± 4.60	0.321
Time on ventilation	5.73 ± 5.40	6.17 ± 9.37	10.50 ± 6..36	5.27 ± 2.84	7.44 ± 5.01	5.31 ± 3.52	11.67 ± 11.93	7.08 ± 3.96	0.535
Patient mean respiration rate (breaths/min)	20.85 ± 2.64	21.00 ± 2.53	32.50 ± 17.58	21.29 ± 3.20	23.40 ± 5.94	21.91 ± 4.01	22.67 ± 3.06	22.86 ± 4.63	**0.0189* C vs A,B,D,F,H**
Maximum C-reactive protein (mg/L)	245.70 ± 96.23	152.52 ± 89.07	198.20 ± 4.38	141.95 ± 57.98	237.90 ± 73.02	134.43 ± 94.12	141.50 ± 61.52	59.54 ± 51.57	**<0.0001* A vs D,F,H E vs H**
SpO^2 on admission (%)	87.23 ± 10.35	87.33 ± 6.19	78.00 ± 16.97	86.67 ± 21.11	84.50 ± 9.15	85.00 ± 13.28	84.00 ± 8.49	90.40 ± 6.11	0.850
Mean body temperature (C^o)	38.27 ± 0.97	37.86 ± 0.77	37.75 ± 0.35	37.45 ± 1.88	38.46 ± 0.55	38.26 ± 0.63	38.75 ± 1.48	38.50 ± 0.86	0.216
Maximum lymphocyte content (%)	13.41 ± 12.77	10.42 ± 3.36	3.50 ± 2.40	13.85 ± 7.57	13.00 ± 8.34	15.40 ± 18.38	8.6 ± 3.39	10.57 ± 3.00	0.828
Heart mass (g)	471.27 ± 96.97	431.00 ± 111.17	383.00 ± 45.25	440.89 ± 89.66	464.29 ± 84.63	406.18 ± 91.42	313.33 ± 77.67	483.33 ± 90.05	**0.0443***
Spleen mass (g)	178.33 ± 96.88	163.63 ± 95.74	134.00 ± 50.91	252.33 ± 138.29	138.57 ± 37.61	169.06 ± 82.47	120.00 ± 17.32	160.00 ± 61.96	0.202
Lung mass G vs H	1729.39 ± 465.11	1,620.63 ± 300.01	1962.50 ± 901.56	1,641.11 ± 425.89	1,467.14 ± 290.62	1,617.64 ± 264.21	2,283.33 ± 325.32	1,499.33 ± 270.49	**0.0484***
CT severity (grade 1–5)	3.33 ± 0.58	2.50 ± 2.12	3.50 ± 0.71	3.14 ± 0.90	3.14 ± 0.89	3.75 ± 0.50	3.67 ± 0.58	3.5 ± 0.71	0.0875 **B vs. F (0.0263*)**

Bold values: statistically significant findings at p < *0.05.*

TABLE 3 | Pulmonary findings (AH, arterial hypertension; OB, obesity; DM, diabetes mellitus; ICD, ischemic heart disease).

Comorbidity	Arterial hypertension only (*n* = 33)	Arterial hypertension and obesity (*n* = 8)	AH + OB + DM + ICD (*n* = 2)	AH + OB + DM (*n* = 9)	AH + DM (*n* = 7)	AH + ICD (*n* = 17)	AH + OB + ICD (*n* = 3)	None (*n* = 15)
DAP phase 1 (*n*, %)	16 (48.48%)	4 (50.00%)	0 (0.00%)	2 (22.22%)	2 (28.57%)	10 (58.82%)	2 (66.67%)	8 (53.33%)
DAP phase 2 (*n*, %)	6 (18.18%)	2 (25.00%)	1 (50.00%)	3 (33.33%)	3 (42.86%)	2 (11.76%)	0 (0.00%)	0 (0.00%)
DAP phase 1–2 (*n*, %)	11 (33.33%)	2 (25.00%)	1 (50.00%)	4 (44.44%)	2 (28.57%)	5 (29.41%)	1 (33.33%)	7 (46.67%)
Hyaline membrane presence	25 (75.76%)	6 (75.00%)	1 (50.00%)	4 (44.44%)	4 (57.14%)	14 (82.35%)	3 (100%)	15 (100%)
Fibrin in alveoli	17 (51.52%)	3 (37.50%)	2 (100%)	7 (77.78%)	5 (71.43%)	6 (35.29%)	2 (66.67%)	7 (46.67%)
Erythrocytes in alveoli	21 (63.64%)	5 (62.50%)	1 (50.00%)	8 (88.89%)	7 (100%)	16 (94.12%)	3 (100%)	11 (73.33%)
Siderophages in alveoli	9 (27.27%)	3 (37.50%)	1 (50.00%)	6 (66.67%)	5 (71.43%)	9 (52.94%)	0 (0.00%)	6 (40.00%)
Interalveolar oedema	22 (66.67%)	4 (50.00%)	1 (50.00%)	5 (55.56%)	3 (42.86%)	10 (58.82%)	3 (100%)	12 (80.00%)
Interstitial inflammation	13 (39.39%)	3 (37.50%)	2 (100%)	4 (44.44%)	4 (57.14%)	5 (29.41%)	0 (0.00%)	4 (26.67%)
Cytopathic effect	14 (42.42%)	7 (87.50%)	0 (0.00%)	5 (55.56%)	5 (71.43%)	14 (82.35%)	0 (0.00%)	7 (46.67%)
Granulations	10 (30.30%)	3 (37.50%)	2 (100%)	3 (33.33%)	5 (71.43%)	2 (11.76%)	0 (0.00%)	1 (6.67%)
Hemorrhagic infarctions	12 (36.36%)	0 (0.00%)	0 (0.00%)	3 (33.33%)	2 (28.57%)	4 (23.53%)	2 (66.67%)	7 (46.67%)
Arterial thrombi	19 (57.58%)	4 (50.00%)	2 (100%)	7 (77.78%)	4 (57.14%)	13 (76.47%)	2 (66.67%)	11 (73.33%)
Venous thrombi	15 (45.45%)	4 (50.00%)	2 (100%)	7 (77.78%)	2 (28.57%)	10 (58.82%)	2 (66.67%)	3 (20.00%)
Neutrophil infiltration	7 (21.21%)	1 (12.50%)	1 (50.00%)	3 (33.33%)	1 (14.29%)	8 (47.06%)	1 (33.33%)	5 (33.33%)
Bronchial epithelial metaplasia	9 (27.27%)	1 (12.50%)	0 (0.00%)	3 (33.33%)	3 (42.86%)	2 (11.76%)	0 (0.00%)	3 (20.00%)
Bronchial epithelial desquamation	21 (63.64%)	3 (37.50%)	2 (100%)	7 (77.78%)	6 (85.71%)	9 (52.94%)	3 (100%)	11 (73.33%)
Alveolar epithelial metaplasia	13 (39.39%)	2 (25.00%)	1 (50.00%)	5 (55.56%)	3 (42.86%)	3 (17.65%)	1 (33.33%)	6 (40.00%)
Alveolar epithelial desquamation	18 (54.55%)	5 (62.50%)	1 (50.00%)	6 (66.67%)	6 (85.71%)	12 (70.59%)	3 (100%)	12 (80.00%)
Macrophage infiltration of alveoli	16 (48.48%)	5 (62.50%)	2 (100%)	4 (44.44%)	5 (71.43%)	9 (52.94%)	1 (33.33%)	9 (60.00%)
Edematous myxoid stroma	6 (18.18%)	3 (37.50%)	0 (0.00%)	2 (22.22%)	2 (28.57%)	3 (17.65%)	0 (0.00%)	2 (13.33%)
Aspiration	0 (0.00%)	0 (0.00%)	0 (0.00%)	0 (0.00%)	0 (0.00%)	0 (0.00%)	0 (0.00%)	0 (0.00%)
Lymphocytes in alveoli	13 (39.39%)	3 (37.50%)	2 (100%)	4 (44.44%)	4 (57.14%)	6 (35.29%)	2 (66.67%)	7 (46.67%)
Siderophages in bronchi	0 (0.00%)	2 (25.00%)	1 (50.00%)	3 (33.33%)	2 (28.57%)	2 (11.76%)	—	1 (6.67%)

hemorrhages have been shown in our study, consistent with other findings [36]. A B-dependent zone reduction and cytotoxic T-lymphocyte depletion with PD-1 superexpression were characteristic of severe coronaviral infection, which, according to several studies, demonstrates immune response reduction [45]. The paracortical zone showed a significant reactive plasmocytosis with T-helper existence—a morphologic substrate of humoral immunity, which may testify a noneffective humoral response in COVID-19-effected patients with simultaneous T-cell immunity failure.

Our data adds value to analysis of certain potential predictors of disease severity. Respiration rate was shown to be significantly greater in patients with more than one comorbidity, indicating the potential prognostic value of this parameter. Pulmonary findings were non-specific to clinical symptoms, prognosis or disease duration, which highlight the vast unpredictability of the disease, hinting and genetic predisposition to severe forms. Our findings that younger patients passed away sooner may be attributed to the fact that they are admitted at later stages and elderly patients are prioritized in acute care. Patients who do not die early and develop granulations, immune infiltration and epithelial changes are at risk of lethal outcome. Arterial thrombosis was the dominant factor in lethal outcome in the elder patients (over 70), while younger patients did not develop thrombosis, but presented with acute DAD phase 1-2, suggesting it's main role in lethal outcome of a predisposed cohort.

CONCLUSION

The new coronaviral infection pathogenesis and its pathological manifestations are being heavily studied. Due to high contagiousness and low autopsy rate worldwide, too few autopsies of the coronavirus-affected patients are performed. As such, our study provides substantial insight into the macro- and micropathological aspects of COVID-19 damage. Our results show high prevalence of diffuse alveolar damage, as well as immune compromise and polyorgan failure in deceased patients.

DATA AVAILABILITY STATEMENT

The raw data supporting the conclusion of this article will be made available by the authors, without undue reservation.

ETHICS STATEMENT

The studies involving human participants were reviewed and approved by Institutional Ethics Committee at the Research

Institute of Human Morphology. Written informed consent was acquired from the relatives of the participants in accordance with the ethical standards of the Research Institute for Human Morphology and the Ministry of Health of the Russian Federation.

AUTHOR CONTRIBUTIONS

LMM, ALC, MVS, and OVZ contributed to conception and organization of the research project, drafted the main manuscript text. LVK, OAV, and AEB, were involved in study conception, participated in design and coordination, visualization. ASK, AVS, and MYS performed the procedures and acquired the data. MYS, ALC were responsible for data acquisition. AEB, ASK: writing, review and editing; LMM, MVS, and OVZ: analysis and interpretation of data, wrote manuscript, and approved the final version of the manuscript. All authors have read and agreed to the published version of the manuscript.

CONFLICT OF INTEREST

The authors declare that the research was conducted in the absence of any commercial or financial relationships that could be construed as a potential conflict of interest.

ACKNOWLEDGMENTS

We thank the relative of the patients included in this study, the staff and personnel assisting with COVID-19 autopsies.

REFERENCES

1. Reicher S, and Stott C. On order and disorder during the COVID-19 pandemic. *Br J Soc Psychol* (2020) 59(3):694–702. doi:10.1111/bjso.12398
2. Dong E, Du H, and Gardner L. An interactive web-based dashboard to track COVID-19 in real time. *Lancet Inf Dis* 20(5):533–4. doi:10.1016/S1473-3099(20)30120-1
3. Kobak D. Excess mortality reveals Covid's true toll in Russia. *Significance* (2021) 18(1):16–9. doi:10.1111/1740-9713.01486
4. Pomeranz JL, and Schwid AR. Governmental actions to address COVID-19 misinformation. *J Public Health Pol* (2021) 42:201–10. doi:10.1057/s41271-020-00270-x
5. Partinen M, Bjorvatn B, Holzinger B, Chung F, Penzel T, and Espie C. A ICOSS; collaboration group. Sleep and circadian problems during the coronavirus disease 2019 (COVID-19) pandemic: the International COVID-19 Sleep Study (ICOSS). *J Sleep Res* (2021) 30(1):e13206. doi:10.1111/jsr.13206
6. Riiser K, Helseth S, Haraldstad K, Torbjørnsen A, and Richardsen K. R. Adolescents' health literacy, health protective measures, and health-related quality of life during the Covid-19 pandemic. *PloS one* (2020) 15(8):e0238161. doi:10.1371/journal.pone.0238161
7. Liu C. H, Stevens C, Conrad R. C, and Hahm H. C. Evidence for elevated psychiatric distress, poor sleep, and quality of life concerns during the COVID-19 pandemic among U.S. young adults with suspected and reported psychiatric diagnoses. *Psychiatry Res* (2020) 292:113345. doi:10.1016/j.psychres.2020.113345
8. Calabrese F, Fortarezza F, Fortarezza F, Hofman P, Kern I, Panizo A, and Lunardi F. Diffuse Idiopathic Pulmonary Neuroendocrine Cell Hyperplasia (DIPNECH). *Virchows archiv* (2020) 1–7. doi:10.1007/978-3-319-28845-1_5073-1
9. Batah S. S, and Fabro A. T. Pulmonary pathology of ARDS in COVID-19: A pathological review for clinicians. *Respir Med* (2020) 106239.
10. Barton L. M, Duval E. J, Stroberg E, Ghosh S, and Mukhopadhyay S. COVID-19 Autopsies, Oklahoma, USA. *Am J Clin Pathol* (2020) 153(6):725–33. doi:10.1093/ajcp/aqaa062
11. Hanley B, Lucas S. B, Youd E, Swift B, and Osborn M. Autopsy in suspected COVID-19 cases. *J Clin Pathol* (2020) 73:239–42. doi:10.1136/jclinpath-2020-206522
12. Mauad T, Hajjar L. A, Callegari G. D, da Silva L. F. F, Schout D, Galas F. R. B. G, et al. Lung pathology in fatal novel human influenza A (H1N1) infection. *Am J Respir Crit Care Med* (2010) 181(1):72–9. doi:10.1164/rccm.200909-1420oc
13. Centers for Disease Control and Prevention. Collection and Submission of Postmortem Specimens from Deceased Persons with Known or Suspected COVID-19, March 2020 (Interim Guidance). Available from: www.cdc.gov/coronavirus/2019-ncov/hcp/guidance-post mortem-specimens.html (Accessed May, 2020).
14. College of American Pathologists (CAP). *Amended COVID-19 autopsy guideline statement from the CAP autopsy committee* (2020). Available from: https://covid19.who.int/ (Accessed May, 2020).
15. Carsana L, Sonzogni A, Nasr A, Rossi RS, Pellegrinelli A, Zerbi P, et al. Pulmonary post-mortem findings in a series of COVID-19 cases from northern Italy: a two-centre descriptive study. *Lancet Infect Dis* (2020) 20(20):1135–40. doi:10.1016/S1473-3099(20)30434-5
16. Wichmann D, Sperhake JP, Lütgehetmann M, Steurer S, Edler C, Heinemann A, et al. Autopsy Findings and Venous Thromboembolism in Patients With COVID-19 [published online ahead of print, 2020 May 6]. *Ann Intern Med* (2020) M20–2003. doi:10.7326/M20-2003
17. Centers for Disease Control and Prevention (CDC). *Interim laboratory biosafety guidelines for handling and processing specimens associated with coronavirus disease 2019 (COVID-19)* (2020). https://www.cdc.gov/coronavirus/2019-nCoV/lab/lab-biosafetyguidelines.html (Accessed May, 2020).
18. World Health Organization. *Laboratory biosafety guidance related to the novel coronavirus (2019-nCoV): interim guidance* (2020). https://www.who.int/publications-detail/laboratory-biosafetyguidance-related-to-coronavirus-disease-2019-(covid-19 (Accessed May, 2020).
19. Iwen P. C, Stiles K. L, and Pentella M. A. Safety Considerations in the Laboratory Testing of Specimens Suspected or Known to Contain the Severe Acute Respiratory Syndrome Coronavirus 2 (SARS-CoV-2). *Lab Med* (2020) 51:239–42. doi:10.1093/labmed/lmaa018
20. Barbareschi M, Ascoli V, Bonoldi E, Cavazza A, Colombari R, Cozzi I, et al. Biosafety in surgical pathology in the era of SARS-Cov2 pandemia. A statement of the Italian Society of Surgical Pathology and Cytology. *Pathologica* (2020) 12(2):59–63. doi:10.32074/1591-951X-14-20
21. Henwood A. F. Coronavirus disinfection in histopathology. *J Histotechnology* (2020) 43:102–4. doi:10.1080/01478885.2020
22. Duarte-Neto AN, Aparecida de Almeida Monteiro R, Ferraz da Silva LF, Costa Malheiros DM. A, de Oliveira E. P, Filho JT, et al. Pulmonary and systemic involvement of COVID-19 assessed by ultrasound-guided minimally invasive autopsy. *Histopathology* 77(2):186–97. doi:10.1111/his.14160
23. Zhang H, Zhou P, Wei Y, Yue H, Hu M, Zhang S, et al. Histopathologic Changes and SARS-CoV-2 Immunostaining in the Lung of a Patient With COVID-19. *Ann Intern Med* (2020) 172(9):629–32.
24. Tang N, Li D, Wang X, and Sun Z. Abnormal coagulation parameters are associated with poor prognosis in patients with novel coronavirus pneumonia. *J Thromb Haemost* (2020) 18(4):844–7. doi:10.1111/jth.14768
25. Tang N, Bai H, Chen X, Gong J, Li D, and Sun Z. Anticoagulant treatment is associated with decreased mortality in severe coronavirus disease 2019 patients with coagulopathy. *J Thromb Haemost* (2020) 18(5):1094–9. doi:10.1111/jth.14817
26. Zhou F, Yu T, Du R, Fan G, Liu Y, Liu Z, et al. Clinical course and risk factors for mortality of adult inpatients т with COVID-19 in Wuhan, China: a retrospective cohort study [published correction appears in Lancet. 2020; 395(10229):1038. doi:10.1016/s0140-6736(20)30566-3
27. Wang Y, Lu X, Li Y, Chen H, Chen T, Su N, et al. Clinical Course and Outcomes of 344 Intensive Care Patients with COVID-19. *Am J Respir Crit Care Med* (2020) 201(11):1430–4. doi:10.1164/rccm.202003-0736le

28. Du Y, Tu L, Zhu P, Mu M, Wang R, Yang P, et al. Clinical Features of 85 Fatal Cases of COVID-19 from Wuhan. A Retrospective Observational Study. *Am J Respir Crit Care Med* (2020) 201(11):1372–9. doi:10.1164/rccm.202003-0543oc
29. Guan W-j., Ni Z-y., Hu Y, Liang W-h., Ou C-q., He J-x., et al. Clinical Characteristics of Coronavirus Disease 2019 in China. *N Engl J Med* (2020) 382:1708–20. doi:10.1056/NEJMoa2002032
30. Wu C, Chen X, Cai Y, Xia J, Zhou X, Xu S, et al. Risk factors associated with acute respiratory distress syndrome and death in patients with coronavirus disease 2019 pneumonia inWuhan, China. *JAMAInternMed* (2020) 180(7): 934–43. doi:10.1001/jamainternmed.2020.0994
31. Zayratyants OV, Samsonova MV, Mikhaleva LM, Chernyaev AL, Mishnev OD, Krupnov NM, et al. Moscow, GBU «NIIOOZM DZM»,.– (2020). p. 142.
32. Xu Z, Shi L, Wang Y, Zhang J, Huang L, Zhang C, et al. Pathological findings of COVID-19 associated with acute respiratory distress syndrome. *Lancet Respir Med* (2020) 8:420–2. doi:10.1016/S2213-2600(20)30076-X
33. Fox S. E, Akmatbekov A, Harbert J. L, Li G, Brown J. Q, and Heide R. S. V. Pulmonary and Cardiac Pathology in Covid-19: The First Autopsy Series from New Orleans. *Lancet Respir Med*. 8(7):681–6. doi:10.1101/2020.04.06.20050575
34. Dolhnikoff M, Duarte-Neto AN, de Almeida Monteiro RA, da Silva LFF, de Oliveira EP, Nascimento Saldiva PH, et al. Pathological evidence of pulmonary thrombotic phenomena in severe COVID-19. *J Thromb Haemost* (2020) 18(6): 1517–9.
35. Lillicrap D. Disseminated intravascular coagulation in patients with 2019-nCoV pneumonia. *J Thromb Haemost* (2020) 18(4):786–7. doi:10.1111/jth.14781
36. Yao XH, Li TY, He ZC, Ping YF, Liu HW, Yu SC, et al. [A pathological report of three COVID-19 cases by minimal invasive autopsies]. *Zhonghua Bing Li Xue Za Zhi* (2020) 49(0):411–7. doi:10.3760/cma.j.cn112151-20200312-00193
37. Tian S, Xiong Y, Liu H, and Niu L. Pathological study of the 2019 novel coronavirus disease (COVID-19) through post-mortem core biopsies. *Mod Pathol* (2020) 33:1007–1014.
38. Mason R. J. Pathogenesis of COVID-19 from a cell biology perspective. *Eur Respir J* (2020) 55(4):2000607, 2020 . Published 2020 Apr 16. doi:10.1183/13993003.00607-2020
39. Lukassen S, Chua R. L, Trefzer T, Kahn N. C, Schneider M. A, Muley T, et al. SARS -CoV-2 receptor ACE 2 and TMPRSS 2 are primarily expressed in bronchial transient secretory cells. *EMBO J* (2020) 39:e105114. doi:10.15252/embj.20105114
40. Ackermann M, Verleden S. E, Kuehnel M, Haverich A, Welte T, Laenger F, et al. Pulmonary Vascular Endothelialitis, Thrombosis, and Angiogenesis in Covid-19. *N Engl J Med* (2020) 383(2):120–8. doi:10.1056/nejmoa2015432
41. Kollias A, Kyriakoulis K. G, Dimakakos E, Poulakou G, Stergiou G. S, and Syrigos K. Thromboembolic risk and anticoagulant therapy in COVID-19 patients: emerging evidence and call for action. *Br J Haematol* (2020) 189(5): 846–7. doi:10.1111/bjh.16727
42. Grasselli G, Zangrillo A, Zanella A, Antonelli M, Cabrini L, Castelli A, et al. Baseline Characteristics and Outcomes of 1591 Patients Infected With SARS-CoV-2 Admitted to ICUs of the Lombardy Region, Italy [published online ahead of print, 2020 Apr 6]. *JAMA* (2020) 323(16):1574–81. doi:10.1001/jama.2020.4031
43. Klok F. A, Kruip M. J. H. A, van der Meer N. J. M, Arbous M. S, Gommers D. A. M. P. J, Kant K. M, et al. Incidence of thrombotic complications in critically ill ICU patients with COVID-19. *Thromb Res* (2020) 191:145–7. doi:10.1016/j.thromres.2020.04.013
44. Oudkerk M, Büller HR, Kuijpers D, Van Es N, Oudkerk S. F, McLoud T, et al. Diagnosis, Prevention, and Treatment of Thromboembolic Complications in COVID-19. *Radiology* (2020) 201629, 2020 . Report of the National Institute for Public Health of the Netherlands [published online ahead of print, 2020 Apr 23]. doi:10.1148/radiol.2020201629
45. Kovrigina A. M, Shalamova EA, Shalamova E. A, Berezovskiy Y. S, Kalinin D. V, Gretsov E. M, et al. Pathomorphological and immunohistochemical features of lymph nodes in COVID-19 patients (autopsy study). *Clin Exp Morphol* (2020) 9(Dec. 2020):12–23. doi:10.31088/CEM2020.9.4.12-23

Pathology & Oncology Research | frontiers

ORIGINAL RESEARCH
published: 26 October 2021
doi: 10.3389/pore.2021.1610039

Syntaxin-1 and Insulinoma-Associated Protein 1 Expression in Breast Neoplasms with Neuroendocrine Features

Sándor Turkevi-Nagy[1], Ágnes Báthori[1], János Böcz[1], László Krenács[2], Gábor Cserni[1,3†] and Bence Kővári[1,4†]*

[1]Department of Pathology, University of Szeged, Szeged, Hungary, [2]Laboratory of Tumor Pathology and Molecular Diagnostics, Szeged, Hungary, [3]Bács-Kiskun County Teaching Hospital, Kecskemét, Hungary, [4]Department of Anatomic Pathology, H. Lee Moffitt Cancer Center & Research Institute, Tampa, FL, United States

Introduction: A subset of breast neoplasia is characterized by features of neuroendocrine differentiation. Positivity for Neuroendocrine markers by immunohistochemistry is required for the diagnosis. Sensitivity and specificity of currently used markers are limited; based on the definitions of WHO Classification of Tumours, 5th edition, about 50% of breast tumors with features of neuroendocrine differentiation express chromogranin-A and 16% express synaptophysin. We assessed the applicability of two novel markers, syntaxin-1 and insulinoma-associated protein 1 (INSM1) in breast carcinomas.

Methods: Hypercellular (Type B) mucinous carcinomas, solid papillary carcinomas, invasive carcinomas of no special type with neuroendocrine features and ductal carcinomas *in situ* of neuroendocrine subtype were included in our study. The immunohistochemical panel included chromogranin A, synaptophysin, CD56, syntaxin-1 and INSM1. The specificity of syntaxin-1 and INSM1 was determined using samples negative for chromogranin A, synaptophysin and CD56.

Results: The sensitivity of syntaxin-1 was 84.7% (50/59), with diffuse positivity in more than 60% of the cases. Syntaxin-1 also had an excellent specificity (98.1%). Depending on the definition for positivity, the sensitivity of INSM1 was 89.8% (53/59) or 86.4% (51/59), its specificity being 57.4% or 88.9%. The sensitivities of chromogranin A, synaptophysin and CD56 were 98.3, 74.6 and 22.4%, respectively.

Discussion: Syntaxin-1 and INSM1 are sensitive and specific markers of breast tumors with neuroendocrine features, outperforming chromogranin A and CD56. We recommend syntaxin-1 and INSM1 to be included in the routine neuroendocrine immunohistochemical panel.

Keywords: immunohistochemistry, syntaxin-1, insulinoma-associated protein 1, breast neuroendocrine neoplasms, solid papillary carcinoma, mucinous carcinoma, carcinoma no special type

OPEN ACCESS

Edited by:
Anna Sebestyén, Semmelweis University, Hungary

****Correspondence:***
Sándor Turkevi-Nagy
tenagysanyi@gmail.com

[†]These authors have contributed equally to this work

Received: *25 August 2021*
Accepted: *11 October 2021*
Published: *26 October 2021*

Citation:
Turkevi-Nagy S, Báthori Á, Böcz J, Krenács L, Cserni G and Kővári B (2021) Syntaxin-1 and Insulinoma-Associated Protein 1 Expression in Breast Neoplasms with Neuroendocrine Features. Pathol. Oncol. Res. 27:1610039. doi: 10.3389/pore.2021.1610039

INTRODUCTION

It has been known for decades, that a subset of breast neoplasia may present with either histomorphological or immunohistochemical (IHC) signs of neuroendocrine (NE) differentiation, or a combination thereof (1). Although these features were primarily described in hypercellular (Type B) mucinous carcinomas, it has become evident that solid papillary carcinomas and many other invasive breast carcinomas of no special type also exhibit such a phenotype (2–5).

NE differentiation, as a histological type defining criterion, was introduced only in the third edition of the World Health Organization (WHO) classification ("blue book" series) of breast tumors (6). This edition, separately from the mucinous carcinomas, mentioned the NE tumors as a distinct category with subcategories: solid, small cell/oat cell and large cell NE carcinomas. These entities were defined on the one hand by the histomorphologic similarities with the NE neoplasms of other organs (e.g., the gastrointestinal tract and lungs), on the other hand by immunoreactivity for NE markers in at least 50% of the tumor cells. Although this category was mainly defined by morphological features, it was not clearly separated from other special types of breast carcinomas known for frequent expression of NE markers. Since its introduction, the classification, definitions and taxonomy have undergone several modifications.

The fourth edition refined the diagnostic criteria by omitting the 50% threshold of immunoreactivity and, separately from "pure" NE tumors and carcinomas, also introduced a new class, namely invasive breast carcinoma with NE differentiation (7). Large cell NE carcinoma was excluded from this edition.

Currently, the fifth and latest classification, harmonized with the newest consensus proposal of the International Agency for Research on Cancer (IARC) and the WHO, adopted the term "neuroendocrine neoplasm" (NEN) (8, 9). It includes well-differentiated NENs also known as NE tumors (NETs) and poorly differentiated NENs or (small cell and large cell) NE carcinomas (NECs). Solid papillary carcinoma and the hypercellular variant (Type B) of mucinous carcinoma remained as distinct entities with frequent NE differentiation. Even though this system seems to have separated the pure NENs from other entities, some of the remaining, much more common categories are unfortunately not so well delineated. If a tumor displays histological features and immunoreactivity for NE markers, but is not "distinct or uniform enough", the appropriate diagnosis should be invasive carcinoma no special type with NE differentiation. Furthermore, if a conventional neoplasm contains areas (between 10 and 90%) consistent with NEN, the term "mixed NEN" should be used.

Besides histomorphology, IHC evaluation is required for confirming NE differentiation. The most commonly applied NE markers are chromogranin A (CGA), synaptophysin (SYP) and CD56. However, none of these markers is sensitive and specific enough to be used alone, and consensus reports recommend their combined application. At the same time, novel, more sensitive or specific and more easily applicable NE marker candidates are being identified. Beside insulinoma-associated protein 1 (INSM1), another example for such a promising molecule is syntaxin-1 (STX1), which we reported to be a generally reliable NE marker (10).

INSM1 is a transcription factor which takes part in the development of NE tissues and neoplasia. Beside regulating transcription, INSM1 is also crucial in arresting cell cycle, therefore it is considered as a key molecule in terminal NE differentiation (11). STX1 is an essential molecule of the neurosecretory machinery and acts as a component of the SNARE complex. Its role is to enable fusion of the secretory vesicle and the presynaptic membrane. Apart from neurons, STX1 has been proven to be specifically expressed by NE cells.

The aim of our study was to evaluate the characteristics of STX1 and INSM1 IHC expression in breast neoplasia showing NE features.

MATERIALS AND METHODS

Formalin-fixed paraffin-embedded samples were collected from the archives of the Departments of Pathology of the Bács-Kiskun County Teaching Hospital and the University of Szeged. Diagnoses of all cases were updated according to the criteria of the 5th edition of WHO classification of breast tumors (8). NE differentiation was defined as immunoreactivity with at least one classical NE marker (CGA, SYP or CD56). However, only tumors raising the possibility of NE differentiation were stained for these markers during the routine work-up.

To evaluate the samples, tissue microarrays (TMAs) were used. The TMA blocks were constructed manually as previously published (12–14). Briefly, cores of 2.2 mm in diameter were sampled from both the periphery and the centre of the lesions; each lesion being represented in either two or three cores.

Three to four-micrometer-thick sections were used for IHC reactions with STX1, CGA, SYP, CD56 and INSM1 antibodies, in all lesions. Primary antibodies and the applied protocols are listed in **Table 1** and have been reported in detail previously (10).

Altogether, 113 cases (79 from the archives of the Bács-Kiskun County Teaching Hospital, the remaining 34 from the University of Szeged) diagnosed between 2001 and 2019 were collected. Fifty-nine tumors from 55 patients (4 of them with bifocal lesions) demonstrated traditional NE marker positivity and the remaining 54 were negative for these markers and formed a negative control group in our study. All lesions with NE marker positivity were diagnosed either as hypercellular (Type B) mucinous carcinoma, solid papillary carcinoma, invasive breast carcinoma of no special type with NE features or ductal carcinoma *in situ*, NE subtype. No tumor in this series fulfilled the criteria of NET or NEC. The included cases are briefly summarized in **Table 2**.

For CGA and SYP, any (at least 1%) cytoplasmic labelling of the tumor cells; for INSM1, any (at least 1%) nuclear positivity; finally, for STX1 and CD56, any (at least 1%) cytoplasmic and/or membranous staining were considered positive. The percentage of the labelled tumor cells, as well as the semiquantitative (0 to 3+, respectively) intensity of the staining was evaluated separately by

TABLE 1 | Primary antibodies and IHC protocols.

Antibody	Clone	Manufacturer	Retrieval	Dilution
STX1 (HPC-1)	sc-12736 (Mouse monoclonal)	Santa Cruz	pH 10.0	1:200
INSM1	A8 (Mouse monoclonal)	Santa Cruz	pH 9.0	1:100
SYP	27G12 (Mouse monoclonal)	Novocastra	pH 9.0	1:400
CGA	LK2H10 (Mouse monoclonal)	Cellmarque	pH 9.0	1:700
CD56	123C3.D5 (Mouse monoclonal)	Cellmarque	pH 9.0	1:200

TABLE 2 | Tumor types of the included cases.

Institute	Diagnosis	No of cases
Bács-Kiskun County Teaching Hospital	Mucinous carcinoma, Type B	10
	Solid papillary carcinoma	12
	Invasive carcinoma NST with NE differentiation	11
	DCIS, NE subtype	1
University of Szeged	Mucinous carcinoma, Type B	12
	Solid papillary carcinoma	11
	Invasive carcinoma NST with NE differentiation	1
	DCIS, NE subtype	1
		59
	Non-NE cases for analysis of specificity	54
Altogether		113

NST, invasive carcinoma of no special type; DCIS, ductal in situ *carcinoma.*

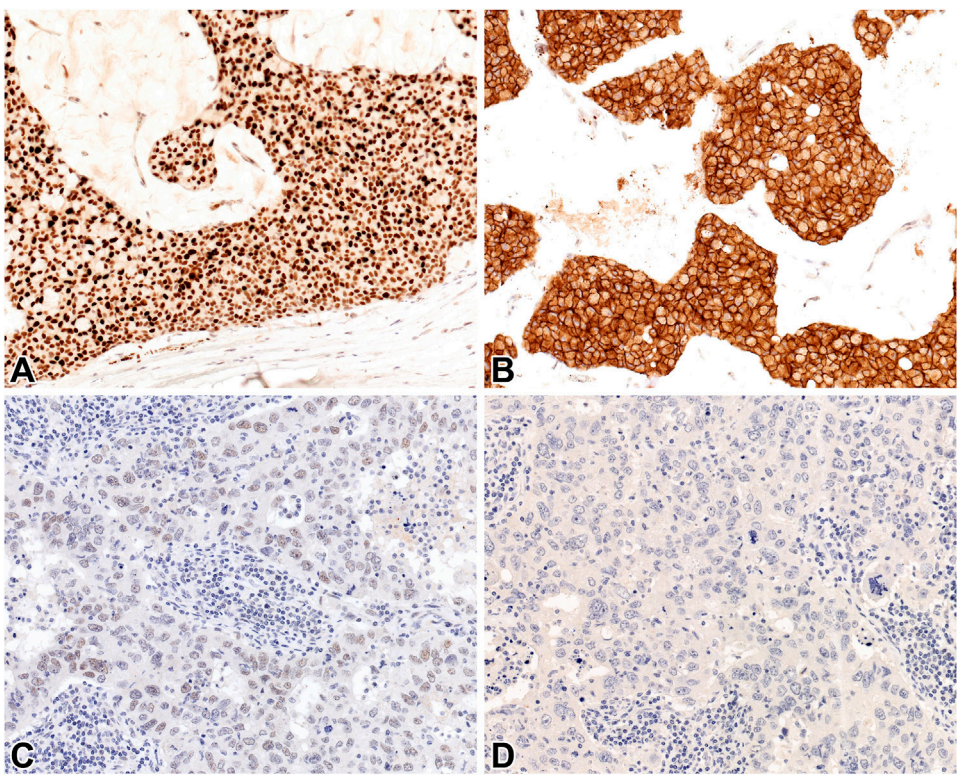

FIGURE 1 | INSM1 **(A, C)** and STX1 **(B, D)** immunoreactivity in a hypercellular (Type B) mucinous carcinoma **(A, B)** and invasive carcinoma NST without NE features **(C, D)** 20x.

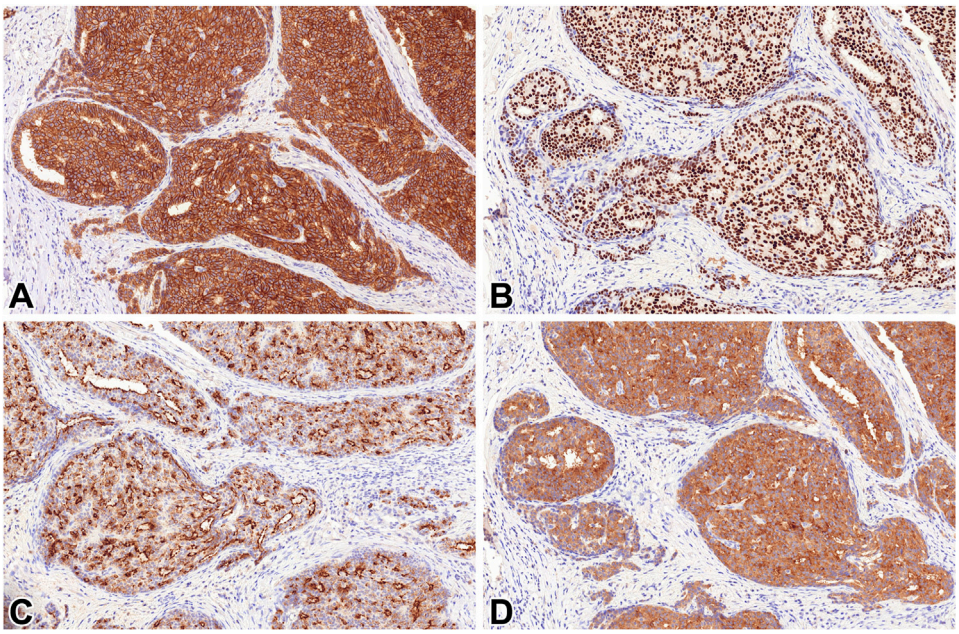

FIGURE 2 | STX1 **(A)**, INSM1 **(B)**, CGA **(C)** and SYP **(D)** immunoreactivity in a solid papillary carcinoma 20x.

3 pathologists. Subsequently, consensus at a multiheaded microscope was reached for discrepant cases. Based on a frequently detected focal and weak INSM1 expression in a pilot series, INSM1-stained slides were also evaluated using two additional practical definitions for positivity; 1) any nuclear staining of any intensity [referred to as high-power (HP) positivity], 2) nuclear staining obvious even at low-power view [referred to as low power (LP) positivity] (**Figure 1**).

To assess the specificity of the novel markers, STX1 and INSM1 IHC reactions were performed on samples derived from other breast carcinomas proven to be negative for CGA, SYP and CD56 (**Table 2**). For this purpose, TMA technique was applied as well.

No patient-related information was collected; materials were collected anonymously and retrospectively with no influence on outcome or treatment. The study was approved by the Clinical Research Coordination Office of the University of Szeged (4430/2018).

RESULTS

STX1 immunoreactivity was detected in 50/59 tumors. The labelling was diffuse in 37 (62.7%) of the 59 lesions. The median percentages of positive tumor cells were 85 and 55% for cytoplasmic or membranous staining patterns, respectively (**Figure 2**).

INSM1 expression was noted in 53/59 lesions on HP and 51/59 on LP, with a uniform nuclear pattern. Independently of the applied threshold, positivity was diffuse in 28/59 (47.5%) lesions, while the median percentage of labelled tumor cells was 50%.

Regarding the classical NE markers, the ratios of the positive cases and the median percentages of positive tumor cells were 58/59 and 80% for SYP, 44/59 and 50% for CGA and 13/58 and 0% for CD56, respectively. Diffuse positivity was present in 69.5% (41/59) for SYP, 47.5% (28/59) for CGA and 5.2% (3/58) for CD56.

The overall sensitivities of the novel markers were 89.8 and 86.4% for INSM1 on HP and LP, respectively, and 84.7% for STX1. Concerning the classical NE molecules, the sensitivities were 98.3% for SYP, 74.6% for CGA and 22.4% for CD56. The median intensity of staining was strong (3+) for each observed marker, with the exception of CD56 (2+). The data and descriptive values are summarized in **Tables 3**, **4**.

Regarding the specificity of the novel markers, only a single STX1 positive case was detected in the negative control group (1/54), resulting in a specificity of 98.1%. As for INSM1, some cases exhibited very faint and generally focal staining which was obviously present at HP (×40 objective) magnification, but was not seen or much less obvious on LP (×4 objective) examination (**Figure 1**). Applying the HP threshold, 23/54 cases were found to be positive while the specificity was 57.4%; however, using LP, the ratio of positive cases was only 6/54, increasing the specificity of INSM1 significantly, to 88.9%. Specificity of the novel markers is outlined in **Table 5**.

DISCUSSION

The classification of breast lesions with NE features or differentiation had undergone several changes and refinements since its introduction but has still not reached an easily and

TABLE 3 | Characteristics and sensitivity of STX1, INSM1, SYP, CGA and CD56 IHC in lesions with NE features.

	STX1	INSM1		SYP	CGA	CD56
		HPF	LPF			
Positive/observed cases	50/59	53/59	51/59	58/59	44/59	13/58
Median % of labelled cells	85% c 55% m	50%	50%	80%	50%	0%
Median % of labelled cells in positive cases	90% c 75% m	55%	55%	82.5%	72.5%	25%
Diffusely positive cases/observed cases (%)	28/59 (47.5%)	37/59 (62.7%)	37/59 (62.7%)	41/59 (69.5%)	28/59 (47.5%)	3/58 (5.2%)
Sensitivity	84.7%	89.8%	86.4%	98.3%	74.6%	22.4%
(95% CI)	(0.725–924)	(0.785–0.958)	(0.745–0.936)	(0.897–0.999)	(0.613–0.846)	(0.129–0.356)

c, cytoplasmic; m, membranous; HPF, high power field; LPF, low power field.

TABLE 4 | Ranges of cases according to the percentage of labelled cells.

		% of labelled cells			
		0–25	26–50	51–75	76–100
STX1	C	17	6	3	33
	M	22	6	7	22
INSM1	LPF	20	11	7	21
	HPF	20	11	7	21
SYP	-	17	1	6	35
CGA	-	24	7	6	22
CD56	-	52	3	1	2

c, cytoplasmic; m, membranous; HPF, high power field; LPF, low power field.

TABLE 5 | Specificity of STX1 and INSM1.

	STX1	INSM1	
		HPF	LPF
Negative/observed cases	53/54	31/54	48/54
Specificity	98.1%	57.4%	88.9%
(95% CI)	(0.888–0.999)	(0.433–0.705)	(0.767–0.954)

HPF, high power field; LPF, low power field.

consistently usable state. Due to the variable and sometimes obscure definitions and classifications as well as the lack of routine IHC examination of NE marker expression, the reported incidence (ranging between 0.1 and 20%) of breast tumors showing NE features is likely unreliable (15). These factors may contribute to the fact that the prognostic significance of NE differentiation in breast tumors is still somewhat uncertain.

In spite of the continuously changing definitions and thresholds, immunoreactivity with NE markers seems to be a constant requirement, and as such, a critical step to make the diagnosis. IHC for the demonstration of several markers has long been applied for this purpose. However, no single marker is known to be sensitive and specific enough to be used on its own. To overcome this challenge, numerous efforts are made to identify other suitable candidates. Conceptually, these novel biomolecules may either serve as components of the neurosecretory apparatus, or act as master regulators of NE differentiation. The latter category is represented by INSM1, a transcription factor which is of particular interest and has been a subject of recent studies in various organs (16–19). An example for the former one is STX1, which has also proved to be a sensitive and specific NE marker (10).

The aim of this study was to assess the applicability of STX1 and INSM1 as NE markers of breast lesions, as well as to compare their performance with the traditional molecules used to assess NE differentiation (i.e., SYP, CGA and CD56). Similarly to results from other organs, STX1 proved to be a reliable marker for the diagnosis of NE breast lesions, with a sensitivity of 84.7%, characterized by a convincing, diffuse immunoreactivity in 62.7% of the cases included. A strong and easy-to-read membranous labelling pattern was also noted beside cytoplasmic staining in the majority of the lesions. Our experience was that the nuclear staining pattern of INSM1 (similarly to the membranous STX1-labelling) was more convenient to interpret than the cytoplasmic expression pattern of other markers. The different subcellular locations of INSM1 and STX1 labelling enable the use of double immunohistochemical staining method in biopsy cases with limited neoplastic tissue. Apart from exhibiting great sensitivity, STX1 was also characterized by an excellent specificity (98.1%), with clear-cut negativity in all but one sample in the control group.

In the case of INSM1, sensitivity was excellent without significant difference between LP and HP definition for positivity (89.8 and 86.4%, respectively); but more than half of the evaluated lesions showed only focal positivity. However, the negativity of the control cases was rather equivocal. If the more permissive LP definition was applied, the specificity of INSM1 was found to be only 57.4%; however, when the HP definition was used, it increased to 88.9%. This observation supports the findings of a recent study of more than one thousand breast carcinomas, in which "a slightly higher cut-off for a positive result" was determined for INSM1 in order to reach a specificity of 98.1% (17). The fact that 17 tumors without NE features in our series would have been misclassified depending on the threshold, raises some concerns regarding the specificity of INSM1. However, given the excellent sensitivity, INSM1 is strongly recommended to be used in combination with other, more specific markers.

As concerns the traditional NE markers, the greatest sensitivity was achieved with SYP (98.3%), nevertheless, STX1 mildly outperformed it in the median percentage of labelled cells (STX1: 85% vs. SYP: 80%). The remaining two classical NE molecules, CGA and especially CD56 exhibited unexpectedly low sensitivities (74.6% for CGA and 22.4% for CD56). Our experience with the latter marker is comparable to the findings of

a recent publication (16), therefore CD56 should probably be decommissioned from the general NE marker arsenal, at least in the setting of breast tumors.

There were obvious limitations and unexplained aspects in the present study. A fraction of the investigated tumors showing INSM1 expression only using the HP definition exhibited immunoreactivity against INSM1 in the absence of every other markers. This phenomenon, which was also observed by other authors, raises the concerns regarding the specificity of INSM1 even further. In a recent study by Zombori et al, focal INSM1 IHC expression was also detected in non-NE pulmonary carcinomas (19). The isolated positivity for INSM1 without detectable expression of other components of the neurosecretory apparatus may be explained by an interrupted cascade of yet-to-be-found intermediate mediators, which transfer the signal of NE differentiation from the transcription factor. This would make INSM1 expression a necessary, but, on its own insufficient condition for this lineage of development (20).

Another possible explanation is the immanent focality of NE differentiation in the majority of breast tumors. Apart from intra-tumoral heterogeneity, these neoplasms are diverse per diagnostic categories, too. It is known that only around 50% of solid papillary carcinomas are positive for NE markers (20), which may be a plausible explanation for the anomaly. Given these facts, despite multiple sampling, the TMA method may have led to false negative results. Furthermore, the retrospective nature of the study and the low number of included cases may have biased our findings. However, NE markers are also needed in the routine reporting of core biopsies that are likewise subject to intra-tumoral heterogeneity; thus, data obtained using the TMA technique may be used to extrapolate how these markers would perform in the core biopsy setting. Altogether, we believed that the few dozens of cases investigated were sufficient to validate the concept of STX1 and to a lesser extent of INSM1 as suitable NE markers of breast tumors, even if we were unable to formulate statements concerning the exceptionally rare primary mammary NETs or NECs.

In conclusion, consistently with data from other organs, we propose that STX1 is a promising novel, highly sensitive and specific, easily applicable NE marker. Along with INSM1, another recently identified and already better studied (16, 18, 20) molecule, we strongly recommend STX1 to be included in the routine diagnostic IHC panel of NE differentiation. Following further studies, STX1 and INSM1 may become ancillary markers of SYP and be able to replace the less sensitive CGA and CD56 in the area of breast neoplasia with NE features.

DATA AVAILABILITY STATEMENT

The raw data supporting the conclusions of this article will be made available by the authors, without undue reservation.

ETHICS STATEMENT

The studies involving human participants were reviewed and approved by Clinical Research Coordination Office, University of Szeged. Written informed consent for participation was not required for this study in accordance with the national legislation and the institutional requirements.

AUTHOR CONTRIBUTIONS

Conceptualization: BK, GC, and LK; case selection: BK, ST-N, and GC; interpretation of stainings: BK, ST-N, and GC; data curation: BK, ST-N, ÁB, and JB; formal analysis: BK, ST-N, and GC; funding acquisition: BK; investigation: BK, ST-N, and GC; methodology: BK and GC; project administration: BK and GC; supervision: BK and GC. Drafting the manuscript: ST-N. All authors have read and accepted the submitted version of the manuscript. GC and BK equally contributed to this work and its supervision.

FUNDING

This research was funded by the University of Szeged, Faculty of medicine Research Fund-Heténi Géza grant, grant number 5S582.

CONFLICT OF INTEREST

The authors declare that the research was conducted in the absence of any commercial or financial relationships that could be construed as a potential conflict of interest.

ACKNOWLEDGMENTS

The authors thank photographer Mihály Dezső for his assistance with the figures.

REFERENCES

1. Feyrter F, and Hartmann G. On the Carcinoid Growth Form of the Carcinoma Mammae, Especially the Carcinoma Solidum (Gelatinosum) Mammae. *Frankf Z Pathol* (1963) 73:24–39.
2. Visscher DW, and Yasir S. Neuroendocrine Tumors of the Breast. *Endocr Pathol* (2017) 28(2):121–7. doi:10.1007/s12022-017-9477-4
3. Osamura RY, Matsui N, Okubo M, Chen L, and Field AS. Histopathology and Cytopathology of Neuroendocrine Tumors and Carcinomas of the Breast: A Review. *Acta Cytol* (2019) 63(4):340–6. doi:10.1159/000500705
4. Hejjane L, Oualla K, Bouchbika Z, Bourhafour M, Lhlou Mimi A, Boubacar E, et al. Primary Neuroendocrine Tumors of the Breast: Two Case Reports and Review of the Literature. *J Med Case Rep* (2020) 14(1):41. doi:10.1186/s13256-020-02361-5
5. Özdirik B, Kayser A, Ullrich A, Savic LJ, Reiss M, Tacke F, et al. Primary Neuroendocrine Neoplasms of the Breast: Case Series and Literature Review. *Cancers* (2020) 12(3):733. doi:10.3390/cancers12030733
6. FA Tavassoli and P Devilee, editors. World Health Organization Classification of Tumours. *Pathology and Genetics of Tumours of the Breast and Female Genital Organs*. 3rd ed. Lyon: IARC Press (2003).

7. SR Lakhani, IO Ellis, SJ Schnitt, PH Tan, and MJ van de Vijver, editors. *WHO Classification of Tumours of the Breast*. 4th ed. Lyon: IARC Press (2012).
8. WHO Classification of Tumours Editorial Board. WHO Classification of Tumours. In: *Breast Tumours*. 5th ed. Lyon: IARC Press (2019).
9. Rindi G, Klimstra DS, Abedi-Ardekani B, Asa SL, Bosman FT, Brambilla E, et al. A Common Classification Framework for Neuroendocrine Neoplasms: an International Agency for Research on Cancer (IARC) and World Health Organization (WHO) Expert Consensus Proposal. *Mod Pathol* (2018) 31(12): 1770–86. doi:10.1038/s41379-018-0110-y
10. Kővári B, Turkevi-Nagy S, Báthori Á, Fekete Z, and Krenács L. Syntaxin 1: A Novel Robust Immunophenotypic Marker of Neuroendocrine Tumors. *Int J Mol Sci* (2020) 21(4):1213. doi:10.3390/ijms21041213
11. Rosenbaum JN, Guo Z, Baus RM, Werner H, Rehrauer WM, and Lloyd RV. INSM1: A Novel Immunohistochemical and Molecular Marker for Neuroendocrine and Neuroepithelial Neoplasms. *Am J Clin Pathol* (2015) 144(4):579–91. doi:10.1309/AJCPGZWXXBSNL4VD
12. Kovári B, Szász AM, Kulka J, Marušic Z, Šarcevic B, Tiszlavicz Ls., et al. Evaluation of P40 as a Myoepithelial Marker in Different Breast Lesions. *Pathobiology* (2015) 82(3-4):166–71. doi:10.1159/000375127
13. Zombori T, and Cserni G. Immunohistochemical Analysis of the Expression of Breast Markers in Basal-like Breast Carcinomas Defined as Triple Negative Cancers Expressing Keratin 5. *Pathol Oncol Res* (2018) 24(2):259–67. doi:10.1007/s12253-017-0246-y
14. Kővári B, Vranic S, Marchio C, Sapino A, and Cserni G. The Expression of GHRH and its Receptors in Breast Carcinomas with Apocrine Differentiation-Further Evidence of the Presence of a GHRH Pathway in These Tumors. *Hum Pathol* (2017) 64:164–70. doi:10.1016/j.humpath.2017.03.026
15. Cserni G. Histological Type and Typing of Breast Carcinomas and the WHO Classification Changes over Time. *Pathologica* (2020) 112(1):25–41. doi:10.32074/1591-951X-1-20
16. Kawasaki T, and Kaira K. Insulinoma-associated Protein 1 (INSM1) Expression in Breast Carcinomas with Neuroendocrine Morphologies: Application and Future Prospective. *Virchows Arch* (2020) 479:191–4. doi:10.1007/s00428-020-02935-0
17. Razvi H, Tsang JY, Poon IK, Chan S-K, Cheung S-Y, Shea K-H, et al. INSM1 Is a Novel Prognostic Neuroendocrine Marker for Luminal B Breast Cancer. *Pathology* (2021) 53(2):170–8. doi:10.1016/j.pathol.2020.07.004
18. Seijnhaeve E, Galant C, and Van Bockstal MR. Nuclear Insulinoma-Associated Protein 1 Expression as a Marker of Neuroendocrine Differentiation in Neoplasms of the Breast. *Int J Surg Pathol* (2021) 29:496. doi:10.1177/1066896920985938
19. Zombori T, Turkevi-Nagy S, Sejben A, Juhász-Nagy G, Cserni G, Furák J, et al. The Panel of Syntaxin 1 and Insulinoma-associated Protein 1 Outperforms Classic Neuroendocrine Markers in Pulmonary Neuroendocrine Neoplasms. *Apmis* (2021) 129:186–94. doi:10.1111/apm.13113
20. Kudo N, Takano J, Kudoh S, Arima N, and Ito T. INSM1 Immunostaining in Solid Papillary Carcinoma of the Breast. *Pathol Int* (2021) 71(1):51–9. doi:10.1111/pin.13043

Pathology & Oncology Research

frontiers

BRIEF RESEARCH REPORT
published: 20 December 2021
doi: 10.3389/pore.2021.1609951

Lactate Upregulates the Expression of DNA Repair Genes, Causing Intrinsic Resistance of Cancer Cells to Cisplatin

Marzia Govoni†, Valentina Rossi†, Giuseppina Di Stefano and Marcella Manerba*

Department of Experimental, Diagnostic and Specialty Medicine (DIMES), University of Bologna, Bologna, Italy

Intrinsic or acquired drug resistance is one of the major problems compromising the success of antineoplastic treatments. Several evidences correlated some therapeutic failures with changes in cell metabolic asset and in line with these findings, hindering the glycolytic metabolism of cancer cells via lactate dehydrogenase (LDH) inhibition was found to overcome the resistance to chemotherapeutic agents. Lactate, the product of LDH reaction, was shown to be involved in epigenetic regulation of gene expression. The experiments described in this paper were aimed at highlighting a possible direct effect of lactate in modifying the response of cancer cells to a chemotherapeutic treatment. To discriminate between the effects potentially caused by glycolytic metabolism from those directly referable to lactate, we selected cancer cell lines able to grow in glucose deprived conditions and evaluated the impact of lactate on the cellular response to cisplatin-induced DNA damage. In lactate-exposed cells we observed a reduced efficacy of cisplatin, which was associated with reduced signatures of DNA damage, enhanced DNA recombination competence and increased expression of a panel of genes involved in DNA repair. The identified genes take part in mismatch and nucleotide excision repair pathways, which were found to contribute in restoring the cisplatin-induced DNA damage. The obtained results suggest that this metabolite could play a role in reducing the efficacy of antineoplastic treatments.

Keywords: DNA repair, cisplatin, glycolysis, lactate, DNA damage

OPEN ACCESS

Edited by:
József Tímár,
Semmelweis University, Hungary

****Correspondence:***
Giuseppina Di Stefano
giuseppina.distefano@unibo.it
orcid.org/0000-0003-0375-0176

†These authors have contributed equally to this work and share first authorship

Received: *14 July 2021*
Accepted: *30 November 2021*
Published: *20 December 2021*

Citation:
Govoni M, Rossi V, Di Stefano G and Manerba M (2021) Lactate Upregulates the Expression of DNA Repair Genes, Causing Intrinsic Resistance of Cancer Cells to Cisplatin. Pathol. Oncol. Res. 27:1609951. doi: 10.3389/pore.2021.1609951

INTRODUCTION

The activated glucose metabolism of cancer cells is functional in coping with their increased energy demand and need of metabolic intermediates, required to build-up new macromolecules [1,2].

Although the discovery of this metabolic feature dates back to almost one century ago [3], it is only in recent years that evidences showing a direct correlation between enhanced glycolysis and changes in gene expression have been obtained. Indeed, the metabolic reprogramming of cancer cells was found to impact on distinct morphological features of cancer cell nucleus [4]. Metabolites originating during the glycolytic cascade have been shown to increase histone acetylation and promote an open chromatin structure [4,5], which facilitates the transcriptional and replication machineries triggered by oncogenes activation.

Interestingly, elevation of glycolysis seems to confer cancer cells resistance to ionizing radiation [6], while its inhibition results in compromised DNA repair [7].

Predictably, facilitated DNA repair could also impact on the response of cancer cells to chemotherapeutic agents, as suggested by several evidences correlating therapeutic failures with changes in cell metabolic asset [8].

Lactate dehydrogenase (LDH) activity is a nodal point for the maintenance of the glycolytic flux of cancer cells [9]. By reducing pyruvate to lactate, LDH rapidly restores NAD+, which is needed for the first steps of glucose metabolism. This enzyme is considered an interesting therapeutic target for developing new antineoplastic treatments and accumulating evidences show that its inhibition or reduced expression can be successful in increasing the efficacy of chemotherapeutic agents [10–13]. A possible explanation to these results resides in the block of energy metabolism potentially caused by LDH inhibition, which hinders the highly ATP consuming reactions involved in DNA repair. A further mechanism could be linked to the non-metabolic functions of this enzyme; in fact, the A isoform of LDH (LDH-A) was found to be located also in cell nucleus, where it takes part in transcription complexes regulating gene expression [14]. Finally, lactate (the product of LDH reaction) is one of the metabolic intermediates shown to be involved in the epigenetic modulation of gene expression [15,16] and for this reason it was proposed as an "oncometabolite" and a key mediator in the metabolic cross-talk between cancer cells and their microenvironment [17–19]. Similar to other metabolites, lactate can hinder HDAC function; furthermore, a possible histone modification through the "lactylation" of lysine residues has been documented [20]. This change was found to serve as an epigenetic modification that directly stimulates gene transcription from chromatin. Furthermore, it was shown to compromise doxorubicin antineoplastic effect [21–22].

With the experiments described in this paper, we explored a possible direct role of lactate in reducing the response of cancer cells to a chemotherapeutic treatment. To this aim, we also verified the effect of this metabolite on the expression of a panel of genes involved in DNA repair, predicting a functional interaction network between the proteins encoded by the upregulated genes. We used cultured human cancer cells maintained in conditions allowing to highlight a possible direct effect of lactate, ruling out interferences from other glycolytic intermediates.

MATERIALS AND METHODS

Cell Cultures and Treatments

SW620 and HepG2 cells (ECACC, #87051203 and #85011430) were cultured in L-15 medium supplemented with 100 U/ml penicillin/streptomycin, 4 mM glutamine and 10% dialyzed FBS. This medium does not contain glucose. For some experiments, cells were also maintained in low-glucose DMEM, with standard supplementations. All the materials used for cell culture and all the reagents were obtained from Sigma-Aldrich, unless otherwise specified. Lactate (L-isomer) was always used at a 10 mM concentration and was administered in L-15 medium 48–72 h before experiments. Both cell cultures were found to express the MCT1 carrier for lactate uptake [23,24]. No significant reduction of lactate concentration in culture medium was observed up to 72 h (**Supplementary Figure S1**).

Cultures were routinely tested for Mycoplasma contamination and found to be free.

Cell Viability Experiments

The effect of cisplatin (CPL, 0–50 μM) on cell viability was assessed at 24 h, in cultures maintained in L-15 medium with or without 10 mM lactate. Results were evaluated with the neutral red assay (NR), which allows a precise estimate of cell number [25]. Before each experiment, a plot reporting the NR absorbance values of scalar amounts of cells was obtained. These data were fitted by using the linear regression analysis; the resulting mathematical equation was used to calculate the number of cells at the end of experiments. SW620 and HepG2 cells (1.0×10^4/well) were seeded in 96-multiwell plates. After 24 h treatment with CPL, they were maintained 3 h at 37°C with the NR dye, dissolved in medium at the final concentration of 30 μg/ml. Medium was then removed and the cells were solubilized with 200 μl of 1% acetic acid in 50% ethanol. Absorbance of the solutions was measured at λ540.

Evaluation of Abasic DNA Sites

The amount of abasic (AB) sites on DNA after CPL treatment was evaluated using a commercially available assay from Cell Biolabs. This assay is based on the use of a probe (ARP) which specifically reacts with the aldehyde group on the open ring form of AB sites [26].

SW620 cells maintained in L-15 with or without 10 mM lactate were exposed for 90 min to CPL (0–50 μM). Genomic DNA was isolated using the phenol/chloroform/isoamyl alcohol extraction procedure [27]. The recovered, water-soluble material was then treated with 2 μg RNase (Thermo-Fisher Scientific) for 75 min at room temperature, after which the enzyme was removed by an additional step of phenol extraction. Finally, DNA was purified by ethanol precipitation. It was dissolved in a 10 mM Tris buffer, pH 7.5, containing 1 mM EDTA at a concentration of 100 μg/ml. Reaction with ARP was performed following the instructions of the assay's manufacturer and the quantification of AB sites in the experimental samples was obtained by generating a standard curve using an ARP-DNA reference sample included in the assay. Experiment was repeated twice, with duplicate samples.

Immunoblotting Experiments

These experiments were performed in SW620 and HepG2 cells cultured in L-15 with or without 10 mM lactate; immunoblotting was used to assess the level of H3 acetylation, H2AX phosphorylation (γ-H2AX, a marker of DNA damage [28]), TP73 and GSTP1. To assess DNA damage, cells were exposed to 12.5 μM CPL for 1 h; medium was then removed and cultures were maintained for additional 16, 24 and 40 h γ-H2AX level was evaluated at the end of each time interval.

For immunoblotting, cells (9×10^5 in T25 flasks) were harvested and lysed in 60 μl RIPA buffer containing protease and phosphatase inhibitors. Proteins (30–50 μg) were loaded onto 4–12% precast polyacrylamide gel for electrophoresis and run at 170 V. Gels were blotted on a low fluorescent PVDF

membrane (GE Healthcare) using a standard apparatus for wet transfer. The blotted membrane was blocked with 5% BSA in TBS-TWEEN and probed with the primary antibodies: rabbit anti-H3 (Cell Signaling); rabbit anti-Panacetyl-H3 (Active Motif), rabbit anti-γ-H2AX (phospho-S139) (Abcam); rabbit anti-TP73 and anti-GSTP1 (Thermo-Fisher Scientific); rabbit anti-β-actin, (Sigma-Aldrich). Binding was revealed by a Cy5-labelled secondary antibody (goat anti rabbit-IgG, GE Healthcare). Fluorescence of the blots was assayed with the Pharos FX Scanner (Bio-Rad) at a resolution of 100 μm.

Study of Episomal Plasmid Recombination

The rate of episomal plasmid recombination in SW620 and HepG2 cells maintained in L-15 with or without 10 mM lactate was assessed by using a commercially available kit (Norgen Biotek). This assay is based on cell transfection with two plasmids that recombinate upon entry. Recombination efficiency can be assessed by real-time PCR, using the primer mixtures included in the assay kit, which allow to discriminate between the original plasmid backbones and their recombination product.

Cells were seeded in a 24-well plate (2×10^5 cells/well, in duplicate) and allowed to adhere overnight. Co-transfection with the two plasmids was performed in Lipofectamine 2000 (Thermo-Fisher Scientific) for 5 h at 37°C. At the end of incubation, cells were washed with PBS and harvested; DNA was isolated using the QIAamp DNA mini kit (Qiagen). 25 ng of purified DNA was used for the real-time PCR, which was performed according to the protocol indicated by the manufacturer. Data analysis was based on the ΔΔCt method and compared the level of recombination assessed in lactate-exposed cells to that measured in control cultures.

Real-Time PCR Array of DNA Repair Genes

This experiment was performed on SW620 and HepG2 cultures, maintained in L-15 with or without 10 mM lactate (72 h). For comparison, a similar experiment was also performed on cultures grown in DMEM (a medium allowing glycolytic metabolism), exposed for 16 h to 40–80 mM oxamate (OXA), a LDH inhibitor hindering glucose metabolism [29].

RNA was extracted from exponentially growing cells seeded in T75 flasks, using the method described in [30]. RNA quantity and quality were assessed spectrophotometrically; for each sample, 2 μg RNA was retro-transcribed with the iScript gDNA Clear cDNA Synthesis kit (Bio-Rad). The expression of DNA damage and repair genes was analyzed using the DNA Damage Tier 1 H96 PrimePCR™ Assay (Bio-Rad). Real-time PCR was conducted as indicated by the manufacturer, in a CFX96 real-time cycler (Bio-Rad). The validation data for this array are available online at: https://www.bio-rad.com/en-uk/prime-pcr-assays/predesigned-plate/sybr-green-dna-damage-tier-1-h96.

The same experimental conditions were followed also for the additional PCR assays reported in **Figure 4D**. The primers' sequences used for assessing the expression of the genes reported in **Figure 4D**, as well as those used for the internal control genes, are reported in the Supplementary Material (**Supplementary Table S1**).

Statistical Analyses

All data were analyzed by using the GraphPad Prism software. Results were obtained from at least two independent experiments. They are expressed as mean ± SE of replicate values; the significance level was set at $p < 0.05$.

RESULTS

Lactate-Exposed SW620 Cells Showed Reduced Response to Cisplatin

CPL was selected as a representative chemotherapeutic agent for the experiments since the pattern of DNA damage produced by this drug has been extensively studied. CPL appeared to potentially trigger all the principal DNA repair pathways: nucleotide excision repair, mismatch repair, homologous recombination and non-homologous end joining [31].

Reduced response to chemotherapeutic agents has been often correlated with increased glycolytic metabolism [8]. In order to evidence a direct contribute of lactate in this phenomenon, we searched human cancer cell lines able to grow in glucose deprived conditions (L-15 medium). According to the ATCC and ECACC indications, L-15 is the optimal medium for culturing the SW620 colon adenocarcinoma cells and, for this reason, they were used in all the reported experiments.

SW620 cells were maintained in L-15 and probed with 0–50 μM CPL for 24 h, with or without a supplementation of 10 mM lactate. This dose of lactate was chosen on the basis of previously published works, suggesting that in cancer cells and extracellular milieu the concentration of this metabolite easily reaches or even overcomes this level [16]. The obtained results are reported in **Figure 1A**. Data were analyzed by two-way ANOVA; according to Bonferroni's post-test, lactate in medium significantly reduced the antiproliferative effect of 50 μM CPL ($p < 0.05$).

The Reduced Response to Cisplatin Caused by Lactate was Associated With Decreased Signatures of DNA Damage and Upregulated DNA Recombination Competence

To explain the data of **Figure 1A**, we estimated the extent of DNA damage caused by CPL in SW620 cells grown in L-15, with or without 10 mM lactate. In the first experiment, DNA damage was evaluated by quantifying the presence of AB sites [26]. For this assay, cells were exposed for 90 min to 0–50 μM CPL. Results are shown in **Figure 1B**; they were statistically analyzed using two-way ANOVA. Lactate in medium was found to significantly decrease the number of AB sites, with $p = 0.0016$.

This experiment showed that initial evidences of DNA damage are obtained starting from 12.5 μM CPL; for this reason, this dose was also applied for assessing γ-H2AX levels [28] (**Figures 1C,D**). In the different samples, the γ-H2AX band intensity was normalized on β-actin; the results of the densitometric reading are reported in the bar graph (**Figure 1D**). Data were analyzed by two-way ANOVA; Bonferroni's post-test indicated a significantly

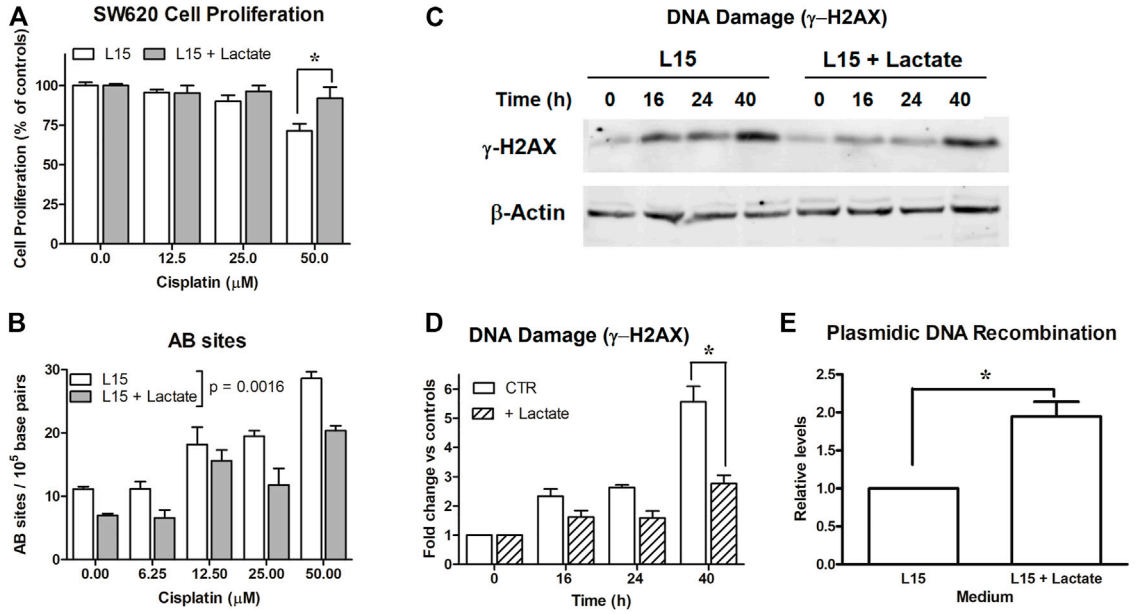

FIGURE 1 | Experiments on SW620 cells. **(A)**: Antiproliferative effects caused by cisplatin on SW620 cultures maintained in L-15. *, $p < 0.05$. **(B)**: Evaluation of AB sites in cultures exposed to scalar doses of cisplatin (0–50 μM) for 90 min, with or without 10 mM lactate. Lactate in medium was found to significantly reduce AB sites ($p = 0.001$). **(C)**: Evaluation of DNA damage (γ-H2AX) in cells maintained with or without 10 mM lactate and exposed to cisplatin (12.5 μM). The densitometric reading of band intensities is shown in **(D)**. *, $p < 0.001$, compared to control cultures. **(E)**: DNA recombination competence assessed in cultures exposed to lactate. *, $p < 0.05$, compared to control cultures.

reduced γ-H2AX level in lactate-exposed cells at the 40-h time interval ($p < 0.001$).

Taken together, these findings suggested enhanced competence in managing DNA damage in cells exposed to lactate. Interestingly, these cells also displayed improved DNA recombination, which was observed independently of CPL exposure.

SW620 cultures were transfected with a couple of plasmids reproducing the LacZ sequence as a result of their recombination. This sequence can be detected by real-time PCR. As shown in **Figure 1E**, lactate-exposed SW620 cells revealed an almost doubled capacity of generating the LacZ sequence, which suggests enhanced activity of enzymes involved in the DNA recombination process. The data of **Figure 1E** were obtained from three independent experiments and were analyzed by applying the paired t-test, which compared the increase measured in lactate-exposed SW620 cultures to the recombination level measured in their respective control cultures, set to 1; p value was 0.0389.

Real-Time PCR Array of DNA Repair Genes

To identify the DNA repair genes upregulated by lactate, we applied to SW620 cells a real-time PCR array specifically developed to study DNA damage and repair (Tier1 H-96 Prime PCR Array).

Experiment was repeated twice and the obtained results were processed with the aid of a dedicated software. The complete list of genes included in this array, together with the internal controls of the PCR reaction, is available at: https://www.bio-rad.com/en-uk/prime-pcr-assays/predesigned-plate/sybr-green-dna-damage-tier-1-h96. Moreover, a table reporting the extended names of the genes cited in the Results' section and in figures have been included in the Supplementary Material file (**Supplementary Table S2**).

In evaluating the obtained results, a lower threshold at 25%-increased expression was set, since comparable effects have been reported in previous studies examining the epigenetic effects of lactate in different experimental settings [22]. Among the 88 genes included in the array, 12 showed a >25% upregulation following lactate exposure; they are reported in the bar graph of **Figure 2A**. Results were analyzed using the column statistics' function of the GraphPad software by applying the one-sample t-test, which computes whether the mean of each data set is different from a given hypothetical value (0, i.e., no change, compared to untreated cultures). All the reported data were found to be statistically significant with the exception of the genes for Cyclin Dependent Kinase 1 (CDK1) and for H2AX variant Histone (H2AFX). The statistically significant changes showed p values ranging from 0.045 to 0.009.

To confirm the findings of **Figure 2A**, additional PCR array experiments were performed on SW620 cells grown in DMEM. Contrary to L-15, DMEM contains glucose and allows the proceeding of glycolytic flux up to lactate. For these PCR experiments we exposed glycolyzing SW620 cells to 40 mM OXA for 16 h. OXA is a pyruvate analog which specifically inhibits LDH [29]; in preliminary experiments, we found that a 40 mM dose of this inhibitor almost completely prevents lactate production in glycolyzing SW620 cells, without reducing their ATP level and viability (Supplementary Material, **Supplementary Figure S2**). **Figure 2B** shows that when glycolyzing SW620 cells were exposed to OXA, all the 12 genes identified in the previous PCR array (**Figure 2A**) reduced their expression below the levels

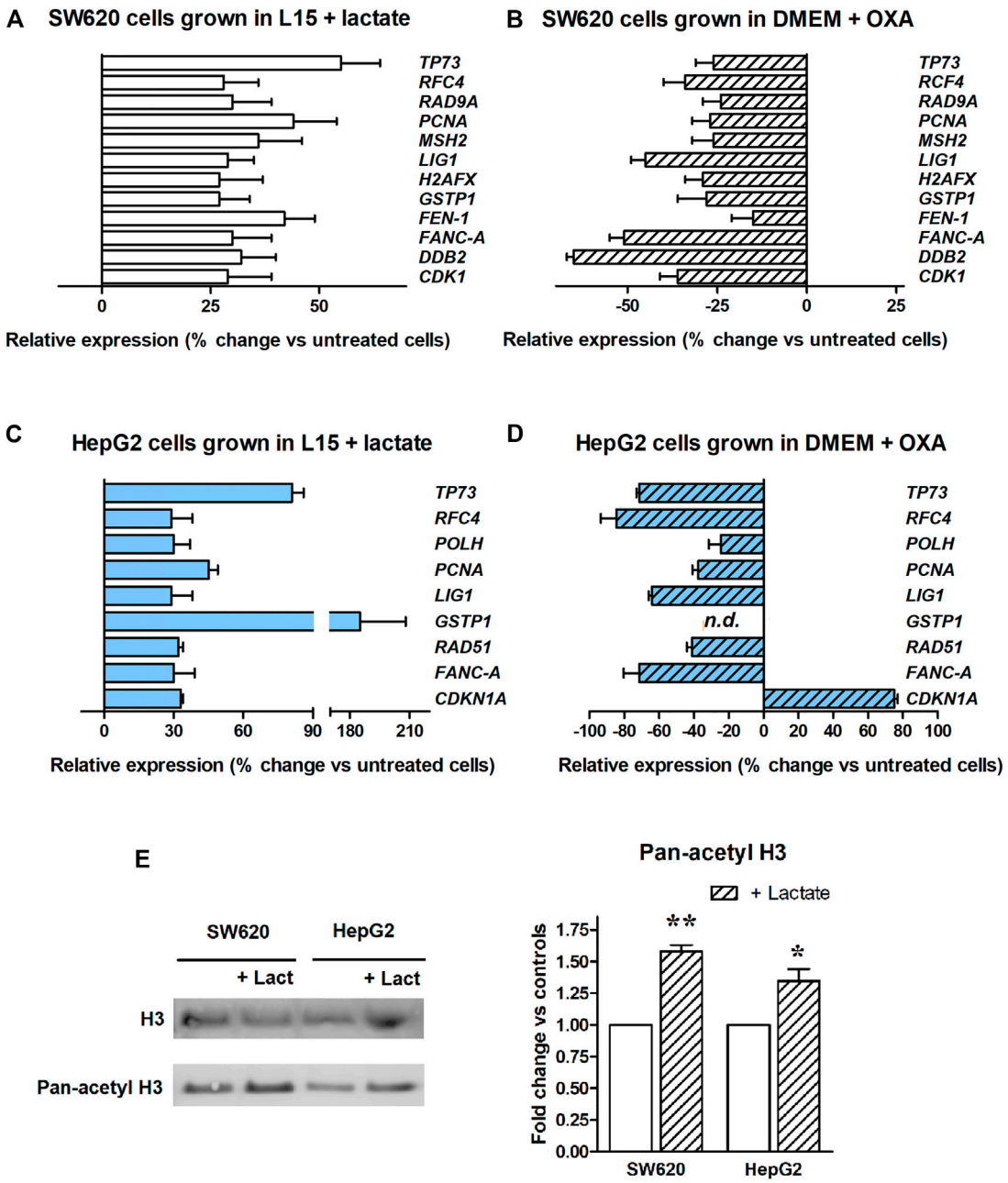

FIGURE 2 | Real-time PCR array of DNA repair genes. The bar graphs display genes showing a >25%-increased expression. **(A)**: Experiment performed in SW620 cells maintained in L-15 medium and exposed to lactate. All the reported data were found to be statistically significant, with the exception of H2AFX and CDK1. **(B)**: Experiment performed in glycolyzing SW620 cells exposed to OXA. Lactate depletion caused by OXA significantly reduced the expression of all the genes, with the exception of FEN1. **(C)**: Experiment performed in HepG2 cultures maintained in L-15 medium and exposed to lactate. All the reported data were found to be statistically significant. The used statistical analysis and the obtained *p* values are reported in the text. **(D)** Experiment performed in glycolyzing HepG2 cells exposed to OXA. Lactate depletion caused by OXA significantly reduced the expression of all the genes, with the exception of CDK1NA. n.d.: GSTP1 expression was not detected in OXA exposed cells. **(E)** Level of H3 acetylation assessed in lactate-exposed cultures. * and **, $p < 0.05$ and <0.01, compared to control cultures, respectively.

measured in untreated, glycolyzing cells. With the exception of Flap structure-specific Endonuclease 1 gene (*FEN1*), all the observed reductions were found to be statistically significant; *p* values ranged from 0.039 to <0.0001. Interestingly, in lactate-deprived cultures a statistically significant reduction was observed also for *CDK1* and *H2AFX*.

To extend our observations, we wondered whether the changes in gene expression caused by lactate could differ among cell types. For this reason, we searched a second culture able to grow in the same glucose-deprived condition as SW620 cells, but from a different tissue. The HepG2 hepatoma cell line was found to tolerate the glucose-deprived L-15 medium

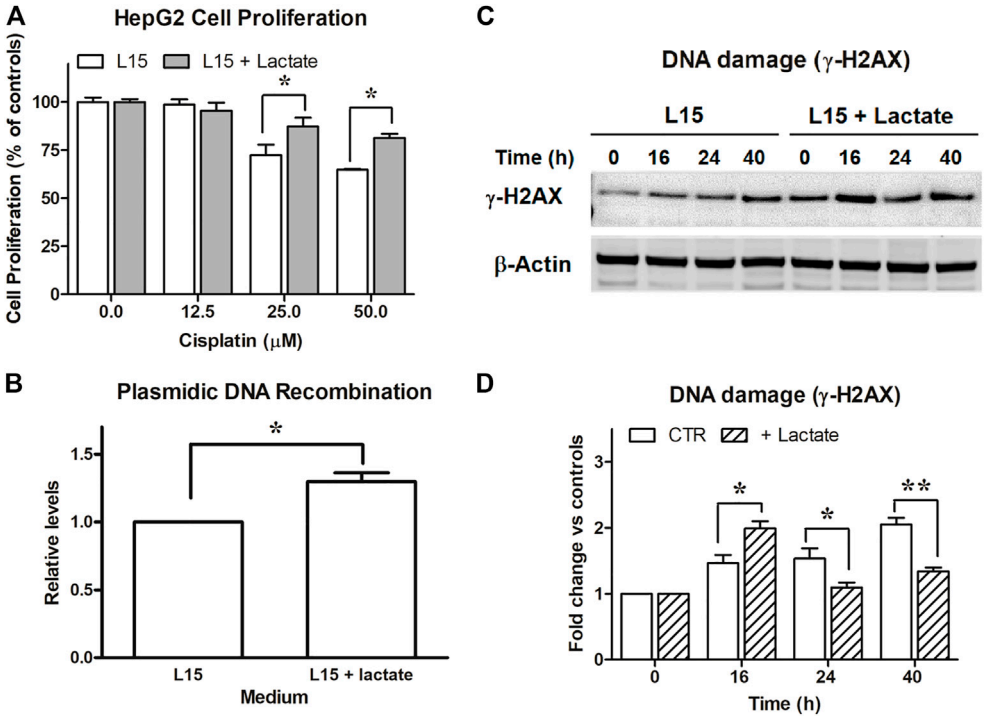

FIGURE 3 | Experiments on HepG2 cells. **(A)**: Antiproliferative effects caused by cisplatin on HepG2 maintained in L-15 and exposed to 10 mM lactate. *, $p < 0.05$, compared to control cultures. **(B)**: DNA recombination competence, assessed as described for SW620 cells. *, $p < 0.05$. **(C)**: Evaluation of DNA damage following CPL exposure in cells maintained with or without 10 mM lactate and assessed by immunoblotting evaluation of γ-H2AX. The densitometric reading of band intensities is shown in **(D)**. Lactate-exposed cells showed a constitutively higher γ-H2AX signal which, after CPL treatment, peaked at T = 16 h. At later time intervals, the γ-H2AX signal increase referred to T = 0 (fold change) was significantly lower in lactate-exposed cells, when compared to control cultures. *, $p < 0.05$; **, $p < 0.01$.

and was then used for additional PCR array experiments, aimed at evaluating the expression of DNA repair genes after lactate exposure. Results are shown in **Figure 2C**. In this case, we found a >25% upregulation in 9 genes and, interestingly, 6 of them were in common with SW620 cells. Results were analyzed as described for SW620 cells. In HepG2 cells, the observed upregulation reached the level of statistical significance for all genes; p values ranged from 0.048 to <0.0001. When these cells were maintained in DMEM and exposed to the OXA dose preventing lactate production (80 mM, **Supplementary Figure S2**), all the observed changes were reversed, except for *CDK1NA*, which was further increased. The p values ranged from 0.039 to <0.0001. The antiproliferative effect caused by OXA in DMEM-cultured HepG2 cells (see **Supplementary Figure S2**) could explain the finding concerning *CDK1NA* (a cell cycle regulator).

Figure 2E shows that lactate-exposed SW620 and HepG2 cells displayed a significantly increased level of H3 acetylation, suggesting inhibition of HDAC as the mechanism underlying the effects observed in **Figures 2A,C**.

Experiments on Lactate-Exposed HepG2 Cells

Following these results, we also investigated whether a different susceptibility to DNA damage could also be detected in lactate-exposed HepG2 cultures, as observed for SW620 cells. Unfortunately, these experiments were hindered by the compromised proliferation shown by these cells in L-15; the obtained results are reported in **Figure 3**. The data of **Figures 3A,B** were in line with those previously observed in SW620 cells. They were statistically analyzed as described for the corresponding experiments in **Figures 1A,E**. In the experiment of **Figure 3A**, lactate was found to significantly reduce the efficacy of 25 and 50 μM CPL ($p < 0.05$, according to Bonferroni's post-test). In the experiment of **Figure 3B**, the plasmidic DNA recombination detected in lactate-exposed cells was significantly increased ($p = 0.045$).

The study of γ-H2AX (**Figure 3C**) showed in HepG2 cells a DNA damage signaling pattern different from that observed in SW620 cultures (**Figures 1C,D**). A γ-H2AX level constantly increasing over time was observed in control cells. Lactate-exposed cultures showed a constitutively higher γ-H2AX signal, which after CPL treatment peaked at 16 h. However, when compared to T = 0, its further increase over time (fold change) was significantly lower than that measured in control cultures not exposed to lactate: at 40 h, a 2-fold increased signal was detected in control cultures, while a 1.3-fold increase was measured in lactate-exposed cells. Data of **Figure 3C** were statistically analyzed as described for the similar experiment performed on SW620 cells (**Figure 1C**). The increase of γ-H2AX signal (fold change) in lactate-exposed cultures was

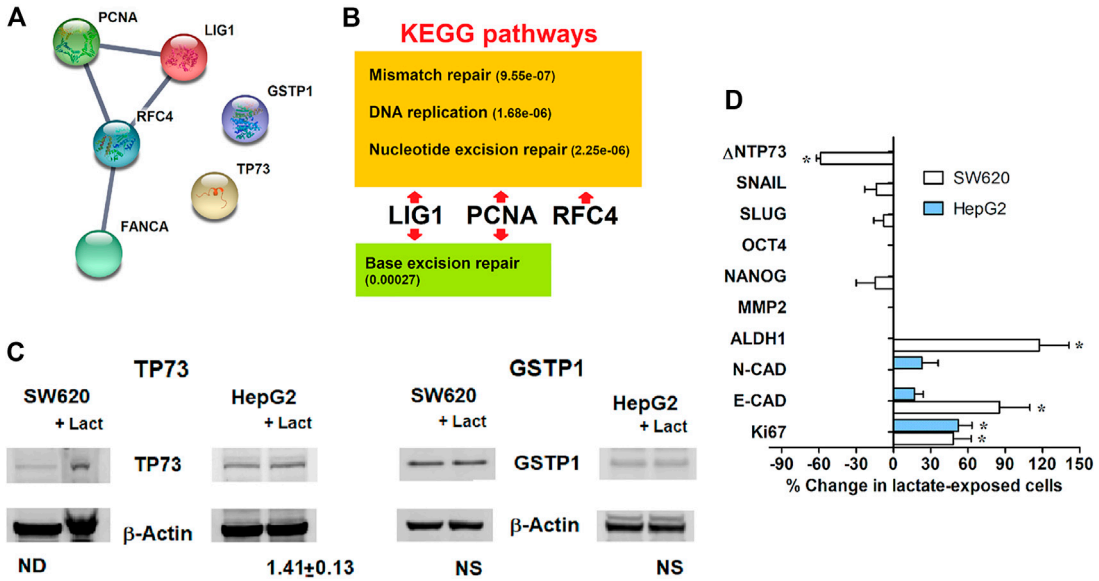

FIGURE 4 | (A): Functional interaction network among the genes identified using the real-time PCR array; downloaded from http://string-db.org. The edge thickness between protein nodes is indicative of a 0.9 confidence score. **(B)**: Biochemical pathways identified by the KEGG analysis. In parentheses, false discovery rates. **(C)**: Immunoblotting evaluation of the proteins not included in the identified DNA repair pathways. The level of TP73 was found to be increased in both lactate-exposed cultures. **(D)**: Expression of representative genes associated with proliferative potential and stem properties, assessed in lactate-exposed SW620 and HepG2 cells. Data were analyzed using the column statistics function of the Prism software, as described for the PCR array of DNA repair genes; *, statistically significant changes; *p* values ranged from 0.040 to 0.004. Missing bars in the graph denote undetectable mRNA.

significantly lower at 24 and 40 h ($p < 0.05$ and 0.01, respectively, according to Bonferroni's post-test).

Functional Interaction Network of Upregulated Genes

The PCR array experiments allowed us to identify a cluster of 6 genes which in both SW620 and HepG2 cells appeared to be potentially regulated through the level of this metabolite: Proliferating Cell Nuclear Antigen (*PCNA*), Tumor Protein p73 (*TP73*), Replication Factor C subunit 4 (*RFC4*), Fanconi Anemia complementation group A (*FANC-A*), DNA Ligase 1 (*LIG1*), Glutathione S-Transferase π1 (*GSTP-1*). To identify the functional connections between the corresponding proteins, we used the Search Tool for the Retrieval of Interacting Genes (STRING) database, a resource which can be reached at: http://string-db.org. The STRING database is able to construct interaction networks among genes, also providing a confidence score; moreover, by applying the Kyoto Encyclopedia of Genes and Genomes (KEGG) analysis, it identifies their related biochemical pathways and cellular functions.

Figures 4A,B show the obtained results. In building the interaction network, the edges representing gene-gene associations have been set on the highest confidence interaction score (0.9), to increase the strength of data support. This setting resulted in the identification of a functional network involving four of the analyzed genes, which gave an interaction enrichment *p* value = 7.35×10^{-05}. Accordingly, three of the four identified KEGG pathways showed very low false discovery rates, reported in the scheme of **Figure 4B**. All of them concern the interaction between *LIG1*, *PCNA* and *RFC4*. Interestingly, the identified pathways include mismatch and nucleotide excision DNA repair, which were found to be involved in cellular response to CPL damage [31]. These data can give a mechanistic explanation to the results obtained in lactate-exposed SW620 and HepG2 cells, treated with CPL; together with the data of **Figures 1–3**, they suggest that the increased gene expression caused by lactate can result in enhanced protein function, leading to modified cell response to DNA damaging agents. According to **Figure 4A**, *TP3* and *GSTP1* cannot be included in the gene network involved in the response to CPL. For this reason, we analyzed the level of the corresponding proteins by immunoblotting. Results (**Figure 4C**) showed increased level of TP73 in both lactate-exposed cultures, while GSTP1 protein appeared to be unchanged. GSTP1 belongs to the family of phase II detoxification enzymes, the activity of which is commonly induced by exposition to xenobiotics [32]; for this reason, it can be hypothesized that the upregulated *GSTP1* gene expression caused by lactate is not sufficient for obtaining enhanced protein levels.

Finally, we focused our attention on the two genes showing the highest increased expression in lactate-exposed cells: *PCNA* and *TP73* (**Figures 2A,C**). PCNA is a DNA polymerase accessory factor playing a regulatory role in both DNA repair and replication [33,34]. It was found to be preferentially expressed in actively proliferating human cancer cells and in transformed normal cells; moreover, it has also been widely used as a tumor marker. TP73 is a member of the TP53 family showing prognostic

significance [35]. *TP73* can be translated into different isoforms with opposite functions; in particular, the A isoform (TAp73) shows tumor-suppressor activity, while the Dominant-Negative isoform (ΔNTP73) fails to induce apoptosis and cell cycle arrest. It negatively regulates TP53 and TAp73 by acting as negative dominant. The primer sequences used for the DNA-damage PCR assay did not allow to discriminate between the TP73 isoforms.

For these reasons, an additional PCR study was performed to better characterize the phenotypic changes induced in both SW620 and HepG2 cells by lactate exposure. We analyzed the expression of representative genes associated with proliferative potential and stem cell properties. Results are shown in **Figure 4D**.

Unfortunately, in HepG2 cultures the only detectable genes were those of the epithelial and neural cadherins (*E-* and *N-CAD*) [36] and *Ki67* [37]. No significant changes were observed concerning *E-* and *N-CAD*; a significant increase was detected for *Ki67* expression ($p < 0.05$). An upregulation of this proliferation marker was also found in SW620 cells; in both cell lines, the increased expression of *Ki67* fits well with the data of PCNA expression.

In SW620 cells, lactate was found to markedly increase *E-CAD* levels and to cause reduced ΔNTP73. Together with the unchanged levels of the colon cancer stem markers *NANOG*, *SLUG* and *SNAIL* [38], these effects suggest that the increased trend in cell proliferation usually associated with Ki67 and PCNA is not characterized by phenotypic traits suggesting cancer progression, at least in this cell model. This idea is in line with the markedly upregulated expression of *GSTP1*, primarily observed in HepG2 cells (**Figure 2C**); the clinical significance of this parameter was repeatedly investigated in hepatocellular carcinoma and was found to correlate with a favorable prognosis [39].

Notably, in lactate-exposed SW620 cultures a doubled level of Aldehyde Dehydrogenase (*ALDH1*) was observed, suggesting that the increased resistance of these cells to CPL could also be linked to their higher capacity to cope with oxidative stress [40].

DISCUSSION

A possible role of lactate in regulating gene expression was hypothesized about 20 years ago [41]. Recently, new data have obtained, suggesting for lactate an important role in linking the metabolic state of the cell to gene expression [15–17].

Lactate has been defined a "mirror and motor" of tumor malignancy [42–44], since the metabolic program characterized by increased glycolysis and lactate production supports neoplastic change and tumor progression. Increased glycolysis is also associated with one of the most serious problems complicating cancer treatment, the increased drug resistance [8].

A better understanding of the linkages between the drug resistant phenotype and glycolytic metabolism is complicated by the difficulty of discriminating between a possible effect of lactate from that of other intermediates originating from glucose metabolism, for which a role in transcriptional regulation has also been suggested [4,5].

The experiments described here attempted to address this issue. To our knowledge, our experiments showed for the first time a direct effect of this metabolite on the expression of genes needed for mismatch and nucleotide excision DNA repair, which appeared to compromise the antineoplastic efficacy of cisplatin. Our data suggest that the increased lactate production of cancer cells could facilitate the onset of chemotherapy resistance.

DATA AVAILABILITY STATEMENT

The original contributions presented in the study are included in the article/**Supplementary Material**, further inquiries can be directed to the corresponding author.

AUTHOR CONTRIBUTIONS

GD: Conceptualization; funding acquisition; project administration; software; supervision; writing—review and editing. MG: investigation; methodology; resources; data curation. VR: investigation; methodology; resources; data curation. MM: supervision; data curation. All authors approved the paper.

FUNDING

This work was supported by Cornelia and Roberto Pallotti's Legacy for Cancer Research and by University of Bologna (RFO funds).

CONFLICT OF INTEREST

The authors declare that the research was conducted in the absence of any commercial or financial relationships that could be construed as a potential conflict of interest.

ACKNOWLEDGMENTS

We gratefully acknowledge the contribution from the STRING database.

SUPPLEMENTARY MATERIAL

The Supplementary Material for this article can be found online at: https://www.por-journal.com/articles/10.3389/pore.2021.1609951/full#supplementary-material

REFERENCES

1. DeBerardinis RJ, Chandel NS. Fundamentals of Cancer Metabolism. *Sci Adv* (2016) 2:e1600200. doi:10.1126/sciadv.1600200
2. Bui T, Thompson CB. Cancer's Sweet Tooth. *Cancer Cell* (2006) 9:419–20. doi:10.1016/j.ccr.2006.05.012
3. Warburg O. *Uber den Stoffwechsel der Tumoren*. Berlin: Verlag Springer (1926). Translated into English by Dickens F. under the title: The metabolism of tumours. Constable (1930), London.
4. Liu X-S, Little JB, Yuan Z-M. Glycolytic Metabolism Influences Global Chromatin Structure. *Oncotarget* (2015) 6:4214–25. doi:10.18632/oncotarget.2929
5. van der Knaap JA, Verrijzer CP. Undercover: Gene Control by Metabolites and Metabolic Enzymes. *Genes Dev* (2016) 30:2345–69. doi:10.1101/gad.289140.116
6. Bhatt AN, Chauhan A, Khanna S, Rai Y, Singh S, Soni R. Transient Elevation of Glycolysis Confers Radio-Resistance by Facilitating DNA Repair in Cells. *BMC Cancer* (2015) 15:335. doi:10.1186/s12885-015-1368-9
7. van Vugt MATM. Shutting Down the Power Supply for DNA Repair in Cancer Cells. *J Cel Biol* (2017) 216:295–7. doi:10.1083/jcb.201701026
8. Bhattacharya B, Mohd Omar MF, Soong R. The Warburg Effect and Drug Resistance. *Br J Pharmacol* (2016) 173:970–9. doi:10.1111/bph.13422
9. Fiume L, Manerba M, Vettraino M, Di Stefano G. Inhibition of Lactate Dehydrogenase Activity as an Approach to Cancer Therapy. *Future Med Chem* (2014) 6:429–45. doi:10.4155/fmc.13.206
10. Le A, Cooper CR, Gouw AM, Dinavahi R, Maitra A, Deck LM. Inhibition of Lactate Dehydrogenase A Induces Oxidative Stress and Inhibits Tumor Progression. *Proc Natl Acad Sci USA* (2010) 107:2037–42. doi:10.1073/pnas.0914433107
11. Fiume L, Vettraino M, Manerba M, Di Stefano G. Inhibition of Lactic Dehydrogenase as a Way to Increase the Anti-proliferative Effect of Multi-Targeted Kinase Inhibitors. *Pharmacol Res* (2011) 63:328–34. doi:10.1016/j.phrs.2010.12.005
12. Manerba M, Di Ianni L, Fiume L, Roberti M, Recanatini M, Di Stefano G. Lactate Dehydrogenase Inhibitors Sensitize Lymphoma Cells to Cisplatin without Enhancing the Drug Effects on Immortalized normal Lymphocytes. *Eur J Pharm Sci* (2015) 74:95–102. doi:10.1016/j.ejps.2015.04.022
13. Zhao Y, Butler EB, Tan M. Targeting Cellular Metabolism to Improve Cancer Therapeutics. *Cell Death Dis* (2013) 4:e532. doi:10.1038/cddis.2013.60
14. Boukouris AE, Zervopoulos SD, Michelakis ED. Metabolic Enzymes Moonlighting in the Nucleus: Metabolic Regulation of Gene Transcription. *Trends Biochem Sci* (2016) 41:712–30. doi:10.1016/j.tibs.2016.05.013
15. Latham T, Mackay L, Sproul D, Karim M, Culley J, Harrison DJ. Lactate, a Product of Glycolytic Metabolism, Inhibits Histone Deacetylase Activity and Promotes Changes in Gene Expression. *Nucleic Acids Res* (2012) 40:4794–803. doi:10.1093/nar/gks066
16. Wagner W, Ciszewski WM, Kania KD. L- and D-Lactate Enhance DNA Repair and Modulate the Resistance of Cervical Carcinoma Cells to Anticancer Drugs via Histone Deacetylase Inhibition and Hydroxycarboxylic Acid Receptor 1 Activation. *Cell Commun Signal* (2015) 13:36. doi:10.1186/s12964-015-0114-x
17. San-Millán I, Julian CG, Matarazzo C, Martinez J, Brooks GA. Is Lactate an Oncometabolite? Evidence Supporting a Role for Lactate in the Regulation of Transcriptional Activity of Cancer-Related Genes in MCF7 Breast Cancer Cells. *Front Oncol* (2020) 9:1536. doi:10.3389/fonc.2019.01536
18. Baltazar F, Afonso J, Costa M, Granja S. Lactate beyond a Waste Metabolite: Metabolic Affairs and Signaling in Malignancy. *Front Oncol* (2020) 10:231. doi:10.3389/fonc.2020.00231
19. Pereira-Nunes A, Afonso J, Granja S, Baltazar F. Lactate and Lactate Transporters as Key Players in the Maintenance of the Warburg Effect. *Adv Exp Med Biol* (2020) 1219:51–74. doi:10.1007/978-3-030-34025-4_3
20. Zhang D, Tang Z, Huang H, Zhou G, Cui C, Weng Y. Metabolic Regulation of Gene Expression by Histone Lactylation. *Nature* (2019) 574:575–80. doi:10.1038/s41586-019-1678-1
21. Wagner W, Kania KD, Blauz A, Ciszewski WM. The Lactate Receptor (HCAR1/GPR81) Contributes to Doxorubicin Chemoresistance via ABCB1 Transporter Up-Regulation in Human Cervical Cancer HeLa Cells. *J Physiol Pharmacol* (2017) 68:555–64.
22. Wagner W, Kania KD, Ciszewski WM. Stimulation of Lactate Receptor (HCAR1) Affects Cellular DNA Repair Capacity. *DNA Repair* (2017) 52:49–58. doi:10.1016/j.dnarep.2017.02.007
23. Sprowl-Tanio S, Habowski AN, Pate KT, McQuade MM, Wang K, Edwards RA. Lactate/pyruvate Transporter MCT-1 Is a Direct Wnt Target that Confers Sensitivity to 3-bromopyruvate in colon Cancer. *Cancer Metab* (2016) 4:20. doi:10.1186/s40170-016-0159-3c
24. Fan Q, Yang L, Zhang X, Ma Y, Li Y, Dong L. Autophagy Promotes Metastasis and Glycolysis by Upregulating MCT1 Expression and Wnt/β-Catenin Signaling Pathway Activation in Hepatocellular Carcinoma Cells. *J Exp Clin Cancer Res* (2018) 37:9. doi:10.1186/s13046-018-0673-y
25. Repetto G, del Peso A, Zurita JL. Neutral Red Uptake Assay for the Estimation of Cell Viability/cytotoxicity. *Nat Protoc* (2008) 3:1125–31. doi:10.1038/nprot.2008.75
26. Asaeda A, Ide H, Terato H, Takamori Y, Kubo K. Highly Sensitive Assay of DNA Abasic Sites in Mammalian Cells-Optimization of the Aldehyde Reactive Probe Method. *Analytica Chim Acta* (1998) 365:35–41. doi:10.1016/s0003-2670(97)00648-x
27. Green MR, Sambrook J. Precipitation of DNA with Ethanol. *Cold Spring Harb Protoc* (20162016) 2016:pdb.prot093377. doi:10.1101/pdb.prot093377
28. Sharma A, Singh K, Almasan A. Histone H2AX Phosphorylation: a Marker for DNA Damage. *Methods Mol Biol* (2012) 920:613–26. doi:10.1007/978-1-61779-998-3_40
29. Papacostantinou J, Colowick SP. The Role of Glycolysis in the Growth of Tumor Cells. I. Effects of Oxamic Acid on the Metabolism of Ehrlich Tumor Cells *In Vitro*. *J Biol Chem* (1961) 236:278–84.
30. Chomczynski P, Sacchi N. Single-step Method of RNA Isolation by Acid Guanidinium Thiocyanate-Phenol-Chloroform Extraction. *Anal Biochem* (1987) 162:156–9. doi:10.1006/abio.1987.999910.1016/0003-2697(87)90021-2
31. Basu A, Krishnamurthy S. Cellular Responses to Cisplatin-Induced DNA Damage. *J Nucleic Acids* (2010) 2010:1–16. pii 201367. doi:10.4061/2010/201367
32. Liska DJ. The Detoxification Enzyme Systems. *Altern Med Rev* (1998) 3:187–98.
33. Stoimenov I, Helleday T. PCNA on the Crossroad of Cancer. *Biochem Soc Trans* (2009) 37:605–13. doi:10.1042/BST0370605
34. Wang S-C. PCNA: a Silent Housekeeper or a Potential Therapeutic Target? *Trends Pharmacol Sci* (2014) 35:178–86. doi:10.1016/j.tips.2014.02.004
35. Rodríguez N, Peláez A, Barderas R, Domínguez G. Clinical Implications of the Deregulated TP73 Isoforms Expression in Cancer. *Clin Transl Oncol* (2018) 20:827–36. doi:10.1007/s12094-017-1802-3
36. Loh C-Y, Chai J, Tang T, Wong W, Sethi G, Shanmugam M. The E-Cadherin and N-Cadherin Switch in Epithelial-To-Mesenchymal Transition: Signaling, Therapeutic Implications, and Challenges. *Cells* (2019) 8:1118. doi:10.3390/cells8101118
37. Sun X, Kaufman PD. Ki-67: More Than a Proliferation Marker. *Chromosoma* (2018) 127:175–86. doi:10.1007/s00412-018-0659-8
38. Katoh M. Network of WNT and Other Regulatory Signaling Cascades in Pluripotent Stem Cells and Cancer Stem Cells. *Curr Pharm Biotechnol* (2011) 12:160–70. doi:10.2174/138920111794295710
39. Liu X, Tan N, Liao H, Pan G, Xu Q, Zhu R. High GSTP1 Inhibits Cell Proliferation by Reducing Akt Phosphorylation and Is Associated with a Better Prognosis in Hepatocellular Carcinoma. *Oncotarget* (2018) 9:8957–71. doi:10.18632/oncotarget.23420
40. Vassalli G. Aldehyde Dehydrogenases: Not Just Markers, but Functional Regulators of Stem Cells. *Stem Cell Int* (2019) 2019:1–15. doi:10.1155/2019/3904645
41. Formby B, Stern R. Lactate-sensitive Response Elements in Genes Involved in Hyaluronan Catabolism. *Biochem Biophysical Res Commun* (2003) 305:203–8. doi:10.1016/s0006-291x(03)00723-x
42. Walenta S, Mueller-Klieser WF. Lactate: Mirror and Motor of Tumor Malignancy. *Semin Radiat Oncol* (2004) 14:267–74. doi:10.1016/j.semradonc.2004.04.004
43. Ippolito L, Morandi A, Giannoni E, Chiarugi P. Lactate: a Metabolic Driver in the Tumour Landscape. *Trends Biochem Sci* (2019) 44:153–66. doi:10.1016/j.tibs.2018.10.011
44. de la Cruz-López KG, Castro-Muñoz LJ, Reyes-Hernández DO, García-Carrancá A, Manzo-Merino J. Lactate in the Regulation of Tumor Microenvironment and Therapeutic Approaches. *Front Oncol* (2019) 9:1143. doi:10.3389/fonc.2019.01143

Pathology & Oncology Research

frontiers

ORIGINAL RESEARCH
published: 20 December 2021
doi: 10.3389/pore.2021.1609972

Quantification of Ki67 Change as a Valid Prognostic Indicator of Luminal B Type Breast Cancer After Neoadjuvant Therapy

Shirong Tan[1†], Xin Fu[2†], Shouping Xu[3], Pengfei Qiu[4], Zhidong Lv[5], Yingying Xu[1] and Qiang Zhang[2*]*

[1]Department of Breast Surgery, The First Affiliated Hospital of China Medical University, Shenyang, China, [2]Department of Breast Surgery, Cancer Hospital of China Medical University, Liaoning Cancer Hospital & Institute, Shenyang, China, [3]Department of Breast Surgery, Harbin Medical University Cancer Hospital, Harbin, China, [4]Breast Cancer Center, Shandong Cancer Hospital and Institute, Shandong First Medical University and Shandong Academy of Medical Sciences, Jinan, China, [5]Breast Center, The Affiliated Hospital of Qingdao University, Qingdao, China

Introduction: Ki67 value and its variation before and after neoadjuvant chemotherapy are commonly tested in relation to breast cancer patient prognosis. This study aims to quantify the extent of changes in Ki67 proliferation pre- and post-neoadjuvant chemotherapy, confirm an optimal cut-off point, and evaluate its potential value for predicting survival outcomes in patients with different molecular subtypes of breast cancer.

Methods: This retrospective real-world study recruited 828 patients at the Department of Breast Surgery of the First Affiliated Hospital of China Medical University and the Cancer Hospital of China Medical University from Jan 2014 to Nov 2020. Patient demographic features and disease pathology characteristics were recorded, and biomarkers were verified through immunohistochemistry. Various statistical methods were used to validate the relationships between different characteristics and survival outcomes irrespective of disease-free and overall survival.

Results: Among 828 patients, statistically significant effects between pathological complete response and survival outcome were found in both HER2-enriched and triple-negative breast cancer ($p < 0.05$) but not in Luminal breast cancer ($p > 0.05$). Evident decrease of Ki67 was confirmed after neoadjuvant chemotherapy. To quantify the extent of Ki67 changes between pre- and post-NAC timepoints, we adopted a computational equation termed *ΔKi67%* for research. We found the optimal cut-off value to be "*ΔKi67%* = −63%" *via* the operating characteristic curve, defining *ΔKi67%* ≤ −63% as positive status and *ΔKi67%* > −63% as negative status. Patients with positive *ΔKi67%* status were 37.1% of the entire cohort. Additionally, 4.7, 39.9, 34.5 and 39.6% of patients with Luminal A, Luminal B, HER2-enriched and triple negative breast cancer were

OPEN ACCESS

Edited by:
Anna Sebestyén, Semmelweis University, Hungary

***Correspondence:**
Yingying Xu
xuyingying@cmu.edu.cn
Qiang Zhang
zhangqiang8220@163.com

[†]These authors share first authorship

Received: *20 July 2021*
Accepted: *28 September 2021*
Published: *20 December 2021*

Citation:
Tan S, Fu X, Xu S, Qiu P, Lv Z, Xu Y and Zhang Q (2021) Quantification of Ki67 Change as a Valid Prognostic Indicator of Luminal B Type Breast Cancer After Neoadjuvant Therapy. Pathol. Oncol. Res. 27:1609972. doi: 10.3389/pore.2021.1609972

Abbreviations: AUC, area under the curve; BMI, body mass index; CI, confidence intervals; DFS, disease-free survival; ER, estrogen receptor; FISH, fluorescent *in situ* hybridization; HR, Hazard Ratio; HR, hormone receptors; HER2, human epidermal growth receptor-2; IBC-NST, invasive breast carcinoma of no special type; IRB, institutional review board; IHC, Immunohistochemical; NAC, neoadjuvant chemotherapy; NRI, net reclassification improvement; OS, overall survival; PR, progesterone receptor; pCR, pathological complete response; ROC, operating characteristic curve; TN, triple negative.

also validated with positive *ΔKi67%* status. The statistically significant differences between *ΔKi67%* status and prognostic outcomes were confirmed by univariate and multivariate analysis in Luminal B (univariate and multivariate analysis: $p < 0.05$) and triple negative breast cancer (univariate and multivariate analysis: $p < 0.05$). We proved *ΔKi67%* as a statistically significant independent prognostic factor irrespective of disease-free or overall survival among patients with Luminal B and triple-negative breast cancer.

Conclusions: *ΔKi67%* can aid in predicting patient prognostic outcome, provide a measurement of NAC efficacy, and assist in further clinical decisions, especially for patients with Luminal B breast cancer.

Keywords: breast cancer, prognosis, neoadjuvant chemotherapy, Ki67, tumor response

INTRODUCTION

Breast cancer is the highest cause of cancer-related morbidity among women worldwide [1]. Established biomarkers, including hormone receptors (HR), estrogen receptor (ER), progesterone receptor (PR), human epidermal growth receptor-2(HER-2), and Ki67 labeling index classify breast cancer into four subtypes: HER2-enriched, triple-negative (TN), and Luminal A and B types [2,3]. Neoadjuvant chemotherapy (NAC) is a standard therapeutic strategy for inoperable breast cancer and for some operable patients who seek decreased primary tumor burden and breast conservation [4]. Patient response to NAC also provides guidance for the long-term systemic therapeutic strategy for each individual patient [5]. A achievement of pathological complete response (pCR), disease-free survival (DFS), and overall survival (OS) [6] were used to estimate treatment efficacy. Only 15–20% of patients who receive NAC reach pCR [7–9]. Although pCR plays an important role in prognostic prediction and assists in treatment decisions for TN and HER2-enriched breast cancer, it is less effective in Luminal breast cancer subtypes [10–12]. Luminal breast cancer still lacks indicators to classify patients who will benefit from NAC.

Ki67, a nuclear indicator of cellular proliferation, has been extensively studied and scrutinized for several years. Although some studies criticize Ki67 for its lack of reproducibility [13,14], many demonstrate that proliferation index relates to patient outcomes [2,4,15–17]. These study showKi67 expression as useful indicator for breast cancer and a useful prognostic factor for patients with Luminal B and node-positive breast cancer, assisting in clinical decision regarding neoadjuvant endocrine therapy [18,19]. Some studies indicates that Ki67 levels pre-NAC can be an independent prognostic predictor for OS and DFS [12,16]. Endocrine therapy can decrease cell proliferation, presenting as changed Ki67 level pre- and post-NAC [20,21]. In the POETIC clinical phase-3 trial, this change in Ki67 levels was able to guide endocrine therapy decisions for women with ER-positive breast cancer [19]. One commonality across studies was that decreased levels of Ki67 post-NAC compared to pre-NAC holds significant prognostic predictive value [12,18,22–25]. However, some researchers contend that post-NAC Ki67 may hold limited prognostic value [26].

Previous researches often define the extent of Ki67 change between pre- and post-NAC simply by subtracting the two values. This definition is simple but insufficient, as illustrated in two scenarios. The first is if pre- and post-NAC Ki67 proliferation are both relatively low, then the extent of the change may not reach the set threshold. In the second, the change may be comparatively large but not large enough to reach the cut-off value. Furthermore, high variation of pre- and post-NAC Ki67 have been classified by several groups, with studies proposing different thresholds of variation based on the attempts.

In this retrospective study, we evaluate the usefulness of Ki67 change before and after NAC for predicting survival outcome across breast cancer molecular subtypes. We further quantify the change in Ki67 by percentage before and after NAC and calculate an optimal threshold to assess its predictive function for long-term survival and its ability to aid in deciding further adjuvant therapy modification across breast cancer subtypes.

METHODS

Patient Selection Criterion

This retrospective study included patients with primary breast cancer who were treated with NAC from Jan 2014 to Nov 2020 at the Department of Breast Surgery of the First Affiliated Hospital of China Medical University and the Cancer Hospital of China Medical University.

Patient Inclusion Criteria

All patients received a minimum of one cycle of NAC ahead of surgery. Patients with cancer *in situ* were excluded, as were patients with invasive breast cancer before NAC could be incorporated in cohort. Patients who received any kind of treatment prior to NAC or who presented with progressive or metastatic breast cancer were excluded. Patients with previous breast cancer, male patients, and those with synchronous invasion, bilateral, or inflammatory breast cancer were also excluded. 68 cases with incomplete or deficient IHC analysis were also excluded. In total, 828 patients met the above restriction standards and were included.

Classifications of Patients

This retrospective study received permission from the institutional review board (IRB) of the First Affiliated Hospital and was in accordance with the Helsinki Declaration. All patients involved in the research gave informed consent in written agreements of specimens used for scientific research. The informed consent of retrospective research involvement could be waived based on the retrospective nature of the study. Pre-NAC core needle biopsy pathology and post-surgery regular pathology was extracted and saved in a database. Patient characteristics were collected including gender, age at diagnosis, body mass index (BMI), maximum tumor diameter, tumor grade and stage, axillary lymph node status, histologic type, NAC schedule and cycle number, histology grade, and clinical response to NAC. The local extent of breast cancer was measured *via* breast ultrasound, mammography, breast MRI, chest CT, bone scan and/or hepatobiliary and splenic ultrasound to verify distant metastasis. The final size of local breast cancer in our database was adopted following priorities: breast MRI > breast ultrasound > mammography. Every patient with suspicious lymph-node metastasis suggested by imaging examinations underwent ultrasound-guided core biopsy of ultrasound-graphically abnormal nodes for axillary node metastasis confirmation before starting NAC. The final histological assessments were all analyzed using hematoxylin and eosin staining and immunohistochemical (IHC). The histological type of specimens from incorporated patients was distinguished between two subgroups: general invasive breast carcinoma of no special type (IBC-NST) and Others. The latter group contained special subtypes such as lobular, mucinous and tubular carcinomas with ≥90% of the tumor as a pure special tumor type and mixed IBC-NST with special subtypes. Lymph nodes with micro-metastasis were considered positive, including the maximum diameter over 0.2 mm or the number of tumor cells over 200. Isolated tumor cells were considered negative.

Assessment of Clinical Effectiveness of Chemotherapy

Pathological complete response (pCR) was defined as no residual invasive tumor upon hematoxylin and eosin evaluation of the complete resected breast specimen and all sampled lymph nodes (noninvasive breast residuals) (ypT0/is, ypN0).

Immunohistochemistry for Biomarker Detection

Histopathology is regarded as the gold standard for diagnosis. All breast tumor specimens were acquired from core needle biopsy or surgical resections, and every specimen was affixed into formalin-fixed, paraffin-embedded tissue sections for preservation. IHC staining was performed using Dako Autostainer Plus and EnVision Dual Link detection reagent (DAKO; Carpinteria, CA) with DAB (Dako). Biomarker status, including ER, PR and HER2, were defined by IHC in strict accordance with European Quality Assurance guidelines. ER and PR staining were assessed based on the American Society of Clinical Oncology/College of American Pathologists Guidelines [27,28]. Antibodies used in IHC include as anti-ER (Clone SP1, Dako), anti-PR (Clone PgR636, Dako), and Ki67 (Clone Mib-1, Dako). Hematoxylin II (Dako As Link 48) was used to counterstain specimens automatically. All tests incorporated external positive and negative controls. ER and PR stains were considered positive if immunostaining was seen in more than 1% of immunoreactive cells. HER2 status was ascertained *via* IHC using the Hercep Test ™kit (code K5204, Dako). HER2 expression was scored as 0, 1+, 2+, and 3 + according to ASCO guidelines. A score of 3+ was regarded as HER2+, with 0/1+ defined as HER2-. For cases scoring HER2 2+, a fluorescent *in situ* hybridization (FISH) test could be conducted. The measurement of Ki67 index was based on the spot with the highest intensity in a high-power field (400x) and 500–2000 cells were counted [29].

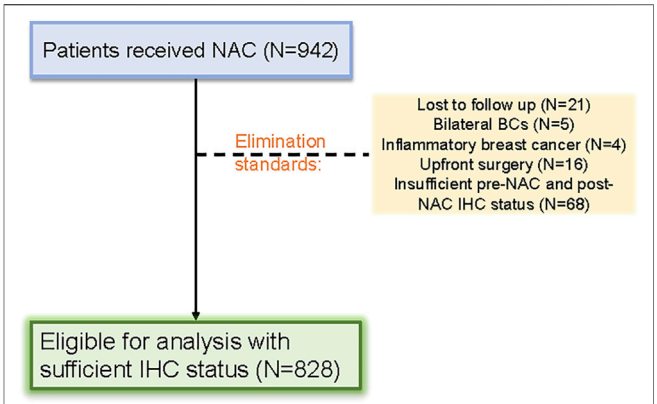

FIGURE 1 | Patient selection flow diagram for the study.

Following the St. Gallen guidelines 2013 [2], high expression of PR was set as ≥20% and low expression of PR was defined as <20%. In accordance with the International Ki67 in Breast Cancer Working Group [30], Ki67 index was classified into two groups: low (<30%), and high (≥30%). To quantify the extent of Ki67 changes between pre- and post-NAC timepoints, we used the following equation: [define post-NAC Ki67 as A, define pre-NAC Ki67 as B, computational formula: $\Delta Ki67\% = (A-B)/B \times 100\%$, maintaining sign]. If a patient achieved pCR after NAC, the post-NAC Ki67 index was defined as 0% and $\Delta Ki67\%$ was mathematically −100%. Representative IHC staining images of Ki67 subgroups are shown in **Supplementary Figure S2**.

Breast Cancer Subtypes Definitions

We classified breast cancers into four subtypes based on HR status, HER2 status and Ki67 index according to the St. Gallen guidelines as follow [2,31]: Luminal A: (ER and PR positive, HER2 negative, "low" Ki-67, and a "low" recurrence risk based on multi-gene-expression assay results if available), Luminal B ["Luminal B-like (HER2 negative)": ER positive, HER2 negative, and at least one of the following: "high" Ki-67, "negative or low" PR, or "high" recurrence risk based on multi-gene-expression assay if available. "Luminal B-like (HER2 positive)": ER positive, HER2 over-expressed or amplified with any Ki-67, and any PR]. HER2-enriched

TABLE 1 | Demographic and clinicopathological features of whole cohort (n = 828).

Parameter	Number (%)
Age at diagnosis (year)	
<40	83 (10.0)
≥40	745 (90.0)
BMI (kg/m^2)	
<18.9 (underweight)	68 (8.2)
18.9–24.9	361 (43.6)
>24.9 (overweight)	399 (48.2)
Histological type at diagnosis	
IBC-NST	699 (84.4)
Others	129 (15.6)
Clinical nodal status at diagnosis	
Positive	676 (81.6)
Negative	152 (18.4)
Chemotherapy cycles	
≤2	199 (24)
3–5	424 (51.2)
>5	205 (24.8)
Chemotherapy regimen	
Taxane -based	89 (10.7)
Anthracycline-based	150 (18.1)
Taxane + anthracycline	589 (71.1)
Anti-HER2 therapy in patients with HER2-positive (n = 261)	
Yes	49 (18.8)
No	212 (81.2)
Clinical tumor stage at diagnosis	
T1	80 (9.7)
T2	556 (67.1)
T3/T4	192 (23.2)
Post-NAC tumor size	
<2 cm	434 (52.4)
2–5 cm	355 (42.9)
>5 cm	39 (4.7)
Response to NAC	
PR/CR	494 (59.7)
SD/PD	334 (40.3)
Achieved pCR	
Yes	138 (16.7)
No	690 (83.3)
ER status[a]	
Positive	526 (63.5)
Negative	302 (36.5)
PR positivity score[b]	
<20%	520 (62.8)
≥20%	308 (37.2)
HER2	
Positive	261 (31.5)
Negative	447 (54.0)
Unknown	120 (14.5)
Pre-NAC Ki67	
<30%	253 (30.6)
≥30%	575 (69.4)
Post-NAC Ki67	
<30%	491 (59.3)
≥30%	337 (40.7)
Molecular subtypes[c]	
Luminal A	43 (5.2)
Luminal B	489 (59.1)
HER2-enriched	148 (17.9)
TNBC	148 (17.9)

[a]*Positivity score<1% including negative status.*
[b]*Positivity score<20% including negative status.*
[c]*Luminal A: (ER and PR positive, HER2 negative, "low" Ki-67, and a "low" recurrence risk based on multi-gene-expression assay results if available), Luminal B ("Luminal B-like (HER2 negative)": ER positive, HER2 negative, and at least one of the following: "high" Ki-67, "negative or low" PR, or "high" recurrence risk based on multi-gene-expression assay if available. "Luminal B-like (HER2 positive)": ER positive, HER2 over-expressed or amplified with any Ki-67, and any PR). HER2-enriched (HER2 over-expressed or amplified, HR absent) and TN (Negative HR and HER2).*
BMI, body mass index; NAC, neoadjuvant chemotherapy; IBC-NST, invasive breast carcinoma of no special Type; pCR, pathological complete response; ER, estrogen receptor; PR, progesterone receptor; HER2, human epidermal growth factor receptor 2; TNBC, triple negative breast cancer.

(HER2 over-expressed or amplified, ER and PR absent) and TN (Negative ER, PR and HER2). The cut-point between "high" and "low" values for Ki67 varies and lacks conclusion. 14% cut-off value of Ki67 for subtype classification was adopted in St. Gallen guidelines 2013.

Statistical Data Analysis

Multiple demographic features were analyzed using the Chi-square test. The survival-related indicators studied were DFS and OS. DFS was calculated from the date of initiation of the first regimen to the date of first event (locoregional relapse, distant relapse, or death) and OS was calculated from the date of surgery to the date of death or last follow-up. The Kaplan–Meier method was used to define the difference ratio, and survival curves were compared using the log-rank test [32]. Significance was assigned as p value < 0.05. Receiver operating characteristic curve (ROC) and area under the curve (AUC) were performed to calculate the optimal cut-off value determined by the Youden index with maximum sensitivity and specificity. Cox proportional hazards regression models were used to estimate relapse and survival risk between subgroups. The multivariate Cox proportional hazards model was implemented for Hazard Ratio (HR) and 95% confidence intervals (CI) to identify independent prognostic factors. Net reclassification improvement (NRI) was used to verify classification accuracy. All statistical data analysis was performed using SPSS 26.0 (SPSS Inc., Chicago, IL, United States) and R programming language (version 3.5.3; https://www.r-project.org/).

RESULTS

Basic Demographic Features and Baseline Characteristics

Patients with primary breast cancer who were treated with NAC were selected based on strict standards. 942 patients were initially included in the cohort, but 114 patients were eliminated for various reasons. A total of 828 female patients with primary breast cancer who received NAC were ultimately included in this retrospective study (**Figure 1**).

Basic demographic and pathologic features are shown in **Table 1**. The median age of entire cohort was 51 ± 9.65 years old (range: 23–76 years), of which 10.0% of patients were under 40 years old at diagnosis. Body mass index was used to distinguish subjects: overweight patients with index greater than or equal to 24.9 accounted for 48.2%, underweight patients with index under 18.9 accounted for 8.2 and 43.6% of patients had a healthy BMI between 18.9–24.9. Breast cancer pathological subtype was

TABLE 2 | The univariate relationship between above features with pCR (n = 828)

Parameter	Pathological response to NAC		
	pCR	Non-pCR	*p* Value
Age at prognosis (years)			0.196
<40	18	65	
≥40	120	625	
BMI (kg/m^2)			0.539
<18.9	11	57	
18.9–24.9	66	295	
>24.9	61	338	
Histological type			<0.001
IBC-NST	95	604	
Others	43	86	
Chemotherapy cycles			0.432
≤2	30	169	
3–5	68	356	
>5	40	165	
Chemotherapy regimen			0.229
Taxane-based	13	76	
Anthracycline-based	32	118	
Taxane + anthracycline	93	496	
Anti-HER2 therapy in patients with HER2-positive (n = 261)			0.293
Yes	12	37	
No	38	174	
Clinical tumor stage at diagnosis			0.267
T1	14	66	
T2	85	471	
T3/T4	39	153	
Post-NAC tumor size			<0.001
<2 cm	104	330	
2–5 cm	30	325	
>5 cm	4	35	
Clinical nodal status			<0.001
Positive	99	577	
Negative	39	113	
ER status[a]			0.014
Positive	75	451	
Negative	63	239	
PR positivity score[b]			0.028
<20%	105	495	
≥20%	33	248	
HER2			0.259
Positive	50	211	
Negative	73	374	
Pre-NAC Ki67			0.147
<30%	35	218	
≥30%	103	472	
Post-NAC Ki67			<0.001
<30%	119	372	
≥30%	19	318	
Molecular subtypes[c]			0.025
Luminal A	3	40	
Luminal B	72	417	
HER2-enriched	29	119	
TNBC	34	114	

[a]*Positivity score<1% including negative status.*

[b]*Positivity score<20% including negative status.*

[c]*Luminal A: (ER and PR positive, HER2 negative, "low" Ki-67, and a "low" recurrence risk based on multi-gene-expression assay results if available), Luminal B ("Luminal B-like (HER2 negative)": ER positive, HER2 negative, and at least one of the following: "high" Ki-67, "negative or low" PR, or "high" recurrence risk based on multi-gene-expression assay if available. "Luminal B-like (HER2 positive)": ER positive, HER2 over-expressed or amplified with any Ki-67, and any PR). HER2-enriched (HER2 over-expressed or amplified, HR absent) and TN (Negative HR and HER2).*

BMI, body mass index; NAC, neoadjuvant chemotherapy; IBC-NST, invasive breast carcinoma of no special Type; pCR, pathological complete response; ER, estrogen receptor; PR, progesterone receptor; HER2, human epidermal growth factor receptor 2; TNBC, triple negative breast cancer.

TABLE 3 | The univariate relationship between above features with DFS and OS (n = 828).

Parameter	DFS (n = 98)			OS (n = 59)		
	Events-free	Events	p Value	Events-free	Events	p Value
Age at prognosis (years)			0.299			0.181
<40	76	7		80	3	
≥40	654	91		689	56	
BMI (kg/m^2)			**0.045**			**0.026**
<18.9	61	7		62	6	
18.9–24.9	323	38		344	17	
>24.9	346	53		363	36	
Histological type			0.849			0.382
IBC-NST	609	90		644	55	
Others	121	8		125	4	
Chemotherapy cycles			0.721			0.567
≤2	174	25		184	15	
3–5	377	47		397	27	
>5	179	26		188	17	
Chemotherapy regimen			0.204			0.364
Taxane-based	77	12		84	5	
Anthracycline-based	138	12		142	8	
Taxane + anthracycline	514	74		542	46	
Anti-HER2 therapy in patients with HER2-positive (n = 261)			0.771			0.712
Yes	44	5		47	2	
No	181	31		195	17	
Clinical tumor stage at diagnosis			0.889			0.499
T1	70	10		72	8	
T2	489	67		519	37	
T3/T4	171	21		178	14	
Post-NAC tumor size			0.871			0.778
<2 cm	384	50		404	30	
2–5 cm	311	44		328	27	
>5 cm	35	4		37	2	
Clinical nodal status			0.256			0.669
Positive	597	78		627	48	
Negative	132	20		141	11	
ER status[a]			0.377			0.293
Positive	471	55		494	32	
Negative	259	43		275	27	
PR positivity score[b]			0.246			0.059
<20%	449	71		474	46	
≥20%	281	27		295	13	
HER2			0.275			0.862
Positive	225	36		242	19	
Negative	402	45		417	30	
Unknown	103	17		110	10	
Pre-NAC Ki67			0.438			0.607
<30%	227	26		237	16	
≥30%	503	72		532	43	
Post-NAC Ki67			**0.008**			**0.004**
<30%	446	45		467	24	
≥30%	284	53		302	35	
Molecular subtypes[c]			0.335			0.571
Luminal A	42	1		42	1	
Luminal B	432	57		456	33	
HER2-enriched	128	20		137	11	
TNBC	128	20		134	14	

[a]*Positivity score<1% including negative status.*

[b]*Positivity score<20% including negative status.*

[c]*Luminal A: (ER and PR positive, HER2 negative, "low" Ki-67, and a "low" recurrence risk based on multi-gene-expression assay results if available), Luminal B ("Luminal B-like (HER2 negative)": ER positive, HER2 negative, and at least one of the following: "high" Ki-67, "negative or low" PR, or "high" recurrence risk based on multi-gene-expression assay if available. "Luminal B-like (HER2 positive)": ER positive, HER2 over-expressed or amplified with any Ki-67, and any PR). HER2-enriched (HER2 over-expressed or amplified, HR absent) and TN (Negative HR and HER2).*

BMI, body mass index; NAC, neoadjuvant chemotherapy; IBC-NST, invasive breast carcinoma of no special Type; pCR, pathological complete response; ER, estrogen receptor; PR, progesterone receptor; HER2, human epidermal growth factor receptor 2; TNBC, triple negative breast cancer.

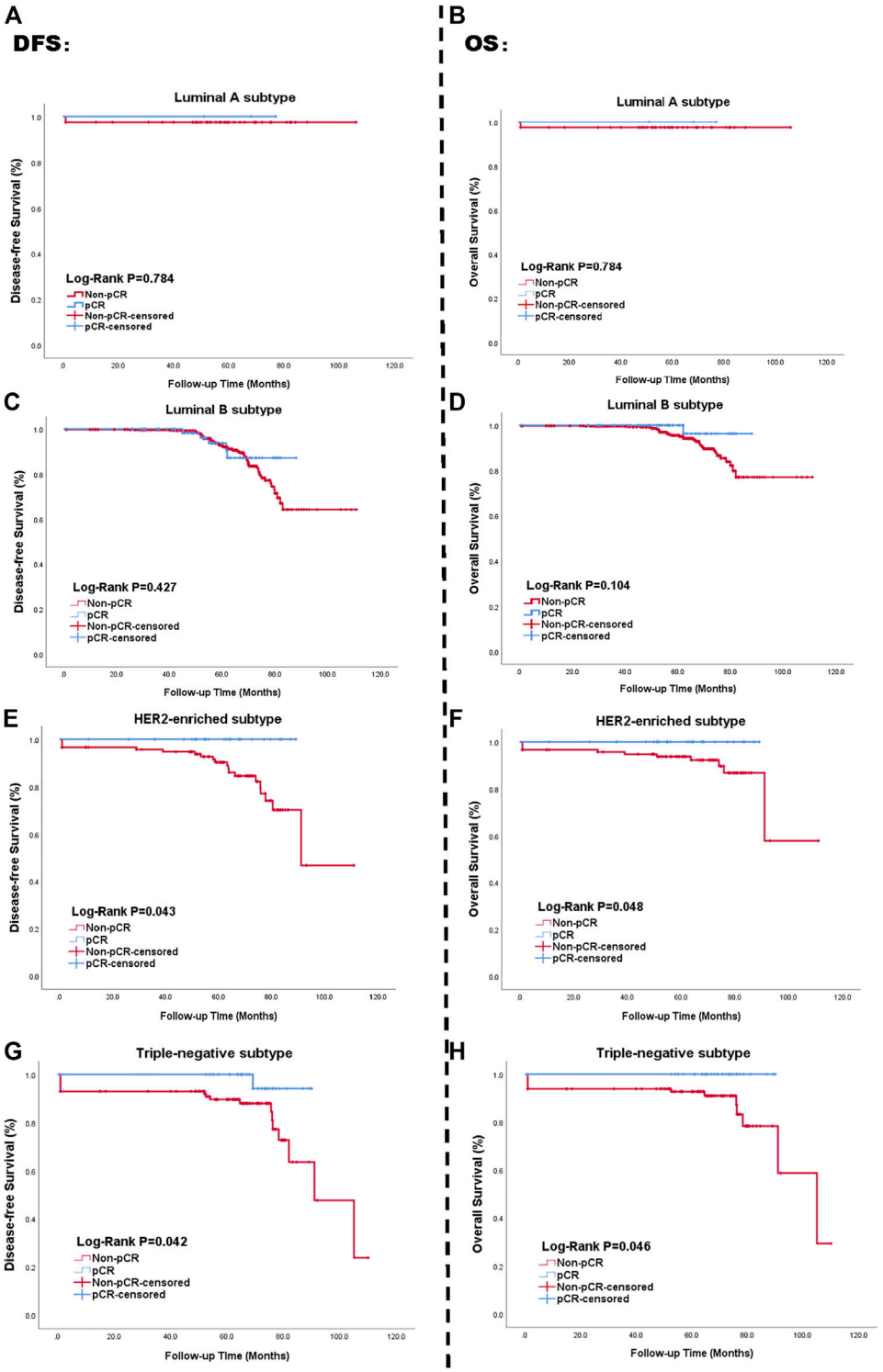

FIGURE 2 | Kaplan-Meier curve of survival in patients with pCR status; Luminal A subtype **(A, B)**, Luminal B subtype **(C, D)**, HER2-enriched subtype **(E, F)**, TN breast cancer subtype **(G, H)**. Blue lines: achieving pCR; Red lines: not achieving pCR. The left side of figure represented the relationship between pCR status and DFS. The right side presented the relationship between pCR status and OS. Abbreviations: pCR, pathological complete response; HER2, human epidermal growth factor receptor 2; TN breast cancer, triple negative breast cancer; DFS, disease-free survival; OS, overall survival.

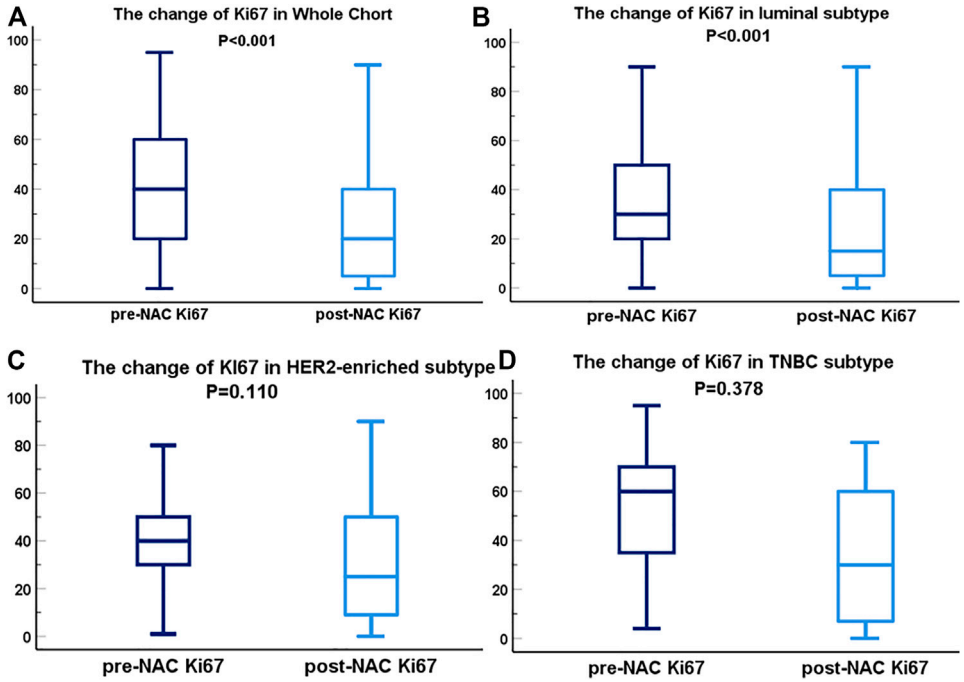

FIGURE 3 | Box-plots of pre- and post-NAC Ki67 expression in diverse molecular subtypes; Ki67 variation in whole cohort **(A)**, Luminal subtype **(B)**, HER2 subtype **(C)** and TN breast cancer subtype **(D)**. The dark blue lines are on behalf of the box-plots of Ki67 before NAC. The light blue lines represent the box-plots of Ki67 after NAC. Abbreviations: pCR, pathological complete response; HER2, human epidermal growth factor receptor 2; TN breast cancer, triple negative breast cancer.

TABLE 4 | The *p* values of AUCs in different subtype and corresponding *ΔKi67%* cut-off point.

Molecular subtype[a]	*p* Value of AUCs	*ΔKi67%* cut-off point
Luminal A	0.107	-
Luminal B	0.047	−63%
HER2-enriched	0.131	-
TNBC	0.009	−68%
Whole cohort	0.004	−63%

[a]*Luminal A: (ER and PR positive, HER2 negative, "low" Ki-67, and a "low" recurrence risk based on multi-gene-expression assay results if available), Luminal B ("Luminal B-like (HER2 negative)": ER positive, HER2 negative, and at least one of the following: "high" Ki-67, "negative or low" PR, or "high" recurrence risk based on multi-gene-expression assay if available. "Luminal B-like (HER2 positive)": ER positive, HER2 over-expressed or amplified with any Ki-67, and any PR). HER2-enriched (HER2 over-expressed or amplified, HR absent) and TN (Negative HR and HER2).*
AUC, area under curve.

confirmed as invasive carcinoma of NST for 84.4% of patients. All other histological types represented 15.6% of the full cohort. A median of 4 NAC cycles were received (range: 1–9), with NAC classified into three groups: texane-based (10.7%), anthracycline-based (18.1%) and texane + anthracycline (71.1%). The average maximum tumor diameters before and after NAC were 3.41 ± 1.651 and 2.26 ± 1.648 cm, respectively. 81.9% patients presented with node-positive status at diagnosis. Finally, 138 subjects (16.7%) who received NAC achieved pCR, a commonly used measurement of NAC efficacy.

We next analyzed IHC biomarkers. Patients with ER positivity made up 59.5% of the cohort. Patients with PR < 20%, or negative status, represented 62.8% of the cohort. Based on strict IHC staining, subjects positive for HER2 accounted for 31.5% of cases 87.6% of all cases had Ki67 expression ≥30% before NAC, while only 58.9% of the cohort had ≥30% Ki67 after NAC. 18.8% of HER2-positive patients received anti-HER2 therapy.

Based on biomarker status, patients were categorized into four subtypes: 43 subjects (5.2%) were categorized as Luminal A subtype breast cancer, 489 subjects (59.1%) had a Luminal B breast cancer, 148 subjects (17.9%) had HER2-enriched breast cancer, and 148 cases (17.9%) had TN breast cancer. IHC status and subtypes distribution are shown in **Table 1**.

Correlation Between Patient Features and Pathological Response to NAC or Survival

We chose pCR as our evaluation criterion of pathological response to NAC. The median follow-up time was 62.00 ± 21.43 months. A associations between patient features and pathological response to NAC or survival were assessed *via* the Chi-square test ($\chi 2$), with results shown in **Table 2**. Age, body mass index, maximum tumor diameter before NAC, and HER2 status all had *p* values > 0.05, indicating no significant influence on prognosis. However, different carcinoma pathology subtypes, maximum diameter after NAC, and nodal status at diagnosis were all significantly associated with pCR, with all *p* values < 0.05. The IHC biomarkers ER, PR and Ki67 status before and after NAC, all associated with pathological response to NAC. The log-rank test was used for in analysis of different parameters with DFS and OS fully considering the follow-up time (**Table 3**).

TABLE 5 | The univariate analysis of relation between basic characteristics with *ΔKi67%* status.

Parameter	*ΔKi67%* status		
	ΔKi67% **≤ −63% (Positive)**	***ΔKi67%*** **> −63% (Negative)**	***p*** **Value**
Age at prognosis (years)			0.105
<40	24	59	
≥40	283	462	
BMI (kg/m^2)			0.208
<18.9	26	42	
18.9–24.9	145	216	
>24.9	136	263	
Histological type			**<0.001**
IBC-NST	228	471	
Others	79	50	
Chemotherapy cycles			**<0.001**
≤2	48	151	
3–5	176	248	
>5	83	122	
Chemotherapy regimen			**<0.001**
Taxane-based	26	63	
Anthracycline-based	81	69	
Taxane + anthracycline	200	389	
Anti-HER2 therapy in patients with HER2-positive (*n* = 261)			0.265
Yes	22	27	
No	77	135	
Clinical tumor stage at diagnosis			**0.002**
T1	21	59	
T2	196	360	
T3/T4	90	102	
Post-NAC tumor size			0.169
<2 cm	174	260	
2–5 cm	120	235	
>5 cm	13	26	
Clinical nodal status			**0.011**
Positive	237	439	
Negative	70	82	
ER status[a]			0.884
Positive	196	330	
Negative	111	191	
PR positivity score[b]			0.532
<20%	197	323	
≥20%	110	198	
HER2			0.771
Positive	99	162	
Negative	161	286	
Unknown	47	73	
Pre-NAC Ki67			**<0.001**
<30%	67	186	
≥30%	240	335	
Post-NAC Ki67			**<0.001**
<30%	303	188	
≥30%	4	333	
Molecular subtypes[c]			**<0.001**
Luminal A	2	41	
Luminal B	195	294	
HER2-enriched	51	97	
TNBC	59	89	

[a]*Positivity score<1% including negative status.*

[b]*Positivity score<20% including negative status.*

[c]*Luminal A: (ER and PR positive, HER2 negative, "low" Ki-67, and a "low" recurrence risk based on multi-gene-expression assay results if available), Luminal B ("Luminal B-like (HER2 negative)": ER positive, HER2 negative, and at least one of the following: "high" Ki-67, "negative or low" PR, or "high" recurrence risk based on multi-gene-expression assay if available. "Luminal B-like (HER2 positive)": ER positive, HER2 over-expressed or amplified with any Ki-67, and any PR). HER2-enriched (HER2 over-expressed or amplified, HR absent) and TN (Negative HR and HER2).*

BMI, body mass index; NAC, neoadjuvant chemotherapy; IBC-NST, invasive breast carcinoma of no special Type; pCR, pathological complete response; ER, estrogen receptor; PR, progesterone receptor; HER2, human epidermal growth factor receptor 2; TNBC, triple negative breast cancer.

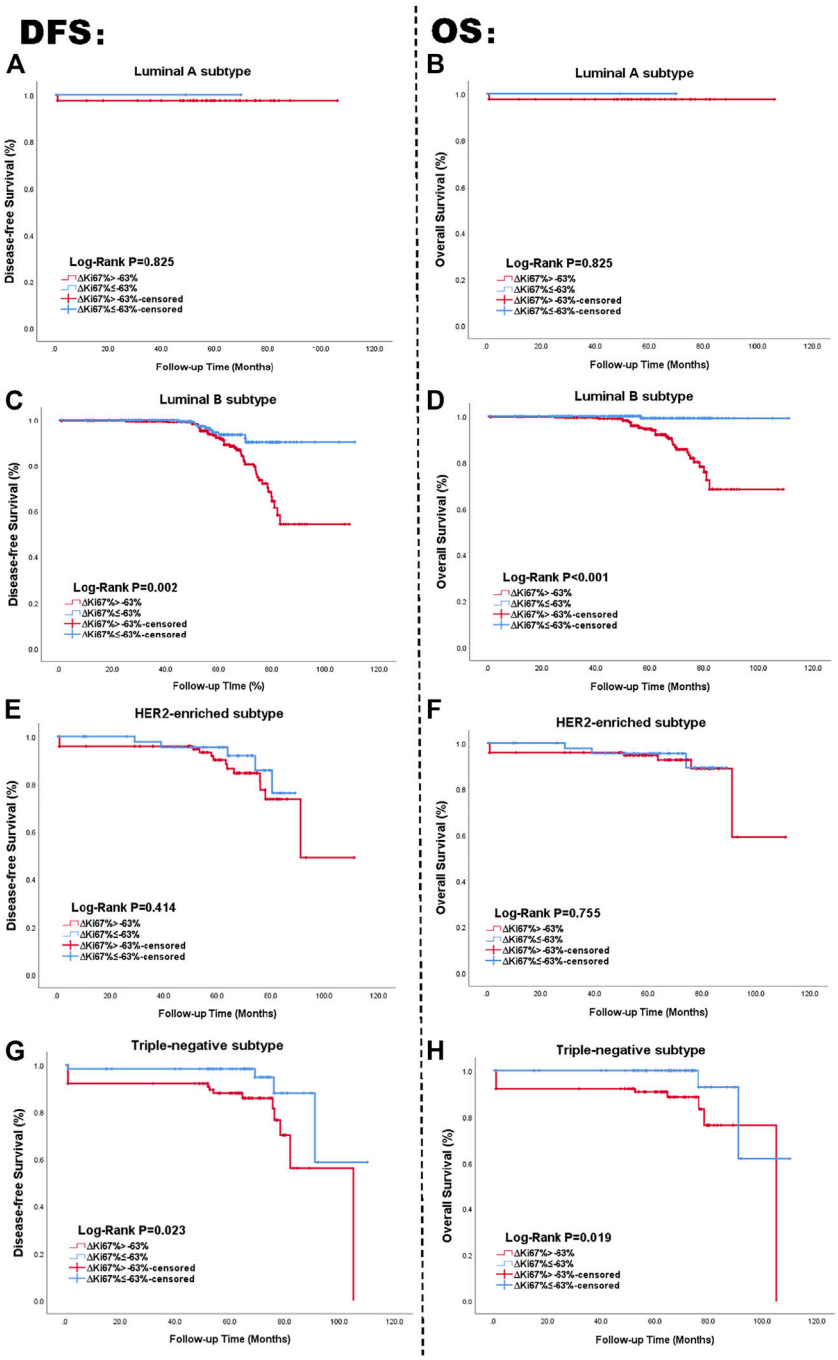

FIGURE 4 | Kaplan Meier curve of DFS and OS in patients with Δ*Ki*67% status; Luminal A subtype **(A, B)**, Luminal B subtype **(C, D)**, HER2-enriched subtype **(E, F)**, TN breast cancer subtype **(G, H)**. The blue lines are on behalf of achieving Δ*Ki*67% -positive status after NAC. The red lines represented the Δ*Ki*67% -negative status after NAC. The left side of the figure shows the relationship between Δ*Ki*67% and DFS. The right side of the figure shows the relationship between Δ*Ki*67% and OS. Abbreviations: HER2, human epidermal growth factor receptor 2; TN, triple negative breast cancer; DFS, disease-free survival; OS, overall survival.

For DFS and OS, BMI and Ki67 after NAC both presented p value < 0.05.

Histological subtype further affected both pCR rates and survival status. Each subtype resulted in different pathological responses, as validated by the Chi-square test ($p < 0.05$), but there was no obvious change on patient prognosis ($p = 0.244 > 0.05$). Rates of pCR across subtypes are shown in **Figure 2**. The left side of the picture presents the relation between pCR and DFS. The right side of the picture presents the univariate analysis of the relationship between OS and pCR based on the Kaplan-Meier method. We calculated survival rates for patients with each subtype using the Kaplan–Meier method.

TABLE 6 | The multivariate Cox analysis of Δ*Ki*67% status in NAC-treated luminal-B subtype patients.

Parameter	Disease-free survival		Overall survival	
	HR (95% CI)	*p* Value	HR (95% CI)	*p* Value
Age at diagnosis (year)		0.741		0.718
<40	1.000		1.000	
≥40	1.171 (0.460–2.983)		1.251 (0.370–4.232)	
BMI (kg/m^2)		**0.001**		0.172
<18.9 (underweight)	1.000		1.000	
18.9–24.9	4.425 (1.288–15.203)	**0.018**	1.347 (0.292–6.217)	0.702
>24.9 (overweight)	7.044 (2.015–24.625)	**0.002**	2.651 (0.591–11.899)	0.203
Histological type		0.625		0.961
IBC-NST	1.000		1.000	
Others	0.732 (0.209–2.565)		Not applicable	
Clinical nodal status at diagnosis		**<0.001**		**0.022**
Positive	1.000		1.000	
Negative	0.264 (0.137–0.511)		0.240 (0.071–0.817)	
Chemotherapy cycles		0.310		0.114
≤2	1.000		1.000	
3–5	0.975 (0.466–2.041)	0.947	1.916 (0.616–5.957)	0.261
>5	1.597 (0.736–3.464)	0.236	3.297 (1.033–10.529)	**0.044**
Chemotherapy regimen		0.216		0.474
Taxane-based	1.000		1.000	
Anthracycline-based	0.307 (0.081–1.154)	0.080	0.326 (0.051–2.076)	0.236
Taxane + anthracycline	0.538 (0.206–1.403)	0.205	0.540 (0.156–1.874)	0.332
Clinical tumor stage at diagnosis		0.585		0.211
T1	1.000		1.000	
T2	0.735 (0.327–1.651)	0.456	0.429 (0.167–1.102)	0.079
T3/T4	0.977 (0.389–2.456)	0.961	0.561 (0.185–1.697)	0.306
Post-NAC tumor size		0.383		0.796
<2 cm	1.000		1.000	
2–5 cm	1.473 (0.819–2.651)	0.196	1.306 (0.597–2.857)	0.504
>5 cm	1.760 (0.481–6.441)	0.393	1.056 (0.125–8.896)	0.960
Post-NAC Ki67		0.454		0.525
<30%	1.000		1.000	
≥30%	0.793 (0.432–1.456)		0.786 (0.375–1.649)	0.635
ΔKi67%		**0.001**		**0.003**
≤−63%	1.000		1.000	
>−63%	3.495 (1.723–7.088)		23.024 (2.956–179.333)	

BMI, body mass index; NAC, neoadjuvant chemotherapy; IBC-NST, invasive breast carcinoma of no special type.

pCR status had no impact on DFS outcome for patients with Luminal A ($p = 0.784 > 0.05$, **Figure 2A**) or Luminal B subtypes ($p = 0.427 > 0.05$, **Figure 2B**). However, both HER2-enriched and TN breast cancer subtype patients showed a significant association between pathological response to NAC and survival outcome ($p = 0.043 < 0.05$, and $p = 0.042 < 0.05$, respectively, **Figures 2C,D**). The corresponding Kaplan-Meier curves of pCR with OS outcome for four subtypes are presented in **Figures 2E–H**. The multivariate Cox analysis for the full cohort is available in **Supplementary Table S1**. The visual result of univariate analysis displayed *via* Kaplan-Meier curves is in **Supplementary Figure S1**.

Assessment of the Prognostic Efficacy of Ki67 Expression Status Before and After NAC

The average Ki67 status before NAC was 39.66% ± 22.61%. In comparison, the average value after NAC was 25.00% ± 22.91%. The downward trend of Ki67 before and after NAC is displayed in **Figure 3** for the whole cohort (A), Luminal subtype (B), HER2-enriched subtype (C), and TN subtype (D). As shown in the figure, Ki67 change before and after NAC presented a statistical difference ($p < 0.001$) in Luminal subtype. However, in HER2-enriched and TN breast cancer, the difference of Ki67 represented no statistical significance. To evaluate the degree of Ki67 decline, we compared post-NAC and pre-NAC proliferation indices [define post-NAC Ki67 as A, define pre-NAC Ki67 as B, the computational formula was $\Delta Ki67\% = (A - B) \div B \times 100\%$, maintaining sign].

We next used ROC curve analysis to determine the optimal cut-off value for *ΔKi67%*. Performing the calculations on SPSS 26.0, we found that *ΔKi67%* had prognostic efficacy on survival outcomes among the full cohort. Based on the ROC calculation results in all patients, we defined an optimal cut-off of $\Delta Ki67\% \leq -63\%$ ($p < 0.05$). The *ΔKi67%* cut-off point in the Luminal B subtype was "−63%" ($p = 0.047$). Meanwhile the cut-off point in the TN breast cancer subtype was "−68%" ($p = 0.009$) (**Table 4**).

Therefore, we defined a reduction of greater than 63% ($\Delta Ki67\% \leq -63\%$) as *ΔKi67%* positive, and a reduction of less than 63% ($\Delta Ki67 > -63\%$) as *ΔKi67%* negative. Positive *ΔKi67%*

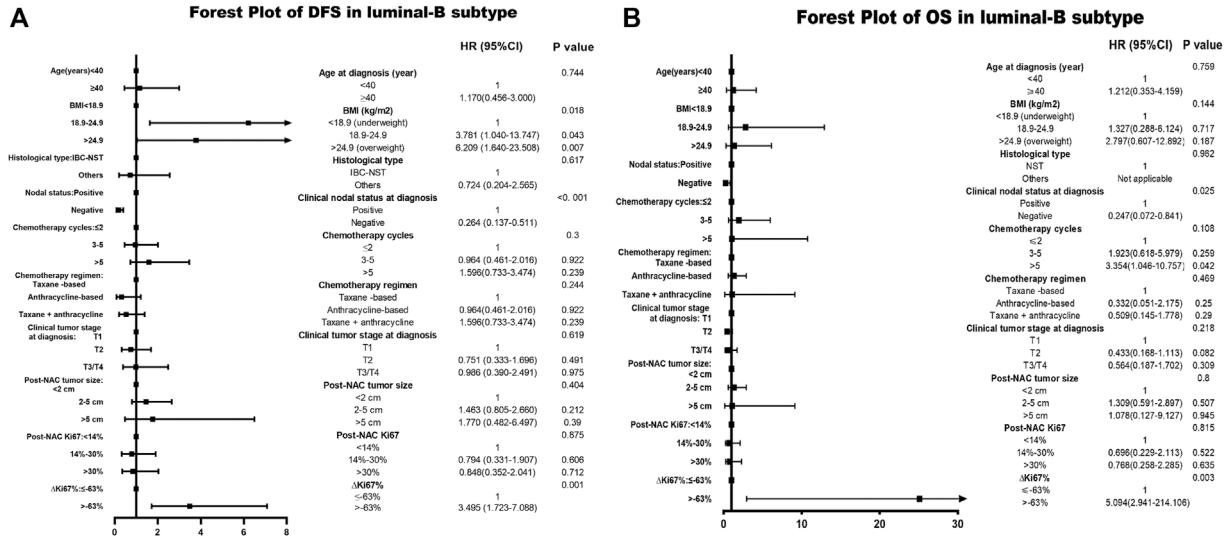

FIGURE 5 | Forest plot of DFS and OS in Luminal B breast cancer; The left side of the figure is exhibiting the forest plot of DFS in Luminal B subtype. The right side of the figure presents the forest plot of OS in Luminal B subtype. The two forest plots both present the multivariate-analyses results; Abbreviations: BMI, body mass index; NAC, neoadjuvant chemotherapy; IBC-NST, invasive breast carcinoma of no special type; DFS, disease-free survival; OS, overall survival.

status presented a larger magnitude of change for *ΔKi67%* between pre- and post- NAC, with negative status showing opposite. We used Chi-square tests to evaluate the relationship between demographic and pathological features and *ΔKi67%* status (**Table 5**). *ΔKi67%* -positive patients represented 37.1% of the full cohort. Histological type, number of chemotherapy cycles, type of chemotherapy regimen, clinical nodal status, molecular subtypes, pre- and post-NAC tumor size, and Ki67 all showed statistically significant relationship with *ΔKi67%* status (p values < 0.05).

In summary, Δ*Ki*67% -positive status related with better survival outcomes. We used the Kaplan-Meier method to affirm the correlation between *ΔKi67%* status and survival outcomes in each molecular subtype. Survival curves of DFS and OS based on Δ*Ki*67% status for the four subtypes are displayed in **Figures 4A–H**. Similar to **Figure 2**, the left side of the figure presents the Kaplan-Meier curves related with DFS and Δ*Ki*67%, with the right side presenting the relationship between OS and Δ*Ki*67%. As shown in the figure, the univariate log-rank test demonstrated Δ*Ki*67% was statistically significantly related to DFS and OS in Luminal B and TN subtype, while it showed no definite effect in Luminal A and HER2-enriched subtypes (all $p > 0.05$).

Based on the multivariate Cox analysis, Δ*Ki*67% status is a significant independent prognostic predictor of survival outcome regardless of DFS and OS, with DFS-HR = 3.495 (95% CI 1.723–7.088, $p = 0.001$) and OS-HR = 23.024 (95% CI 2.956–179.333, $p = 0.003$) for the Luminal B subtype (**Table 6**, corresponding forest plot in **Figure 5**.

Not only that, we tentatively continued to explore the subgroups of Luminal B patients based on the HER2-status. In Luminal B patients from our research, who with negative HER2 status were 256 (52.4%). The patients with positive HER2 status were 113 (23.3%). The patients with unknown HER2 status were 120 (24.5%). The Kaplan-Meier curves and multivariate-analysis results of relationship between *ΔKi67%* and survival outcome were attached in the **Supplementary Presentation S1**. Based on the statistical calculation, the analytical results of all subdivisions in Luminal B tumors fully supported the statistical significance of *ΔKi67%* (univariate and multivariate $p < 0.05$) except the DFS in HER2-positive Luminal B subtypes (univariate and multivariate $p > 0.05$). Combined, *ΔKi67%* was confirmed the statistically significant relationship with disease-free and overall survival outcome.

Among patients with TN breast cancer, Δ*Ki*67% status also provided meaningful survival forecasts on DFS ($p = 0.023 < 0.05$) and OS ($p = 0.019 < 0.05$) presented in **Figure 4**. The relationship between Δ*Ki*67% status and survival outcomes in the TN breast cancer subtype was confirmed by multivariate Cox analysis as well, with DFS-HR = 3.354 (95% CI 1.103–10.196, $p = 0.033$) and OS-HR = 30.774 (95% CI 3.552–266.644, $p = 0.002$) (**Table 7**, corresponding forest plot in **Figure 6**). Two forest plots represented that negative Δ*Ki*67% status is a valid indicator for better prognostics. We further used the Kaplan-Meier method to affirm the correlation between Δ*Ki*67% status and survival outcomes in each molecular subtype. Survival curves based on Δ*Ki*67% status for the four subtypes are displayed in **Figure 6**. Δ*Ki*67% status shows statistically significant differences in Luminal B and TN breast cancer patients. The NRI value comparing the prognostic capacity between Δ*Ki*67% status and pCR in TN breast cancer subtype was 0.685 (95% CI 0.3336–1.0294, $p < 0.001$), also supporting our conclusions. In both **Figures 5**, **6** Δ*Ki*67% had a statistically significant relationship with prognostic outcome.

DISCUSSION

NAC is currently widely applied to shrink tumors and decrease carcinoma volume, allowing patients to preserve breasts or

TABLE 7 | The multivariate Cox analysis of Δ*Ki*67% status in NAC-treated TNBC subtype patients.

Parameter	Disease-free survival		Overall survival	
	HR (95% CI)	*p* Value	HR (95% CI)	*p* Value
Age at diagnosis (year)		0.715		0.988
<40	1.000		1.000	
≥40	1.628 (0.173–15.306)		Not applicable	
BMI (kg/m^2)		0.743		0.154
<18.9 (underweight)	1.000		1.000	
18.9–24.9	0.462 (0.056–3.807)	0.473	0.076 (0.005–1.056)	0.055
>24.9 (overweight)	0.444 (0.055–3.577)	0.446	0.179 (0.018–1.834)	0.179
Histological type		0.325		0.905
IBC-NST	1.000		1.000	
Others	0.429 (0.080–2.315)		1.154 (0.109–12.233)	
Clinical nodal status at diagnosis		0.105		**0.027**
Positive	1.000		1.000	
Negative	0.307 (0.074–1.281)		0.132 (0.022–0.798)	
Chemotherapy cycles		0.225		0.469
≤2	1.000		1.000	
3–5	1.647 (0.476–5.693)	0.431	0.879 (0.203–3.811)	0.863
>5	0.484 (0.096–2.449)	0.380	0.315 (0.043–2.294)	0.254
Clinical tumor stage at diagnosis		0.378		0.308
T1	1.000		1.000	
T2	2.265 (0.328–15.616)	0.407	9.973 (0.513–194.007)	0.129
T3/T4	0.557 (0.038 8.260)	0.671	6.405 (0.167–246.220)	0.319
Post-NAC tumor size		0.462		0.405
<2 cm	1.000		1.000	
2–5 cm	1.048 (0.369–2.976)	0.929	0.939 (0.217–4.060)	0.933
>5 cm	4.088 (0.435–38.418)	0.218	5.091 (0.414–62.551)	0.204
Pre-NAC Ki67		0.137		0.089
<30%	1.000		1.000	
≥30%	4.442 (0.624–31.635)		8.686 (0.722–104.507)	
Post-NAC Ki67		0.027		**0.032**
<30%	1.000		1.000	
≥30%	6.880 (1.238–38.224)		7.221 (1.181–44.133)	
ΔKi67%		0.033		**0.002**
≤−63%	1.000		1.000	
>−63%	3.354 (1.103–10.196)		30.774 (3.552–266.644)	

BMI, body mass index; NAC, neoadjuvant chemotherapy; IBC-NST, invasive breast carcinoma of no special type.

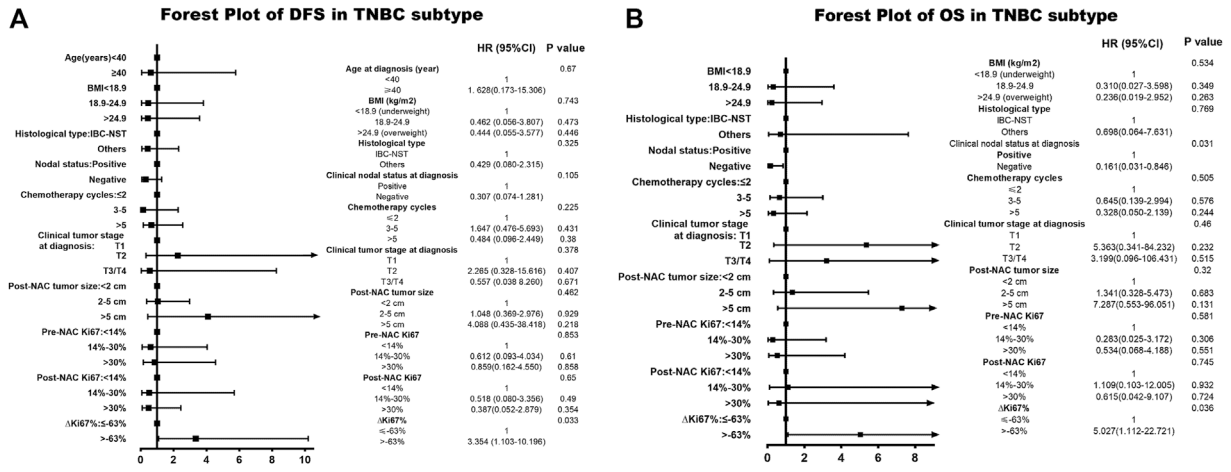

FIGURE 6 | Forest plot of DFS and OS in TN breast cancer. The left side of the figure is exhibiting the forest plot of DFS in triple-negative subtype. The right side of the figure presents the forest plot of OS in triple-negative breast cancer. The two forest plots both present the multivariate-analyses results. Abbreviations: TN, triple negative; BMI, body mass index; NAC, neoadjuvant chemotherapy; IBC-NST, invasive breast carcinoma of no special type; DFS, disease-free survival; OS, overall survival.

become operable [15]. Moreover, the pathological response to NAC is also beneficial for optimizing chemotherapy regimens and predicting relapse possibility and survival outcomes. Patients with pCR to NAC show improved rates of relapse and better survival [33,34].

Many studies have verified correlations between the degree of Ki67 reduction and pathological response to NAC [10,35,36], yet controversies exist regarding the relationships between Ki67 index, pathological response, and survival grates. Some studies only find significant Ki67 proliferation index differences when comparing pre-NAC with post-surgery in Luminal subtypes [37,38] while other studies have demonstrated that Ki67 reduction also plays a role in TN breast cancer [39,40]. While a separate investigation mentioned Δ*Ki*67%, it only discussed its prognostic role and predictive value within 90 Luminal subtype patients with neoadjuvant letrozole-based treatment without classifying it more broadly [20].

In this retrospective real-world study, we analyzed basic demographic and pathological characteristics relative to pCR following to NAC. We confirmed that breast cancer pathological subtype, chemotherapy cycle number, maximum tumor diameter after NAC, nodal state at diagnosis, and Ki67 index pre-NAC and post-NAC all presented statistically significant differences. Furthermore, ER and PR status and molecular subtypes all showed significant effects on pCR rate, as verified in previous studies [41].

As mentioned above, pCR rate ranged from 15 to 20% in previous studies [7–9]. Patients who achieved pCR following NAC represented 16.7% of our cohort, a relatively small portion of the total patients. This implies that pCR status increases the specificity of survival outcome predictions but lowered the sensitivity. Many patients were eliminated in the evaluation system, especially those with the Luminal B subtype who represent the largest portion of all breast cancer patients. This is consistent with previous large trials showing pCR rates to have limited prognostic value in patients with Luminal B subtype [11,12]. ΔKi67% status could help improve this deficiency.

Our study has many strengths. Our fundamental statistical data of post-NAC Ki67 is in accordance with previous research about the relevance of clinical response to NAC and prognostic value [12,24,25]. Subtracting pre- and post-NAC Ki67 is insufficient to account for all situations, therefore we used Δ*Ki*67% as a rational solution. Δ*Ki*67% is an indicator capable of considering the extent of Ki67 changes in all individuals. Since achievement of pCR is not a useful prognostic indicator in the Luminal B subtype, the field currently lacks efficient parameters to predict outcome and assist in clinical decisions makings for these patients [11,12].

ΔKi67% is a useful indicator for more than just Luminal B subtype patients. In patients with TN breast cancer, pCR rate and Δ*Ki*67% status both predicted survival outcome with statistical significance. The multivariate analysis confirmed that Δ*Ki*67% status independently predicted long-term outcomes as well. Δ*Ki*67% status may be capable to aid with NAC regimen modification with pCR status in the TN subtype. In Luminal B subtypes, we made the research based on different HER2-status subgroups. Nearly all results of subgroups support our conclusions regardless of DFS and OS. Except the HER2-positive Luminal B tumors, the DFS *p* value of univariate and multivariate analysis is over 0.05. Meanwhile, considering the function of Δ*Ki*67% in HER2-enriched subtype, it also prompted that HER2(human epidermal growth factor receptor 2) could influence the predictive efficacy of Ki67. The results enlightened us to collect relative data and dig the thoughts deeper.

This study has inherent limitations. Missing data is a common issue in most retrospective single center studies. Hence, we excluded patients whose information was incomplete or inadequate to be incorporated in the study cohort. The second limitation when using Ki67 staining and assessment is lack of stable measurement results [13,14]. To account for this, we adopted the 'hottest-spot' method and performed pathological assessments strictly following international guidelines to improve reproducibility. In the future, artificial intelligence in precision pathology could dramatically improve this method.

In this study, we demonstrate that Δ*Ki*67% status serves as an independent prognostic factor in Luminal B subtype patients. According to the POETIC clinical phase-3 trial, Ki67 variation in women with operable ER-positive primary breast cancer after preoperative and perioperative aromatase inhibitor (POAI) therapy assisted in deciding further adjuvant endocrine therapy and chemotherapy [19]. This indicates that Δ*Ki*67% could fill the current gap for predicting prognostic outcomes in Luminal B subtype patients and assist in further clinical treatment decisions to help modify further adjuvant regimens.

CONCLUSION

In this study, we validated that the extent of Ki67 change before and after NAC, termed Δ*Ki*67%, associates with patient survival outcomes across subtypes. Our statistical calculations defined a cut-off value for Δ*Ki*67% of (−63%). We confirmed that Δ*Ki*67% status presents an independent prognostic prediction indicator for long-term outcome in Luminal B and TN breast cancer subtypes. As pCR achievement is not a statistically significant predictor for Luminal B subtype patients, Δ*Ki*67% status may fill this clinical vacancy, assisting with measuring efficacy of neoadjuvant therapy and providing data for adjuvant therapy adjustment [42].

DATA AVAILABILITY STATEMENT

The raw data supporting the conclusions of this article will be made available by the authors, without undue reservation.

ETHICS STATEMENT

This study was allowed by the Ethics Committee of the First Affiliated Hospital of China Medical University. The protocol of this study was approved by the institutional review board (IRB) of the First Affiliated Hospital and was in accordance with the Helsinki Declaration (AF-SOP-07-1.1-01/2019-13). Written informed consent for participation was not required for this study in accordance with the national legislation and the institutional requirements.

AUTHOR CONTRIBUTIONS

ST analyzed the collected data and wrote the first draft of the manuscript. XF wrote the first draft of the manuscript. XF, SX, PQ, and ZL collected the data and gave assistance on paper revision. YX and QZ were responsible for supervising the whole project and finalizing the manuscript. All authors have read and approved the manuscript.

FUNDING

This work was supported by the National Natural Science Foundation of China (81773083), Scientific and Technological Innovation Leading Talent Project of Liaoning Province (XLYC1802108), Support Project for Young and Technological Innovation Talents of Shenyang (RC190393) and Chinese Young Breast Experts Research Project (CYBER-2021-A02). These projects provided all the funds necessary for the collection of cases, analyses of results, statistical interpretation of data and for the submission of the manuscript.

CONFLICT OF INTEREST

The authors declare that the research was conducted in the absence of any commercial or financial relationships that could be construed as a potential conflict of interest.

SUPPLEMENTARY MATERIAL

The Supplementary Material for this article can be found online at: https://www.por-journal.com/articles/10.3389/pore.2021.1609972/full#supplementary-material

Supplementary Figure S1 | The Kaplan-Meier curves of Δ*Ki*67% in whole cohort. The Supplementary Figure S1 exhibits the results of univariate analysis, Kaplan-Meier method. The left side of the picture presents the relationship between the Δ*Ki*67% status and DFS. The right side of the picture shows the relationship between the Δ*Ki*67% status and OS. The red lines represent the Δ*Ki*67% -positive status after NAC. The blue lines represent the Δ*Ki*67% -negative status after NAC. Abbreviations: DFS, disease-free survival; OS, overall survival.

Supplementary Figure S2 | Representative immunohistochemical staining of Ki67. Ki67<30% **(A, B)**, Ki67≥30% **(C, D)**.

Supplementary Presentation S1 | The results of univariate and multivariate analyses in subdivisions of Luminal B patients. The PDF file contains the Kaplan-Meier curves and tabular-forms of multivariate results regardless of DFS and OS. Luminal B subtype was sorted into four subdivisions: negative HER2 status, positive HER2 status, luminal B subtype excluded HER2-positive status (containing negative and unknown HER2 status) and luminal B subtype excluded HER2-negative status (containing positive and unknown HER2 status). The blue lines are on behalf of achieving Δ*Ki*67% -positive status after NAC. The red lines represented the Δ*Ki*67% -negative status after NAC. The left side of the figure shows the relationship between Δ*Ki*67% and DFS. The right side of the figure shows the relationship between Δ*Ki*67% and OS; Abbreviations: BMI, body mass index; NAC, neoadjuvant chemotherapy; IBC-NST, invasive breast carcinoma of no special type; pCR, pathological complete response; ER, estrogen receptor; PR, progesterone receptor; HER2, human epidermal growth factor receptor 2; TNBC, triple negative breast cancer; DFS, disease-free survival; OS, overall survival.

REFERENCES

1. Siegel RL, Miller KD, Jemal A, et al. Cancer Statistics, 2020. *CA A Cancer J Clin* (2020) 70(1):7–30. doi:10.3322/caac.21590
2. Goldhirsch A, Winer EP, Coates AS, Gelber RD, Piccart-Gebhart M, Thürlimann B, et al. Personalizing the Treatment of Women With Early Breast Cancer: Highlights of the St Gallen International Expert Consensus on the Primary Therapy of Early Breast Cancer 2013. *Ann Oncol* (2013) 24(9): 2206–23. doi:10.1093/annonc/mdt303
3. Cancer Genome Atlas N. Comprehensive Molecular Portraits of Human Breast Tumours. *Nature* (2012) 490(7418):61–70. doi:10.1038/nature11412
4. Van de Wiel M, Dockx Y, Van den Wyngaert T, Stroobants S, Tjalma WAA, and Huizing MT. Neoadjuvant Systemic Therapy in Breast Cancer: Challenges and Uncertainties. *Eur J Obstet Gynecol Reprod Biol* (2017) 210:144–56. doi:10.1016/j.ejogrb.2016.12.014
5. von Minckwitz G, Blohmer JU, Costa SD, Denkert C, Eidtmann H, Eiermann W, et al. Response-Guided Neoadjuvant Chemotherapy for Breast Cancer. *Jco* (2013) 31(29):3623–30. doi:10.1200/JCO.2012.45.0940
6. Cortazar P, Zhang L, Untch M, Mehta K, Costantino JP, Wolmark N, et al. Pathological Complete Response and Long-Term Clinical Benefit in Breast Cancer: the CTNeoBC Pooled Analysis. *The Lancet* (2014) 384(9938):164–72. doi:10.1016/s0140-6736(13)62422-8
7. Wang-Lopez Q, Chalabi N, Abrial C, Radosevic-Robin N, Durando X, Mouret-Reynier M-A, et al. Can Pathologic Complete Response (pCR) Be Used as a Surrogate Marker of Survival After Neoadjuvant Therapy for Breast Cancer? *Crit Rev Oncology/Hematology* (2015) 95(1):88–104. doi:10.1016/j.critrevonc.2015.02.011
8. von Minckwitz G, Fontanella C, et al. Comprehensive Review on the Surrogate Endpoints of Efficacy Proposed or Hypothesized in the Scientific Community Today. *JNCI Monogr* (2015) 2015(51):29–31. doi:10.1093/jncimonographs/lgv007
9. Rodrigues-Ferreira S, Nehlig A, Moindjie H, Monchecourt C, Seiler C, Marangoni E, et al. Improving Breast Cancer Sensitivity to Paclitaxel by Increasing Aneuploidy. *Proc Natl Acad Sci USA* (2019) 116(47):23691–7. doi:10.1073/pnas.1910824116
10. Li L, Han D, Wang X, Wang Q, Tian J, Yao J, et al. Prognostic Values of Ki-67 in Neoadjuvant Setting for Breast Cancer: a Systematic Review and Meta-Analysis. *Future Oncol* (2017) 13(11):1021–34. doi:10.2217/fon-2016-0428
11. von Minckwitz G, Untch M, Blohmer J-U, Costa SD, Eidtmann H, Fasching PA, et al. Definition and Impact of Pathologic Complete Response on Prognosis After Neoadjuvant Chemotherapy in Various Intrinsic Breast Cancer Subtypes. *Jco* (2012) 30(15):1796–804. doi:10.1200/JCO.2011.38.8595
12. Fasching PA, Heusinger K, Haeberle L, Niklos M, Hein A, Bayer CM, et al. Ki67, Chemotherapy Response, and Prognosis in Breast Cancer Patients Receiving Neoadjuvant Treatment. *BMC Cancer* (2011) 11:486. doi:10.1186/1471-2407-11-486
13. Leung SCY, Nielsen TO, Nielsen TO, Zabaglo L, Arun I, Badve SS, et al. Analytical Validation of a Standardized Scoring Protocol for Ki67: Phase 3 of an International Multicenter Collaboration. *NPJ Breast Cancer* (2016) 2:16014. doi:10.1038/npjbcancer.2016.14
14. Andre F, Arnedos M, Goubar A, Ghouadni A, and Delaloge S. Ki67-no Evidence for its Use in Node-Positive Breast Cancer. *Nat Rev Clin Oncol* (2015) 12(5):296–301. doi:10.1038/nrclinonc.2015.46
15. Yoshioka T, Hosoda M, Yamamoto M, Taguchi K, Hatanaka KC, Takakuwa E, et al. Prognostic Significance of Pathologic Complete Response and Ki67 Expression after Neoadjuvant Chemotherapy in Breast Cancer. *Breast Cancer* (2015) 22(2):185–91. doi:10.1007/s12282-013-0474-2
16. Nishimura R, Osako T, Nishiyama Y, Tashima R, Nakano M, Fujisue M, et al. Prognostic Significance of Ki-67 Index Value at the Primary Breast Tumor in Recurrent Breast Cancer. *Mol Clin Oncol* (2014) 2(6):1062–8. doi:10.3892/mco.2014.400
17. Curigliano G, Burstein HJ, Winer EP, Gnant M, Dubsky P, Loibl S, et al. De-Escalating and Escalating Treatments for Early-Stage Breast Cancer: the St. Gallen International Expert Consensus Conference on the Primary Therapy of Early Breast Cancer 2017. *Ann Oncol* (2017) 28(8):1700–12. doi:10.1093/annonc/mdx308
18. Criscitiello C, Disalvatore D, De Laurentiis M, Gelao L, Fumagalli L, Locatelli M, et al. High Ki-67 Score Is Indicative of a Greater Benefit From Adjuvant Chemotherapy When Added to Endocrine Therapy in Luminal B HER2 Negative and Node-Positive Breast Cancer. *The Breast* (2014) 23(1):69–75. doi:10.1016/j.breast.2013.11.007

19. Smith I, Robertson J, Kilburn L, Wilcox M, Evans A, Holcombe C, et al. Long-Term Outcome and Prognostic Value of Ki67 After Perioperative Endocrine Therapy in Postmenopausal Women With Hormone-Sensitive Early Breast Cancer (POETIC): an Open-Label, Multicentre, Parallel-Group, Randomised, Phase 3 Trial. *Lancet Oncol* (2020) 21(11):1443–54. doi:10.1016/s1470-2045(20)30458-7
20. Ianza A, Giudici F, Pinello C, Corona S, Strina C, Bernocchi O, et al. ΔKi67 Proliferation Index as Independent Predictive and Prognostic Factor of Outcome in Luminal Breast Cancer: Data from Neoadjuvant Letrozole-Based Treatment. *Tumour Biol* (2020) 42(6):101042832092530. doi:10.1177/1010428320925301
21. Bazzola L, Foroni C, Andreis D, Zanoni V, Milani M, Cappelletti G, et al. Combination of Letrozole, Metronomic Cyclophosphamide and Sorafenib Is Well-Tolerated and Shows Activity in Patients With Primary Breast Cancer. *Br J Cancer* (2015) 112(1):52–60. doi:10.1038/bjc.2014.563
22. Tanei T, Shimomura A, Shimazu K, Nakayama T, Kim SJ, Iwamoto T, et al. Prognostic Significance of Ki67 Index after Neoadjuvant Chemotherapy in Breast Cancer. *Eur J Surg Oncol (Ejso)* (2011) 37(2):155–61. doi:10.1016/j.ejso.2010.10.009
23. Avci N, Deligonul A, Tolunay S, Cubukcu E, Fatih Olmez O, Ulas A, et al. Neoadjuvant Chemotherapy-Induced Changes in Immunohistochemical Expression of Estrogen Receptor, Progesterone Receptor, HER2, and Ki-67 in Patients with Breast Cancer. *J BUON* (2015) 20(1):45–9. https://pubmed.ncbi.nlm.nih.gov/25778295/#affiliation-1.
24. Kim KI, Lee KH, Kim TR, Chun YS, Lee TH, and Park HK. Ki-67 as a Predictor of Response to Neoadjuvant Chemotherapy in Breast Cancer Patients. *J Breast Cancer* (2014) 17(1):40–6. doi:10.4048/jbc.2014.17.1.40
25. Chen R, Ye Y, Yang C, Peng Y, Zong B, Qu F, et al. Assessment of the Predictive Role of Pretreatment Ki-67 and Ki-67 Changes in Breast Cancer Patients Receiving Neoadjuvant Chemotherapy According to the Molecular Classification: a Retrospective Study of 1010 Patients. *Breast Cancer Res Treat* (2018) 170(1):35–43. doi:10.1007/s10549-018-4730-1
26. Guarneri V, Piacentini F, Ficarra G, Frassoldati A, D'Amico R, Giovannelli S, et al. A Prognostic Model Based on Nodal Status and Ki-67 Predicts the Risk of Recurrence and Death in Breast Cancer Patients With Residual Disease After Preoperative Chemotherapy. *Ann Oncol* (2009) 20(7):1193–8. doi:10.1093/annonc/mdn761
27. Wolff AC, Hammond MEH, Hicks DG, Dowsett M, McShane LM, Allison KH, et al. Recommendations for Human Epidermal Growth Factor Receptor 2 Testing in Breast Cancer: American Society of Clinical Oncology/College of American Pathologists Clinical Practice Guideline Update. *Arch Pathol Lab Med* (2014) 138(2):241–56. doi:10.5858/arpa.2013-0953-SA
28. Hammond MEH, Hayes DF, Dowsett M, Allred DC, Hagerty KL, Badve S, et al. American Society of Clinical Oncology/College of American Pathologists Guideline Recommendations for Immunohistochemical Testing of Estrogen and Progesterone Receptors in Breast Cancer. *Jco* (2010) 28(16):2784–95. doi:10.1200/JCO.2009.25.6529
29. Kobayashi T, Iwaya K, Moriya T, Yamasaki T, Tsuda H, Yamamoto J, et al. A Simple Immunohistochemical Panel Comprising 2 Conventional Markers, Ki67 and P53, Is a Powerful Tool for Predicting Patient Outcome in Luminal-Type Breast Cancer. *BMC Clin Pathol* (2013) 13:5. doi:10.1186/1472-6890-13-5
30. Nielsen TO, Leung SCY, Rimm DL, Dodson A, Acs B, Badve S, et al. Assessment of Ki67 in Breast Cancer: Updated Recommendations From the International Ki67 in Breast Cancer Working Group. *J Natl Cancer Inst* (2021) 113(7):808–19. doi:10.1093/jnci/djaa201
31. Goldhirsch A, Wood WC, Coates AS, Gelber RD, Thürlimann B, Senn H-J, et al. Strategies for Subtypes-Dealing With the Diversity of Breast Cancer: Highlights of the St Gallen International Expert Consensus on the Primary Therapy of Early Breast Cancer 2011. *Ann Oncol* (2011) 22(8):1736–47. doi:10.1093/annonc/mdr304
32. Schemper M, and Smith TL. A Note on Quantifying Follow-Up in Studies of Failure Time. *Controlled Clin Trials* (1996) 17(4):343–6. doi:10.1016/0197-2456(96)00075-x
33. Schott AF, and Hayes DF. Defining the Benefits of Neoadjuvant Chemotherapy for Breast Cancer. *Jco* (2012) 30(15):1747–9. doi:10.1200/jco.2011.41.3161
34. Ellis MJ, Suman VJ, Hoog J, Goncalves R, Sanati S, Creighton CJ, et al. Ki67 Proliferation Index as a Tool for Chemotherapy Decisions During and After Neoadjuvant Aromatase Inhibitor Treatment of Breast Cancer: Results from the American College of Surgeons Oncology Group Z1031 Trial (Alliance). *Jco* (2017) 35(10):1061–9. doi:10.1200/JCO.2016.69.4406
35. Tao M, Chen S, Zhang X, and Zhou Q. Ki-67 Labeling index Is a Predictive Marker for a Pathological Complete Response to Neoadjuvant Chemotherapy in Breast Cancer. *Medicine (Baltimore)* (2017) 96(51):e9384. doi:10.1097/MD.0000000000009384
36. Cabrera-Galeana P, Muñoz-Montaño W, Lara-Medina F, Alvarado-Miranda A, Pérez-Sánchez V, Villarreal-Garza C, et al. Ki67 Changes Identify Worse Outcomes in Residual Breast Cancer Tumors after Neoadjuvant Chemotherapy. *Oncol* (2018) 23(6):670–8. doi:10.1634/theoncologist.2017-0396
37. Ács B, Zámbó V, Vízkeleti L, Szász AM, Madaras L, Szentmártoni G, et al. Ki-67 as a Controversial Predictive and Prognostic Marker in Breast Cancer Patients Treated With Neoadjuvant Chemotherapy. *Diagn Pathol* (2017) 12(1):20. doi:10.1186/s13000-017-0608-5
38. Kim HS, Park S, Koo JS, Kim S, Kim JY, Nam S, et al. Risk Factors Associated With Discordant Ki-67 Levels Between Preoperative Biopsy and Postoperative Surgical Specimens in Breast Cancers. *PLoS One* (2016) 11(3):e0151054. doi:10.1371/journal.pone.0151054
39. Keam B, Im S-A, Lee K-H, Han S-W, Oh D-Y, Kim JH, et al. Ki-67 Can Be Used for Further Classification of Triple Negative Breast Cancer Into Two Subtypes With Different Response and Prognosis. *Breast Cancer Res* (2011) 13(2):R22. doi:10.1186/bcr2834
40. Munzone E, Botteri E, Sciandivasci A, Curigliano G, Nolè F, Mastropasqua M, et al. Prognostic Value of Ki-67 Labeling Index in Patients With Node-Negative, Triple-Negative Breast Cancer. *Breast Cancer Res Treat* (2012) 134(1):277–82. doi:10.1007/s10549-012-2040-6
41. Battisti NML, True V, Chaabouni N, Chopra N, Lee K, Shepherd S, et al. Pathological Complete Response to Neoadjuvant Systemic Therapy in 789 Early and Locally Advanced Breast Cancer Patients: The Royal Marsden Experience. *Breast Cancer Res Treat* (2020) 179(1):101–11. doi:10.1007/s10549-019-05444-0
42. Tyanova S, Albrechtsen R, Kronqvist P, Cox J, Mann M, Geiger T, et al. Proteomic Maps of Breast Cancer Subtypes. *Nat Commun* (2016) 7:10259. doi:10.1038/ncomms10259

Pathology & Oncology Research

POR is dedicated to keeping scientists informed of developments in its focused biomedical fields which span the gap between basic research and clinical medicine.

A special aim of POR is to promote publishing activity in pathology and oncology of colleagues in the Central and East European region. The journal will interest pathologists, and a broad range of experimental and clinical oncologists, and related experts.

Discover more of our Special Issues

See more →

fro.ntiers.in/Liquid-Biopsy
por-journal.com

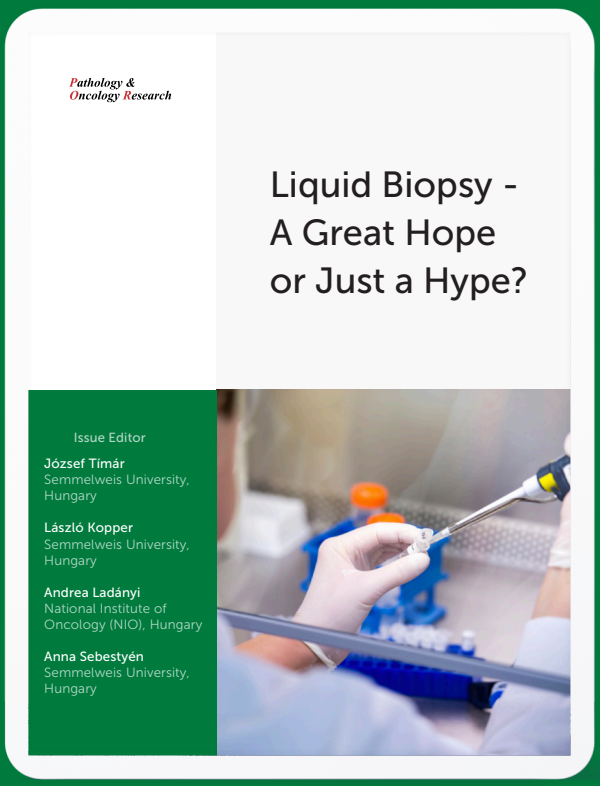

Contact

editorialoffice@por-journal.com